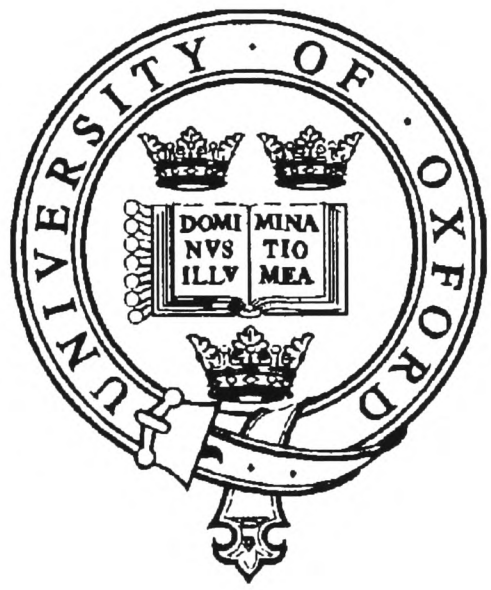
Numerical Modelling of Damage to Masonry Buildings Due to Tunnelling

by

Gang LIU

A thesis submitted to the University of Oxford
for the degree of Doctor of Philosophy



RADCLIFFE SCIENCE LIBRARY OXFORD
DEPOSITED
18 SEP 1997
THESIS

Brasenose College

Trinity Term, 1997

Numerical Modelling of Damage to Masonry Buildings Due to Tunnelling

Gang Liu
Brasenose College

A thesis submitted to the University of Oxford for the Degree of Doctor of Philosophy, Trinity Term, 1997

Accurate assessment of the damage to buildings due to tunnelling in soft ground becomes an important issue when a tunnel is constructed under historic masonry buildings in urban areas. The current two-stage approach in which settlements estimated from a Gaussian curve are applied to a building does not consider soil-structure interaction and fails to give a correct prediction of the damage. This thesis describes a complete three-dimensional finite element model for assessment of the settlement damage to masonry buildings induced by tunnelling in London Clay, and an investigation of the interaction between a masonry building and the ground.

A macroscopic elastic no tension model, which assumes the material has zero tensile strength but infinite compressive strength, is developed to simulate the behaviour of masonry. Numerical techniques are proposed to improve the stability of the calculation.

The comparison of the no tension and elastic models, by applying Gaussian curve settlement troughs to both a plain wall and a facade, shows that the no tension model predicts different behaviour of the masonry building during tunnelling, including different cracking patterns and damage grades.

Two-dimensional finite element analyses combining the building, modelled by the no tension material, and the ground, modelled by a nested yield surface model, give insight into the interaction between the masonry structure and the ground. They suggest the importance of the stresses in the soil prior to the excavation in affecting the ground movements during tunnelling. Thus the weight of the building controls the overall magnitude of the ground movements beneath the building, while the stiffness of the building affects the shape of the trough. A key aspect of the behaviour of the masonry building is the formation of stress arches.

Finally the three-dimensional finite element analyses are described. Both symmetric and unsymmetric cases are analysed. The results show that the three-dimensional analysis gives more realistic modelling of the problem and is likely to be necessary for practical situations, especially when a building is not symmetrically located with respect to the tunnel - a case which cannot be analysed in two-dimensions.

A special tying scheme is proposed for the connection of the nodes belonging to elements of different types, which are defined in their own local co-ordinate systems. Different types of tie elements are formulated and implemented for connection between two-dimensional and three-dimensional elements in various combinations.

Acknowledgements

First of all, I would like to express my sincere thanks to Professor Guy Houlsby. As my supervisor, he has given me tremendous patience, guidance and stimulating discussion. He also generously allowed me to use his programs 2CAN, OXMESH and OXOPT.

I would like to thank Dr Harvey Burd for his helpful advice during my study and providing the access to his program OXPRE.

I am grateful to Mr Charles Augarde, Dr Cong Luan Ngo-Tran and Dr Jianqing Zhou with whom I worked to update OXFEM. I must thank Mr Charles Augarde for his co-operation and help as we worked on the same project.

My special thanks go to Mr Alan Bloodworth, who gave me invaluable help during my preparation of this thesis. I could not imagine how I could have completed it promptly without his kind help.

I gratefully acknowledge the financial supports from the SBFSS Foundation and Brasenose College which made my study at Oxford possible.

Last but not least, I would like to express my deepest gratitude to my wife Xu. Thanks for her support, patience and understanding throughout my study. She is the constant source of love and encouragement. I owe too much to her.

Contents

List of Notations vii

1 Introduction 1

1.1 Background 1

1.2 Current Research 2

1.3 Objective and Outline of This Thesis 5

2 Masonry Modelling 7

2.1 Literature Review on Masonry Models 7

2.1.1 Microscopic Models 8

2.1.2 Macroscopic Models 13

2.1.3 Elastic No Tension Model 17

2.2 Elastic No Tension Model and Its Implementation 18

2.2.1 Constitutive Equations 18

2.2.2 Stress and State Updating 20

2.2.3 Numerical Stability 29

2.3 Test Problems for the Elastic No Tension Model 34

2.3.1 Cavity Expansion with Elastic No Tension Model 34

2.3.2 Bending Beam of Elastic No Tension Model 40

2.4 Summary 45

3 Tying Scheme 46

3.1 Introduction 46

3.2 Current Approaches 47

3.2.1 Common Nodes 47

3.2.2 Constraint of Displacement 48
3.2.3 Tying Scheme 52
3.3 Implementation of Tying Scheme in OXFEM 52
3.3.1 Local Co-ordinate System 52
3.3.2 Construction of Tie Elements 57
3.3.3 Sequence of Gauss Elimination 70
3.3.4 Examples for Using Tie Elements 71
3.4 Summary 75

4 Masonry Wall and Facade on Gaussian Curve Settlement Profile 76
4.1 Current Practice 76
4.1.1 Empirical Estimate of Ground Movement 76
4.1.2 Calculation of the Strain in the Buildings due to Ground Settlement 79
4.1.3 Damage Classification and Building Strain 80
4.2 Models of Plain Walls and Facades 81
4.2.1 Plain Wall 81
4.2.2 Facade 83
4.2.3 Facade Box 83
4.3 Presentation of Results 85
4.3.1 State 85
4.3.2 Cracking Strain 85
4.3.3 Average Cracking Strain 86
4.3.4 Cracked Area Proportion 87
4.4 Plain Wall on Gaussian Curve 87
4.4.1 Burland-Wroth Method 88
4.4.2 Finite Element Analysis: Elastic Wall 88
4.4.3 Finite Element Analysis: Masonry Wall 90
4.4.4 S_{max}-i Curves for Damage Grades 93
4.5 Facade on Gaussian Curve 96
4.5.1 Finite Element Analysis: Elastic Facade 96

4.5.2 Finite Element Analysis: Masonry Facade 98
4.6 Masonry Facade Box on Greenfield Troughs 101
4.6.1 Masonry Facade Box on the Symmetrically Excavated Tunnel . . 103
4.6.2 Masonry Facade Box on the Skew Tunnel 103
4.7 Effect of the Material Parameters 107
4.8 Summary and Conclusions 113

5 2-D Analysis of the Settlement Damage Due to Tunnelling 114
5.1 Soil Model and Tunnelling Simulation 114
5.1.1 Nested Yield Surface Model 115
5.1.2 Soil Properties 115
5.1.3 Tunnelling Simulation 116
5.2 Greenfield Trough by Finite Element Method 117
5.2.1 Settlement Trough 117
5.2.2 Masonry Facade on the Greenfield Trough 118
5.3 Combined Analysis 119
5.3.1 The Models 119
5.3.2 Standard Facade on Standard Tunnel 120
5.3.3 Stability during Tunnelling 123
5.4 Parametric Study 127
5.4.1 Selection and Normalisation of Parameters 127
5.4.2 Test Problems 128
5.4.3 Discussion of Results 133
5.5 A Study on the Position of the Facade 147
5.5.1 The Models 148
5.5.2 Discussion of the Results 150
5.6 Summary and Conclusion 156

6 3-D Analysis of Settlement Damage Due to Tunnelling 160
6.1 Introduction 160
6.2 Model used in Symmetric Runs 162

6.2.1 Building 162
6.2.2 Ground 163
6.2.3 Boundary Condition 163
6.2.4 Loading Process 164
6.3 Symmetric Runs 165
6.3.1 Greenfield, Run SG 165
6.3.2 Combined Analysis with Building of Standard Weight 165
6.3.3 Combined Analysis with Light Weight Building 179
6.4 Models used in Unsymmetric Runs 180
6.4.1 Building 182
6.4.2 Ground 184
6.5 Unsymmetric Runs 184
6.5.1 Greenfield, Run UG 184
6.5.2 Combined Analysis with Standard Building, Run UHN 192
6.5.3 A Comment on the Accuracy of the Solution 200
6.6 Summary and Conclusion 202

7 Concluding Remarks **205**
7.1 Summary and Main Findings of This Study 205
7.2 Recommendation for the Future Research 208

References **210**

List of Notations

a	radius of the inner edge in cavity expansion problem
b	radius of the outer edge in cavity expansion problem
$\boldsymbol{C}$	constraint matrix
c_{lm} $(l, m = 1, 2, ...)$	items of $\boldsymbol{C}$
C	height of soil coverage above a tunnel
C'	dimensionless form of C
c	residual tensile strength
c_i	shear strength of the i-th surface in the nested yield surface model
$c_i' = c_i'/c_u$	dimensionless form of c_i
c_u	undrained shear strength
c_{u0}	undrained shear strength at the ground surface level
$\boldsymbol{D}$	material stiffness matrix
$\boldsymbol{D}^*$	(1) material stiffness matrix in principal space (2) material stiffness matrix in working co-ordinate system
D	diameter of circular tunnel
$\boldsymbol{d}$	total unknown vector
$\boldsymbol{d}_e$	part of total unknown vector to be eliminated in the elimination of redundant displacements
$\boldsymbol{d}_r$	part of total unknown vector to remain in the elimination of redundant displacements
$\boldsymbol{d}_N^G$	displacement vector of Node N in the global co-ordinate system
$\boldsymbol{d}_N^i = (u_N^i, v_N^i, w_w^i)$	displacement vector of Node N in the i-th co-ordinate system
$\boldsymbol{d}_N = (u_N, v_N, w_w)$	displacement vector of Node N in its own local co-ordinate system
d	depth of cracked area in bending beam problem

E	Young's modulus
$(Et)'$	dimensionless form of Et for facade or wall
E_r	residual Young's modulus after cracking
e	the distance between the centrelines of the facade and the tunnel
$\boldsymbol{F}$	total nodal force vector
$\boldsymbol{F'}$	total nodal force vector after eliminating the redundant displacements
$\boldsymbol{f}$	force vector in displacement space $\boldsymbol{u}$
f	residual stiffness factor
G	shear modulus
G_0	shear modulus at the ground surface level
G_i	tangential shear stiffness after activating the i-th surface in the nested yield surface model
$g_i' = G_i/G$	dimensionless form of g_i
H	height of a facade or wall
h	height of beam in the bending beam problem
h_i	hardening parameter of the i-th surface in the nested yield surface model
$h_i' = h_i/G$	dimensionless form of h_i
$\boldsymbol{i}, \boldsymbol{j}, \boldsymbol{k}$	unit vectors corresponding to the x-, y-, z-axes
$\boldsymbol{i}^L, \boldsymbol{j}^L, \boldsymbol{k}^L$	unit vectors corresponding to the x^L-, y^L-, z^L-axes
I	second moment of area of a beam
i	the horizontal distance from the centreline of a tunnel and the point of inflexion of the settlement trough
$\boldsymbol{K}$	global stiffness matrix
k_{lm} $(l, m = 1, 2, ...)$	items of $\boldsymbol{K}$
$\boldsymbol{K'}$	global stiffness matrix after eliminating the redundant displacements
K	ratio between z_0 and i

K_0	coefficient of earth pressure
L	(1) length of beam in the bending beam problem
	(2) length of facade or plain wall
L_s	length of the part of a facade of wall within sagging area
L_h	length of the part of a facade of wall within hogging area
L'	dimensionless form of $L(2)$
M_b	moment about the bottom in the bending beam problem
N	stability number
N_{ground}	stability number in the greenfield condition
N_{total}	stability number when building present
$\boldsymbol{P}_c$	force vector in the displacement space $\boldsymbol{q}$
$\boldsymbol{P}$	force vector in the global space equivalent to $\boldsymbol{P}_c$
P	concentrated force
$\boldsymbol{p}_0 = (x_0, y_0, z_0)$	three points used to define a local co-ordinate system
$\boldsymbol{p}_1 = (x_1, y_1, z_1)$	
$\boldsymbol{p}_2 = (x_2, y_2, z_2)$	
p_0	initial pressure in the cavity expansion and bending problems
p_a, p_b	pressures at the inner and outer edges in the cavity expansion
Δp	increase of the pressure at the inner edge in cavity expansion problem
Δp_{cr}	increase of the pressure at the boundary of cracked area in cavity expansion problem
Δp_{in}	increase of the pressure when the cracks emerge at the inner edge in cavity expansion problem
Δp_{out}	increase of the pressure when the cracks reach the outer edge in cavity expansion problem
$\boldsymbol{Q}$	the right item vector of the constraint equation
$\boldsymbol{q}$	displacement space constructed by the constraint equation
$\boldsymbol{R}$	transformation matrix between different co-ordinate systems

$\boldsymbol{R_x}$	co-ordinate transformation matrix for rotation about x-axis
$\boldsymbol{R_y}$	co-ordinate transformation matrix for rotation about y-axis
$\boldsymbol{R_z}$	co-ordinate transformation matrix for rotation about z-axis
$\boldsymbol{R^i}$	transformation matrix from the global co-ordinate system to i-th local co-ordinate system
$\boldsymbol{R^{ij}}$	transformation matrix from the j-th to i-th local co-ordinate systems
r_{lm}^{ij} or r_{lm} $(l,m=1,2,3)$	items of $\boldsymbol{R^{ij}}$
(r,θ)	polar co-ordinate system
r_c	radius of the boundary of cracked area in cavity expansion problem
S_{max}	maximum settlement
$\boldsymbol{T}$	(1)co-ordinate transformation matrix for strain vector (2)transformation matrix between displacement spaces
t	(1) intersection of incremental strain between different states (2) thickness of a facade of wall (3) distance from the neutral axis to the edge of a beam
U,V,W	displacements in reference co-ordinate system (X,Y,Z) used to construct tie elements
U,v,W	displacements in reference co-ordinate system (X,y,Z) used to construct tie elements
$(u_N,v_N,w_N)=\boldsymbol{d}_N$	the displacements of Node N in its own local co-ordinate system
$(u_N^i,v_N^i,w_N^i)=\boldsymbol{d}_N^i$	the displacements of Node N in the i-th local co-ordinate system
u	radial displacement in the cavity expansion problem
u_a	radial displacement at the inner edge in the cavity expansion problem
u_{r_c}	radial displacement at the boundary between cracked and uncracked areas in the cavity expansion problem

Δu_a	radial displacement change at the inner edge due to the increase of pressure in the cavity expansion problem
V_l	ground loss ratio during excavation
$\boldsymbol{X}^G = (x, y, z)$	global co-ordinate system
$\boldsymbol{X}^L = (x^L, y^L, z^L)$	local co-ordinate system
(x^i, y^i, z^i)	i-th local co-ordinate system
(X, Y, Z)	a reference co-ordinate system used to construct tie elements
(X, y, Z)	a reference co-ordinate system used to construct tie elements
z_0	the depth of the tunnel axis
α^i	the angle between y-axis of i-th local co-ordinate system and its intersection line with other co-ordinate systems.
γ_b	unit weight of masonry material
$(\gamma_b t)'$	dimensionless form of $\gamma_b t$ for facade or wall
γ_s	unit weight of soil
γ_s'	dimensionless form of γ_s
Δ	maximum deflection for simple beam model
Δ_s	maximum deflection within sagging area
Δ_h	maximum deflection within hogging area
δ	settlement
δ'	dimensionless settlement
$\boldsymbol{\epsilon}$	total strain vector
$\epsilon_x, \epsilon_y, \gamma_{xy}$	total strain components in x-y-space
$\epsilon_1, \epsilon_2, \gamma_{12}$	total strain components in working co-ordinate system
ϵ_b	maximum fibre strain in simple beam model
ϵ_d	maximum diagonal strain in simple beam model
$\epsilon_r, \epsilon_\theta$	radial and circumferential strains in polar co-ordinate system
$d\boldsymbol{\epsilon}$, $\Delta\boldsymbol{\epsilon}$	incremental strain vector
$d\epsilon_1, d\epsilon_2$	incremental strain components in the working co-ordinate system
$\Delta\epsilon_x, \Delta\epsilon_y, \Delta\gamma$	incremental strain components in x-y-space

$\Delta\epsilon_1, \Delta\epsilon_2$	strain increment components in the working co-ordinate system
$d\boldsymbol{\epsilon}^e$	elastic strain vector
ϵ_θ^e	circumferential elastic strain
$\boldsymbol{\epsilon}^{cr}$	cracking strain vector
$\epsilon_1^{cr}, \epsilon_2^{cr}, \gamma_{12}^{cr}$	cracking strain components in working co-ordinate system
$\boldsymbol{\epsilon}^{cr(i)}$	cracking strain vector at the end of i-th loading step
$\epsilon_1^{cr(i)}, \epsilon_2^{cr(i)}, \gamma_{12}^{cr(i)}$	cracking strain components at the end of of i-th loading step in working co-ordinate system
ϵ_θ^{cr}	circumferential cracking strain
$\overline{\boldsymbol{\epsilon}}^{cr}$	average cracking strain
$\boldsymbol{\epsilon}^r$	residual strain vector after reclosure of cracks
ϵ_0^{cr}	stiffness reduction ratio
θ, ϕ, ψ	three rotation angles to define a local co-ordinate system
θ	(1) the orientation of major principal stress to x-axis (2) rotation angle of the ends of beam in the bending beam problem (3) see entry for θ, ϕ, ψ (4) see entry for (r, θ)
θ^i	the angle between the i-th local co-ordinate system and the reference system
θ_{top}	rotation angle due to onset of cracks at the top in bending beam problem
ν	Poisson's ratio
$\boldsymbol{\lambda}$	Lagrange multiplier vector
λ	increase ratio of the shear modulus with depth
Π_p	total potential energy
ρ	increase ratio of the undrained strength with depth
$\boldsymbol{\sigma}$	stress vector
$\sigma_x, \sigma_y, \tau_{xy}$	stress components in x-y-space
σ_1, σ_2	(1) major and minor principal stresses

	(2) stress components in the working co-ordinate system
σ_r, σ_θ	radial and circumferential stresses in polar co-ordinate system
$\boldsymbol{\sigma}^{(i)}$	stress vector at the end of i-th loading step
$\sigma_1^{(i)}, \sigma_2^{(i)}$	stresses at the end of i-th loading step in the working co-ordinate system
$\boldsymbol{\sigma}^0$	initial stress vector
σ_1^0, σ_2^0	initial stress components in the working co-ordinate system
σ_0	initial stress in bending beam problem
$d\boldsymbol{\sigma}$, $\Delta\boldsymbol{\sigma}$	incremental stress vector
$d\sigma_1, d\sigma_2$	incremental stress components in the working co-ordinate system
σ_s	surcharge at the ground surface
σ_t	pressure in the tunnel

Subscripts

$1, 2$	(1) major and minor principal stress directions
	(2) two axes in working co-ordinate system
r, θ	radial and circumferential directions in polar co-ordinate system

Superscripts

cr	cracking portion
e	elastic portion
T	transpose of matrix

1

Introduction

1.1 Background

Tunnelling is a common activity in civil engineering, especially in transportation and other infrastructure development in urban areas. A variety of tunnels have been constructed for underground railways, water and power supply and sewerage without disturbing the daily life above. However, the excavation of a tunnel induces ground deformation, which may affect the existing surface structures when the tunnel is constructed in soft ground such as clay or sand.

Although the ground settlement only rarely causes structural damage to buildings, it may cause aesthetic and serviceability damage. Figure 1.1 shows the cracking pattern of a brickwork house located above twin tunnels (Breth, 1974). The adjacent structures, in particular old masonry buildings, may either undergo serious damage resulting in costly repairs or require costly protective measures such as underpinning or compensation grouting. These expenditures may exceed ten percent of the total project cost (Mensah-Dwumah, 1984). In some cases the proposed tunnel alignment had to be altered to avoid an important historic building, for example in the case of the Mansion House in London (Frischmann *et al.*, 1994).

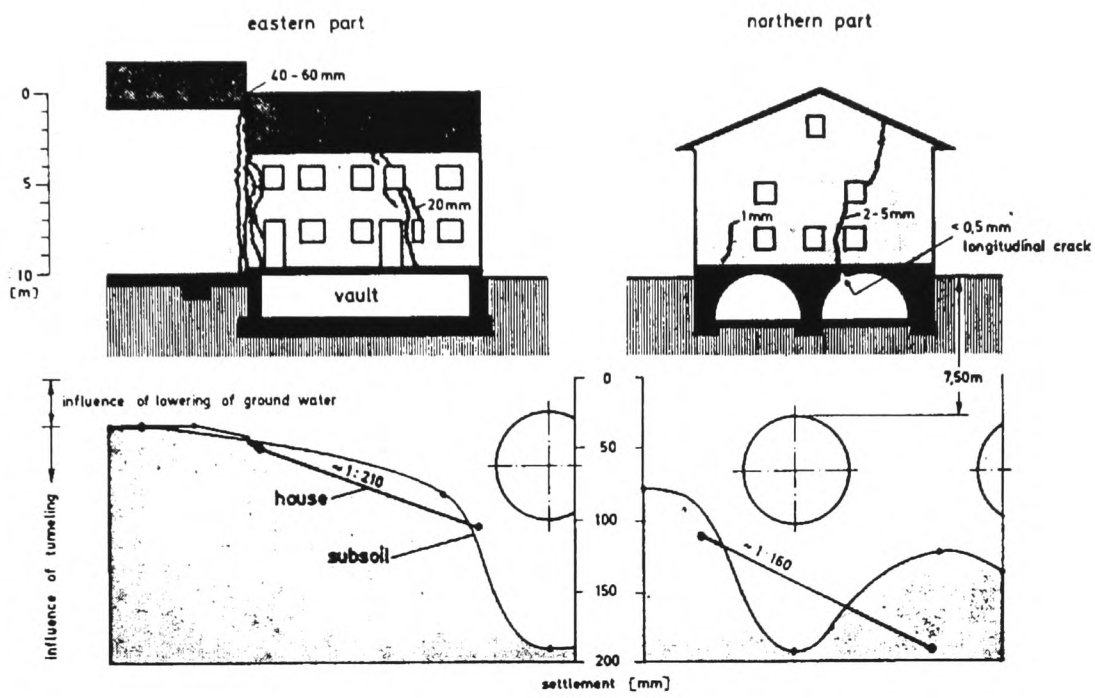


Figure 1.1: Settlement and Cracking of a Brickwork House (Breth, 1974)

It was reported that a large portion of the petitions against the Jubilee Line Extension in London were settlement related (Addenbrooke, 1996), since it involved excavation under many important buildings. At Contract 102, there are 70 highly sensitive buildings on the tunnel route. At Westminster a $17,000\text{m}^2$ area of buildings, structures and services needs to be protected from damage during excavation. The area includes some of London's most historic landmarks, namely Big Ben and Westminster Bridge, the Houses of Parliament, the Treasury Building and the Institution of Civil Engineers. The overall ground treatment at Contract 102 accounts for up to 25% of the civil contract (Wright *et al.*, 1996).

Because of such critical consequences of tunnelling activities, prediction of the ground movements induced by tunnelling and assessment of the influence of tunnelling on adjacent buildings, especially old masonry buildings, and other structures has become an important issue.

1.2 Current Research

As the basis of the analysis of settlement damage, the behaviour of a tunnel itself and the induced ground movements in the "greenfield" condition (*i.e.* with no buildings present)

have been addressed by previous researchers using various methods. These include empirical expression based on case studies (Peck, 1966), centrifuge testing (Mair, 1979), other physical experiments (Kim, 1996) and the finite element method (Lee and Rowe, 1990a,b).

The work addressing the building responses to the ground movements can be categorised into three basic approaches (Boone, 1996). The first approach, the empirical method, is based on compilation of case histories and development of an empirical relationship between damage and readily measured or defined case data. It attempts to use the angular distortion, *i.e.* the ratio of the change of the slope of the settlement trough to the distance between two points (Breth, 1974), or the radius of curvature of the settlement curve (Kerisel, 1975) as the criterion for the onset of cracking damage. The shortcoming of this approach is obvious: it tries to find an "universal" law for buildings without considering the properties of a particular structure.

The second approach considers structural engineering principles to arrive at relationships that define tolerable settlement limits based on selected building dimensions and material properties. These methods often compare their results with case histories. A building is usually modelled as a simply supported elastic deep beam. The ground movements are estimated in the greenfield condition first, then are applied to the elastic beam. The maximum tensile strain in the building can then be calculated and used to judge the possible damage (Burland and Wroth, 1974). As numerical methods are now well developed, buildings can be analysed by finite element methods giving more details than the beam assumption. The investigation of the behaviour of a building is carried out by applying the greenfield movements to the finite element model of the building (Mensah-Dwumah, 1984) (Parry-Jones and Cline, 1993). This approach takes the structural behaviour of buildings into account and is widely used in industry. However, it is based on the greenfield settlement profile without any consideration of the interaction between the building and the ground. The presence of a building will modify the settlement beneath it, which is illustrated in Figure 1.2 showing the actual and predicted settlement profiles beneath the Mansion House in London (Frischmann *et al.*, 1994). The horizontal movement is also considerably reduced by the building in many cases

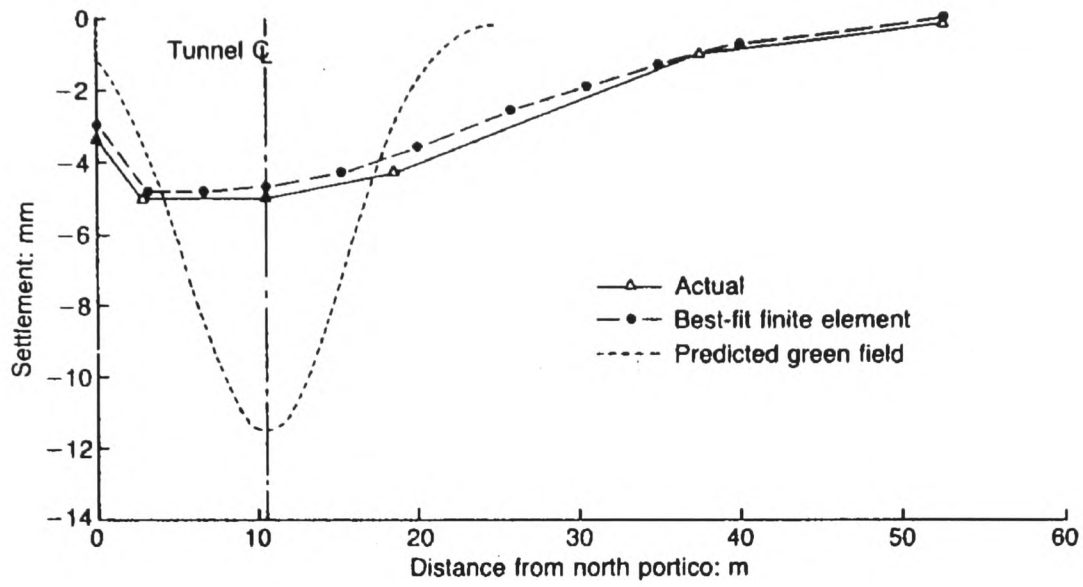


Figure 1.2: Settlement beneath the Mansion House in London (Frischmann *et al.*, 1994)

(Geddes, 1991).

Therefore the third approach, which attempts to include the interaction between the building and ground in prediction of settlement damage, has been used. The simplest form of this approach is a simple beam or a frame on the "Winkler ground" (ground modelled as elastic springs), which is subject to a greenfield settlement profile (Attewell *et al.*, 1986). A more sophisticated study was made by Simpson (1994). A masonry facade consisting of solid masonry, windows and attached floor slabs was modelled by a combination of several strata with different stress strain relationships. To simulate the interaction between the facade and the ground, a cushion of ground was placed between the "remote" greenfield curve and the structure itself. Although these models are able to provide some useful insights into the ground-structure interaction, they still assume that the effects of the building are confined to near the ground surface.

As a part of a research project into the geotechnical aspects of tunnelling at Imperial College (Addenbrooke, 1996), the structure's influence on the ground movement was also addressed (Potts and Addenbrooke, 1997). The ground is simulated by a 2-D finite element model with a non-linear elastic-plastic material model. At the ground surface, an existing surface building is simplified as a weightless elastic beam without any surcharge. This is an attempt to investigate the interaction between the ground and a building. However, an elastic beam without cracking analysis cannot represent the behaviour of

a real building, particularly a masonry building, during the construction of a tunnel. It also emerges in the research reported here that the weight of the building itself may be important.

It can be concluded that the current methods to assess the damage to masonry buildings due to tunnelling do not correctly take the interaction between the building and the ground into account. Generally they overestimate the potential damage. The costly protective measures based on such estimates may not be necessary. On the other hand, the 2-D analysis used by most researchers can only cope with some simplified cases where a building is parallel or orthogonal to the centreline of the tunnel. Therefore development of a suitable 3-D model for correct assessment of the settlement damage to masonry buildings is necessary.

1.3 Objective and Outline of This Thesis

This thesis is the result of a part of a project carried out at Oxford University, which aimed at developing a complete 3-D finite element model for the study of damage of surface buildings caused by the construction of nearby shallow tunnels (Burd *et al.*, 1994).

The project focussed on a shallow tunnel constructed in London Clay below a masonry building. It involved developing and implementing constitutive models for the masonry material and the overconsolidated clay, developing simulation methods for tunnel excavation and liner installation, developing special tie elements to combine the different parts of a building and the building with the ground, revising and upgrading the existing *OX*ford *F*inite *E*lement *M*ethod program *OXFEM* and its pre- and post-processing utilities.

The research reported here was carried out in close co-operation with Augarde(1997), who concentrated principally on the modelling of the 3-D block of ground and the tunnelling process. This thesis is concerned primarily with developing procedures to model masonry buildings and investigating the interaction between the building and the ground. Some issues of interaction between the building and the ground are addressed both here and in Augarde(1997), but from different perspectives. The contents of this

thesis are as follows.

Chapter 1 gives an introduction to this study. In Chapter 2, after a literature review on the constitutive models for the masonry material, the elastic no tension model is chosen for use in this study and is implemented. Some numerical techniques for ensuring the stability of the calculation are discussed.

A tying scheme is proposed and implemented in Chapter 3 for connection of the different walls and the building with the ground, after comparing the current approaches to connect the nodes in elements of different types.

In Chapter 4, a plain wall and a facade are analysed by using the current practice, the two-stage method. A comparison of different material models is made.

Chapter 5 describes 2-D combined analyses. A parametric study is carried out to investigate the interaction between a masonry structure and the ground.

In Chapter 6, 3-D analyses are carried out for a masonry facade box below which a tunnel is excavated. Both symmetric and unsymmetric cases are analysed. The results are compared with the greenfield condition and the 2-D analysis.

Main findings of this study and the consideration of possible future work are discussed in Chapter 7.

2

Masonry Modelling

2.1 Literature Review on Masonry Models

Masonry has been used as a building material for thousands of years. Its wide application has attracted many researchers to carry out studies to generate an appropriate masonry model, especially after the finite element method became popular and powerful.

Although masonry has been widely used for a long time, correctly modelling its behaviour is not straightforward. It is obvious that masonry is an inhomogeneous composite material since it consists of two different components, brick or stone units and mortar joints. Compared with the brick or stone, the mortar has lower stiffness and strength, and higher Poisson's ratio. Thus even simple uniaxial compression of a masonry panel can be a complex process: tension and compression in the orthogonal directions will locally develop in the brick and mortar units respectively. Since the mortar joints act as planes of weakness, masonry exhibits distinct anisotropy. Therefore the layout of brick and mortar units and the direction of loading will affect the behaviour of masonry considerably. Another significant characteristic of masonry is its low tensile strength; consequently tensile cracking is likely to appear in loaded masonry. Therefore, correctly modelling the cracking process and masonry's post-cracking behaviour becomes another

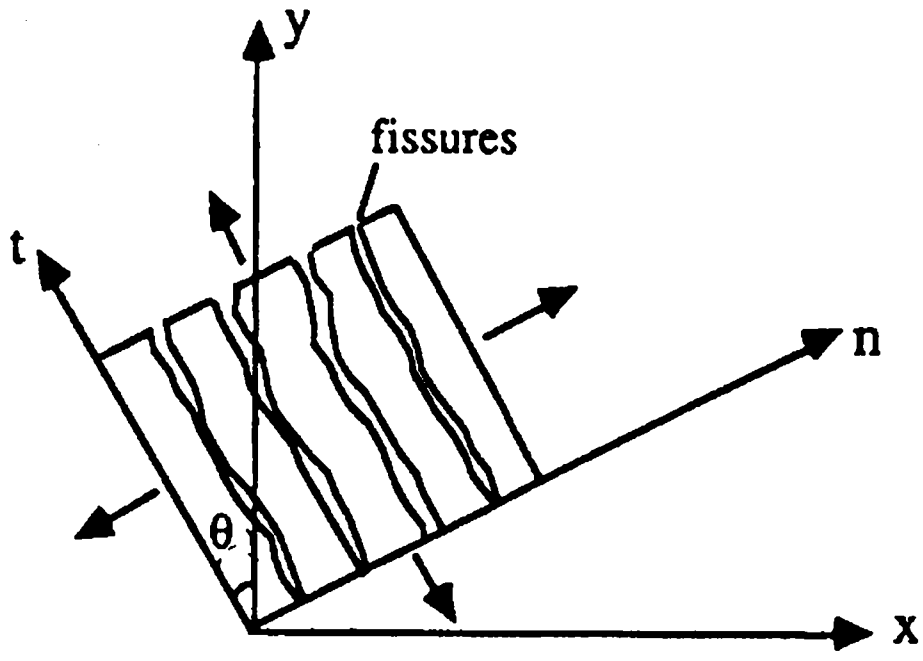


Figure 2.1: Smeared Approach (Loo and Yang, 1991)

important issue.

There are two kinds of masonry models: microscopic and macroscopic models. Microscopic models take bricks and mortar joints into account separately, and give the details of the stress distribution and crack patterns. Macroscopic models treat the masonry as a continuum with the average properties of the bricks and mortar joints, give the stress in terms of the "average" of both parts as well.

There are also two main approaches to simulate the cracking. The discrete crack approach, known as DCA, considers each discrete crack in detail, while in the smeared crack approach, SCA, the cracked masonry is assumed to remain as a continuum rather than embodying a single discrete crack. The smeared crack is represented by an infinite number of parallel fissures across the cracked element or a part of it (Figure 2.1). Usually SCA is adopted to simulate the tensile cracking of the masonry material, either in microscopic or macroscopic models.

2.1.1 Microscopic Models

Because masonry consists of brick units and mortar joints which have different properties, it is reasonable to mimic them separately. In terms of finite element analysis they are different elements with different properties.

After a series of experiments on masonry panels under in-plane loads, Page(1978) summarised the main characteristics of masonry's behaviour.

1. Brick behaves as an elastic-brittle material.

2. Mortar's non-linear stress-strain relation allows significant inelastic deformation of masonry to occur.

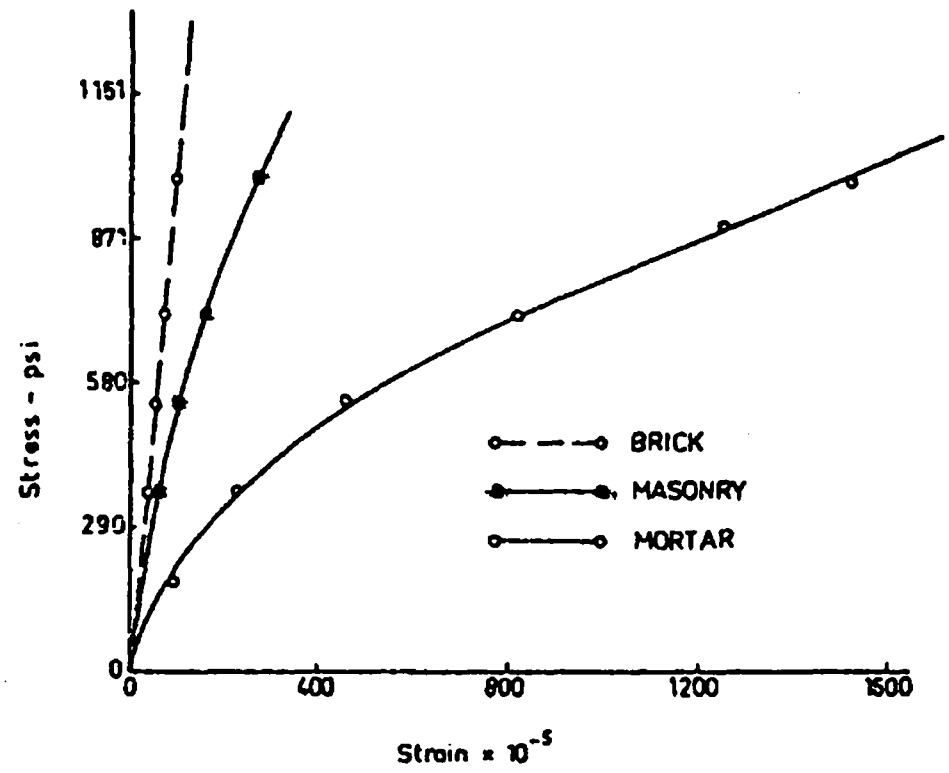
3. Masonry transmits compressive loads very effectively while its tensile strength is extremely low due to its low tensile bond capacity.

4. The behaviour of masonry subjected to a complex stress state is markedly influenced by the orientation of the mortar joint to the applied loads.

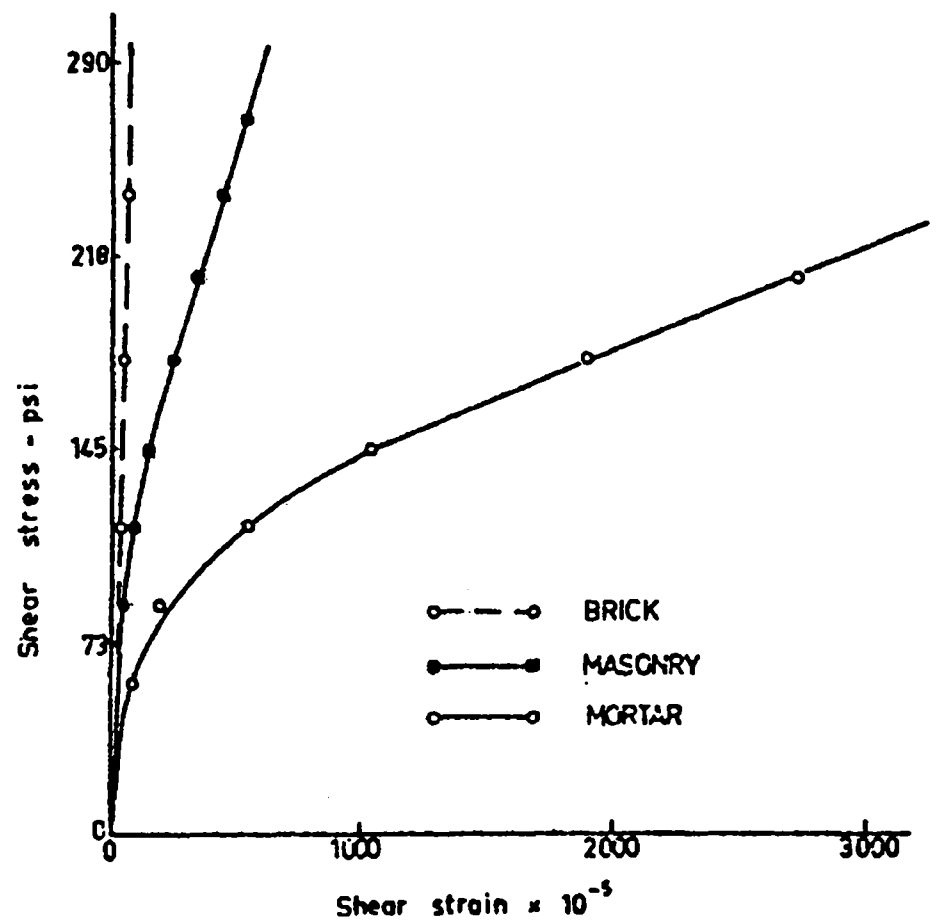
5. Depending upon the degree of compression present, failure can occur in the joints alone, or as a combined brick-joint failure.

Based on these conclusions Page(1978) suggested a microscopic finite element model for the masonry material where elastic continuum elements are used for the bricks and linkage elements for the mortar joints. The properties of mortar joints can be derived from the properties of bricks and overall masonry which are obtained directly from experiments. Some typical strain-stress curves are shown in Figure 2.2. It is seen that for both normal and shear stress-strain curves the high non-linearity of the mortar is evident when compared to the masonry and brick curves. Only bond failure is simulated in this model. The failure envelope is divided into three regions (Figure 2.3). If the criterion of region 1 is violated, tensile bond failure is assumed to occur and no residual capacity is assigned to the joint element. If failure occurs under a combination of compressive and shear stresses a shear bond failure is simulated (region 2 and 3). A reduced shear stiffness is allocated depending upon the τ/σ ratio. When the normal compression is high, some frictional shear capacity remains in the joint after initial cracking. When the normal stress decreases, the residual capacity will reduce to zero under the condition of pure shear.

Although this model is able to reproduce the non-linear behaviour of masonry due to the non-linear joint model and the local bond failure, and to predict the cracking pattern,



(1)



(2)

Figure 2.2: Stress-Strain Curves Used by Page(1978), (1) Uniaxial Compression and (2) Shearing

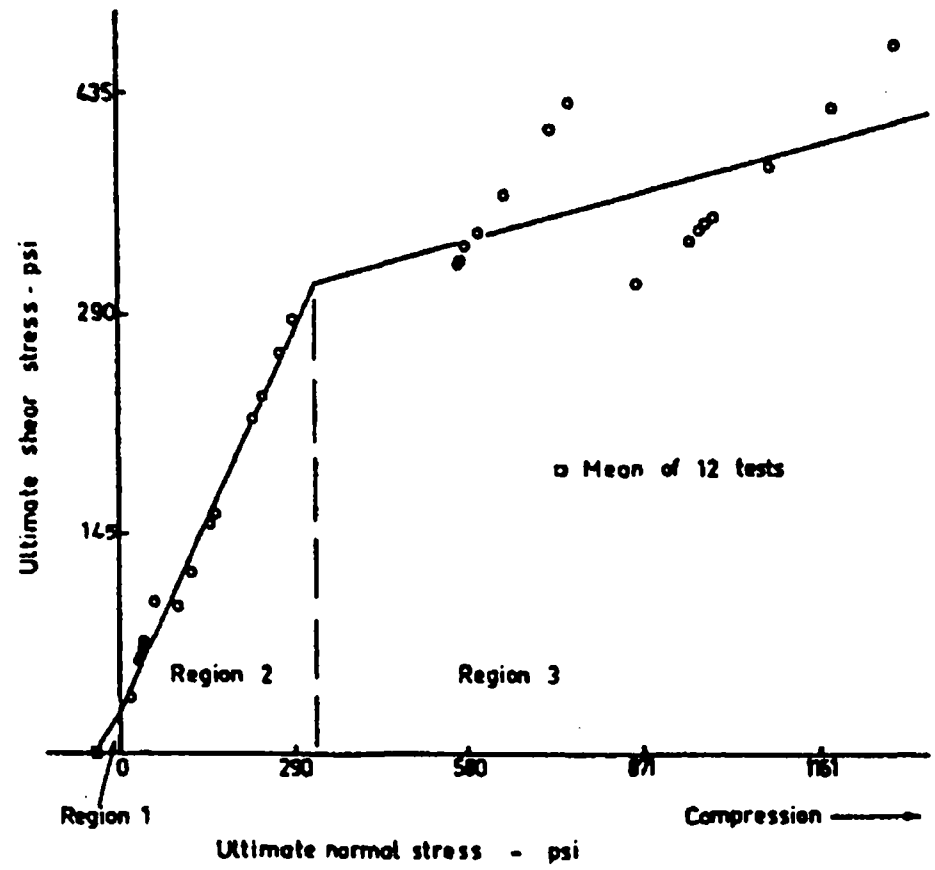


Figure 2.3: Bond Failure Surface Used by (Page, 1978)

it does not consider the failure in bricks and mortar and cannot be used under high stress.

To study a masonry wall subjected to concentrated loads, Ali and Page(1988) proposed a refined finite element model in which both the brick units and mortar joints are modelled by similar non-linear continuum elements. The tensile and compressive failures in either material under the biaxial stress state are controlled by a von Mises failure criterion with a tension cut-off (Figure 2.4). Figure 2.5 gives the three-dimensional failure surface showing the bond failure of a mortar joint subjected to shear and tensile normal stresses in terms of the normal, parallel and shear stresses at the interface. For each failure mode occurring, material stiffness reduces to a specific nominal value when the post-failure behaviour of masonry is modelled. As the sudden reduction of stress for the brittle material would cause numerical instability, a stress softening scheme is adopted to achieve solution convergence (Figure 2.6).

Based on the same philosophy, Ignatakis *et al.*(1990) suggested a microscopic model. As the compressive capacity of the masonry is governed by the transverse tensile stress in the bricks caused by the differential lateral expansion of the stiffer brick and more

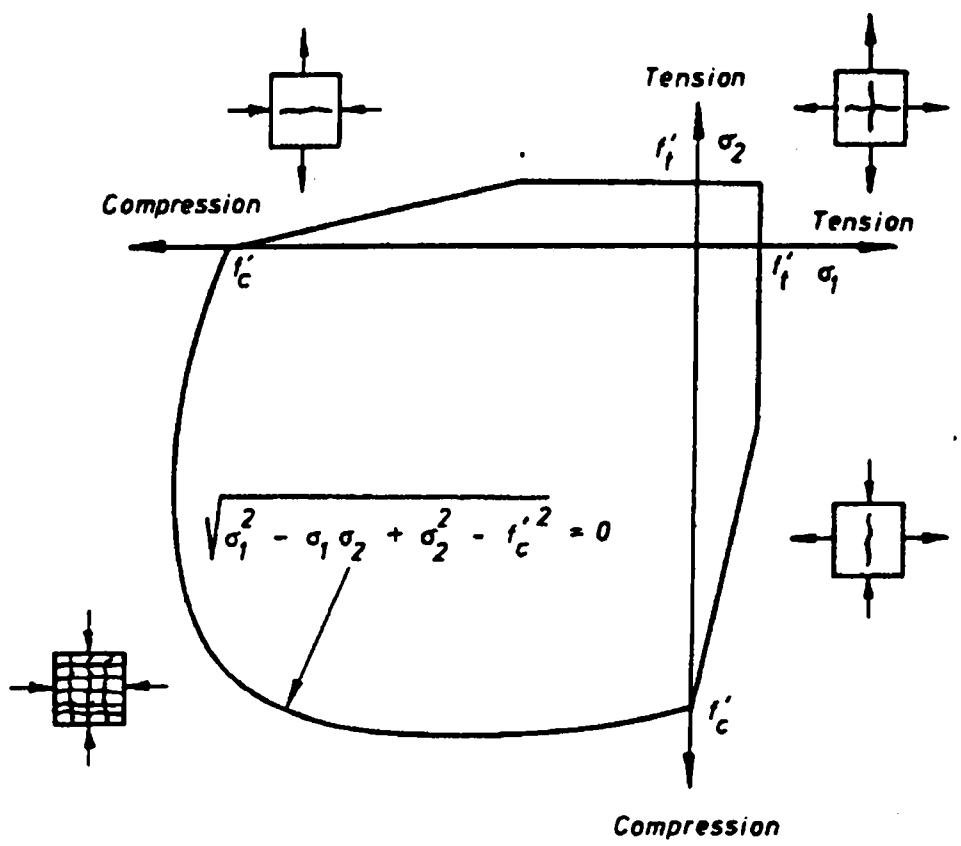


Figure 2.4: Failure Envelope for Brick and Mortar (Ali and Page, 1988)

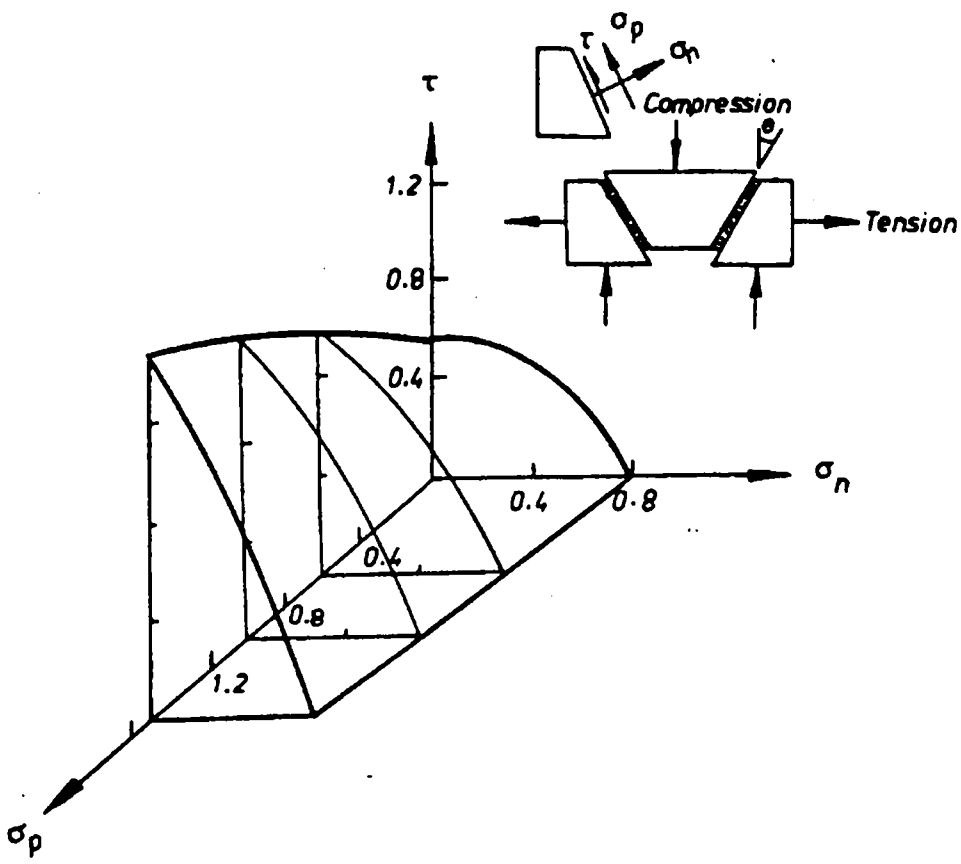


Figure 2.5: Failure Envelope for Bond Failure (Ali and Page, 1988)

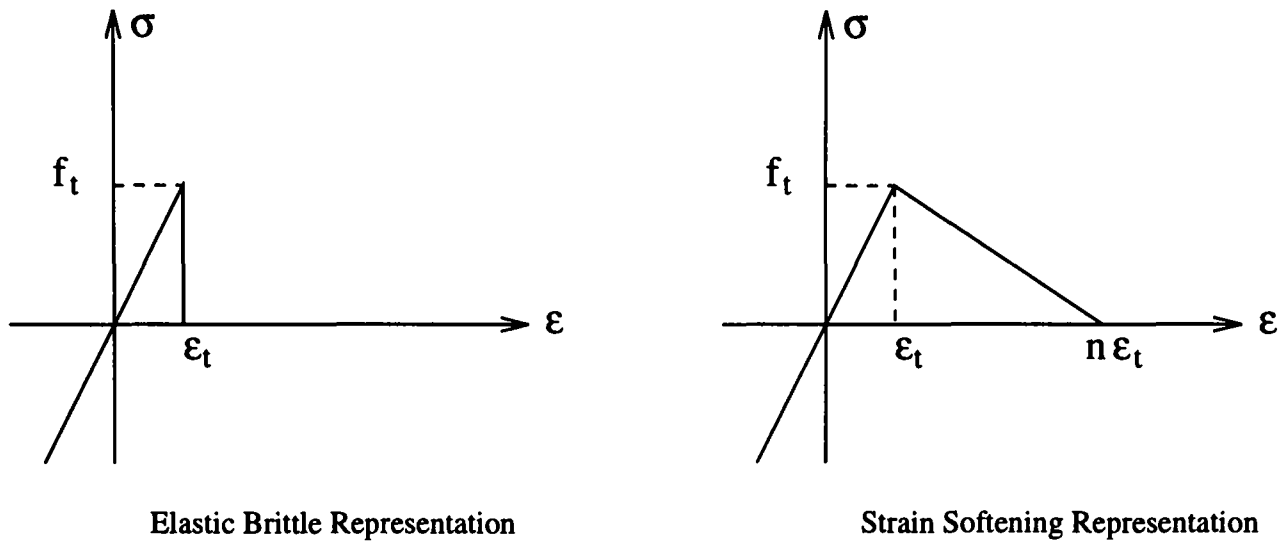


Figure 2.6: Stress Softening Approach (Ali and Page, 1988)

flexible mortar, a triaxial constitutive model and triaxial failure surface are used for both mortar and bricks. The joint failure is also taken into account.

Lotfi and Shing(1994) paid more attention to the joints. Along with a von Mises plasticity model with a tension cut-off failure surface for the masonry units, a dilatant interface element is proposed to simulate the behaviour of mortar joints. The smeared crack approach is used for cracking of masonry units and the interface element is capable of simulating the initiation and propagation of fracture along the mortar joints under combined normal and shear stresses.

Although these comprehensive microscopic models are successful for prediction of masonry behaviour in detail, the extensive amount of computation involved limits their practical application. Usually they are used to mimic the behaviour of small laboratory specimens as an alternative to costly and more time-consuming laboratory experiments.

2.1.2 Macroscopic Models

The other approach, using macroscopic models, considers a homogeneous material law which takes into account the effect of mortar joints in an average sense for the masonry composite. Since the mesh does not need to represent the geometry of the brick and mortar layout, it allows the use of a coarser mesh than the microscopic model in finite element analysis.

Based on their extensive experimental works on the behaviour of brick masonry

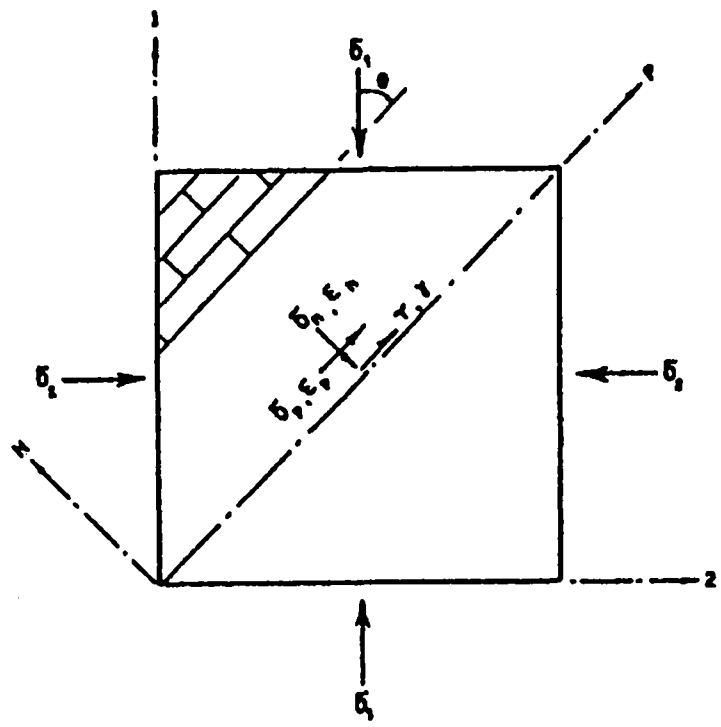


Figure 2.7: Co-ordinate Transfer (Page *et al.*, 1985)

under biaxial stress states, Page *et al.*(1985) made a numerical investigation of the experimental data and developed a macroscopic continuum model for the stress-strain relation and a failure envelope which is directly derived from the experimental results. Although the mortar joint is not considered explicitly, the mortar interface as a weakness plane in masonry is included in the model by generating the constitutive equation and failure envelope in the stress space $(\sigma_n, \sigma_p, \tau_{np})$ where the subscripts n and p stand for the directions normal and parallel to the mortar joint bed direction (Figure 2.7). The strains are decomposed into the elastic and plastic strains. In the $(\sigma_n, \sigma_p, \tau_{np})$ space, it is assumed that:

1. A plastic strain component in a given axial direction is dependent only on the stress in that direction.

2. Plastic strains are related to stresses by a power law and are evident at all stress levels.

The model uses the following relations:

$$\epsilon_n^p = 10^{-3}(\sigma_n/B_n)^{3.3}$$

$$\epsilon_p^p = 10^{-3}(\sigma_p/B_p)^{3.3} \tag{2.1}$$

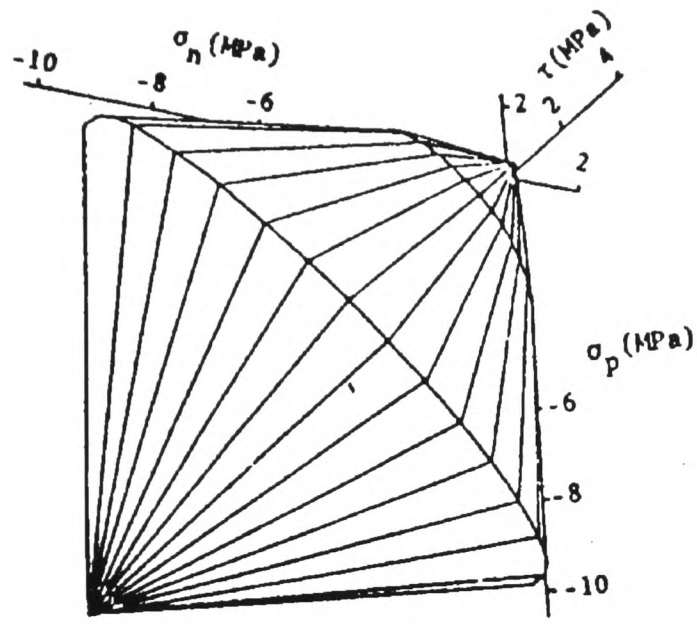


Figure 2.8: Failure Surface in n-p Space (Page *et al.*, 1985)

$$\gamma_{np}^{p} = 10^{-3}(\tau_{np}/B_s)^{4.0}$$

where B_n, B_p, B_s are the parameters derived from the experiments.

Also in the $(\sigma_n, \sigma_p, \tau_{np})$ space, the failure surface is idealised by three elliptic cones, each described by the following equation,

$$c_1\sigma_n^2 + c_2\sigma_p^2 + c_3\tau_{np}^2 + c_4\sigma_n\sigma_p + c_5\sigma_n + c_6\sigma_p + 1 = 0 \tag{2.2}$$

where $c_i (i = 1, 2, \cdots, 7)$ are a set of parameters derived from the experiments. The failure modes include tension failure normal and parallel to the bed joint, shear failure and biaxial tension or biaxial compression failure. Though this is a very sophisticated model, unfortunately it is directly related to a set of laboratory results for a particular masonry. For a masonry with different structural layout or of different material properties there is a need for a new series of both experimental and analytical investigations.

Loo and Yang(1991) used a similar macroscopic model to carry out a cracking and failure analysis of a masonry arch bridge with average masonry properties neglecting the effect of the orientation of the mortar joint. As the mortar contributes non-linear characteristics to the masonry, such an assumption may lead to a stiffer arch.

In their model, the stress-strain relation before failure is assumed as

$$\begin{pmatrix} d\sigma_x \\ d\sigma_y \\ d\tau_{xy} \end{pmatrix} = \frac{E_t}{1-\nu^2} \begin{pmatrix} 1 & \nu & 0 \\ \nu & 1 & 0 \\ 0 & 0 & \frac{1-\nu}{2} \end{pmatrix} \begin{pmatrix} d\epsilon_x \\ d\epsilon_y \\ d\gamma_{xy} \end{pmatrix}. \tag{2.3}$$

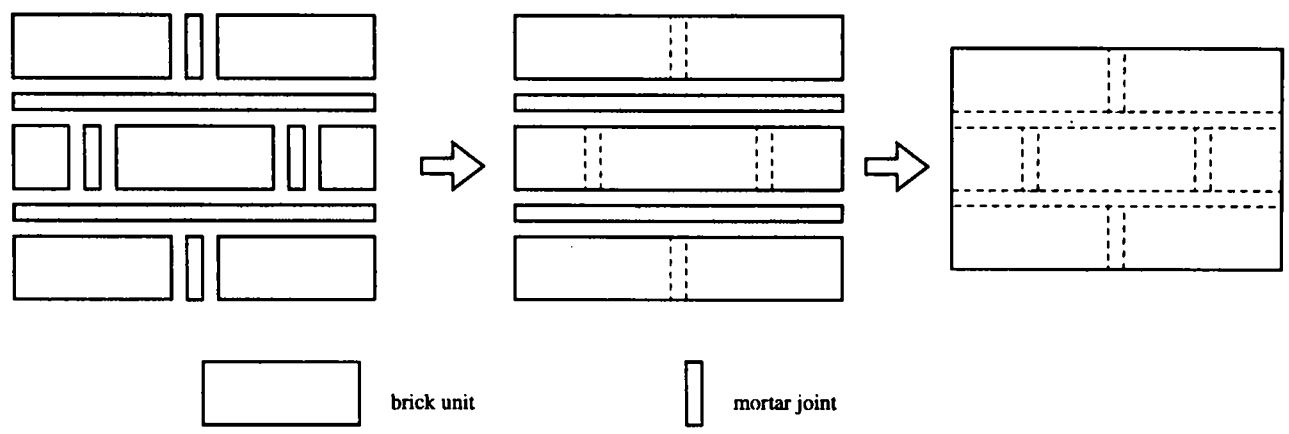


Figure 2.9: Equivalent Material Approach

When the material is in either biaxial tension-tension or tension-compression stress states, E_t is the elastic Young's modulus. In biaxial compression, E_t is derived from a parabolic stress-strain curve

$$\frac{\sigma}{f'_c} = 2\left(\frac{\epsilon}{\epsilon_{cu}}\right) - \left(\frac{\epsilon}{\epsilon_{cu}}\right)^2. \tag{2.4}$$

The failure surface used here is similar to that used by Page *et al.*(1988),*i.e.* a von Mises yield envelope with tension cut-off. For different failure modes, the stiffness matrix is modified to a nominal value and the corresponding stresses are reduced.

Pande *et al.*(1989) derived equivalent moduli for brick masonry using an "equivalent" material approach. A stacked brick/mortar system consisting of a series of parallel elastic layers is introduced (Figure 2.9). The expression for the elastic properties of the equivalent material is derived in terms of the elastic properties of brick and mortar, together with relative thickness under the assumption that no slippage occurs between the mortar layers and the brick units. Once the stresses at a point in the equivalent material are known, then the stresses in the constituent layers at that point can be retrieved. From this information it is possible to assess the failure of the brick units and mortar joints. This approach can be extended to non-linear constitutive models (Middleton *et al.*, 1991). As it is assumed that no slippage occurs between mortar and brick units, this model is only applicable prior to initial cracking and can not cope with post-cracking analysis.

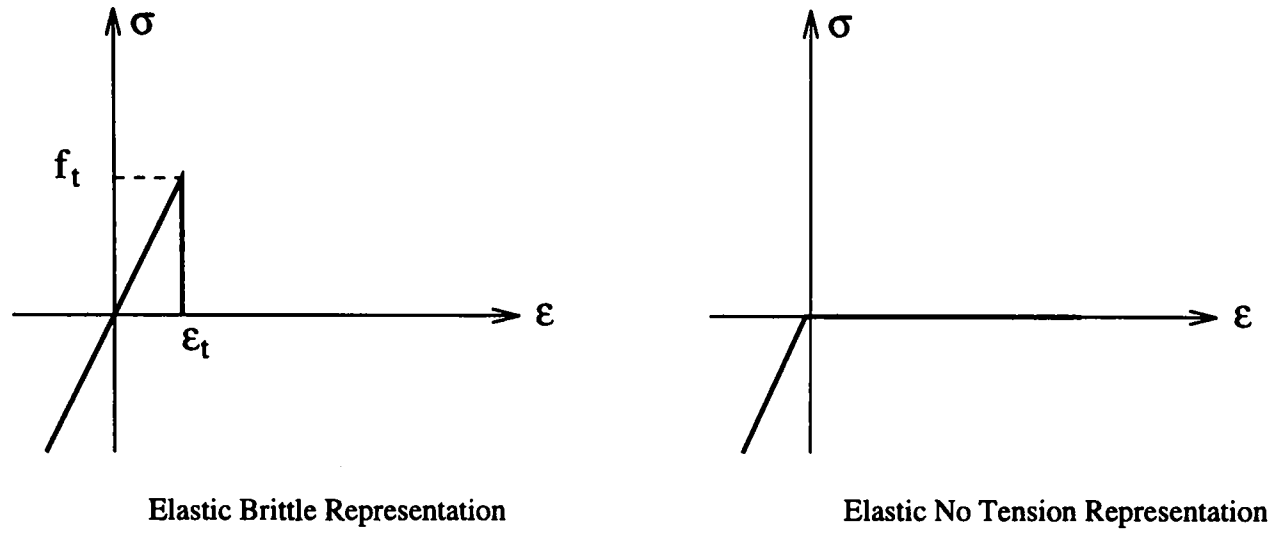


Figure 2.10: Elastic No Tension Model

2.1.3 Elastic No Tension Model

An elastic no tension model which assumes material can not sustain any tensile stress but infinite compressive stress has been used for rock mass analysis for a long time (Zienkiewicz *et al.*, 1968). This model can be applied to plain masonry material as its tensile strength is very low compared with its compressive strength (Di Pasquale, 1992).

The no tension state can be achieved by iterating the solution process, reducing stiffness to zero in the area where tensile stress is developed (Zienkiewicz *et al.*, 1968). It also can be achieved by iterating the solution process using 'stress transfer' with or without reducing the material stiffness (Zienkiewicz *et al.*, 1968). In Di Pasquale(1992) the no tension solution is solved as a free boundary value problem by means of the Haar-Karman principle.

The advantages of the elastic no tension model are

1. it is simple and straightforward and therefore easy to understand and implement,
2. it is material independent and universal for plain masonry and plain concrete,
3. it does not require many material parameters, and
4. it does not cause the sudden stress relief which leads to numerical instability (Figure 2.10).

In addition, tensile cracking dominates in the damage to masonry buildings caused by

tunnelling induced ground movements. Therefore the elastic no tension model is a good starting point for this project.

Since the no tension model involves cracking analysis, the detailed solution will depend on the numerical implementation, *i.e.*, the solution is sensitive to the sizes of loading increments and the mesh used. This problem is inherent to any model that includes fracture or strain softening. These effects can be reduced by carrying out parametric studies to choose a suitable loading step and mesh size. The Cosserat Continuum model as used for the strain softening materials by de Borst (1991) and Sluys(1992) could be adopted in the no tension model to eliminate the mesh sensitivity. However it would involve a very complicated continuum mechanics study and will not be used in this research.

2.2 Elastic No Tension Model and Its Implementation

The elastic no tension model has been chosen to model the masonry material in this study. Its behaviour is highly dependent on the stress state. Under compression the material behaves elastically, while it will crack when and where tensile stress develops. After cracking the material will lose its stiffness. Three states — elastic intact, singly cracked and doubly cracked — are considered and the corresponding stiffness matrices are derived. This model has been implemented into OXFEM where the modified Euler scheme is adopted to cope with the non-linearity of the problem (Burd, 1986).

2.2.1 Constitutive Equations

In the incremental algorithm, the stress increment d$\boldsymbol{\sigma}$ and strain increment dϵ are connected by the tangent stiffness $\boldsymbol{D}$ via

$$d\boldsymbol{\sigma} = \boldsymbol{D} d\epsilon \tag{2.5}$$

For any possible stress $\boldsymbol{\sigma} = (\sigma_x, \sigma_y, \gamma_{xy})^T$, the principal stresses can be obtained by

$$\sigma_{1,2} = \frac{\sigma_x + \sigma_y}{2} \pm \sqrt{\left(\frac{\sigma_x - \sigma_y}{2}\right)^2 + \tau_{xy}^2}. \tag{2.6}$$

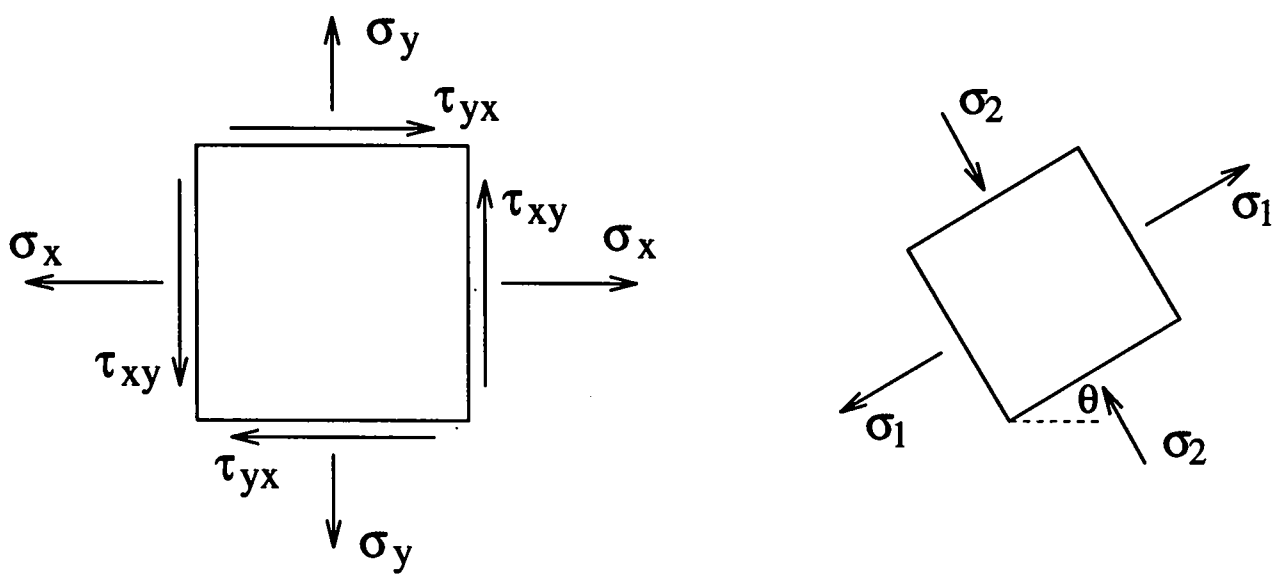


Figure 2.11: Principal Stresses

The orientation of the major principal stress to the x-axis (Figure 2.11) is

$$\theta = \frac{1}{2}\arctan\frac{2\tau_{xy}}{\sigma_x - \sigma_y}. \tag{2.7}$$

When both of the principal stresses σ_1 and σ_2 are compressive, the material is in an *elastic state* and the $\boldsymbol{D}$ matrix is

$$\boldsymbol{D} = \frac{E}{1-\nu^2}\begin{pmatrix} 1 & \nu & 0 \\ \nu & 1 & 0 \\ 0 & 0 & \frac{1-\nu}{2} \end{pmatrix} \tag{2.8}$$

which is the same as the usual elastic equation.

If the major principal stress σ_1 becomes tensile while the minor one σ_2 is still compressive, *single cracking* will occur at the direction normal to the major principal stress(Figure 2.12-(2)). The crack is smeared within the material and the stiffness in the direction of σ_1 will be lost. The tangent stiffness matrix of the material in the principal space becomes

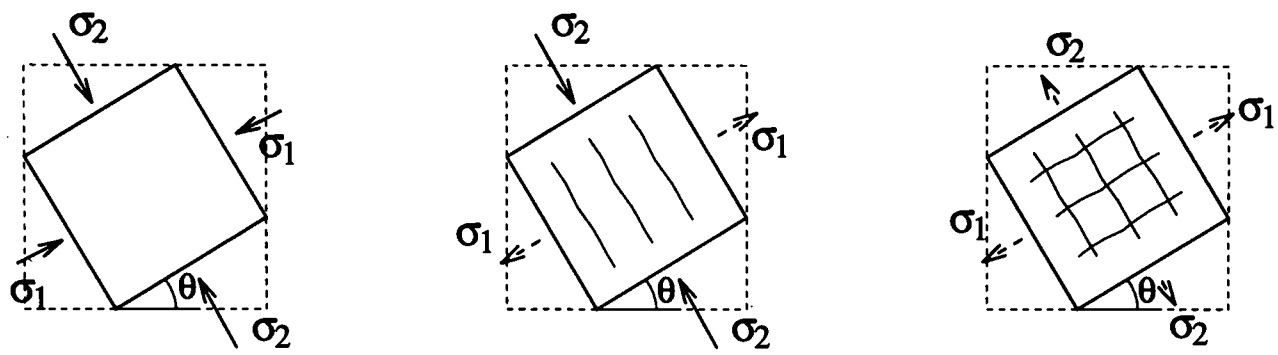
$$\boldsymbol{D}^* = \begin{pmatrix} 0 & 0 & 0 \\ 0 & E & 0 \\ 0 & 0 & 0 \end{pmatrix} \tag{2.9}$$

The $\boldsymbol{D}$ in $x-y-$space will be

$$\boldsymbol{D} = \boldsymbol{T}^T\boldsymbol{D}^*\boldsymbol{T}. \tag{2.10}$$

Here $\boldsymbol{T}$ is the co-ordinate transform matrix

$$\boldsymbol{T} = \begin{pmatrix} c^2 & s^2 & sc \\ s^2 & c^2 & -sc \\ -2sc & 2sc & c^2-s^2 \end{pmatrix} \tag{2.11}$$



(1) elastic *(2) single cracking* *(3) double cracking*

Figure 2.12: Three stress states

where $c = \cos\theta, s = \sin\theta$.

If both of the principal stresses become tensile, *double cracking* will happen (Figure 2.12-(3)) and the material will lose its stiffness completely and $\boldsymbol{D}$ will be assigned to zero.

$$\boldsymbol{D} = \begin{pmatrix} 0 & 0 & 0 \\ 0 & 0 & 0 \\ 0 & 0 & 0 \end{pmatrix} \tag{2.12}$$

2.2.2 Stress and State Updating

As loading is applied incrementally, the stress and state of the material, which determine the future material stiffness, will change gradually. At the end of each increment the stress and state have to be updated according to the material response.

The sign of the principal stress governs the transfers from the elastic intact state to single cracking and double cracking states. Under more complicated loading the cracked material may reclose. As the stress normal to the cracking direction is always zero after cracking, it can not be used to monitor reclosure. A cracking strain ϵ^{cr} has been introduced to detect the reclosure and represent the width of cracks. For simplicity, the reclosed material is treated as completely "healed" for the stiffness. Its unrecoverable cracking deformation is recorded by a residual strain ϵ^{r}.

Choice of the Co-ordinate System

Stresses and strains are usually described in the local co-ordinate system of an element. For the elastic no tension material the principal stresses are of concern as they control the state change from uncracked to cracked. In an elastic state without initial shear stress or strain, the directions of the principal stresses and strains are identical and vary with the loading.

When the major principal stress becomes tensile a crack develops normal to the major principal stress. As the cracked material cannot transmit shear stress, the principal stress directions remain normal and tangential to the crack surface after cracking, whilst the principal strain directions may vary. The principal stress directions are very useful because the material properties are described in these directions, and it is the cracking strain normal to the crack which is used to measure crack opening and reclosure. Thus the principal stress directions are used as a working co-ordinate system for further discussion.

The symbols used in the further discussion are defined as follows.

Subscripts 1 and 2 stand for major and minor principal stress directions. In the elastic state $\sigma_{1,2}$ and $\epsilon_{1,2}$ are therefore the major and minor principal stresses and strains.

After cracking, subscripts 1 and 2 indicate the directions normal(n) and tangential(t) to the first crack to form (Figure 2.13). As the first crack always occurs in the direction normal to the major principal stress, the subscript 1 refers to the major principal stress direction except for one special situation. The only exception occurs when the first crack to form in the doubly cracked material also recloses first. In this case σ_1 will be in compression while σ_2 is still zero.

As discussed before, after cracking, $\epsilon_{1,2}$ only refer to the strain components in the directions 1(n) and 2(t), not to the principal strains.

Cracking Strain

Generally strain ϵ consists of two parts: the elastic strain ϵ^e and the cracking strain ϵ^{cr}.

$$\epsilon = \epsilon^e + \epsilon^{cr} \tag{2.13}$$

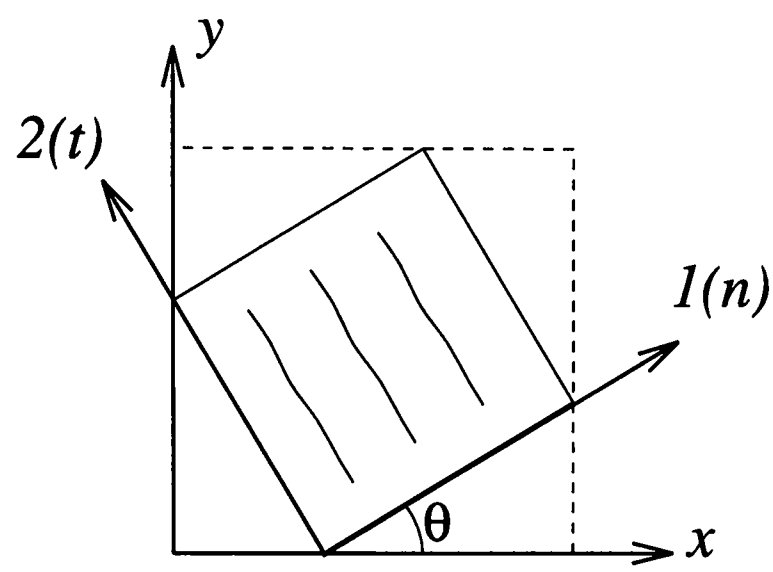


Figure 2.13: Working Co-ordinate Systems

In the working co-ordinate system, the relation between the total stress $\boldsymbol{\sigma}$ and the total strain $\boldsymbol{\epsilon}$ is

$$E(\epsilon_1 - \epsilon_1^{cr}) = (\sigma_1 - \sigma_1^o) - \nu(\sigma_2 - \sigma_2^o) \tag{2.14}$$

$$E(\epsilon_2 - \epsilon_2^{cr}) = (\sigma_2 - \sigma_2^o) - \nu(\sigma_1 - \sigma_1^o) \tag{2.15}$$

where $\sigma_{1,2}^o$ are the initial stresses.

Elastic State

When the material is elastic, the cracking strain is zero, and equations 2.14 and 2.15 become

$$E\epsilon_1 = (\sigma_1 - \sigma_1^o) - \nu(\sigma_2 - \sigma_2^o) \tag{2.16}$$

$$E\epsilon_2 = (\sigma_2 - \sigma_2^o) - \nu(\sigma_1 - \sigma_1^o) \tag{2.17}$$

In the terms of the incremental stress and strain, the equations 2.16 and 2.17 are

$$Ed\epsilon_1 = d\sigma_1 - \nu d\sigma_2 \tag{2.18}$$

$$Ed\epsilon_2 = d\sigma_2 - \nu d\sigma_1 \tag{2.19}$$

which can be rewritten as

$$\begin{pmatrix} d\sigma_1 \\ d\sigma_2 \end{pmatrix} = \frac{E}{1-\nu^2} \begin{pmatrix} 1 & \nu \\ \nu & 1 \end{pmatrix} \begin{pmatrix} d\epsilon_1 \\ d\epsilon_2 \end{pmatrix} \tag{2.20}$$

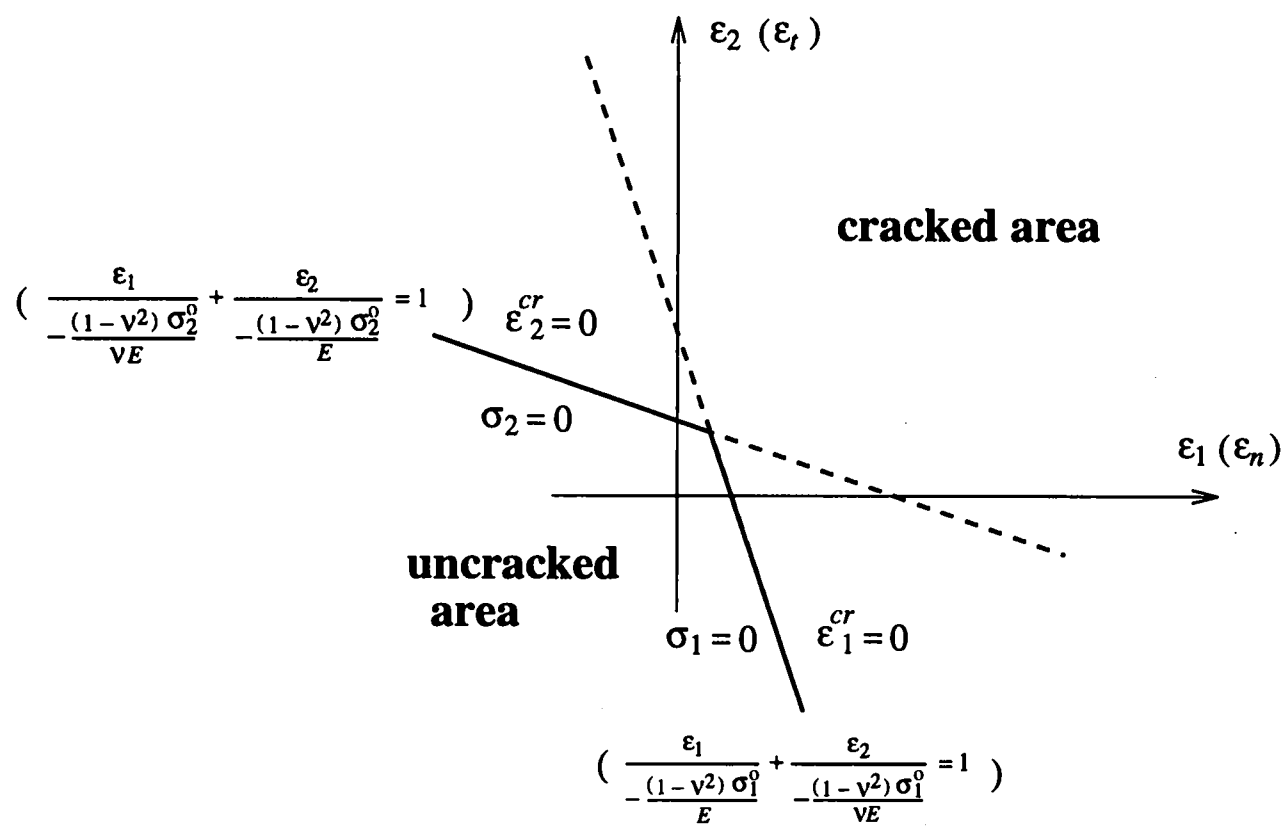


Figure 2.14: Transfer between Elastic and Single Cracking States

When both principal stresses are compressive the material is elastic. When one of the principal stresses, say σ_1, becomes tensile, the material will singly crack in the direction normal to it. Putting the condition $\sigma_1 = 0$ into equations 2.16 and 2.17

$$E\epsilon_1 = -\sigma_1^o - \nu(\sigma_2 - \sigma_2^o) \tag{2.21}$$

$$E\epsilon_2 = (\sigma_2 - \sigma_2^o) + \nu\sigma_1^o \tag{2.22}$$

Thus the boundary between the intact state and single cracking in strain space is a straight line (Figure 2.14)

$$\frac{\epsilon_1}{-\frac{(1-\nu^2)\sigma_1^o}{E}} + \frac{\epsilon_2}{-\frac{(1-\nu^2)\sigma_1^o}{E\nu}} = 1. \tag{2.23}$$

In fact there is another boundary between the elastic and single cracking states which controls when cracking happens at the direction normal to the other principal stress axis. This boundary is also a straight line whose equation is

$$\frac{\epsilon_1}{-\frac{(1-\nu^2)\sigma_2^o}{E\nu}} + \frac{\epsilon_2}{-\frac{(1-\nu^2)\sigma_2^o}{E}} = 1 \tag{2.24}$$

The elastic area in the strain space is located to the bottom left of these two lines (Figure 2.14).

Single Cracking State

After single cracking related to σ_1, σ_1 and ϵ_2^{cr} remain zero. The constitutive equations are similar to 2.21 and 2.22.

$$E(\epsilon_1 - \epsilon_1^{cr}) = -\sigma_1^o - \nu(\sigma_2 - \sigma_2^o) \tag{2.25}$$

$$E\epsilon_2 = (\sigma_2 - \sigma_2^o) + \nu\sigma_1^o \tag{2.26}$$

The incremental form is

$$\begin{pmatrix} d\sigma_1 \\ d\sigma_2 \end{pmatrix} = \begin{pmatrix} 0 & 0 \\ 0 & E \end{pmatrix} \begin{pmatrix} d\epsilon_1 \\ d\epsilon_2 \end{pmatrix} \tag{2.27}$$

and

$$d\epsilon_1^{cr} = d\epsilon_1 + \frac{\nu d\sigma_2}{E} = d\epsilon_1 + \nu d\epsilon_2 \tag{2.28}$$

When σ_2 becomes positive as well, the material will doubly crack. Using the control condition of $\sigma_2 = 0$, the boundary between singly and doubly cracked areas can be deduced. It is a horizontal line

$$\epsilon_2 = \frac{-\sigma_2^o + \nu\sigma_1^o}{E} \tag{2.29}$$

The cracking strain ϵ_1^{cr} is used to measure the opening of the crack. As the condition of $\epsilon_1^{cr} = 0$ is equivalent to the equation 2.23 of the boundary line, when ϵ_1^{cr} has reduced to zero, the crack will close.

Similar conclusions can be drawn for the material singly cracked in the σ_2 direction (Figure 2.15).

Doubly Cracking State

In this case both the principal stresses remain equal to zero and the stiffness matrix is null. In the incremental form:

$$d\sigma_1 = 0 \quad d\sigma_2 = 0 \tag{2.30}$$

$$d\epsilon_1^{cr} = d\epsilon_1 \quad d\epsilon_2^{cr} = d\epsilon_2 \tag{2.31}$$

The cracking strains are used to monitor the reclosure in either direction. As ϵ_1^{cr} becomes zero the initial crack will reclose, while the second crack closes when ϵ_2^{cr} is zero (Figure 2.15).

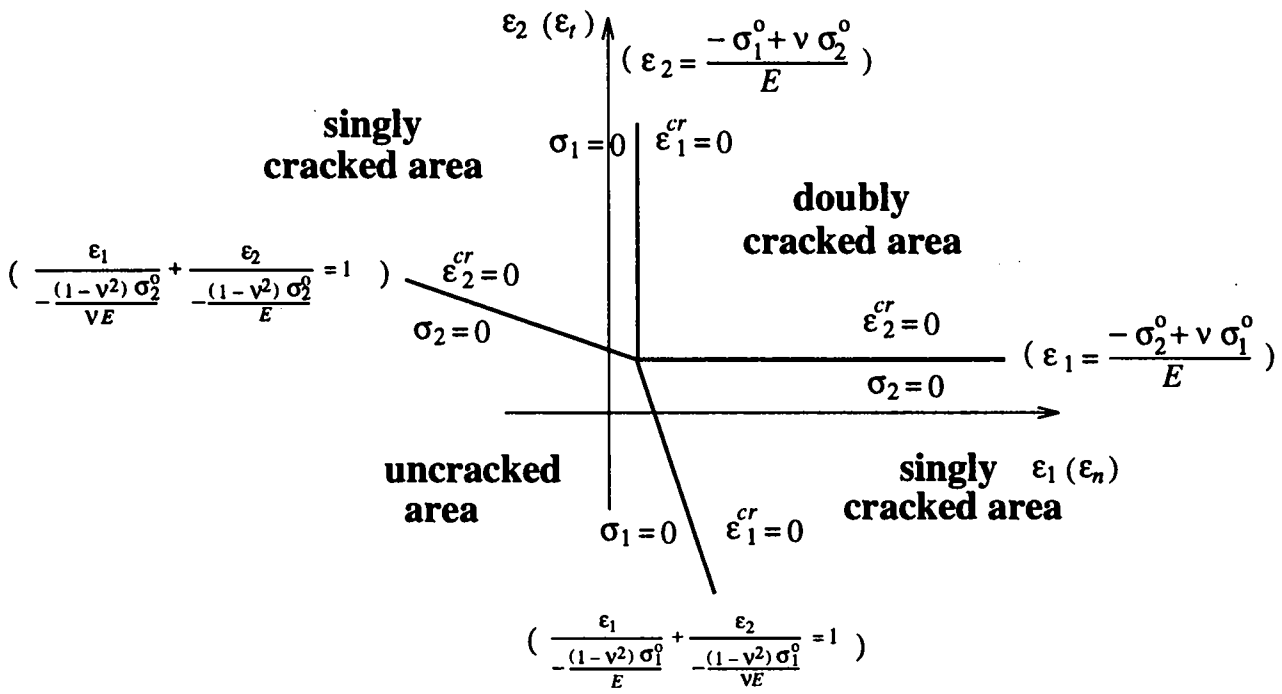


Figure 2.15: Transfer between All the States

The Algorithm for Stress and State Updating

According to the modified Euler scheme employed in OXFEM, load is applied incrementally. The results of the previous steps are the initial state for the current increment so that the current stiffness matrix can then be determined. During the current increment, the stiffness matrix is assumed unchanged and the incremental strain $\Delta\epsilon$ is obtained. Under these incremental strains and the initial status, the new stress is

$$\boldsymbol{\sigma}^{(i)} = \boldsymbol{\sigma}^{(i-1)} + \boldsymbol{D}\Delta\epsilon. \tag{2.32}$$

If the criteria for cracking and reclosure are not violated, the above calculated stress and the unchanged state are the result of the current increment and the updating is finished. If either criterion for cracking or reclosure is violated, the state in the material is changed. The strain increment is divided into two parts: $t\Delta\epsilon$ before the state change and $(1-t)\Delta\epsilon$ after it. The stress response to the first $t\Delta\epsilon$ is calculated using the initial state. The remainder of the strain increment is passed to the new state and the corresponding stress response is calculated. It can be dealt with like the first part but with the new state.

From an initial elastic state, there are two possible responses (Figure 2.16):

1. there is no state change and the stress is updated by the elastic matrix.

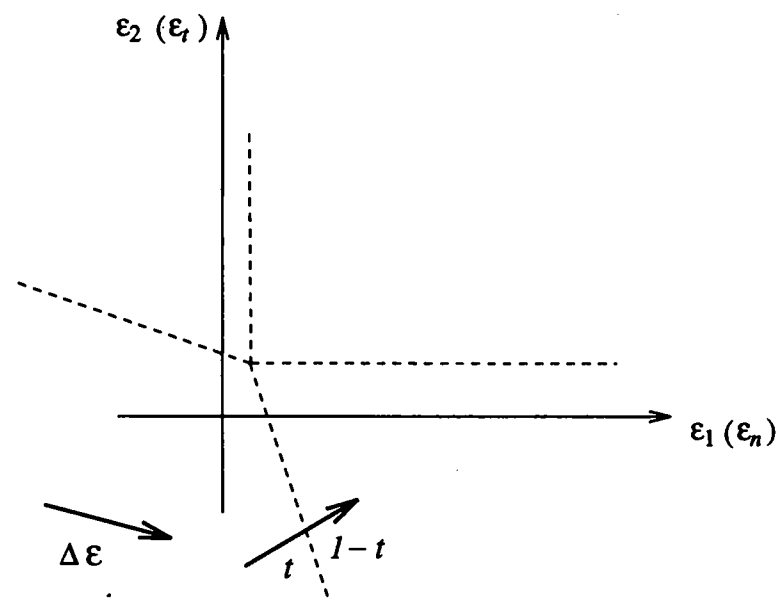


Figure 2.16: Possible Routes from Elastic State

2. single cracking occurs. The intersection t is determined by the condition that the principal stress is zero and is the root of the following equation within the region $(0 \leq t \leq 1)$:

$$At^2 + Bt + C = 0 \tag{2.33}$$

where

$$\begin{aligned} A &= \frac{E^2}{(1-\nu)^2}(\Delta\epsilon_x + \Delta\epsilon_y)^2 - \frac{E^2}{(1+\nu)^2}(\Delta\epsilon_x - \Delta\epsilon_y)^2 \\ &\quad - \frac{E^2}{(1+\nu)^2}(\Delta\gamma_{xy})^2 \end{aligned} \tag{2.34}$$

$$\begin{aligned} B &= \frac{2E}{1-\nu}(\sigma_x^{(i-1)} + \sigma_y^{(i-1)})(\Delta\epsilon_x + \Delta\epsilon_y) \\ &\quad - \frac{2E}{1+\nu}(\sigma_x^{(i-1)} - \sigma_y^{(i-1)})(\Delta\epsilon_x - \Delta\epsilon_y) \\ &\quad - \frac{4E}{1+\nu}(\tau_{xy}^{(i-1)}\Delta\gamma_{xy}) \end{aligned} \tag{2.35}$$

$$C = 4(\sigma_x^{(i-1)}\sigma_y^{(i-1)} - (\tau_{xy}^{(i-1)})^2). \tag{2.36}$$

From the initial single cracking, there are three possible responses (Figure 2.17):

1. the stress point remains in the same single cracking area,

2. double cracking occurs and the intersection is equal to the following equation, determined by the condition that the minor principal stress is zero.

$$t = -\frac{\sigma_2^{(i-1)}}{E\Delta\epsilon_2} \tag{2.37}$$

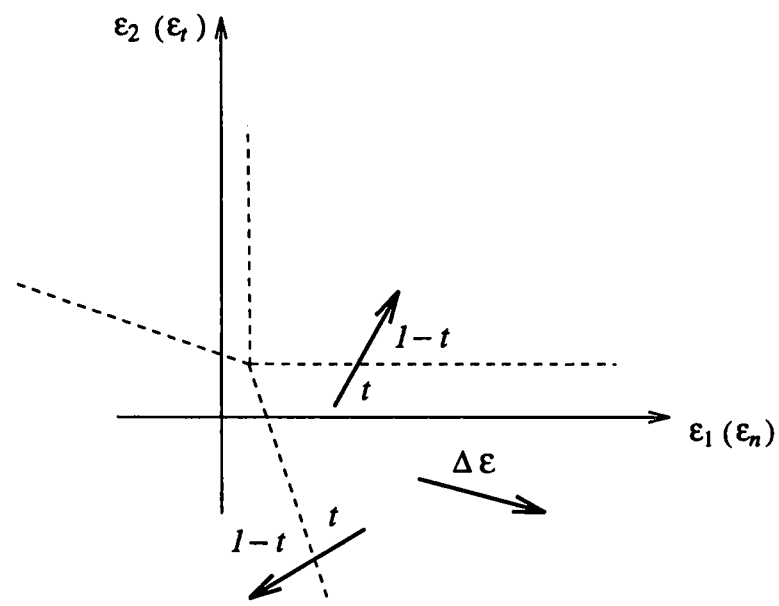


Figure 2.17: Possible Routes from Single Cracking State

3. reclosure occurs and the intersection is decided by the condition that the crack opening strain ϵ_1^{cr} becomes zero.

$$t = -\frac{\epsilon_1^{cr(i-1)}}{\Delta\epsilon_1 + \nu\Delta\epsilon_2} \tag{2.38}$$

From a initial stress state of double cracking, there are also three possible responses (Figure 2.18):

1. the stress remains in double cracking state

2. reclosure occurs in the direction 1 which is monitored by $\epsilon_1^{cr} = 0$ and the intersection is

$$t = -\frac{\epsilon_1^{cr(i-1)}}{\Delta\epsilon_1} \tag{2.39}$$

3. reclosure occurs at the direction 2 and the intersection is

$$t = -\frac{\epsilon_2^{cr(i-1)}}{\Delta\epsilon_2} \tag{2.40}$$

Although only the situations where the strain increment crosses one boundary during one loading step have been discussed above, the cases crossing two boundaries in one step are also covered in the analysis. Any such a strain increment will cross one boundary first and change the state. The second part of the increment, $(1-t)\Delta\ \epsilon$, will be examined due to its new state. Such a process will be repeated until no state change happens (Figure 2.19).

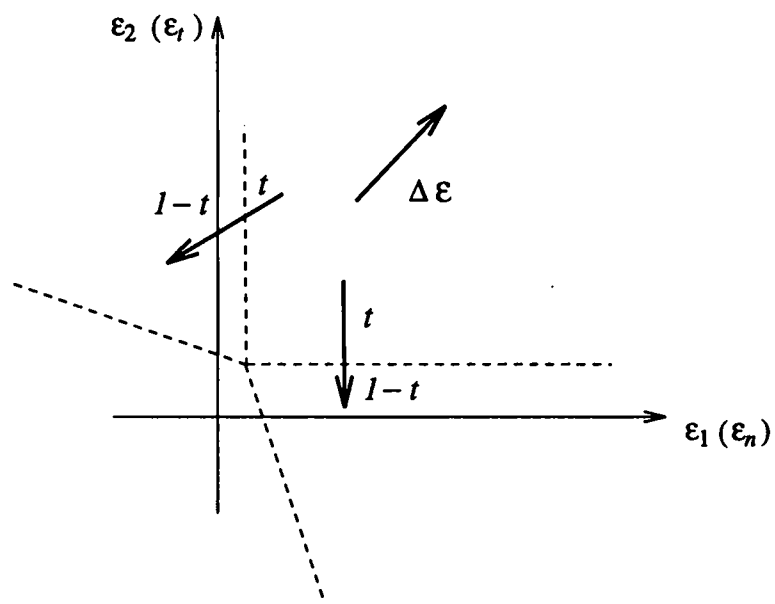


Figure 2.18: Possible Routes from Double Cracking State

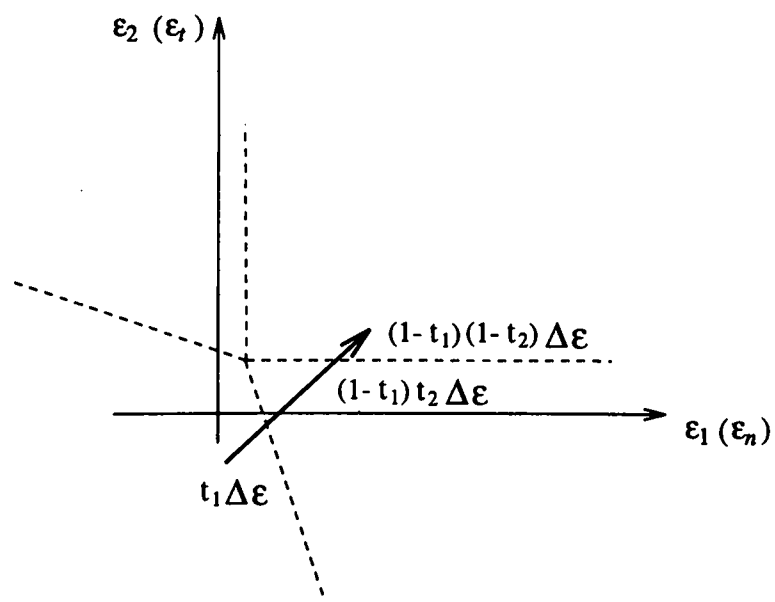


Figure 2.19: Possible Double Crossing Strain Increment

2.2.3 Numerical Stability

As an idealised model the elastic no tension material has no reaction to tension. Once tension develops, the material will crack and lose its stiffness immediately. Such an assumption will cause some numerical problems since the cracked stiffness matrix will be partially singular for the degrees of freedom relating to the cracking. When an element is partially cracked, the stiffness distribution within the element is highly non-linear and the usual numerical integration may not reproduce the stiffness correctly. At the end of the load increment when the material cracks, the tensile stress is eliminated. The "unsupported" tension will be transferred to unbalanced nodal forces applied to the surrounding elements. If these elements are previously cracked and have zero stiffness, the unbalanced force may cause unrealistic reclosure and a very large local compression which is also unrealistic. Some techniques have been introduced to prevent these numerical problems.

Non-Zero Residual Stiffness

To avoid the singularity, a non-zero residual stiffness has been applied to the cracked material. The residual Young's modulus is

$$E_r = fE \tag{2.41}$$

where E is the original modulus and f is a residual stiffness factor. Values of f from 0.01 to 0.001 have been used in this study. The more complicated the stress distribution is, the larger is the residual stiffness required. The stiffness matrices for all the states can be found in Table 2.1.

Over-integration

In finite element analysis, the stiffness matrix is the result of integration of the material stiffness over all elements. The Gauss-Legendre quadrature is commonly used for isoparametric elements. Generally, the integration of a function $\Phi(\xi)$ over the range $(-1 \leq$

	mode	stiffness matrix
0	elastic	$\frac{E}{1-\nu^2}\begin{pmatrix} 1 & \nu & 0 \\ \nu & 1 & 0 \\ 0 & 0 & \frac{1-\nu}{2} \end{pmatrix}$
1	single cracking	$\begin{pmatrix} fE & 0 & 0 \\ 0 & E & 0 \\ 0 & 0 & \frac{fE}{2(1+\nu)} \end{pmatrix}$
2	double cracking	$\begin{pmatrix} fE & 0 & 0 \\ 0 & fE & 0 \\ 0 & 0 & \frac{fE}{2(1+\nu)} \end{pmatrix}$

Table 2.1: Stiffness matrices for all modes

$\xi \leq 1$) can be approximated as follows:

$$I = \int_{-1}^{1} \Phi(\xi) d\xi \approx \sum_{i=1}^{n} W_i \Phi(\xi_i) \tag{2.42}$$

where $\xi_i (i = 1, \ldots, n)$ is the Gauss point co-ordinate and W_i is its weight. For a polynomial of order $(2n - 1)$ the accurate integration can be obtained by Gauss-Legendre quadrature with n Gauss points. The more highly non-linear the function is, the more Gauss points are needed.

For the partially cracked element, there is a steep jump in its stiffness distribution which makes the integrated function highly non-linear, and therefore requires more Gauss points. Taking the one-dimensional case as an example, the accurate integration of function

$$\Phi(\xi) = 0 \qquad -1 \leq \xi < 0 \tag{2.43}$$

$$\Phi(\xi) = 1 \qquad 0 \leq \xi < 1 \tag{2.44}$$

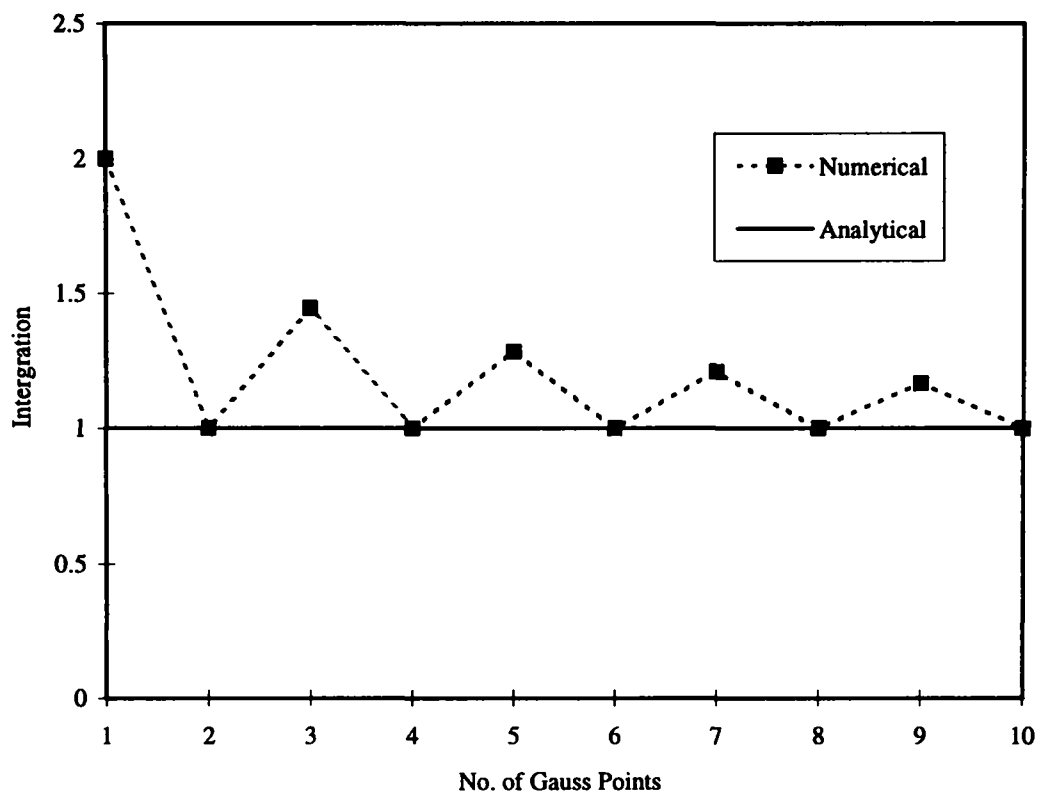


Figure 2.20: Gauss quadrature results of different numbers of Gauss points

over the range $(-1 \leq \xi \leq 1)$ is

$$\int_{-1}^{1} \Phi(\xi) d\xi = 1 \tag{2.45}$$

The comparison with the numerical results of 1 to 10 Gauss points in Figure 2.20 shows the importance of more Gauss points.

For the six-noded triangular element used in this study, the shape function is quadratic and 3 Gauss points are enough for elastic analysis, but for post-cracking analysis a higher number of Gauss points is necessary (16 Gauss points are used in this study). On the other hand, fine mesh for the masonry building is not feasible due to the limitation of computer resources. To carry out the calculation within a reasonable computation time, coarse meshing is necessary. A small number of Gauss points in a large element will cause more sudden cracking. Over-integration is helpful to make the cracking process smooth.

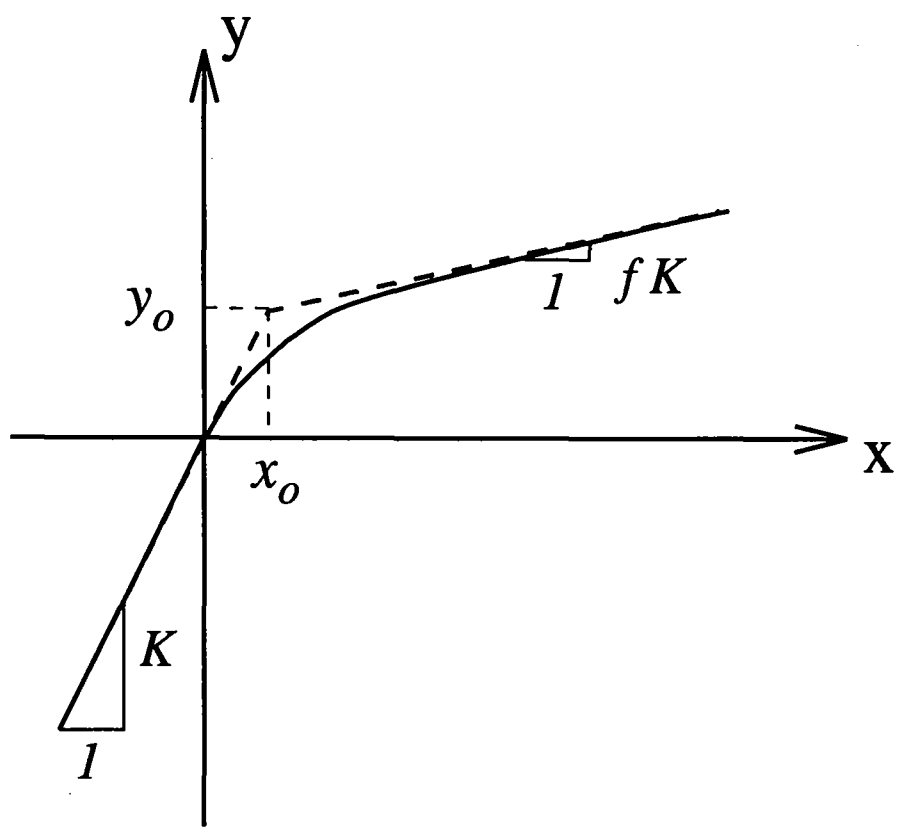


Figure 2.21: Curve with gradually changed slope

Gradual Reduction of Stiffness

After cracking the material loses its stiffness. Since its stiffness is assumed not to change during the calculation of displacements and strains of each load increment, the cracked material does not have a compressive stiffness either within one load increment. This may cause two problems. Firstly, overlapping of material occurs where the reclosure occurs and unrealistic large compression will develop. Secondly, due to the existence of the unbalanced nodal forces, false reclosure may emerge, especially at the early stage after cracking. A gradual reduction of the stiffness has been introduced to eliminate these problems.

The post-cracking stiffness is assumed to depend on the cracking opening, *i.e.* cracking strain. It decreases as the cracking strain increases and vice versa. When the cracking strain is small – the crack is likely to close – the stiffness is still large to prevent significant overlapping. When the cracking strain is quite large, the crack is unlikely to close, and the stiffness becomes small.

The gradually reducing stiffness is derived from the slope of the curve shown in Figure 2.21.

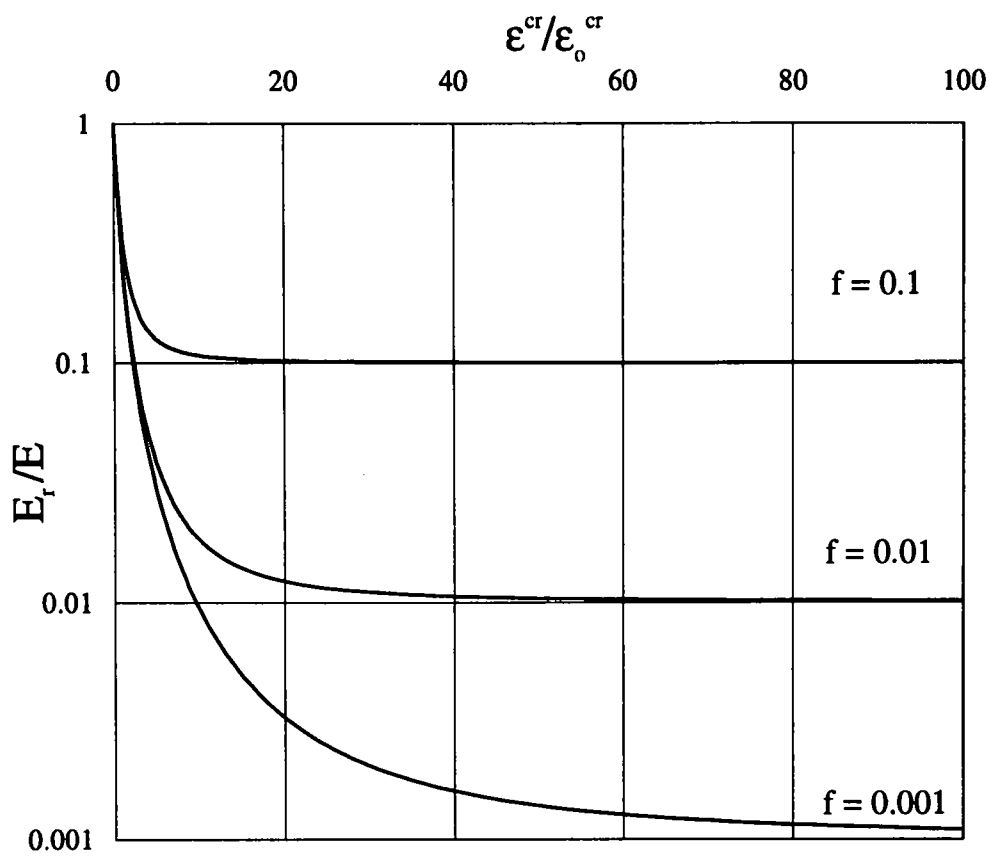


Figure 2.22: Gradually reduced stiffness

The function of this curve is

$$y = Kx\left(\frac{x_0 + fx}{x_0 + x}\right) \tag{2.46}$$

Then

$$\frac{dy}{dx} = K\left[\frac{1-f}{(1+\frac{x}{x_0})^2} + f\right] \tag{2.47}$$

For this study, the form of the equation becomes

$$E_r(\epsilon^{cr}) = E\left[\frac{1-f}{(1+\frac{\epsilon^{cr}}{\epsilon_o^{cr}})^2} + f\right] \tag{2.48}$$

where ϵ_o^{cr}, the stiffness reduction rate parameter, controls the speed at which the stiffness decreases. Figure 2.22 gives some typical $E_r/E \sim \epsilon^{cr}/\epsilon_o^{cr}$ curves for the given f values.

Residual Tensile Strength

The ideal elastic no tension model requires that the material has zero tensile strength. But such a zero tensile strength may cause numerical problems, as the state of unloaded material is uncertain because it is at the boundary between safe and cracked. In addition, zero tensile strength will lead to a vast amount of tiny cracks being exhibited

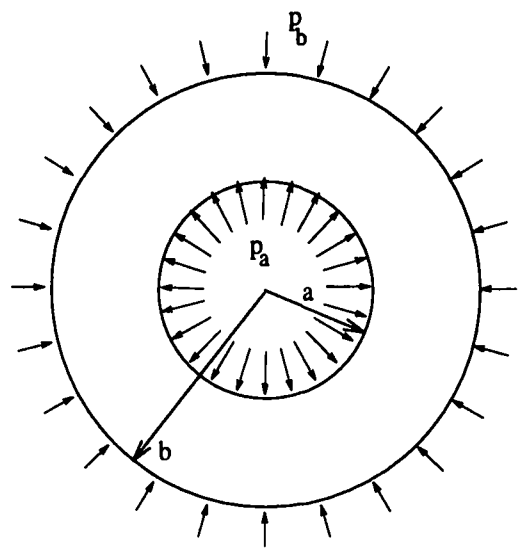


Figure 2.23: Cavity Expansion

in the material which are not the main concern of damage assessment. To avoid these problems, a small residual tensile strength, c is assigned to the model. Usually, a value of 10kPa is used in this study which is negligible compared with the real strengths and the compressive stresses occurring in buildings.

2.3 Test Problems for the Elastic No Tension Model

After implementation in OXFEM, the elastic no tension model has been validated by two test problems: a cavity expansion and a beam bending problem.

2.3.1 Cavity Expansion with Elastic No Tension Model

Analytical Solution for Elastic Cylinder Subject to Inner and Outer Pressure

For axi-symmetric plane stress elastic problems, the equations in the polar coordinate system are (Reisman and Pawlik, 1980):

1) Compatibility Equation.

$$\epsilon_r = \frac{du}{dr} \text{ and } \epsilon_\theta = \frac{u}{r} \Rightarrow \epsilon_r = \frac{d}{dr}(r\epsilon_\theta) \tag{2.49}$$

2) Equilibrium Equation.

$$\frac{d\sigma_r}{dr} + \frac{\sigma_r - \sigma_\theta}{r} = 0 \Rightarrow \sigma_\theta = \frac{d}{dr}(r\sigma_r) \tag{2.50}$$

3) Hooke's Law.

$$E\epsilon_r = \sigma_r - \nu\sigma_\theta \tag{2.51}$$

$$E\epsilon_\theta = -\nu\sigma_r + \sigma_\theta \tag{2.52}$$

4) Boundary Conditions.

For the cavity expansion problem (Figure 2.23), the boundary conditions are

$$\sigma_r\,|_{r=a} = -p_a \tag{2.53}$$

$$\sigma_r\,|_{r=b} = -p_b \tag{2.54}$$

From the above equations stress and strain distributions in the cylinder can be solved.

$$\sigma_r = A + \frac{B}{r^2} \tag{2.55}$$

$$\sigma_\theta = A - \frac{B}{r^2} \tag{2.56}$$

$$\epsilon_r = \frac{1}{E}\left((1-\nu)A + (1+\nu)\frac{B}{r^2}\right) \tag{2.57}$$

$$\epsilon_\theta = \frac{1}{E}\left((1-\nu)A - (1+\nu)\frac{B}{r^2}\right) \tag{2.58}$$

where

$$A = \frac{-p_b b^2 + p_a a^2}{b^2 - a^2} \tag{2.59}$$

$$B = \frac{a^2 b^2}{b^2 - a^2}(p_b - p_a) \tag{2.60}$$

The radial displacement is

$$u = \epsilon_\theta r = \frac{1}{E}\left((1-\nu)Ar - (1+\nu)\frac{B}{r}\right) \tag{2.61}$$

At the inner edge

$$u_a = u\,|_{r=a} = \frac{1}{E}\left((1-\nu)aA - (1+\nu)\frac{B}{a}\right) \tag{2.62}$$

Analytical Solution for Cavity Expansion with Elastic No Tension Material

The cavity expansion problem is a plane stress cylinder subject to inner pressure $(p_o+\Delta p)$ and outer pressure p_o. The stress and displacement for the increasing Δp are analysed.

At the initial state both inner and outer pressures p_o cause uniform compressive stress p_o within the cylinder.

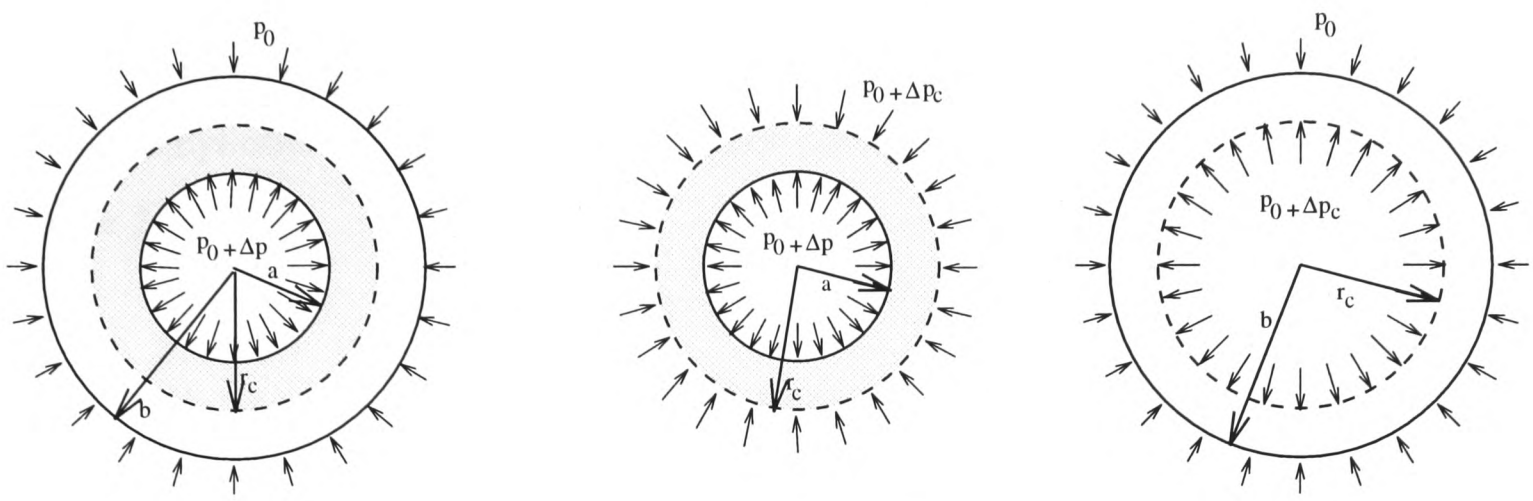


Figure 2.24: Cracked Cylinder

As Δp increases the material is still under compression initially. The stress and displacement can be obtained by substituting $p_a = p_o + \Delta p$ and $p_b = p_o$ into the elastic solutions.

$$\sigma_r = \frac{-p_0\,(b^2 - a^2) + \Delta p a^2}{b^2 - a^2} - \frac{a^2 b^2 \Delta p}{b^2 - a^2}\frac{1}{r^2} \tag{2.63}$$

$$\sigma_\theta = \frac{-p_0\,(b^2 - a^2) + \Delta p a^2}{b^2 - a^2} + \frac{a^2 b^2 \Delta p}{b^2 - a^2}\frac{1}{r^2} \tag{2.64}$$

$$u_a = -\frac{1-\nu}{E} a p_0 + \frac{a}{E}\left(\frac{b^2 + a^2}{b^2 - a^2} + \nu\right)\Delta p \tag{2.65}$$

where the initial displacement due to the uniform compression is

$$u_a^0 = -\frac{1-\nu}{E} a p_0 \tag{2.66}$$

and the displacement due to Δp is

$$\Delta u_a = \frac{a}{E}\left(\frac{b^2 + a^2}{b^2 - a^2} + \nu\right)\Delta p \tag{2.67}$$

It is seen that the radial stress becomes more compressive and the circumferential stress becomes less compressive as Δp increases. At a specific Δp the circumferential stress at the inner edge will become zero. This value of Δp can be obtained from the condition

$$\sigma_\theta|_{r=a,\ \Delta p = \Delta p_{in}} = 0. \tag{2.68}$$

It is

$$\Delta p_{in} = \frac{p_0(b^2 - a^2)}{b^2 + a^2}. \tag{2.69}$$

When $\Delta p \geq \Delta p_{in}$, the cylinder will crack from the inner edge outwards. Within the uncracked area, the elastic solution is still valid and the stress and displacement are the same as a cylinder ($r_c \leq r \leq b$) under inner pressure ($p_o + \Delta p_c$) and outer pressure p_o (Figure 2.24).

$$\sigma_r = \frac{-p_0\left(b^2 - r_c^2\right) + \Delta p_c r_c^2}{b^2 - r_c^2} - \frac{r_c^2 b^2 \Delta p_c}{b^2 - r_c^2}\frac{1}{r^2} \tag{2.70}$$

$$\sigma_\theta = \frac{-p_0\left(b^2 - r_c^2\right) + \Delta p_c r_c^2}{b^2 - r_c^2} + \frac{r_c^2 b^2 \Delta p_c}{b^2 - r_c^2}\frac{1}{r^2} \tag{2.71}$$

$$u_{r_c} = -\frac{1-\nu}{E} r_c p_0 + \frac{r_c}{E}\left(\frac{b^2 + r_c^2}{b^2 - r_c^2} + \nu\right)\Delta p_c \tag{2.72}$$

In the cracked area the governing equations are different. Equilibrium equations lead to

$$-2\pi r \sigma_r = 2\pi a\left(p_0 + \Delta p\right) \Rightarrow \sigma_r = -\frac{\left(p_0 + \Delta p\right) a}{r} \tag{2.73}$$

$$\sigma_\theta = 0 \tag{2.74}$$

As the material has cracked along the radial direction, the radial strain and displacement will be related to the radial stress only.

$$\epsilon_r = \frac{du}{dr} = \frac{\sigma_r}{E} \tag{2.75}$$

ϵ_θ consists of elastic and cracking parts.

$$\epsilon_\theta^e = -\nu\frac{\sigma_r}{E}, \quad \epsilon_\theta^{cr} = \frac{u}{r} + \nu\frac{\sigma_r}{E} \tag{2.76}$$

At the boundary between the cracked and uncracked areas these two zones are matched by the condition that the radial stresses in both areas are the same at r_c and that the circumferential stress just falls to zero in the elastic part.

$$\Delta p_c + p_0 = \frac{\left(p_0 + \Delta p\right) a}{r_c} \tag{2.77}$$

$$\sigma_\theta\,|_{r=r_c} = \frac{-p_0\left(b^2 - r_c^2\right) + \Delta p_c r_c^2}{b^2 - r_c^2} + \frac{r_c^2 b^2 \Delta p_c}{b^2 - r_c^2}\frac{1}{r_c^2} = 0 \tag{2.78}$$

From these two equations the cracking radius r_c can be found.

$$\left(p_0 + \Delta p\right) a r_c^2 - 2 p_0 b^2 r_c + \left(p_0 + \Delta p\right) a b^2 = 0 \tag{2.79}$$

which has real roots if

$$\left(2p_o b^2\right)^2 - 4(p_o + \Delta p)^2 a^2 b^2 \geq 0 \tag{2.80}$$

i.e.

$$\Delta p \leq p_o \frac{b-a}{a} = \Delta p_{out}. \tag{2.81}$$

Actually, when $\Delta p = \Delta p_{out}$, the cracked area reaches the outer edge.

The only solution for r_c is

$$r_c = \frac{p_0 b^2 - \sqrt{p_0^2 b^4 - (p_0 + \Delta p)^2 a^2 b^2}}{(p_0 + \Delta p)a} \tag{2.82}$$

Now for any given value of Δp between Δp_{in} and Δp_{out}, the cracked area is decided and stresses in both areas are determined.

The radial displacement in the cracked area can be calculated by integrating the radial strain.

$$\begin{aligned} u &= u_{r_c} - \int_r^{r_c} d\epsilon_r \\ &= u_{r_c} - \int_r^{r_c} \frac{\sigma_r}{E} dr \\ &= u_{r_c} + \frac{a(p_0 + \Delta p)}{E} \ln \frac{r_c}{r} \end{aligned} \tag{2.83}$$

At the inner edge

$$u_a = u_{r_c} + \frac{a(p_0 + \Delta p)}{E} \ln \frac{r_c}{a} \tag{2.84}$$

from which

$$\Delta u_a = u_a - u_a^0 = u_{r_c} + \frac{a(p_0 + \Delta p)}{E} \ln \frac{r_c}{a} + \frac{1-\nu}{E} a p_0 \tag{2.85}$$

After Δp reaches Δp_{out}, the cracks go through the whole cylinder and Δp cannot increase further.

The stress distributions along the radius of a cylinder with $a/b = 0.6$ subjected to the increasing inner pressure can be found in Figure 2.25. The typical $\Delta p - \Delta u_a$ curve of the same cylinder with Poisson's ratio of 0.2 is also given in Figure 2.26.

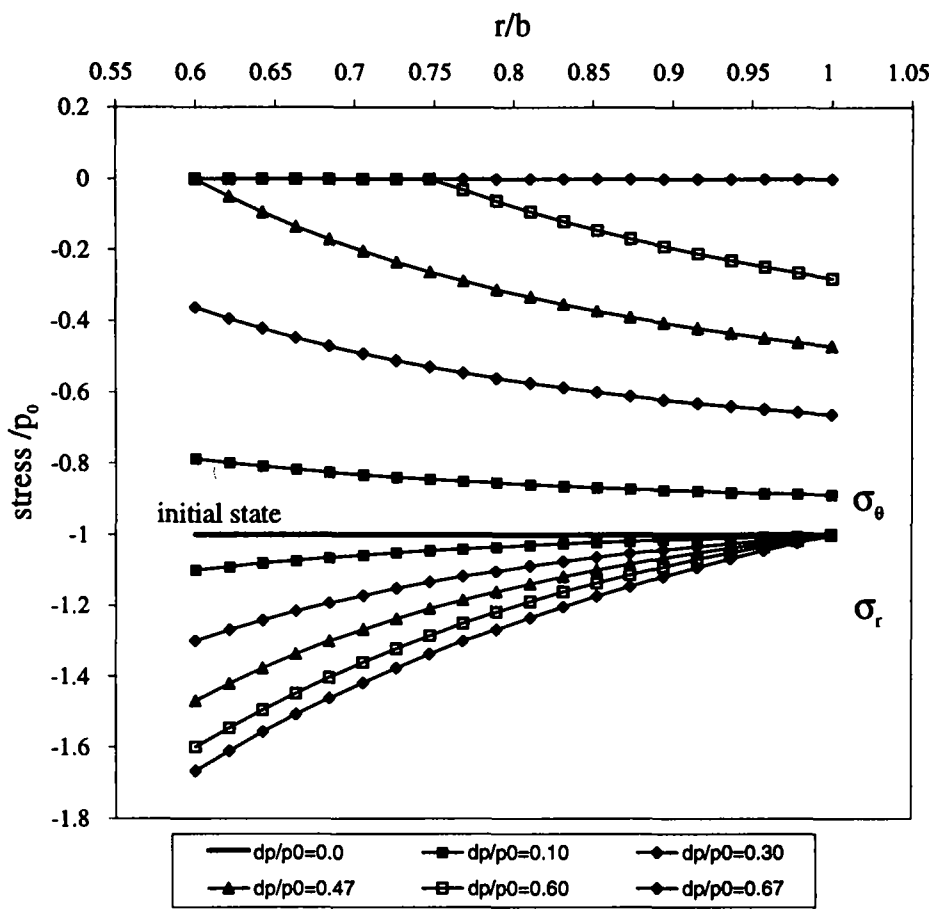


Figure 2.25: Stress Distribution under Different Pressures, Analytical Solution.

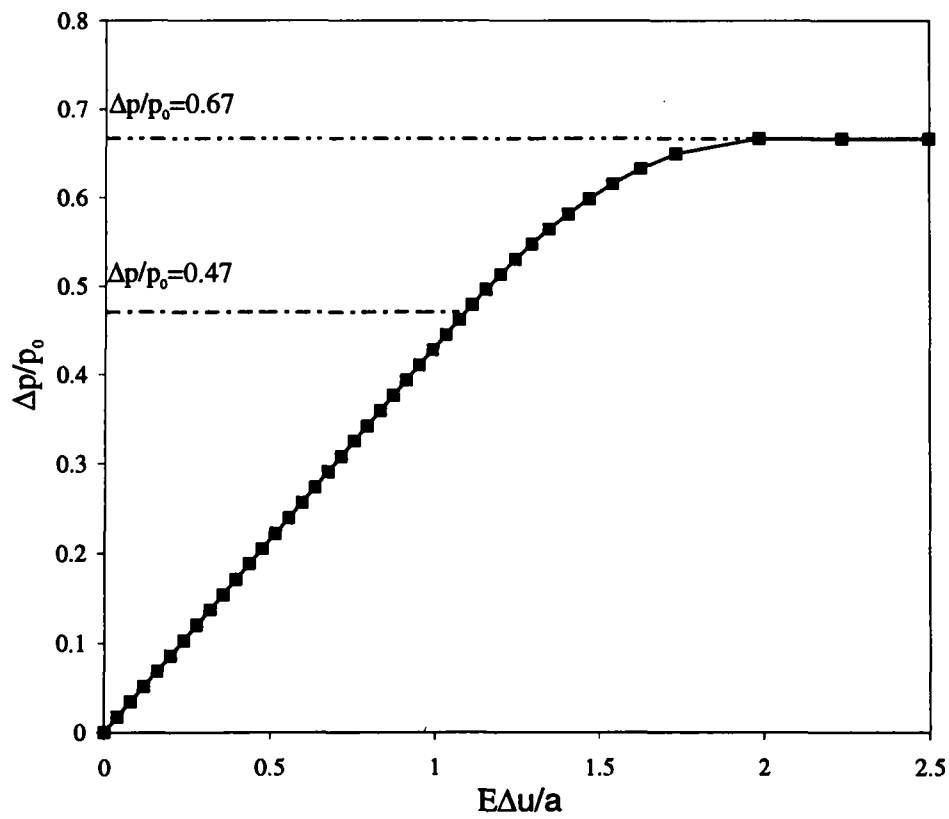


Figure 2.26: $\Delta p - \Delta u_a$ Curve, Analytical Solution

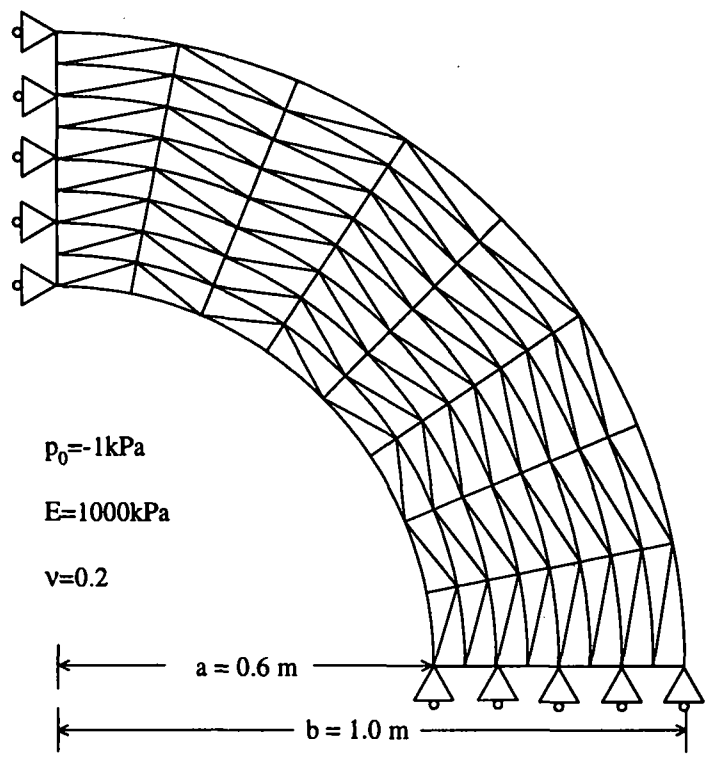


Figure 2.27: finite element mesh for cavity expansion

Finite Element Solution for Cavity Expansion with Elastic No Tension Model

The cavity expansion problem has been solved by the finite element method with the elastic no tension model. Due to its symmetry, a quarter of the cylinder with $a/b = 0.6$ is analysed. The mesh is shown in Figure 2.27. The comparisons between the analytical and finite element results made in Figures 2.28 and 2.29 show a good agreement between two analyses, except for the stage just after the cylinder cracks through its entire thickness. At this stage the finite element analysis shows a slight overshoot (Figure 2.29). Such an overshoot is adjusted after several steps. At the end of the calculation, finite element analysis gives the same results as the analytical method (Figure 2.30).

2.3.2 Bending Beam of Elastic No Tension Model

A prestressed beam subject to rotation at its ends is used as another test problem for the model (Figure 2.31). The initial stress is a compression of σ_o and both ends are supported at the bottom.

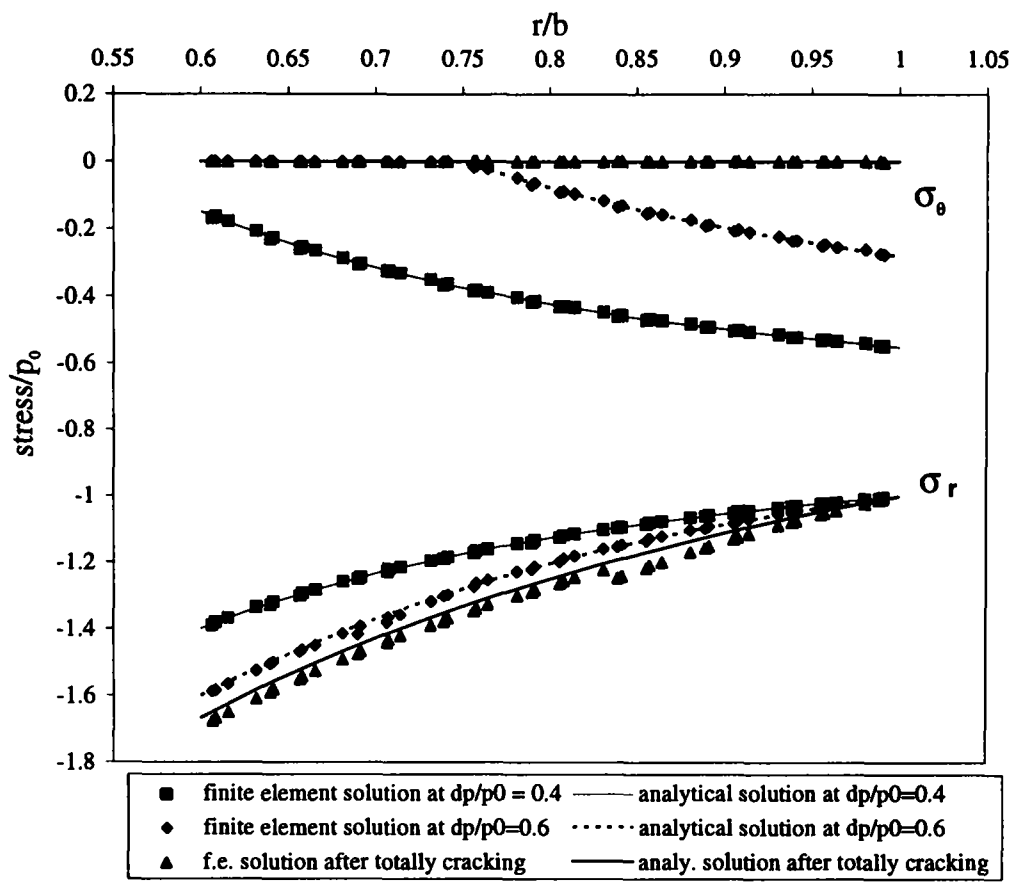


Figure 2.28: Stress Distribution along the Radius, Finite Element Solution

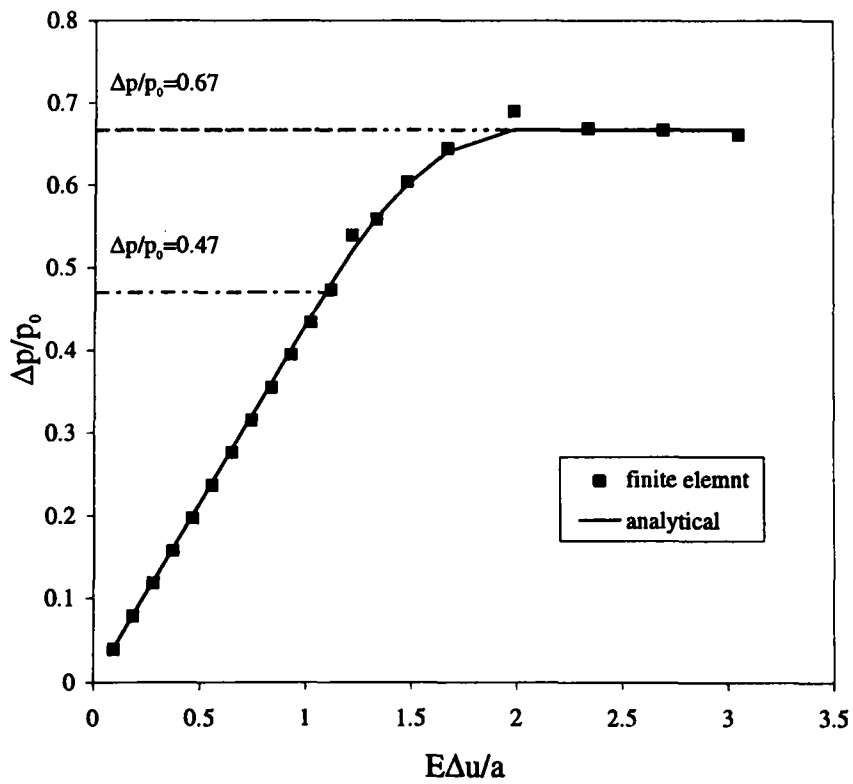


Figure 2.29: $\Delta p - \Delta u_a$ Curves, Finite Element Solution.

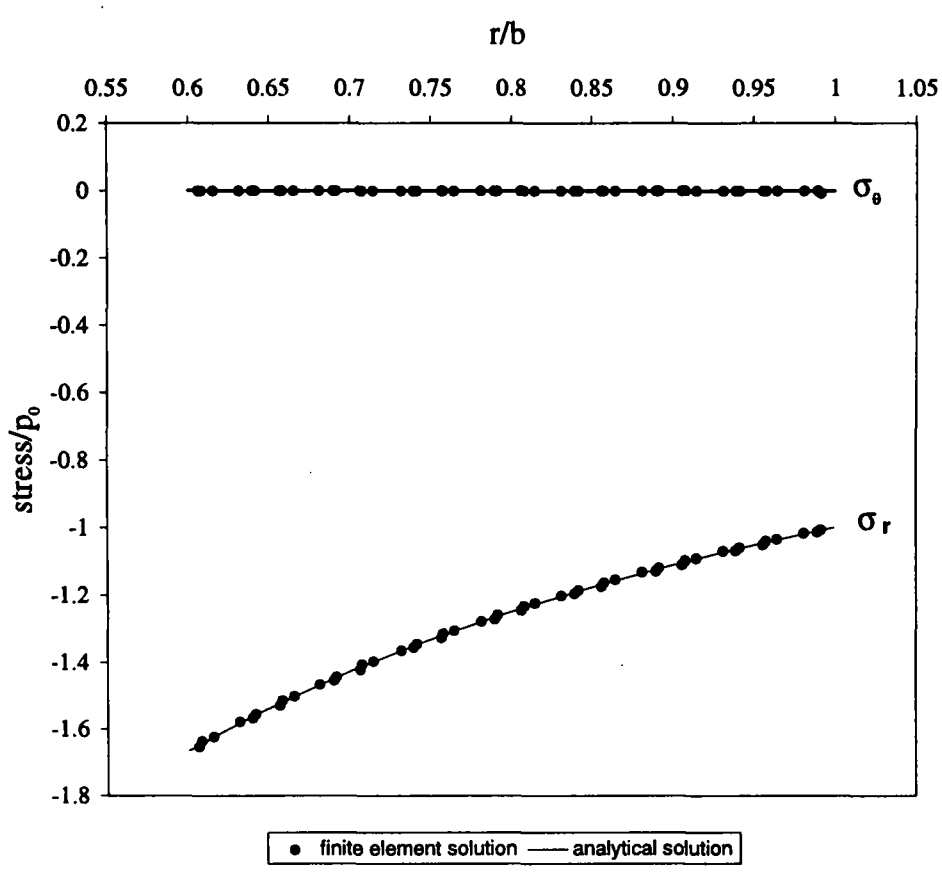


Figure 2.30: Stress distribution at the end of calculation of cavity expansion

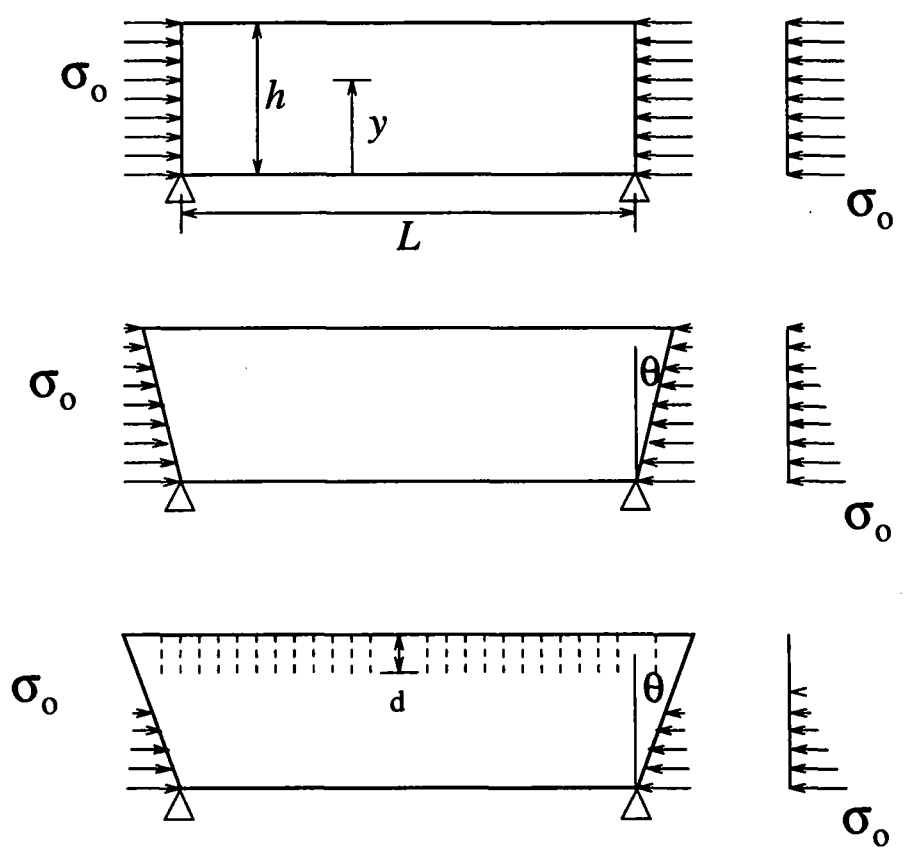


Figure 2.31: Bending Beam of Elastic No Tension Model

Analytical Solution

Under the rotation θ, the axial strain at y is

$$\epsilon_x = \frac{2\theta h}{L}\frac{y}{h} = \frac{2\theta}{L}y. \tag{2.86}$$

At the early stage of bending the material is still in the elastic state and the axial stress is

$$\sigma_x(y) = -\sigma_0 + E\epsilon_x = -\sigma_0 + \frac{2\theta E}{L}y. \tag{2.87}$$

The moment per thickness about the bottom edge M_b is

$$M_b = \int_0^h \left(-\sigma_0 + \frac{2\theta E}{L}y\right) y dy = -\frac{\sigma_0}{2}h^2 + \frac{2\theta E}{3L}h^3 \tag{2.88}$$

in which the part corresponding to θ is

$$\Delta M_b = \frac{2\theta E}{3L}h^3. \tag{2.89}$$

As the rotation increases, the cracks will occur at the top of the beam. In this case,

$$\sigma_x|_{y=h} = -\sigma_0 + \frac{2\theta_{top}h}{L}E = 0. \tag{2.90}$$

Therefore,

$$\theta_{top} = \frac{\sigma_0}{E}\frac{L}{2h} \tag{2.91}$$

Under $\theta \geq \theta_{top}$, the depth of the cracked area, d, is determined by

$$\sigma_x|_{y=h-d} = -\sigma_0 + \frac{2\theta E}{L}(h-d) = 0. \tag{2.92}$$

Therefore

$$d = h - \frac{\sigma_0 L}{2E}\frac{1}{\theta} \tag{2.93}$$

Now the bending moment about the bottom point at the ends M_b is

$$M_b = \int_0^{h-d} \left(-\sigma_0 + \frac{2\theta E}{L}y\right) y dy = -\frac{\sigma_0}{2}(h-d)^2 + \frac{2\theta E}{3L}(h-d)^3 \tag{2.94}$$

Substituting d from Equation 2.93, it becomes

$$M_b = -\frac{1}{24}\frac{\sigma_0^3 L^2}{E^2}\frac{1}{\theta^2}. \tag{2.95}$$

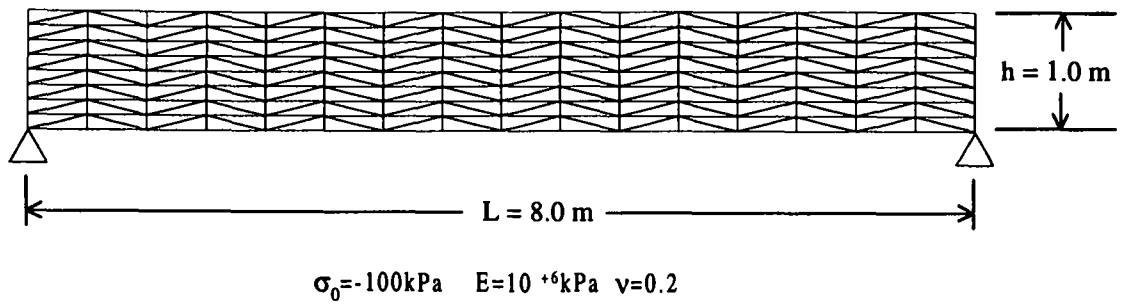


Figure 2.32: Mesh Used for Bending Analysis

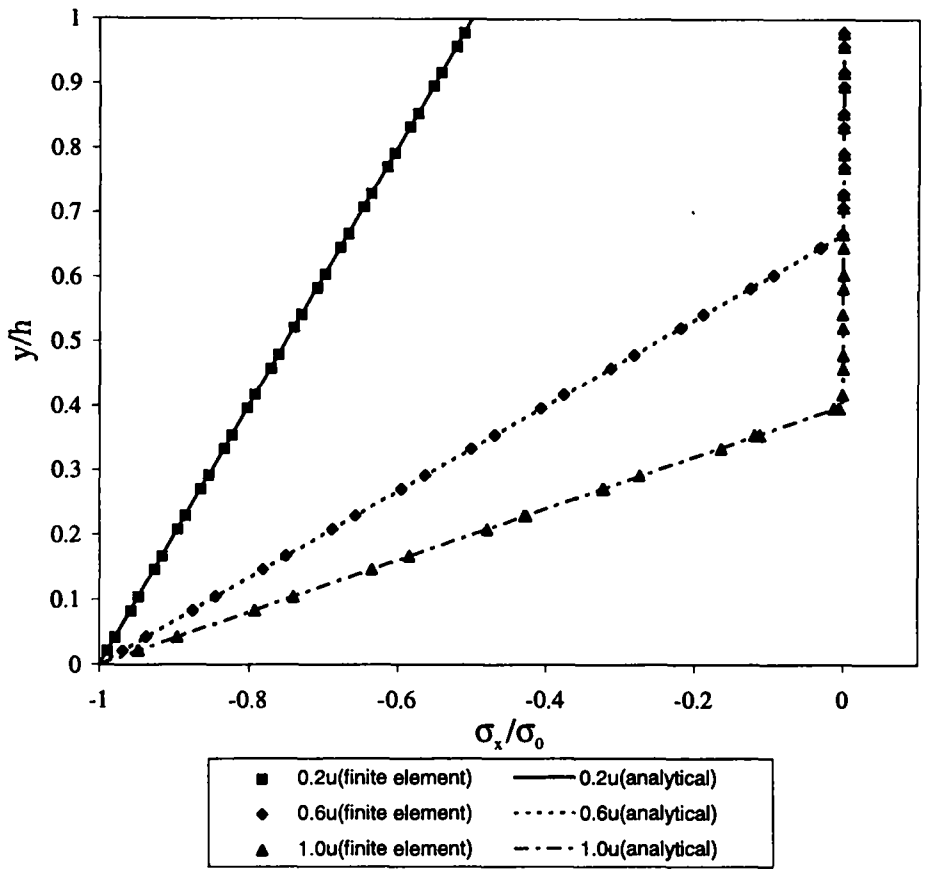


Figure 2.33: Axial Stress

Removing the part corresponding to the initial stress, ΔM_b is

$$\Delta M_b = \frac{\sigma_0}{2}h^2 - \frac{1}{24}\frac{\sigma_0^3 L^2}{E^2}\frac{1}{\theta^2}. \tag{2.96}$$

This problem is solved by the elastic no tension model with the mesh shown in the Figure 2.32. The finite element solution has an excellent agreement with the analytical one (Figures 2.33 and 2.34).

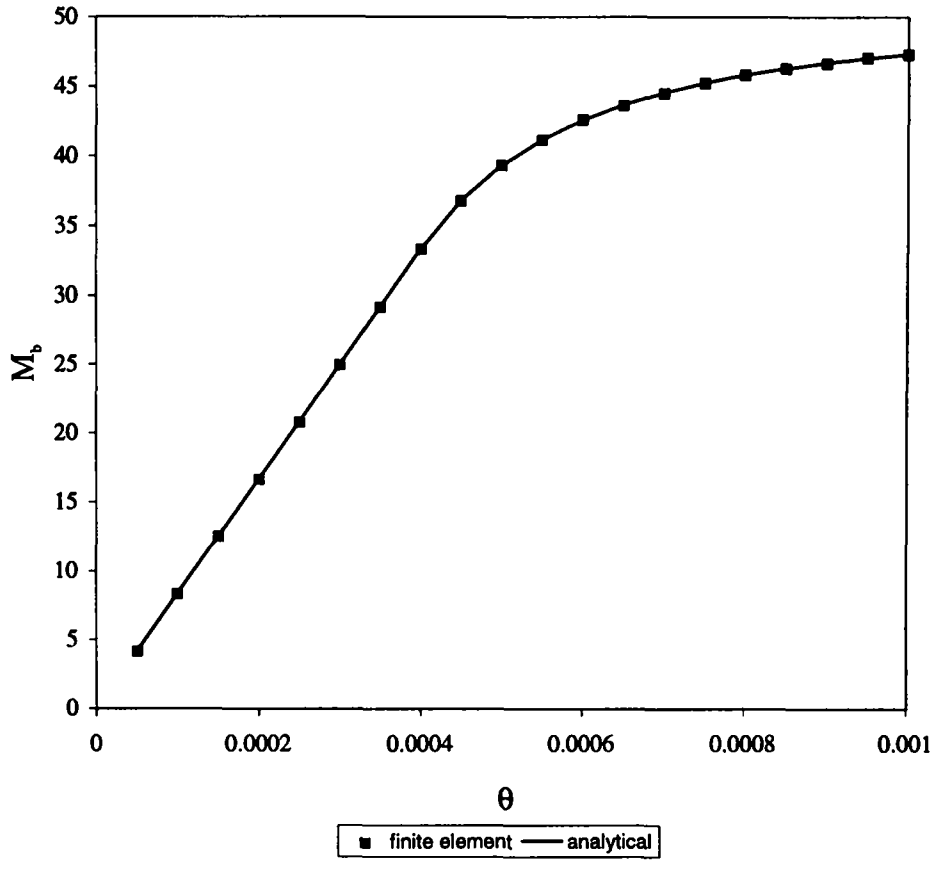


Figure 2.34: $\Delta M_b - \theta$ Curves

2.4 Summary

After a review of the current literature on masonry modelling, the elastic no tension model has been chosen for the masonry material. The macroscopic and smeared crack approach has been used for the finite element analysis. The material stiffness matrix and the corresponding algorithm have been derived and implemented in OXFEM. Several techniques are used to improve the stability of the calculation. The model has been validated by cavity expansion and beam bending problems and is ready for use in the subsequent study.

3

Tying Scheme

3.1 Introduction

In the finite element analysis a structure and the ground are meshed into elements which are defined by nodes. The responses of the elements to loads are described in their own element co-ordinate systems, while nodes are usually defined in a specific global co-ordinate system. The first task after entering the data for a finite element program is assembling these elements as a whole system.

Real buildings have different parts to fulfill various purposes. These different parts are simulated by different types of elements in the finite element analysis. For example, a building consisting of floors, columns and walls may be modelled by the plate, beam and plane stress elements respectively. Different types of elements have different responses to loads and different numbers of degrees of freedom. Element assembly must be able to cope with this situation.

Describing nodes in one specific global co-ordinate system does not work efficiently on all occasions. For example, two connected walls can each be modelled by 2D plane stress elements in their own planes (Figure 3.1). There is not any specific global co-ordinate which can describe the independent displacements of all the nodes along the

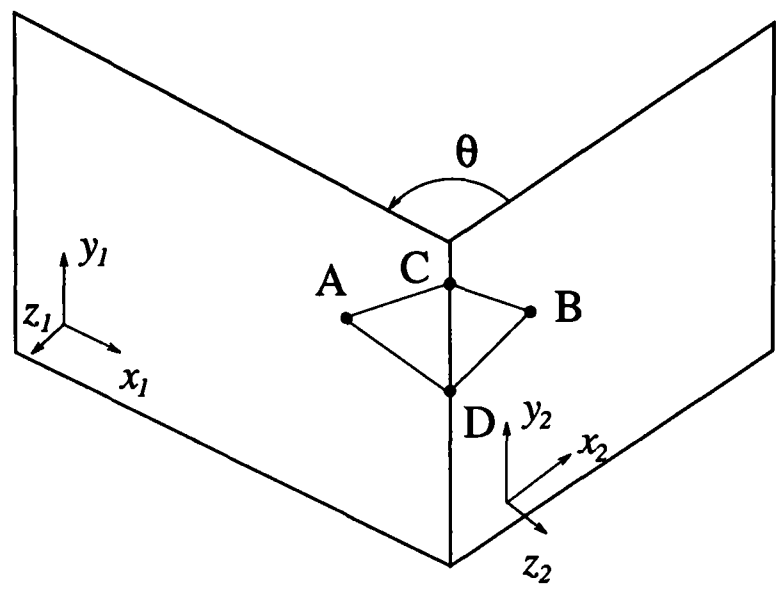


Figure 3.1: Two Connected Walls

same axes. Whatever co-ordinate system is chosen as the global co-ordinate system, it is essential to suppress the out-of-plane displacements of the nodes in the other plane. Thus the use of local co-ordinate systems is advantageous.

The previous version of OXFEM was able to cope with problems where all the nodes have the same number of degrees of freedom in one global co-ordinate system. Thus the modification to OXFEM has been made to cover the aspects discussed above.

3.2 Current Approaches

3.2.1 Common Nodes

The usual approach to connect different elements which are in different co-ordinate systems is by use of common nodes at the connecting points. The common nodes can be described in either of the co-ordinate systems used for the elements. The stiffness related to the nodes is contributed by the connected elements. For the walls in Figure 3.1, the nodes in each plane are described in the corresponding co-ordinate system and have two independent displacements. For the nodes A and B their displacements appear in the total unknown vector $\boldsymbol{d}$ as

$$(\boldsymbol{d})_{n\times 1} = \left(..., u_A^1, v_A^1, ..., u_B^2, v_B^2, ...\right)^T \tag{3.1}$$

where the superscripts indicate the local co-ordinate systems and the subscripts stand for the different nodes. This convention will be used through this chapter. The nodes on

the boundary (the nodes C and D) will have three independent displacements as they obtain stiffness from the elements in both planes, provided the walls are not parallel. Their displacements can be defined in either one of the local co-ordinate systems. Now the total unknown vector $\boldsymbol{d}$ looks like

$$\boldsymbol{d} = \left(..., u_A^1, v_A^1, ..., u_B^2, v_B^2, ..., u_C^1, v_C^1, w_C^1, ..., u_D^2, v_D^2, w_D^2, ...\right)^T \tag{3.2}$$

Using the displacement-force equation

$$(\boldsymbol{K})_{n\times n}(\boldsymbol{d})_{n\times 1} = (\boldsymbol{F})_{n\times 1} \tag{3.3}$$

the total unknown vector $\boldsymbol{d}$ can be solved. The same approach can also be used to connect 2D and 3D nodes.

This approach is straightforward and easy to implement in a finite element program. But a critical problem will occur when two walls are almost parallel since the displacement-force equation approaches singularity as the out-of-plane stiffness is very small. The other shortcoming of this approach is that the numbering of the meshes of the different parts are coupled. Any slight change in the mesh of one part will require renumbering of the whole system. This is particularly inconvenient for this project, as the different parts of the mesh preparation are carried out by different researchers. The latter problem might be solved by using the link or joint element described in (Hibbitt and Karlsson and Sorensen, Inc., 1989). This element can link two nodes geometrically almost coincident but in different local co-ordinate systems with a spring or dashpot between them. If the stiffness of the spring is set up to a very large value, it can represent the connection between these two nodes. However, such a large value of stiffness could cause singularity in the global stiffness matrix. In addition, this element can only connect two nodes and assume that these nodes have full active degrees of freedom and therefore is not suitable for this study.

3.2.2 Constraint of Displacement

In an alternative approach, discussed in this section, the nodes to be connected are generated separately in different elements, then are subject to specific constraints to ensure the connection.

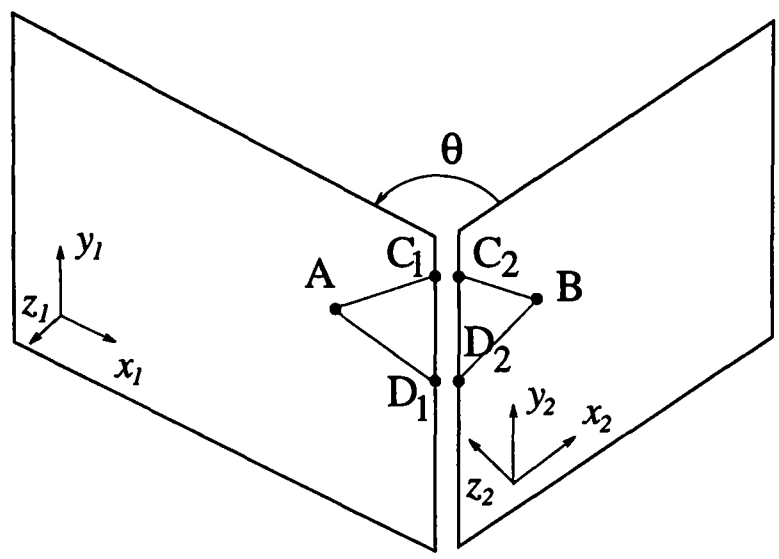


Figure 3.2: Two Independent Walls with Constraints

In terms of mathematics, any constraint on displacements is an equation. For the connection of the nodes in different co-ordinate systems, the constraints are linear equations. For the nodes C_1 and C_2 in Figure 3.2, the condition that requires two nodes have the same vertical displacements is

$$v_{c_1}^1 - v_{c_2}^2 = 0 \tag{3.4}$$

In general, the constraint equations are

$$(\boldsymbol{C})_{m\times n}(\boldsymbol{d})_{n\times 1} = (\boldsymbol{Q})_{m\times 1} \tag{3.5}$$

The displacement force equation and this constraint equation form the governing equations as follows

$$\boldsymbol{K}\boldsymbol{d} = \boldsymbol{F} \tag{3.6}$$

$$\boldsymbol{C}\boldsymbol{d} = \boldsymbol{Q} \tag{3.7}$$

Now the main concern is how to solve these equations.

Eliminating the Redundant Displacements

From the m constraint equations (Equation 3.7), m displacements,$\boldsymbol{d}_e$, can be expressed by the $(n-m)$ remaining displacements, $\boldsymbol{d}_r$, so that the total unknown variable vector can be decomposed into two parts,

Substituting $\boldsymbol{d}_e$ with $\boldsymbol{d}_r$ in Equation 3.6, the modified displacementforce equation will be

$$(\boldsymbol{K}')_{(n-m)\times(n-m)}\,\boldsymbol{d}_r = (\boldsymbol{F}')_{(n-m)\times 1} \tag{3.9}$$

which can be solved as usual (Cook, 1981).

This approach does not require extra new variables but does require modification of the assembled total stiffness matrix, which demands a lot of computation. In addition such a total stiffness matrix is never formed in OXFEM, so the common point approach will not be employed in this study.

Lagrange Multiplier

Lagrange's method of undetermined multipliers is used to find the maximum or minimum of a function whose variables are not independent but have some prescribed relation. In the displacement constraint problem, the function is total potential energy Π_p and the variables are those in $\boldsymbol{d}$ (Cook, 1981). After introducing the Lagrange multipliers $\boldsymbol{\lambda}$, the system unknowns become $\boldsymbol{d}$ and $\boldsymbol{\lambda}$.

$$\Pi_p = \frac{1}{2}\boldsymbol{d}^T\boldsymbol{K}\boldsymbol{d} - \boldsymbol{d}^T\boldsymbol{F} + \boldsymbol{\lambda}^T(\boldsymbol{C}\boldsymbol{d} - \boldsymbol{Q}) \tag{3.10}$$

Differentiating the total potential energy function gives

$$\frac{\partial \Pi_p}{\partial \boldsymbol{d}} = \boldsymbol{K}\boldsymbol{d} - \boldsymbol{F} + \boldsymbol{C}^T\boldsymbol{\lambda} = \boldsymbol{O} \tag{3.11}$$

$$\frac{\partial \Pi_p}{\partial \boldsymbol{\lambda}} = \boldsymbol{C}\boldsymbol{d} - \boldsymbol{Q} = \boldsymbol{O} \tag{3.12}$$

Rewriting these two equations, the resulting equation will be

$$\begin{pmatrix} \boldsymbol{K} & \boldsymbol{C}^T \\ \boldsymbol{C} & \boldsymbol{O} \end{pmatrix}\begin{pmatrix} \boldsymbol{d} \\ \boldsymbol{\lambda} \end{pmatrix} = \begin{pmatrix} \boldsymbol{F} \\ \boldsymbol{Q} \end{pmatrix} \tag{3.13}$$

Though the Lagrange's method introduces extra new unknowns into the equation, it does not require the modification to the original total stiffness matrix.

The Lagrange multiplier $\boldsymbol{\lambda}$ can be interpreted as the forces related to the displacement constraint, explained as follows.

First some equations for displacement transformation are reviewed here (Cook, 1981). For any transformation between two displacement spaces $\boldsymbol{u}$ and $\boldsymbol{u}'$

$$(\boldsymbol{u}')_{p\times 1} = (\boldsymbol{T})_{p\times l}(\boldsymbol{u})_{l\times 1} \tag{3.14}$$

the transformation between the corresponding forces $\boldsymbol{f}$ and $\boldsymbol{f}'$ is

$$(\boldsymbol{f})_{l\times 1} = \left(\boldsymbol{T}^T\right)_{l\times p}(\boldsymbol{f}')_{p\times 1} \tag{3.15}$$

If the constraint equation (Equation 3.7) is seen as a transformation of the displacements, it will construct a new displacement space $(\boldsymbol{q})_{m\times 1}$

$$(\boldsymbol{q})_{m\times 1} = (\boldsymbol{C})_{m\times n}(\boldsymbol{d})_{n\times 1} \tag{3.16}$$

where the corresponding force is $(\boldsymbol{P}_c)_{m\times 1}$. Constraining the displacement can be seen as applying this constraint force to the unconstrained system to satisfy all the conditions. Transformed back to the original space, the equivalent force is

$$\boldsymbol{P} = \boldsymbol{C}^T\boldsymbol{P}_c \tag{3.17}$$

and should be added to the force term. Thus the governing equations for the constrained system are

$$\boldsymbol{K}\boldsymbol{d} = \boldsymbol{F} + \boldsymbol{C}^T\boldsymbol{P}_c \tag{3.18}$$

$$\boldsymbol{C}\boldsymbol{d} = \boldsymbol{Q} \tag{3.19}$$

which can be rewritten as

$$\begin{pmatrix} \boldsymbol{K} & \boldsymbol{C}^T \\ \boldsymbol{C} & \boldsymbol{O} \end{pmatrix}\begin{pmatrix} \boldsymbol{d} \\ -\boldsymbol{P}_c \end{pmatrix} = \begin{pmatrix} \boldsymbol{F} \\ \boldsymbol{Q} \end{pmatrix} \tag{3.20}$$

Compared with the equation with Lagrange's multipliers (Equation 3.13), the multipliers' physical meanings are clear: they are simply the (negative) constraint force. For the constraint given by Equation 3.4, this constraint force is a pair of nodal forces applied to Nodes C_1 and C_2 with the same magnitude but in the opposite directions along the local y-axes.

3.2.3 Tying Scheme

From Equation 3.20 it is seen that applying a constraint to an unconstrained system is similar to adding a new element with special stiffness matrix

$$\begin{pmatrix} O & C^T \\ C & O \end{pmatrix} \tag{3.21}$$

This similarity suggests that displacement constraints could be treated as a special kind of element, which are named as "ties" in this study, between different nodes. This tying scheme is very suitable for use in OXFEM where a frontal solver which operates elementwise is employed. Thus the main task in implementing the tying scheme is to formulate these special elements for different conditions.

3.3 Implementation of Tying Scheme in OXFEM

A tying scheme which applies specific tie elements to a system to connect different nodes defined in different local co-ordinate systems has been implemented into OXFEM. This scheme is able to cope with not only the node connection problem but also any linear constraint to displacements, provided the corresponding type of tie is constructed.

3.3.1 Local Co-ordinate System

Local co-ordinate systems are introduced to describe elements and nodes in terms of their geometry and properties. A local co-ordinate system can be defined in two different ways to suit different situations.

Three Points

Any co-ordinate system can be determined by three points which do not lie on the same line. Three reference points defined by the origin and two unit vectors along the local x^L-, y^L-axes are chosen to define a local co-ordinate system.

These reference points are given by their co-ordinates in the global co-ordinate system.

	global co-ordinates	local co-ordinates
$\boldsymbol{p}_0$	(x_0, y_0, z_0)	$(0,0,0)$
$\boldsymbol{p}_1$	(x_1, y_1, z_1)	$(0,1,0)$
$\boldsymbol{p}_2$	(x_2, y_2, z_2)	$(0,0,1)$

Thus the three unit vectors along the local axes are

$$\boldsymbol{i}^L = \boldsymbol{p}_1 - \boldsymbol{p}_0 = (x_1 - x_0)\,\boldsymbol{i} + (y_1 - y_0)\,\boldsymbol{j} + (z_1 - z_0)\,\boldsymbol{k} \tag{3.22}$$

$$\boldsymbol{j}^L = \boldsymbol{p}_2 - \boldsymbol{p}_0 = (x_2 - x_0)\,\boldsymbol{i} + (y_2 - y_0)\,\boldsymbol{j} + (z_2 - z_0)\,\boldsymbol{k} \tag{3.23}$$

$$\begin{aligned} \boldsymbol{k}^L = \boldsymbol{i}^L \times \boldsymbol{j}^L = {} & ((y_1 - y_0)(z_2 - z_0) - (y_2 - y_0)(z_1 - z_0))\,\boldsymbol{i} \\ & + ((z_1 - z_0)(x_2 - x_0) - (z_2 - z_0)(x_1 - x_0))\,\boldsymbol{j} \\ & + ((x_1 - x_0)(y_2 - y_0) - (x_2 - x_0)(y_1 - y_0))\,\boldsymbol{k} \end{aligned} \tag{3.24}$$

Therefore, for any point in the global space $\boldsymbol{x}^G = (x, y, z)^T$, its co-ordinates in the local space $\boldsymbol{x}^L = (x^L, y^L, z^L)^T$ will be

$$\boldsymbol{x}^L = \boldsymbol{R}\left(\boldsymbol{x}^G - \boldsymbol{p}_0\right) \tag{3.25}$$

where the transformation matrix $\boldsymbol{R}$ is

$$\boldsymbol{R} = \begin{pmatrix} x_1 - x_0 & y_1 - y_0 & z_1 - z_0 \\ x_2 - x_0 & y_2 - y_0 & z_2 - z_0 \\ \begin{pmatrix} (y_1 - y_0)(z_2 - z_0) \\ -(y_2 - y_0)(z_1 - z_0) \end{pmatrix} & \begin{pmatrix} (z_1 - z_0)(x_2 - x_0) \\ -(z_2 - z_0)(x_1 - x_0) \end{pmatrix} & \begin{pmatrix} (x_1 - x_0)(y_2 - y_0) \\ -(x_2 - x_0)(y_1 - y_0) \end{pmatrix} \end{pmatrix} \tag{3.26}$$

The transformation matrix is an orthogonal matrix, *i.e.*

$$\boldsymbol{R}^T = \boldsymbol{R}^{-1} \tag{3.27}$$

Thus

$$\boldsymbol{x}^G = \boldsymbol{R}^T \boldsymbol{x}^L + \boldsymbol{p}_0 \tag{3.28}$$

Three Angles

A local co-ordinate system can also be defined by moving the old origin point to a new position and rotating the z-, y-, x-axes by θ, ϕ, ψ respectively clockwise in order.

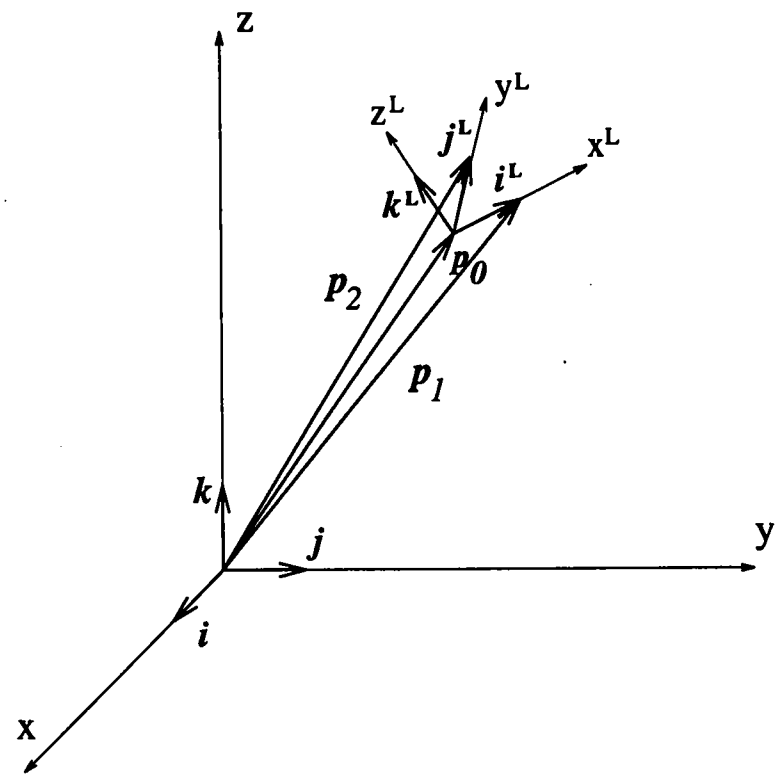


Figure 3.3: Definition of A Co-ordinate System Using Three Points

For these individual rotations, the transformation matrices are

$$\boldsymbol{R}_z = \begin{pmatrix} \cos\theta & \sin\theta & 0 \\ -\sin\theta & \cos\theta & 0 \\ 0 & 0 & 1 \end{pmatrix} \tag{3.29}$$

$$\boldsymbol{R}_y = \begin{pmatrix} \cos\phi & 0 & -\sin\phi \\ 0 & 1 & 0 \\ \sin\phi & 0 & \cos\phi \end{pmatrix} \tag{3.30}$$

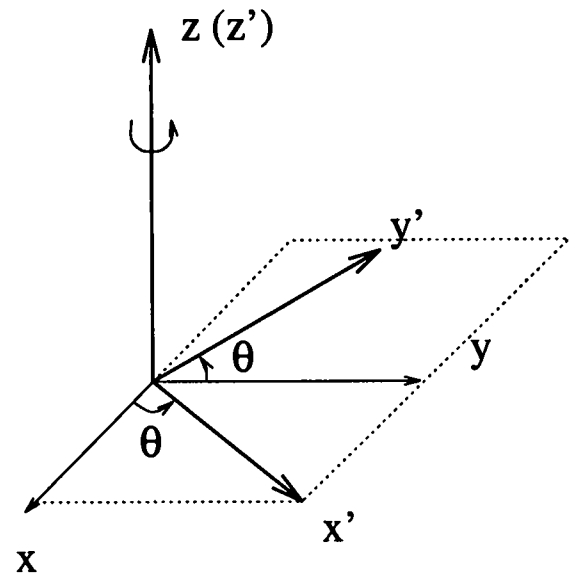
$$\boldsymbol{R}_x = \begin{pmatrix} 1 & 0 & 0 \\ 0 & \cos\psi & \sin\psi \\ 0 & -\sin\psi & \cos\psi \end{pmatrix} \tag{3.31}$$

The ultimate transformation matrix is

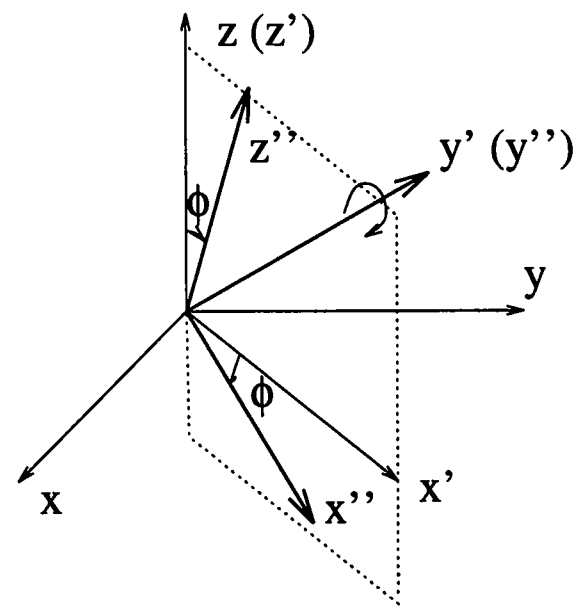
$$\boldsymbol{R} = \boldsymbol{R}_x \boldsymbol{R}_y \boldsymbol{R}_z \tag{3.32}$$

$$= \begin{pmatrix} \cos\theta\ \cos\phi & \sin\theta\ \cos\phi & -\sin\phi \\ \begin{pmatrix} \cos\theta\ \sin\phi\ \sin\psi \\ -\sin\theta\cos\psi \end{pmatrix} & \begin{pmatrix} \sin\theta\ \sin\phi\ \sin\psi \\ +\cos\theta\cos\psi \end{pmatrix} & \cos\phi\ \sin\psi \\ \begin{pmatrix} \cos\theta\ \sin\phi\ \cos\psi \\ +\sin\theta\sin\psi \end{pmatrix} & \begin{pmatrix} \sin\theta\ \sin\phi\ \cos\psi \\ -\cos\theta\sin\psi \end{pmatrix} & \cos\phi\ \cos\psi \end{pmatrix} \tag{3.33}$$

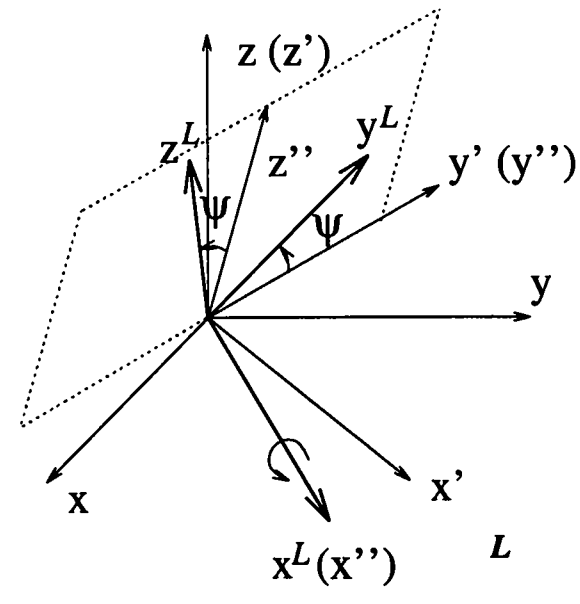
For any local co-ordinate system (x^L, y^L, z^L) in the global co-ordinate system (x, y, z), these angles may be determined by the following procedures (Figure 3.5). There are two possibilities concerning the directions of x^L-axis and z-axis.



(1)

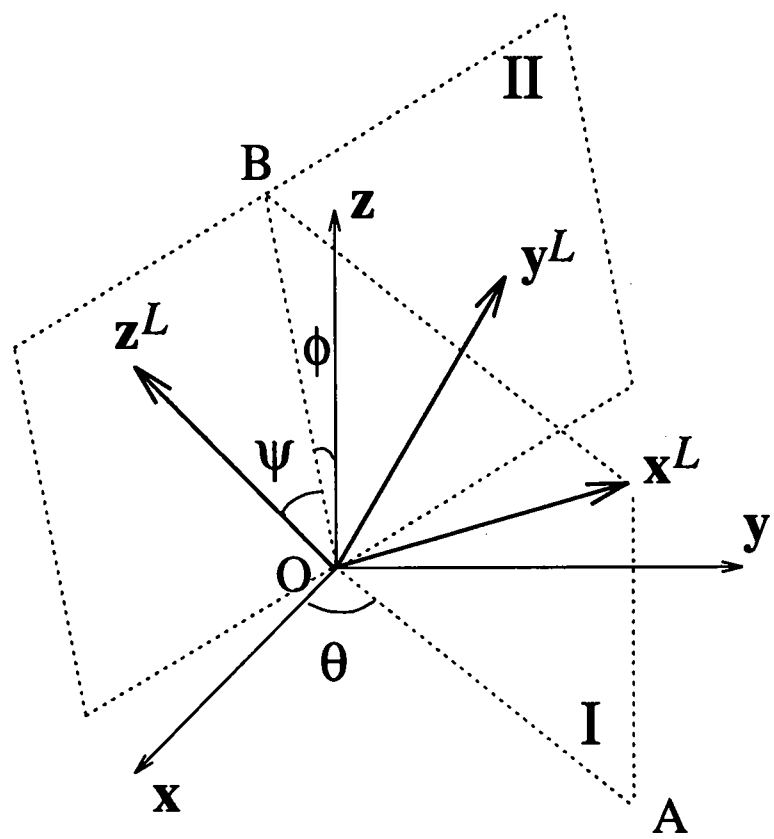


(2)

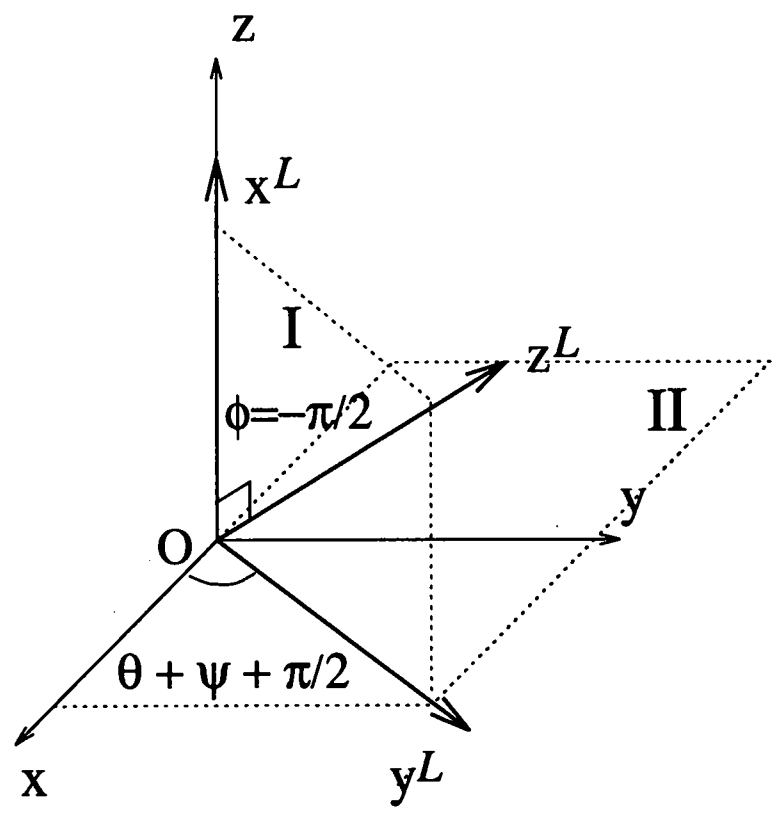


(3)

Figure 3.4: Definition of A Co-ordinate System by Rotating Axes



(1)



(2)

Figure 3.5: Determination of the Three Angles

1) x^L-axis and z-axis do not coincide In this case two planes can be determined by x^L- and z-axes (plane *I*) and y^L- and z^L-axes (plane *II*) respectively. The plane I intersects the plane Oxy at line OA and the plane II at line OB. Thus the angles between Ox and OA, Oz and OB, Oz^L and OB are the required angles θ,ϕ and ψ.

2) x^L-axis and z-axis coincide In this case the plane I is not unique, θ and ψ can be any value, but $\theta + \psi + \frac{\pi}{2}$ is equal to the angle between y- and y^L-axes. The angle $\phi = -\frac{\pi}{2}$ is also uniquely determined. (Note all positive angles are defined around the axes clockwise.)

3.3.2 Construction of Tie Elements

As discussed before, displacement constraints can be achieved by applying suitable tie elements between the nodes which need to be constrained. From Equations 3.20 and 3.21 it is seen that the variables of a tie element contain not only the displacements of the relevant nodes, but also some constraint reactions. These constraint reactions can be considered as the unknown variables associated with a set of "imaginary" nodes composing a tie element, in the same way as the displacements are the unknown variables for the real nodes. As the stiffness matrices of tie elements depend on the corresponding constraint equations, the key issue for constructing tie elements is to establish these constraint equations.

It is assumed that nodes N_1 and N_2 described in the local co-ordinate systems (x^1, y^1, z^1) and (x^2, y^2, z^2) have displacements $\boldsymbol{d}_1^1$ and $\boldsymbol{d}_2^2$ in their own co-ordinate systems respectively. The transformations between them and the global system are

$$\boldsymbol{d}_1^1 = \boldsymbol{R}^1 \boldsymbol{d}_1^G \qquad \boldsymbol{d}_1^G = \left(\boldsymbol{R}^1\right)^T \boldsymbol{d}_1^1 \tag{3.34}$$

$$\boldsymbol{d}_2^2 = \boldsymbol{R}^2 \boldsymbol{d}_2^G \qquad \boldsymbol{d}_2^G = \left(\boldsymbol{R}^2\right)^T \boldsymbol{d}_2^2 \tag{3.35}$$

Thus

$$\boldsymbol{d}_1^2 = \boldsymbol{R}^{12} \boldsymbol{d}_1^1 \quad \text{where} \quad \boldsymbol{R}^{12} = \boldsymbol{R}^2 \left(\boldsymbol{R}^1\right)^T \tag{3.36}$$

$$\boldsymbol{d}_2^1 = \boldsymbol{R}^{21} \boldsymbol{d}_2^2 \quad \text{where} \quad \boldsymbol{R}^{21} = \boldsymbol{R}^1 \left(\boldsymbol{R}^2\right)^T \tag{3.37}$$

Here the superscripts indicate the co-ordinate systems and the subscripts represent the different nodes. It should be pointed out that the movement of the origin of a co-ordinate system does not affect the transformation of the displacements, therefore the following study need not consider such movement.

Various types of connection between different co-ordinate systems for different types of elements will be discussed.

Connection between 3D Nodes

The connection of two 3D nodes N_1,N_2 in the local co-ordinate systems (x^1, y^1, z^1) and (x^2, y^2, z^2) requires that both nodes have same displacements. After transformation into the local co-ordinate system (x^1, y^1, z^1), all the displacements will be

$$\boldsymbol{d}_1^1 = \begin{pmatrix} u_1^1 \\ v_1^1 \\ w_1^1 \end{pmatrix} \tag{3.38}$$

$$\boldsymbol{d}_2^1 = \boldsymbol{R}^{21}\boldsymbol{d}_2^2 = \begin{pmatrix} r_{11}^{21} & r_{12}^{21} & r_{13}^{21} \\ r_{21}^{21} & r_{22}^{21} & r_{23}^{21} \\ r_{31}^{21} & r_{32}^{21} & r_{33}^{21} \end{pmatrix} \begin{pmatrix} u_2^2 \\ v_2^2 \\ w_2^2 \end{pmatrix} \tag{3.39}$$

The connection condition is

$$u_2^1 - u_1^1 = 0 \tag{3.40}$$

$$v_2^1 - v_1^1 = 0 \tag{3.41}$$

$$w_2^1 - w_1^1 = 0 \tag{3.42}$$

Therefore

$$u_1^1 - r_{11}^{21}u_2^2 - r_{12}^{21}v_2^2 - r_{13}^{21}w_2^2 = 0 \tag{3.43}$$

$$v_1^1 - r_{21}^{21}u_2^2 - r_{22}^{21}v_2^2 - r_{23}^{21}w_2^2 = 0 \tag{3.44}$$

$$w_1^1 - r_{31}^{21}u_2^2 - r_{32}^{21}v_2^2 - r_{33}^{21}w_2^2 = 0 \tag{3.45}$$

For the displacement vector $(u_1, v_1, w_1, u_2, v_2, w_2)$, the constraint matrix is

$$\boldsymbol{C} = \begin{pmatrix} 1 & 0 & 0 & r_{11}^{21} & r_{12}^{21} & r_{13}^{21} \\ 0 & 1 & 0 & r_{21}^{21} & r_{22}^{21} & r_{23}^{21} \\ 0 & 0 & 1 & r_{31}^{21} & r_{32}^{21} & r_{33}^{21} \end{pmatrix} \tag{3.46}$$

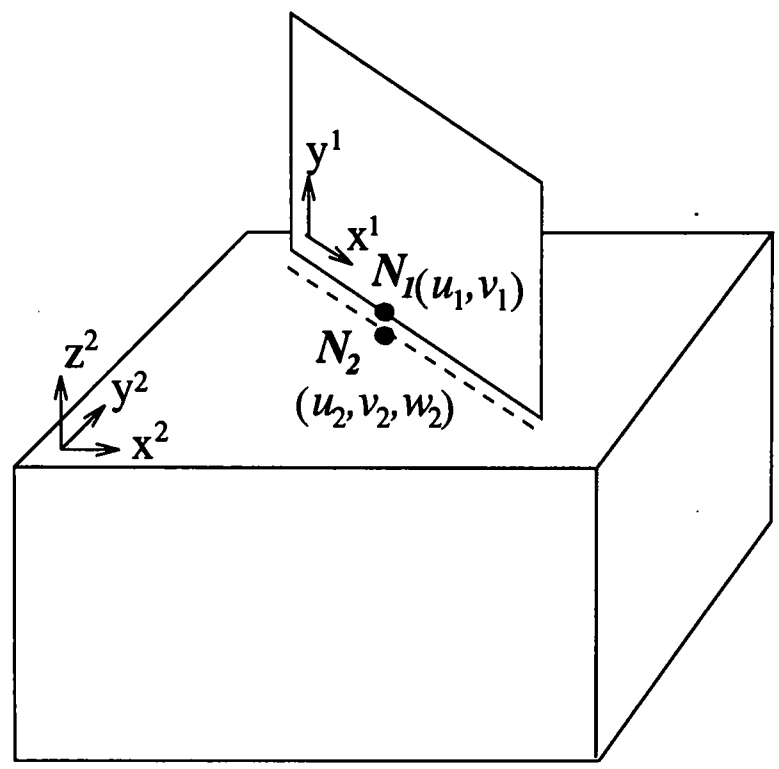


Figure 3.6: Connection between 2D and 3D Nodes

Connection between 2D and 3D Nodes

Similarly the connection of 2D node N_1 and 3D node N_2 requires that both nodes have the same displacements (Figure 3.6). After the same transformation as for two 3D nodes, the connection equations are the same as Equations 3.43, 3.44 and 3.45. Since w_1 is arbitrary as the node N_1 is two-dimensional, the third equation is automatically satisfied. For the displacement vector $(u_1, v_1, u_2, v_2, w_2)$, the constraint matrix is

$$C = \begin{pmatrix} 1 & 0 & r_{11}^{21} & r_{12}^{21} & r_{13}^{21} \\ 0 & 1 & r_{21}^{21} & r_{22}^{21} & r_{23}^{21} \end{pmatrix} \tag{3.47}$$

Connection between Two or More 2D Nodes

The connection of 2D nodes is more complicated than the previous situations and is studied first in terms of a simplified case of two 2D nodes with the same local y-axes. This is later extended to the more general situation. It is assumed that the x- and y-axes are in plane and the z-axis is out of plane.

1) Two 2D Nodes with the same local y-axes When two nodes have the same y-axes (Figure 3.7), their x-, z-axes will be in parallel planes. Also the intersection line

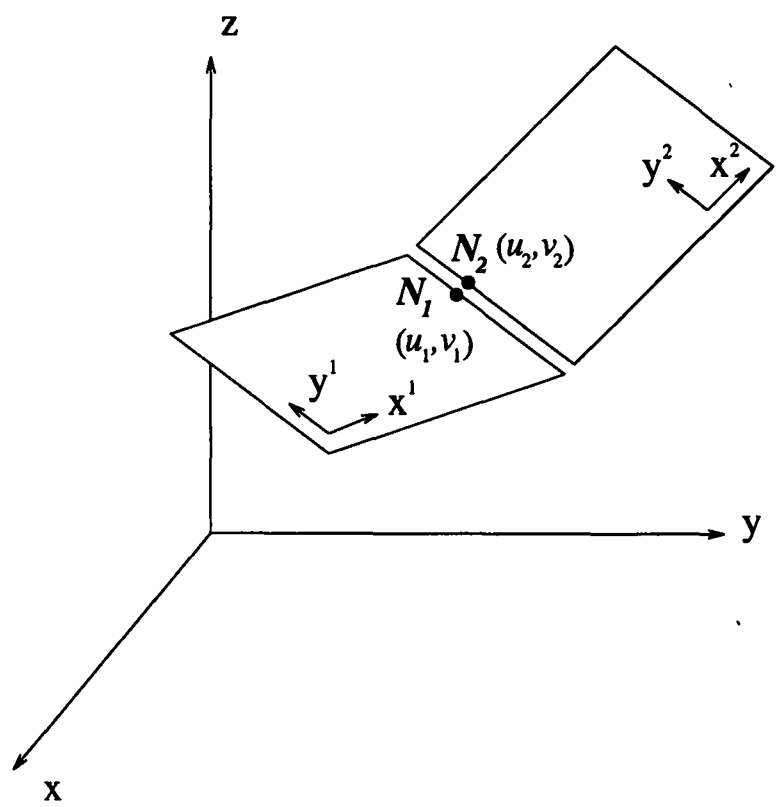


Figure 3.7: Connection between 2D Nodes with the Same y-axes

of the planes containing x^1- and y^1-axes and x^2- and y^2-axes should be parallel to their y-axes. If the node N_1 has displacement $(u_1, v_1, w_1)^T$ in its own local system (x^1, y^1, z^1) and the node N_2 has $(u_2, v_2, w_2)^T$ in (x^2, y^2, z^2) then as they are connected together, they should have the same displacement $(U, v, W)^T$ in a reference system (X, y, Z) which shares the y-axis with the local co-ordinate systems (Figure 3.8). It can be shown that

$$u_1 = U\cos\theta^1 + W\sin\theta^1 \tag{3.48}$$

$$u_2 = U\cos\theta^2 + W\sin\theta^2 \tag{3.49}$$

$$v_1 = v \tag{3.50}$$

$$v_2 = v \tag{3.51}$$

Equations 3.50 and 3.51 give a condition

$$v_1 = v_2 \tag{3.52}$$

From Equations 3.48 and 3.49 the common displacements can be expressed by

$$U = \frac{1}{\sin(\theta^2 - \theta^1)}(\ u_1\sin\theta^2 + u_2\sin\theta^1) \tag{3.53}$$

$$W = \frac{1}{\sin(\theta^2 - \theta^1)}(-u_1\cos\theta^2 + u_2\cos\theta^1) \tag{3.54}$$

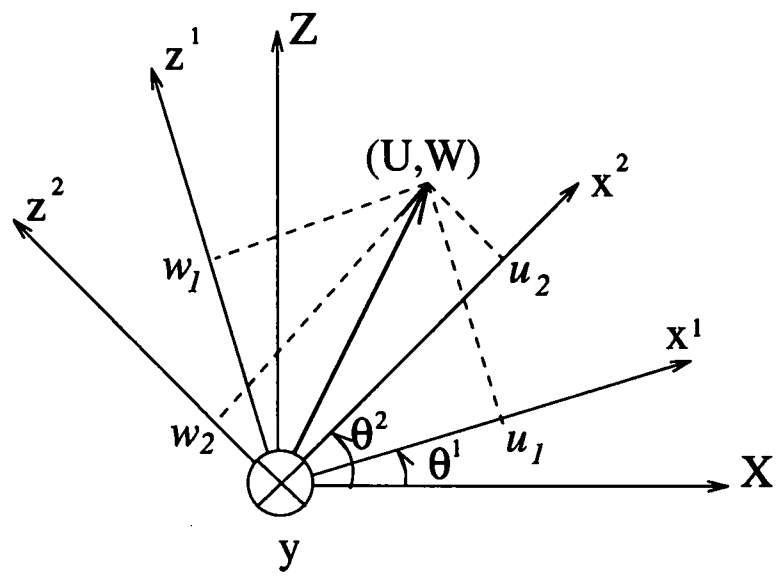


Figure 3.8: Connection Condition of Displacements along Local x- and z-axes

When $\theta^1 \neq \theta^2$, for any pair of u_1, u_2 there always exist unique U, W with the adjustment of arbitrary w_1 and w_2, which means that the two nodes can move together without any constraint to u_1,u_2. For the case of $\theta^1 = \theta^2$, Equations 3.48 and 3.49 will become identical so that the following condition will be needed.

$$u_1 = u_2 \tag{3.55}$$

Therefore two conclusions can be made.

a) For any two non-parallel planes, the nodes of different planes at the same position along the intersection line must have same displacement components parallel to the intersection line. There is no constraint for the displacement normal to this line.

b) For two parallel planes, in addition to the constraint to the displacement components parallel to the intersection line, they must have same displacement components normal to this line.

In addition to these displacement constraints, the equilibrium condition should be considered. For the non-parallel planes, the external load along their intersection line can be applied to a node of either plane and will be distributed between nodes automatically by the displacement constraint condition. The external load normal to the intersection line on these nodes must be resolved into components parallel to each plane and applied

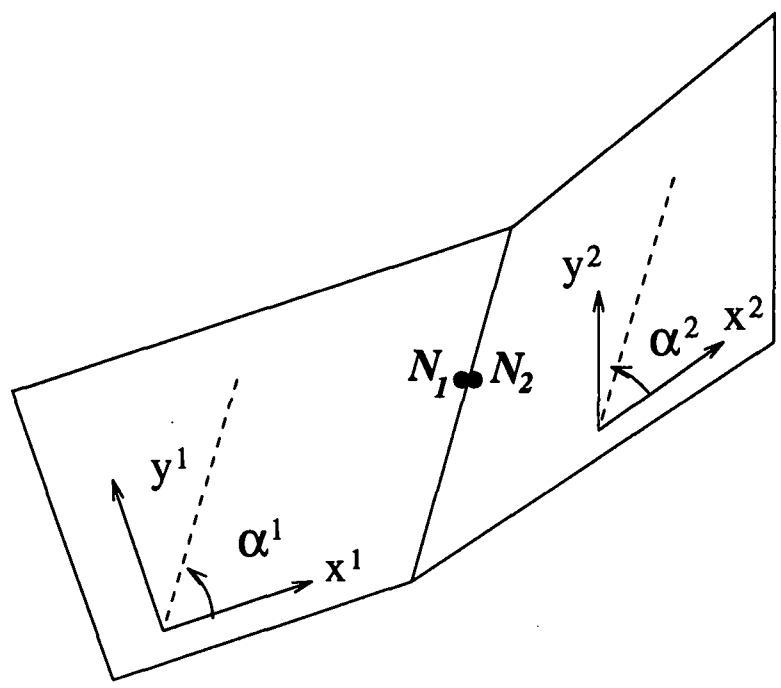


Figure 3.9: Two 2D Nodes with Different Local y-axes

within them as these 2D nodes do not have out-of-plane stiffness. For the parallel planes the external loads can be applied to either plane, decomposing the loads is not necessary and is not unique.

2) Two 2D nodes with different local y-axes The conclusions of Section 1) are independent of the co-ordinate system and can be used in this case. However the displacements need transforming to the directions parallel and normal to the intersection line for using the conclusions.

For the co-ordinate systems (x^1, y^1, z^1) and (x^2, y^2, z^2) shown in Figure 3.9, their transformation matrices from the global co-ordinate system are $\boldsymbol{R}^1$ and $\boldsymbol{R}^2$, and the transformation matrix from (x^1, y^1, z^1) to (x^2, y^2, z^2) will be

$$\boldsymbol{R}^{12} = \boldsymbol{R}^2 \left(\boldsymbol{R}^1\right)^T = \begin{pmatrix} r_{11} & r_{12} & r_{13} \\ r_{21} & r_{22} & r_{23} \\ r_{31} & r_{32} & r_{33} \end{pmatrix} \tag{3.56}$$

In (x^1, y^1, z^1) space the equation for the plane Ox^1y^1 which contains the x^1- and y^1-axis is $z^1 = 0$. Similarly the equation of the plane of Ox^2y^2 in (x^2, y^2, z^2) is $z^2 = 0$. After transformation, the co-ordinates of the nodes in the plane Ox^1y^1 will become

$$\boldsymbol{R}^{12} \begin{pmatrix} x^1 \\ y^1 \\ 0 \end{pmatrix} = \begin{pmatrix} r_{11}x^1 + r_{12}y^1 \\ r_{21}x^1 + r_{22}y^1 \\ r_{31}x^1 + r_{32}y^1 \end{pmatrix} \tag{3.57}$$

in the (x^2, y^2, z^2) space.

This plane intersects the plane Ox^2y^2 by

$$r_{31}\, x^1 \;+\; r_{32}\, y^1 \;=\; 0 \tag{3.58}$$

The same procedures can be operated in reverse to express the intersection line in (x^2, y^2, z^2) space, *i.e.*

$$r_{13}\, x^2 \;+\; r_{23}\, y^2 \;=\; 0 \tag{3.59}$$

From these equations the slope of the intersection line in both spaces can be determined.

$$\tan\alpha^1 \;=\; -\frac{r_{31}}{r_{32}} \tag{3.60}$$

$$\tan\alpha^2 \;=\; -\frac{r_{13}}{r_{23}} \tag{3.61}$$

Therefore the displacements in each plane can be transformed to the directions normal and parallel to the intersection line by rotating about z^1- and z^2-axes by angles of $-(\frac{\pi}{2} - \alpha^1)$ and $-(\frac{\pi}{2} - \alpha^2)$ in order to have the same y-axes. For two nodes within both planes at the same position (nodes N_1 and N_2 in Figure 3.9) the new displacements are

$$\begin{aligned} \boldsymbol{d}_1^{1N} &= \begin{pmatrix} \cos\left(-\left(\frac{\pi}{2}-\alpha^1\right)\right) & \sin\left(-\left(\frac{\pi}{2}-\alpha^1\right)\right) & 0 \\ -\sin\left(-\left(\frac{\pi}{2}-\alpha^1\right)\right) & \cos\left(-\left(\frac{\pi}{2}-\alpha^1\right)\right) & 0 \\ 0 & 0 & 1 \end{pmatrix} \begin{pmatrix} u_1 \\ v_1 \\ w_1 \end{pmatrix} \\ &= \begin{pmatrix} u_1 \sin\alpha^1 - v_1 \cos\alpha^1 \\ u_1 \cos\alpha^1 + v_1 \sin\alpha^1 \\ w_1 \end{pmatrix} \end{aligned} \tag{3.62}$$

$$\begin{aligned} \boldsymbol{d}_2^{2N} &= \begin{pmatrix} \cos\left(-\left(\frac{\pi}{2}-\alpha^2\right)\right) & \sin\left(-\left(\frac{\pi}{2}-\alpha^2\right)\right) & 0 \\ -\sin\left(-\left(\frac{\pi}{2}-\alpha^2\right)\right) & \cos\left(-\left(\frac{\pi}{2}-\alpha^2\right)\right) & 0 \\ 0 & 0 & 1 \end{pmatrix} \begin{pmatrix} u_2 \\ v_2 \\ w_2 \end{pmatrix} \\ &= \begin{pmatrix} u_2 \sin\alpha^2 - v_2 \cos\alpha^2 \\ u_2 \cos\alpha^2 + v_2 \sin\alpha^2 \\ w_2 \end{pmatrix} \end{aligned} \tag{3.63}$$

For two oblique planes, the constraint condition is

$$u_1\, \cos\alpha^1 \;+ v_1\, \sin\alpha^1 \;=\; u_2\, \cos\alpha^2 \;+ v_2\, \sin\alpha^2 \tag{3.64}$$

When the two planes are parallel, an extra condition is applied.

$$u_1\, \sin\alpha^1 \;- v_1\, \cos\alpha^1 \;=\; u_2\, \sin\alpha^2 \;- v_2\, \cos\alpha^2 \tag{3.65}$$

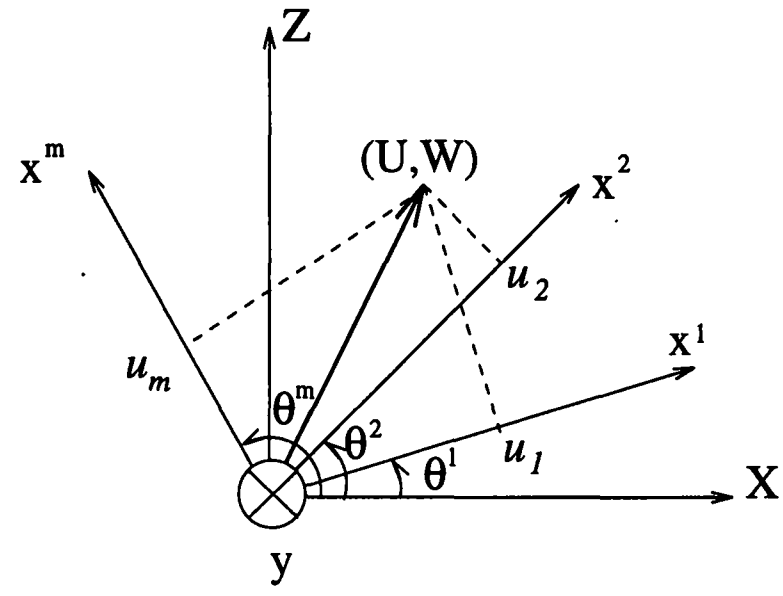


Figure 3.10: Multi-plane Connection

3) Three or more 2D nodes in planes with a common intersection line as the same local y-axes In this simple case a reference co-ordinate system (X, y, Z) whose y-axis is the same as the local co-ordinate system is also used (Figure 3.10). For the displacement components parallel to the intersection line which is parallel to the common y-axis, there are still $m - 1$ equations to ensure that the displacements in the direction of the axis have the same value.

$$v_1 = v_2 = v_3 = \cdots = v_{m-1} = v_m \tag{3.66}$$

The displacements normal to the intersection line must be compatible so that

$$u_1 = U\cos\theta^1 + W\sin\theta^1 \tag{3.67}$$

$$u_2 = U\cos\theta^2 + W\sin\theta^2 \tag{3.68}$$

$$u_3 = U\cos\theta^3 + W\sin\theta^3 \tag{3.69}$$

$$\cdots$$

$$u_m = U\cos\theta^m + W\sin\theta^m \tag{3.70}$$

If more than two planes intersect on a common line, then at least two of these planes will be non-parallel, including say node 1 and 2. Thus from Equations 3.67 and 3.68, U and W can be solved as $\theta^1 \neq \theta^2$.

$$U = \frac{1}{\sin(\theta^2 - \theta^1)}\left(\ u_1\ \sin\theta^2 - u_2\ \sin\theta^1\right) \tag{3.71}$$

$$W = \frac{1}{\sin(\theta^2 - \theta^1)}\left(-u_1\ \cos\theta^2 + u_2\ \cos\theta^1\right) \tag{3.72}$$

The displacements $u_3, u_4, \cdots, u_m$ are not independent and are determined by the following equations:

$$\begin{aligned} u_i &= U\cos\theta^i + W\sin\theta^i \\ &= \frac{1}{\sin(\theta^2-\theta^1)}\left(u_1\ \sin(\theta^2-\theta^i) + u_2\ \sin(\theta^i-\theta^1)\right) \qquad (3.73) \\ &\qquad\qquad (i\ =\ 3,\ \cdots,\ m) \end{aligned}$$

The condition can be rewritten as

$$u_1\sin(\theta^2-\theta^i)\ +\ u_2\sin(\theta^i-\theta^1)\ +\ u_i\sin(\theta^1-\theta^2)\ =\ 0 \qquad (3.74)$$
$$(i\ =\ 3,\ \cdots,\ m)$$

In conclusion, for m ($m \geq 3$) planes intersecting at the same line, there are $m-1$ constraints on their displacements parallel to the intersection line and $m-2$ constraints on their displacements normal to the intersection line. They are

$$v_1 = v_2 \qquad (3.75)$$

$$v_2 = v_3 \qquad (3.76)$$

$$\cdots\ \cdots\ \cdots$$

$$v_{m-1} = v_m \qquad (3.77)$$

$$u_1\sin(\theta^2-\theta^3)\ +\ u_2\sin(\theta^3-\theta^1)\ +\ u_3\sin(\theta^1-\theta^2)\ =\ 0 \qquad (3.78)$$

$$u_1\sin(\theta^2-\theta^4)\ +\ u_2\sin(\theta^4-\theta^1)\ +\ u_4\sin(\theta^1-\theta^2)\ =\ 0 \qquad (3.79)$$

$$\cdots\cdots\cdots\cdots\cdots$$

$$u_1\sin(\theta^2-\theta^m)\ +\ u_2\sin(\theta^m-\theta^1)\ +\ u_m\sin(\theta^1-\theta^2)\ =\ 0 \qquad (3.80)$$

The constraint conditions depend on the included angles between the different planes. They can be expressed as follows.

For any two local co-ordinate systems (x^i, y^i, z^i) and (x^j, y^j, z^j) which share a common local y-axis, the transformation matrix between them can be calculated from their transformation matrices in the global co-ordinate system $\boldsymbol{R}^i$ and $\boldsymbol{R}^j$.

$$\boldsymbol{R}^{ji} = \boldsymbol{R}^i\left(\boldsymbol{R}^j\right)^T = \begin{pmatrix} r_{11}^{ji} & r_{12}^{ji} & r_{13}^{ji} \\ r_{21}^{ji} & r_{22}^{ji} & r_{23}^{ji} \\ r_{31}^{ji} & r_{32}^{ji} & r_{33}^{ji} \end{pmatrix} \qquad (3.81)$$

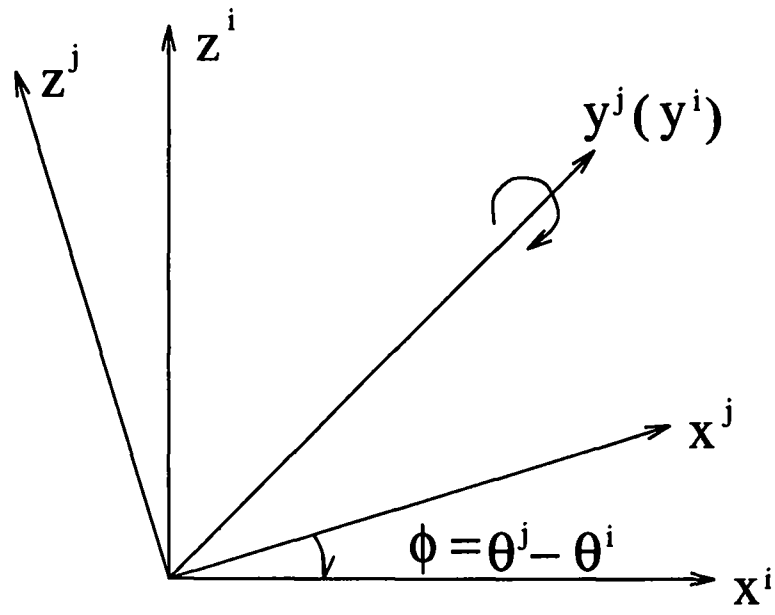


Figure 3.11: Calculation of Sine of Included Angle

Meanwhile (x^i, y^i, z^i) can be achieved by rotating (x^j, y^j, z^j) about the y^j-axis by an angle of $(\theta^j - \theta^i)$. Using Equation 3.30 the transformation matrix is

$$\boldsymbol{R}^{ji} = \begin{pmatrix} \cos(\theta^j - \theta^i) & 0 & -\sin(\theta^j - \theta^i) \\ 0 & 1 & 0 \\ \sin(\theta^j - \theta^i) & 0 & \cos(\theta^j - \theta^i) \end{pmatrix} \tag{3.82}$$

Comparison of thes two expressions of $\boldsymbol{R}^{ji}$ will give

$$\sin(\theta^j - \theta^i) = -r_{13}^{ji} \tag{3.83}$$

4) Three or more 2D nodes of planes with arbitrary local y-axes but a common intersection line In a similar way to the case of two 2D nodes with different local y-axis in Section 2), the first step in this case is to calculate the slopes of the intersection line in all planes. After establishing the transformation matrices between the local coordinate system (x^1, y^1, z^1) and others,

$$\boldsymbol{R}^{1i} = \boldsymbol{R}^i \left(\boldsymbol{R}^1\right)^T = \begin{pmatrix} r_{11}^{1i} & r_{12}^{1i} & r_{13}^{1i} \\ r_{21}^{1i} & r_{22}^{1i} & r_{23}^{1i} \\ r_{31}^{1i} & r_{32}^{1i} & r_{33}^{1i} \end{pmatrix} \qquad (\, i = 2, 3, \cdots, m\,) \tag{3.84}$$

the slopes can be obtained using Equations 3.60 and 3.61.

$$\tan\alpha^1 = -\frac{r_{31}^{12}}{r_{32}^{12}} \tag{3.85}$$

$$\tan\alpha^2 = -\frac{r_{13}^{12}}{r_{23}^{12}} \tag{3.86}$$

$$\tan\alpha^3 = -\frac{r_{13}^{13}}{r_{23}^{13}} \tag{3.87}$$

$$\cdots \quad \cdots \quad \cdots$$

$$\tan\alpha^m = -\frac{r_{13}^{1m}}{r_{23}^{1m}} \tag{3.88}$$

All the local co-ordinate systems can be rotated about their own z-axes by $-\left(\frac{\pi}{2}-\alpha^i\right)$ to new systems which share a common y-axis.

$$\begin{aligned} \boldsymbol{d}_i^N &= \begin{pmatrix} \cos\left(-\left(\frac{\pi}{2}-\alpha^i\right)\right) & \sin\left(-\left(\frac{\pi}{2}-\alpha^i\right)\right) & 0 \\ -\sin\left(-\left(\frac{\pi}{2}-\alpha^i\right)\right) & \cos\left(-\left(\frac{\pi}{2}-\alpha^i\right)\right) & 0 \\ 0 & 0 & 1 \end{pmatrix} \begin{pmatrix} u_i \\ v_i \\ w_i \end{pmatrix} \\ &= \begin{pmatrix} u_i \sin\alpha^1 - v_i \cos\alpha^1 \\ u_i \cos\alpha^1 + v_i \sin\alpha^1 \\ w_i \end{pmatrix} \\ &\qquad (i = 1, 2, \cdots, m) \end{aligned} \tag{3.89}$$

Therefore the conditions on the displacement components parallel to the intersection line become

$$u_i \cos\alpha^i + v_i \sin\alpha^i = u_{i+1} \cos\alpha^{i+1} + v_{i+1} \sin\alpha^{i+1} \tag{3.90}$$
$$(i = 1, 2, \cdots, m-1)$$

The constraints on the displacement normal to the intersection line are

$$\begin{aligned} &\left(u_1 \sin\alpha^1 - v_1 \cos\alpha^1\right) \sin\left(\theta^2 - \theta^i\right) \\ + &\left(u_2 \sin\alpha^2 - v_2 \cos\alpha^2\right) \sin\left(\theta^i - \theta^1\right) \\ + &\left(u_i \sin\alpha^i - v_i \cos\alpha^i\right) \sin\left(\theta^1 - \theta^2\right) = 0 \end{aligned} \tag{3.91}$$
$$(i = 3, 4, \cdots m)$$

Combination of Various Tie Types

The combinations of the different types of ties discussed above can be used to cope with various situations. Here are some examples.

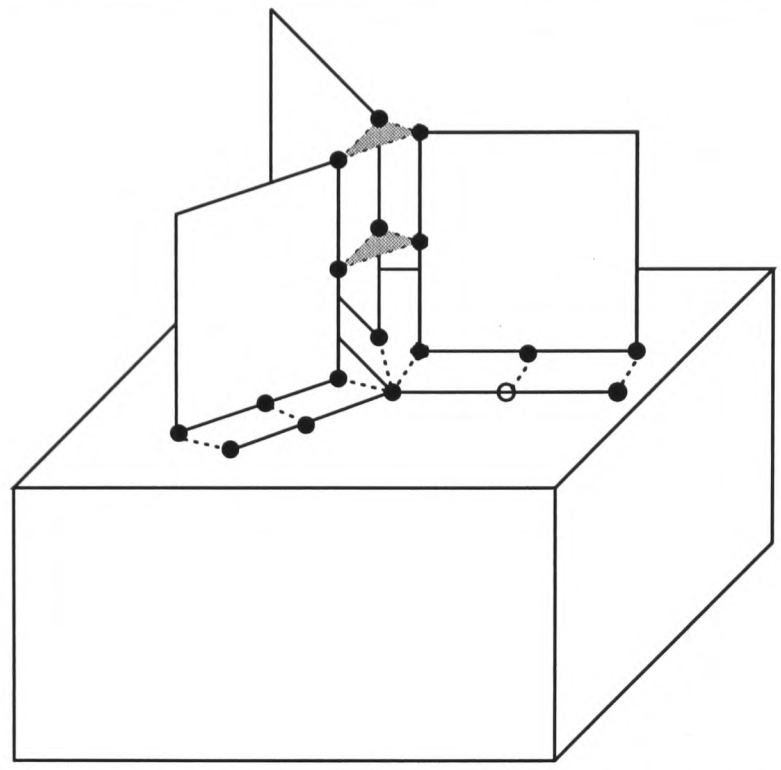


Figure 3.12: Multiple Planes Connected with 3D Block

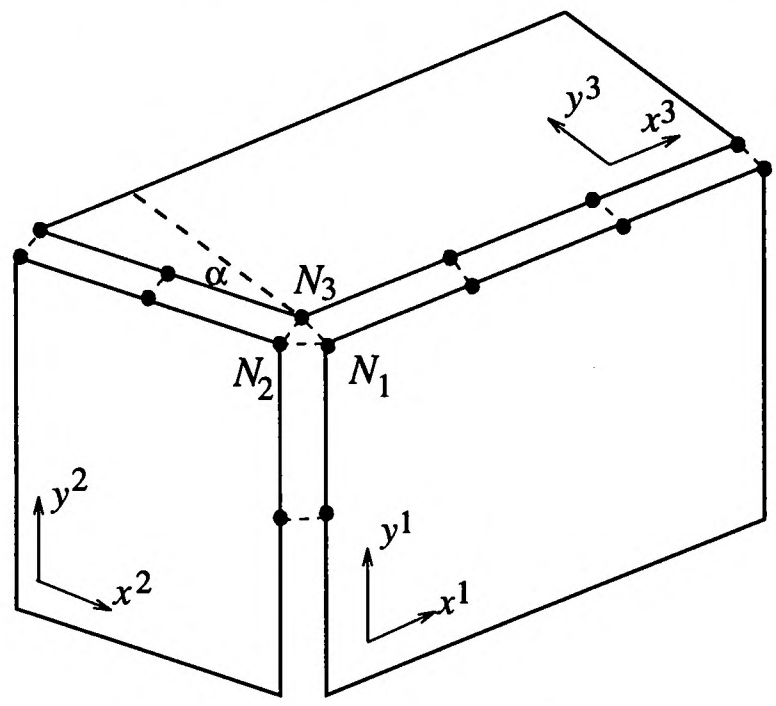


Figure 3.13: Three Planes Intersecting at One Point

1) Multiple planes connected with 3D block In this case (Figure 3.12), the 2D planes can be connected by the ties for 2D nodes already developed except for the nodes connected to the 3D block. As these nodes are tied to the same 3D node by the ties for 2D and 3D nodes, they are automatically connected.

2) Three planes intersecting at a point In Figure 3.13 the planes *I* and *II* are obliquely connected with an included angle of $\frac{\pi}{2} + \alpha$ while the plane *III* is normal to both of them. For the nodes on the intersection lines which do not lie on the corner, the ties for two 2D nodes can be used to connect them. Only the connection condition for

the corner nodes need be considered in detail.

Local co-ordinate systems are set up in order that the y^1- and y^2-axes are parallel to the intersection line between the plane I and II and x^1- and x^3-axes are parallel to the intersection line between the plane I and III. A reference co-ordinate system is also set up using x^1-, y^3- and y^1-axes as its X-, Y- and Z-axes.

The connection of the nodes N_1, N_2 and N_3 requires their displacements $(u_1, v_1, w_1)^T$, $(u_2, v_2, w_2)^T$ and $(u_3, v_3, w_3)^T$ to satisfy the following equations

$$u_1 = U \tag{3.92}$$

$$v_1 = W \tag{3.93}$$

$$w_1 = -V \tag{3.94}$$

$$u_2 = U \sin\alpha - V \cos\alpha \tag{3.95}$$

$$v_2 = W \tag{3.96}$$

$$w_2 = -U \cos\alpha + V \sin\alpha \tag{3.97}$$

$$u_3 = U \tag{3.98}$$

$$v_3 = V \tag{3.99}$$

$$w_3 = W \tag{3.100}$$

where $(U, V, W)^T$ is their common displacement.

The first six equations give

$$U = u_1 \tag{3.101}$$

$$V = \frac{u_1 \sin\alpha - u_2}{\cos\alpha} \tag{3.102}$$

$$W = v_1 = v_2 \tag{3.103}$$

Substituting these equations to Equations 3.98 - 3.100 establishes the following relations,

$$u_3 = u_1 \tag{3.104}$$

$$u_2 = u_3 \sin\alpha - v_3 \cos\alpha \tag{3.105}$$

$$w_3 = v_1 = v_2. \tag{3.106}$$

Since the out-of-plane displacements of these planes are arbitrary, the effective constraints are

$$v_1 = v_2 \tag{3.107}$$

$$u_1 = u_3 \tag{3.108}$$

$$u_2 = u_3 \sin\alpha - v_3 \cos\alpha \tag{3.109}$$

It is obvious that applying the ties for two 2D nodes between N_1 and N_2, N_2 and N_3, N_1 and N_3 can satisfy these conditions and all these ties are necessary.

The connection condition for other less common situations could be studied using the same principles of this chapter.

3.3.3 Sequence of Gauss Elimination

After assembly into an unconstrained system, tie elements will couple some degrees of freedom of the existing nodes and introduce some constraint reaction forces. For a constraint force, which is a new component in the total unknown variables, the corresponding diagonal term in the total stiffness matrix is zero. During a Gauss elimination, pivoting on such a zero diagonal item will fail. Fortunately this diagonal item will become non-zero after its coupled displacement of a real node is eliminated. Equation 3.110 shows such a process.

$$\begin{pmatrix} \ddots & & & & \\ & k_{ii} & \cdots & c_{ij} & \\ & \vdots & \ddots & \vdots & \\ & c_{ij} & \cdots & 0 & \\ & & & & \ddots \end{pmatrix} \Rightarrow \begin{pmatrix} \ddots & & & & \\ & k_{ii} & \cdots & c_{ij} & \\ & \vdots & \ddots & \vdots & \\ & 0 & \cdots & \frac{-(c_{ij})^2}{k_{ii}} & \\ & & & & \ddots \end{pmatrix} \tag{3.110}$$

Because all contributions from the coupled nodes have the same sign, the non-zero values will fill in the diagonal terms corresponding to the constraint forces when the displacements of these nodes are eliminated before the constraint forces, provided the original stiffness matrix is positive definite.

The easiest way to ensure that the constraint forces are eliminated after the real nodes is strict partition, *i.e.* putting all the constraint forces after the real nodes in

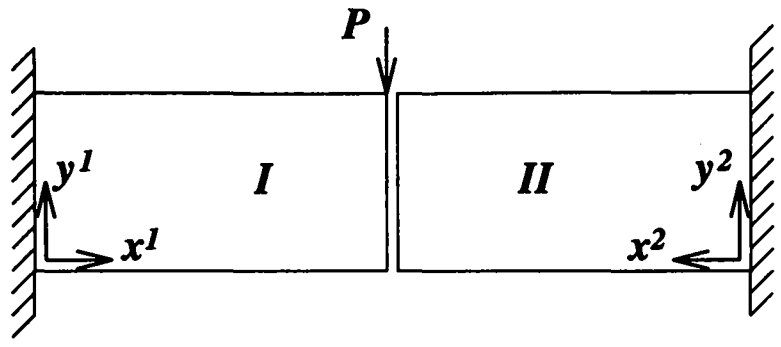


Figure 3.14: Two Parallel Deep Beams

the elimination sequence. But such an arrangement, which requires an expanded total stiffness matrix, is not feasible. In fact the strict partition is not necessary as a constraint force can be eliminated just after its connected displacements.

In OXFEM each node has a life which indicates that this node is eliminated after a specific element has been assembled. To ensure that a node which is coupled by tie elements is not eliminated before the relevant constraint forces, its life should be decided by not only the real elements but also the tie elements.

In addition, prescribed displacements are not involved in Gauss elimination in the frontal solver of OXFEM, so that any constraint for two prescribed degrees of freedom will never result in non-zero diagonal terms in the stiffness matrix. Therefore such redundant ties constraining the prescribed displacements should be avoided.

3.3.4 Examples for Using Tie Elements

Different types of tie elements can be used for various displacement constraints. Here are some examples showing the application of tie elements in the connection of initially separated deep beams.

Connection of Two Parallel Deep Beams

Two plane stress rectangles of 2m $\times$ 1m with unit thickness are used to simulate two deep beams (Figure 3.14). The two beams use the same meshes and the co-ordinate system for the second beam is obtained by rotating about the y_1-axis by 180°. The Young's modulus for both beams is $E = 10^8$kPa and the Poisson's ratio is $\nu = 0.2$. A vertical concentrated force $P = 10^4$N is applied to the top right point of the first beam.

1) The two parts deform individually without any connection between them. It is obvious that the first beam behaves as a cantilever while the second one remains unstrained (Figure 3.15(1)). The vertical displacement of the loading point is 0.0406m.

2) Tie elements which constrain vertical displacements are installed between the two beams. Under the same load, the two parts deform together and provide vertical stiffness twice that of an individual part against the load. The deformation pattern is the same as in case 1, but the displacements are reduced by half. The vertical displacement of the loading point now is 0.0203m. (Figure 3.15(2))

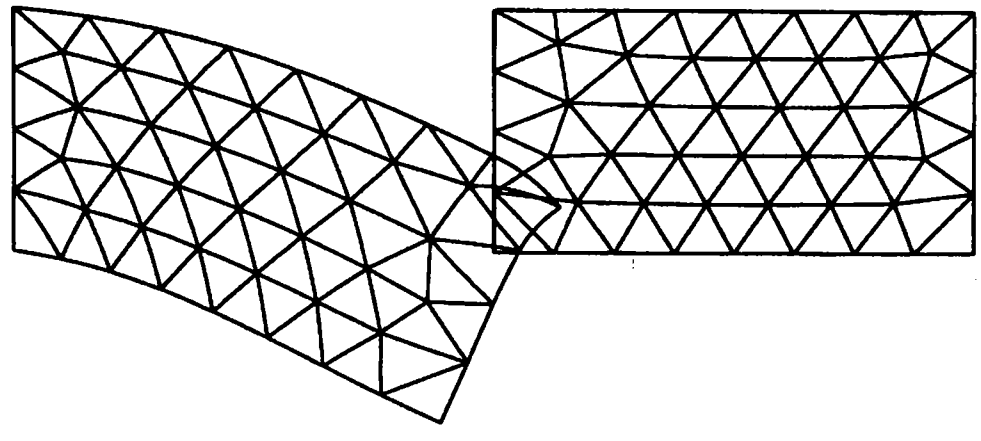
3) Both beams are fully tied with constraints on vertical and horizontal displacements. The whole system behaves like a fixed ended beam now rather than two cantilevers. The stiffness of the system against the same load is much higher than before and the vertical displacement of the loading point is only 0.008m. (Figure 3.15(3))

Connection of Three Oblique Deep Beams

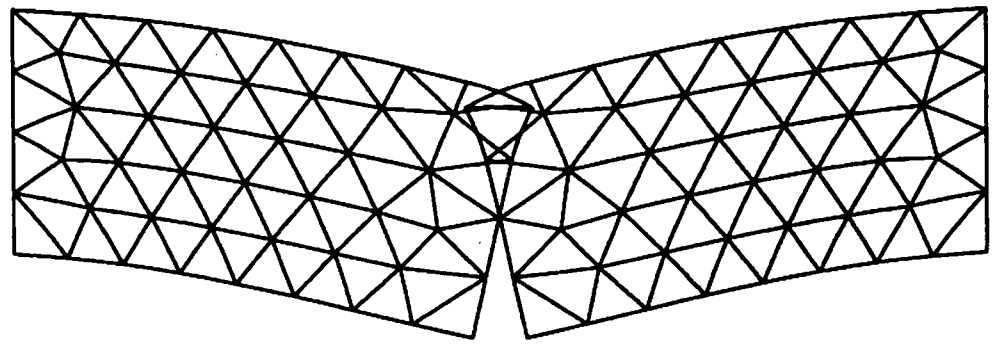
Three individual deep beams with the same properties and geometry as before are located obliquely as shown in Figure 3.16. The local co-ordinate systems for the beam *II* and *III* may be constructed by rotating about the y^1-axis by -120^o and 120^o respectively. Similarly a vertical concentrated load is applied to the beam *I* and three cases are analysed.

1) Three parts deform individually without any connection between each other. Only the first beam behaves as a cantilever while the others remain undeformed (Figure 3.17 (1)). The vertical displacement of the loading point is the same as case 1 for two beams.

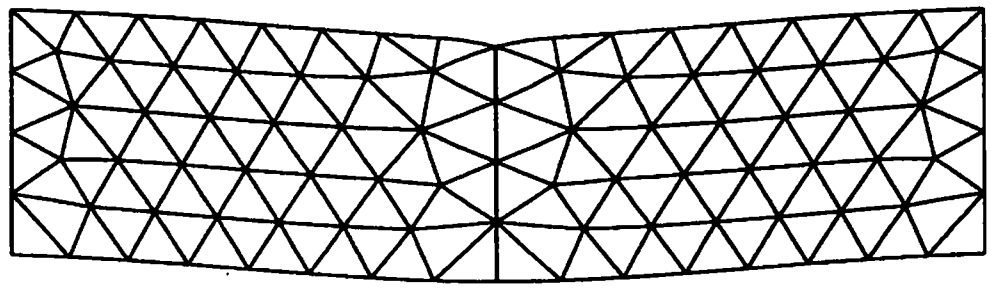
2) Constraints on the vertical displacements are applied by adding tie elements between beam *I*, *II* and *I*, *III*. They force the beams to behave like three cantilevers with the same deformation patterns. As the total stiffness against the load has increased to three times the value for one beam, the vertical displacement of the loading point becomes 0.0135m, a third of the value in case 1 (Figure 3.17 (2)).



(1)



(2)



(3)

Figure 3.15: Deformation of Two Parallel Deep Beams with No, Partial and Full Ties (Scale=20:1)

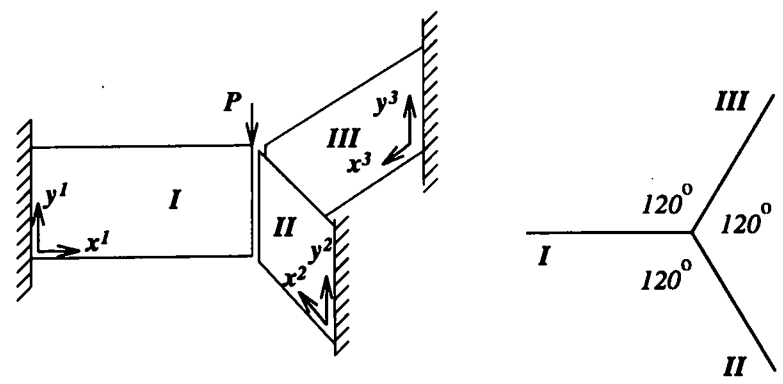
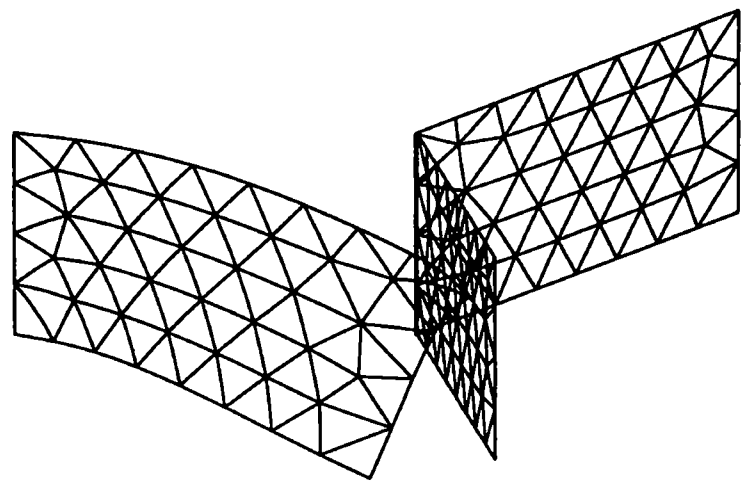
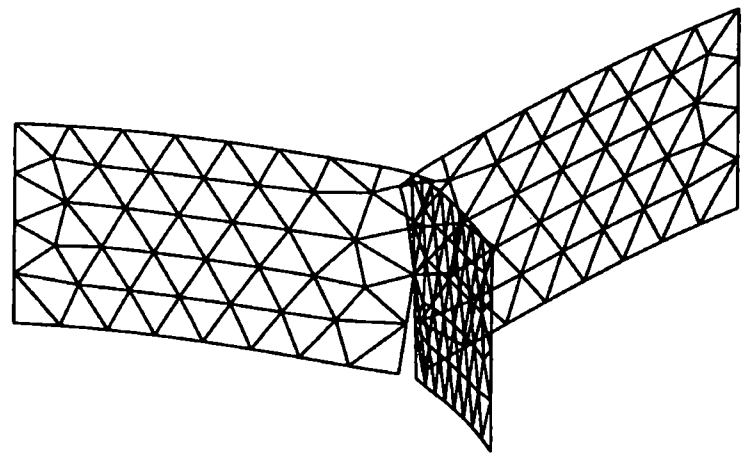


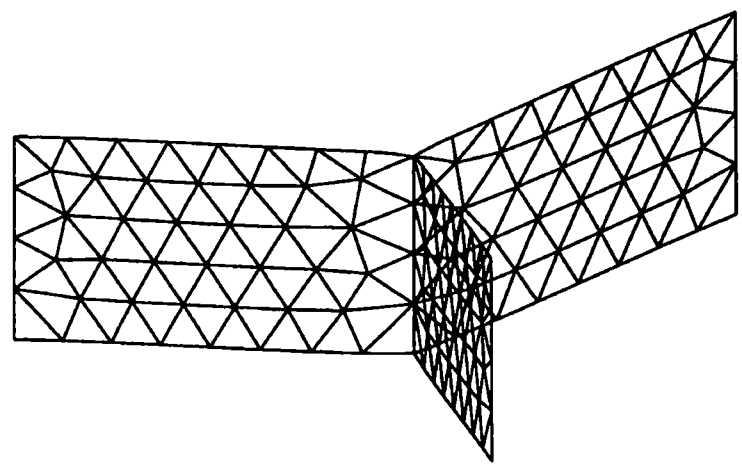
Figure 3.16: Three Obliquely Located Deep Beams



(1)



(2)



(3)

Figure 3.17: Deformation of Three Obliquely Located Deep Beams with No, Partial and Full Ties Scale=20:1

	2 beams	3 beams
case 1	0.0406m	0.0406m
case 2	0.0203m	0.0135m
case 3	0.0080m	0.0053m

Table 3.1: Comparison of Vertical Displacements of Loading Point

3) Three beams are connected by full ties which adjust their horizontal and vertical displacements to that the three beams act as a fixed ended frame. Such constraints give the system a large increase in stiffness and a different deformation pattern. The vertical displacement of the loading point is only 0.0053m (Figure 3.17 (3)). Compared with the third case of the two beam test, this value is two thirds of the displacement of 0.008m of the two beam case.

3.4 Summary

A tying scheme which connects separated parts to form a whole system has been discussed in this chapter. Local co-ordinate systems have been introduced to describe the different parts of a structure and the ground individually due to their properties and geometry. These separated parts can be connected together by installing specific tie elements between them. The ties for connecting 2D and 3D elements, 2D and 2D elements have been formulated. This tying scheme has been installed into OXFEM. Several examples are given to show the application of these tie elements.

4

Masonry Wall and Facade on Gaussian Curve Settlement Profile

The current practice to assess settlement damage to masonry buildings due to tunnelling is a two stage approach. Firstly, the settlement trough in the greenfield situation is estimated by the Gaussian curve, in accordance with the configuration of the tunnel. Then the settlement is applied to the building which is assumed to remain as an elastic beam. In this chapter, the settlement damage will be analysed by such a two stage method, but the masonry model will be employed to simulate the building.

4.1 Current Practice for Ground Movement and Building Damage Prediction

4.1.1 Empirical Estimate of Ground Movement

An empirical expression for the ground settlement due to tunnelling was suggested by Peck(1966) and then developed by other researchers (Institution of Structural Engineers, 1989) (New and O'Reilly, 1991) (Mair *et al.*, 1993). Figure 4.1 shows the general situation of the ground movement caused by an advancing tunnel with its axis at depth z_0 below the ground level. Analysis of case records has demonstrated that the trans-

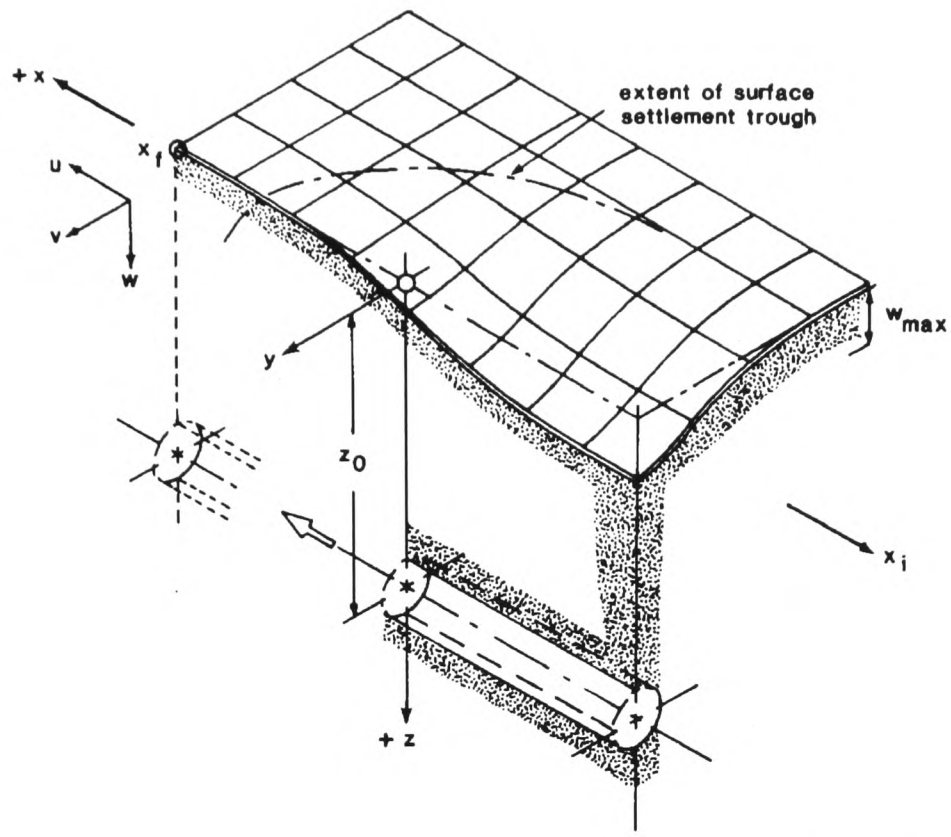


Figure 4.1: Ground Movement Induced by Tunnelling (Attewell *et al.*, 1986)

verse settlement trough immediately after a tunnel has been built is well described by a Gaussian distribution curve,

$$w(y) = S_{max} e^{-\frac{y^2}{2i^2}} \tag{4.1}$$

where w is settlement,

S_{max} is the maximum settlement on the tunnel centreline,

y is the horizontal distance from the centreline,

i is the horizontal distance from the centreline to the point of inflexion on the settlement trough.

Tunnelling also induces horizontal movement in the ground and the horizontal movement within the transverse plane is

$$v(y) = -\frac{y}{z_0} w \tag{4.2}$$

which is towards the tunnel axis.

For settlement at the ground surface, a simple approximate relationship

$$i = K z_0 \tag{4.3}$$

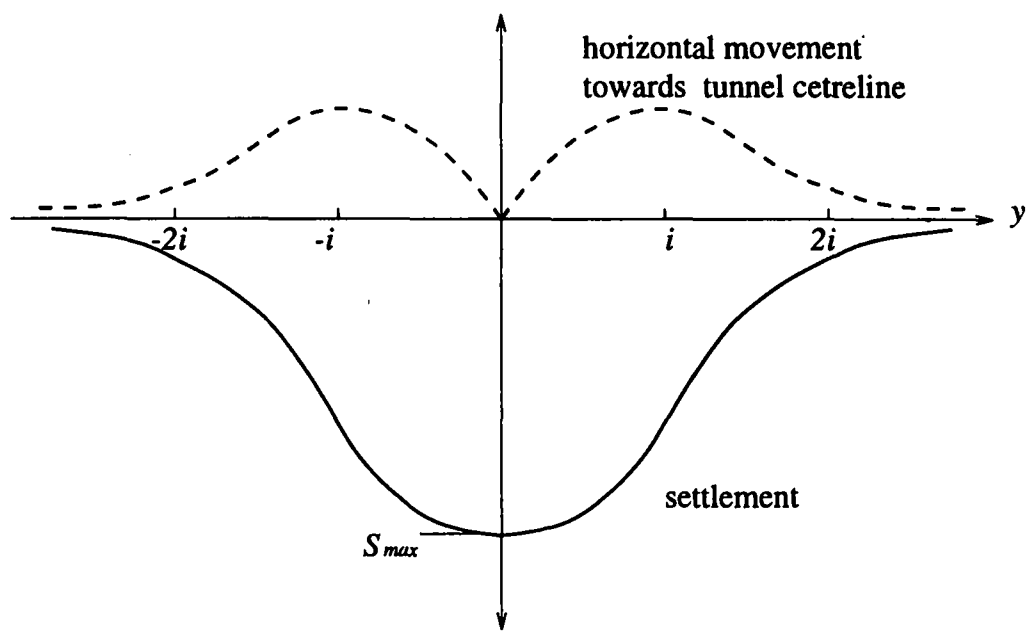


Figure 4.2: Ground Movement within Transverse Plane

can be used to calculate i. The values of the trough width parameter K for tunnels in clay, and sands or gravels are approximately equal to 0.5 and 0.25 respectively although research has shown that K may increase slightly with depth for subsurface settlement in clays (Mair *et al.*, 1996).

Since the deformation in the ground during tunnelling is considered to be an undrained process, the volume of the settlement trough, which is evaluated by integrating Equation 4.1, must be equal to the ground loss occurring around the tunnel, which is usually expressed as a proportion V_l of the excavated area of the tunnel. For a circular tunnel, it will give the value for S_{max},

$$S_{max} = \frac{\sqrt{2\pi}}{8} \frac{V_l \, D^2}{K \, z_0} \tag{4.4}$$

For tunnels in London Clay volume loss is likely to be in the range of $1-2\%$ for shield tunnelling (O'Reilly and New, 1982) and $1-1.5\%$ for New Austrian Tunnelling Method (NATM) (New and Bowers, 1994).

When a tunnel advances, the longitudinal settlement profile along the tunnel centreline is expressed by a cumulative distribution curve which is shown in Figure 4.3 (Attewell *et al.*, 1986).

$$w(x) = S_{max} \left(1 - \int_{-\infty}^{x/i} e^{-\frac{\beta^2}{2}} d\beta \right) \tag{4.5}$$

The settlement right above the tunnel face is equal to $0.5 \, S_{max}$.

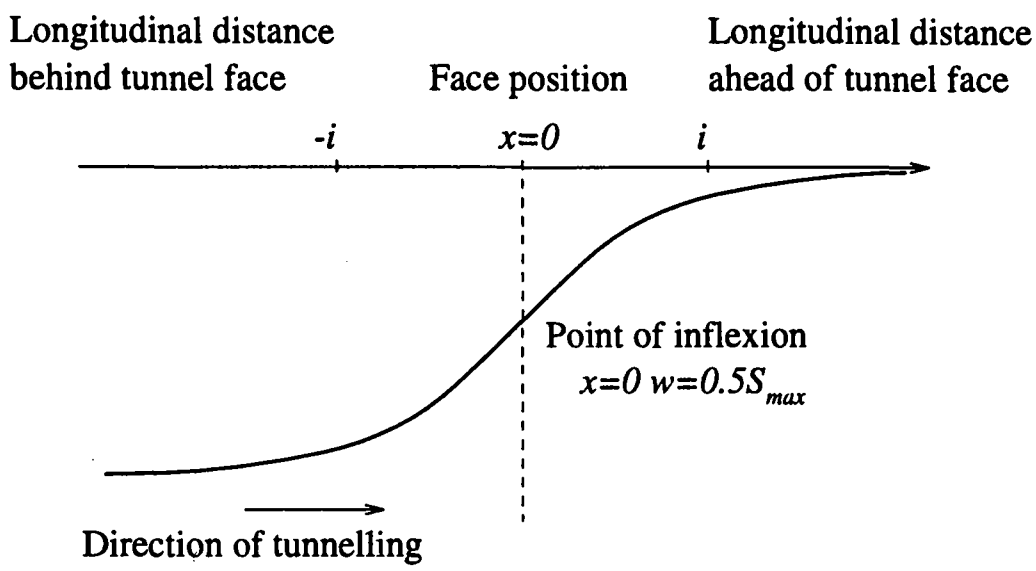


Figure 4.3: Ground Movement within Longitudinal Plane

The horizontal movement along the tunnel axis is:

$$u(x) = -\frac{1}{\sqrt{2\pi}}\frac{S_{max}i}{z_0}e^{-\frac{x^2}{2i^2}} \tag{4.6}$$

The i used in Equations 4.5 and 4.6 is assumed the same as that for the transverse curve. This assumption is generally valid for most practical problems (Attewell *et al.*, 1986).

There are cases where a building close to the tunnel centreline might experience more damage from this progressive longitudinal settlement trough emerging ahead of the tunnel face than from the final transverse settlement trough.

4.1.2 Calculation of the Strain in the Buildings due to Ground Settlement

Ground movements will usually generate tensile strains in buildings which lead to cracking and damage. Burland and Wroth (1974) suggested that a building can be simulated as an idealised beam with span L and height H deforming under a central point load giving a maximum deflection Δ (Figure 4.4). In the hogging area, the ground deformation lowers the neutral axis, which could be taken to the lower extreme fibre of the beam; while for a building in the sagging mode, the neutral axis would remain in the middle of the beam. Combined with bending and shear deformations, the general expressions for the maximum fibre strain, ϵ_b, and maximum diagonal strain, ϵ_d are,

$$\frac{\Delta}{L} = \left(\frac{L}{12t} + \frac{3IE}{2tLHG}\right)\epsilon_b \tag{4.7}$$

$$\frac{\Delta}{L} = \left(1 + \frac{HL^2G}{18IE}\right)\epsilon_d \tag{4.8}$$

whrere H is the height of the building,

L is the length of the building (but limited by any point of inflexion or extent of the settlement trough),

E, G are the Young's modulus and shear modulus of the building acting as a beam,

I is the second moment of area of the equivalent beam,

$I = H^3/12$ in the sagging area

$I = H^3/3$ in the hogging area

t is the furthest distance from the neutral axis to the edge of the beam.

$t = H/2$ in the sagging area

$t = H$ in the hogging area

For use in the sagging or hogging areas, these two equations will be used with Δ_s/L_s and Δ_h/L_h (Figure 4.4). It is noticed that for a beam on the Gaussian curve, Δ_s and Δ_h do not always occur at the midpoints of L_s and L_h.

For each area of the building (sagging or hogging), the maximum ϵ_b and ϵ_d are likely to be at the centrepoint and quarter span points respectively.

Masonry is assumed to have uniform E and G though it is an anisotropic material in practice.

In some cases the horizontal ground movement will contribute to building damage, especially if the tensile horizontal strain occurs in the ground beneath the building. In these cases, its effect should be added into the maximum fibre strain ϵ_b and maximum diagonal strain ϵ_d (Mair *et al.*, 1996).

4.1.3 Damage Classification and Building Strain

The damage for masonry structures is classified in five categories from negligible, very slight, slight, moderate, severe to very severe, as summarised in Mair *et al.*(1996). Such a

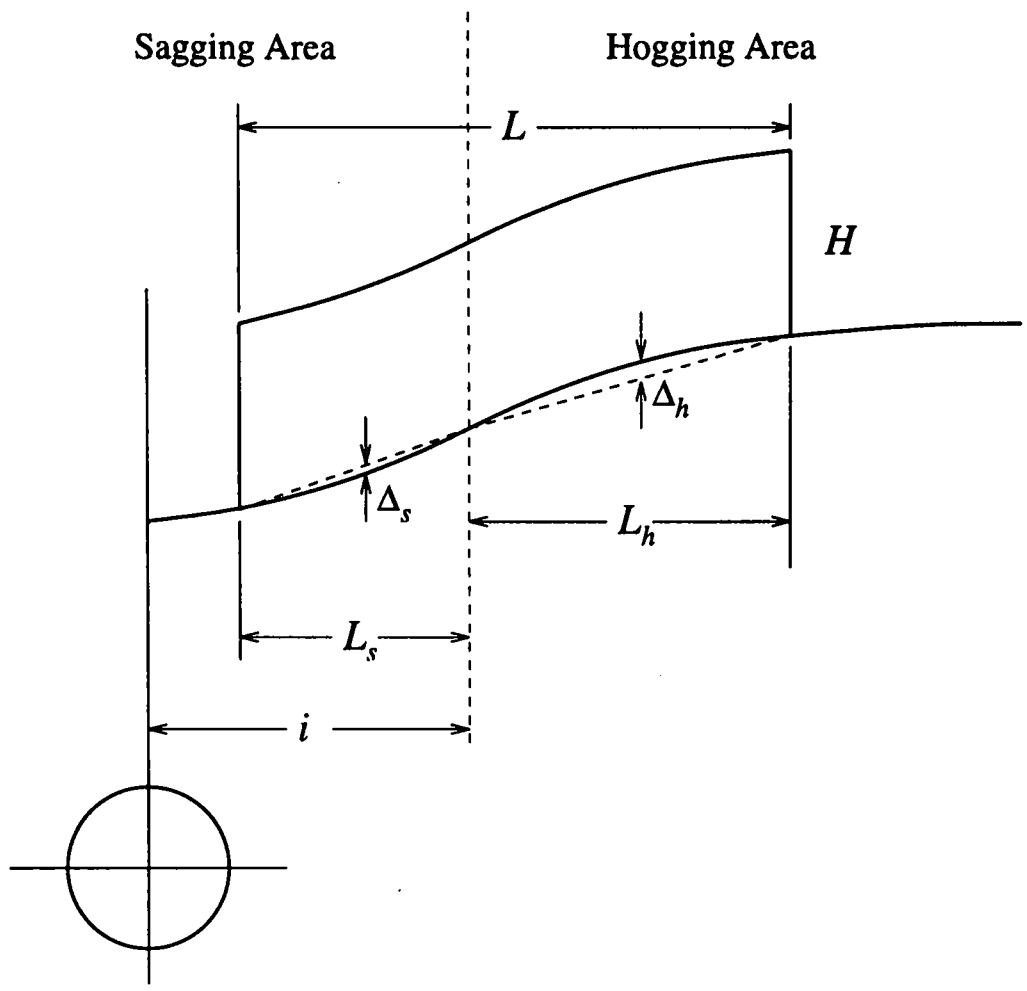


Figure 4.4: Building Deformation (Mair *et al.*, 1996)

classification system is adopted by the Institution of Civil Engineers and the Institution of Structural Engineers in the U.K.(Mair *et al.*, 1996).

Burland and Wroth (1974) proposed the use of "critical tensile strain", which was later renamed as "limiting strain" (Burland *et al.*, 1977), as a parameter to determine the onset of cracking. Boscardin and Cording (1989) analysed case histories of excavation induced settlement and showed the damage categories to be related to the magnitude of the tensile strain induced in the building (Table 4.1) (Boscardin and Cording, 1989). This classification was used in the recent Jubilee Line Extension Project in London (Mair *et al.*, 1996).

4.2 Models of Plain Walls and Facades

4.2.1 Plain Wall

A plain wall of 20m × 8m with unit thickness is analysed. The elastic and non-linear masonry models are compared in the study and the relevant property parameters are

Category of damage	Normal degree of severity	Limiting tensile strain (%)
0	Negligible	0.000 - 0.050
1	Very Slight	0.050 - 0.075
2	Slight	0.075 - 0.150
3	Moderate	0.1500 - 0.300
4 to 5	Severe to Very Severe	> 0.300

Table 4.1: Relationship between Damage Category and Tensile Strain

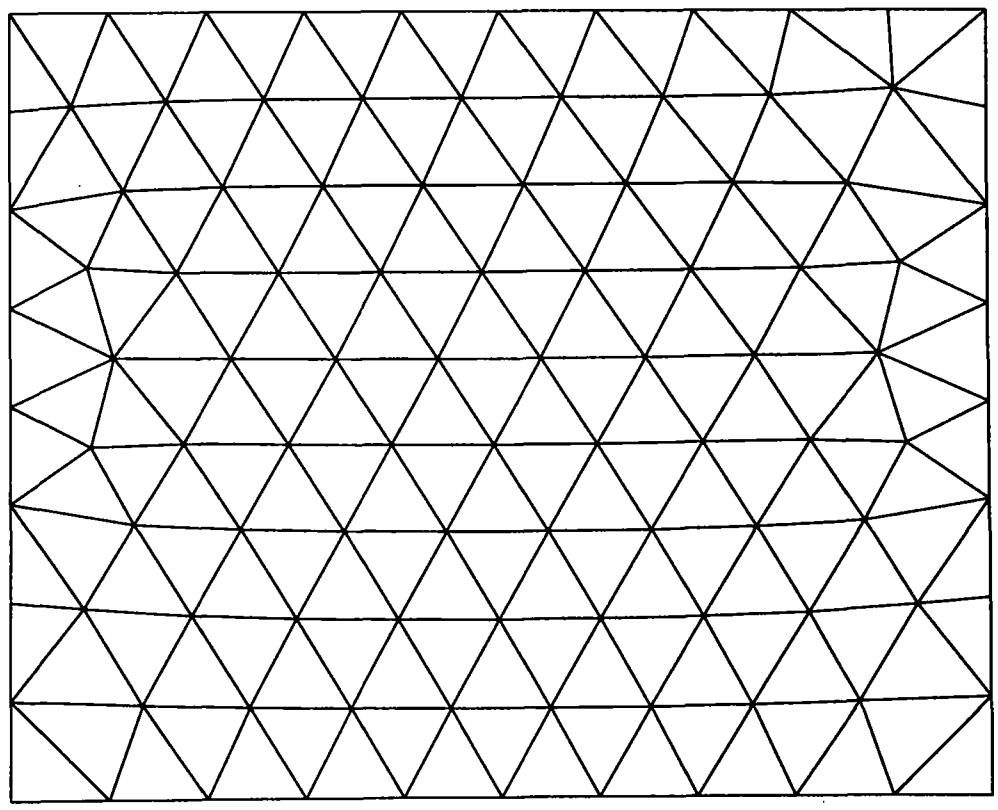


Figure 4.5: Finite Element Mesh for the Plain Wall

	E (kPa)	ν	γ(kPa/m)	f	c (kPa)	ϵ_0^{cr} ($\mu\epsilon$)
Elastic	1.0×10^7	0.2	20	–	–	-
Masonry	1.0×10^7	0.2	20	0.01	10	4

Table 4.2: Material Properties Used for Elastic and Masonry Models

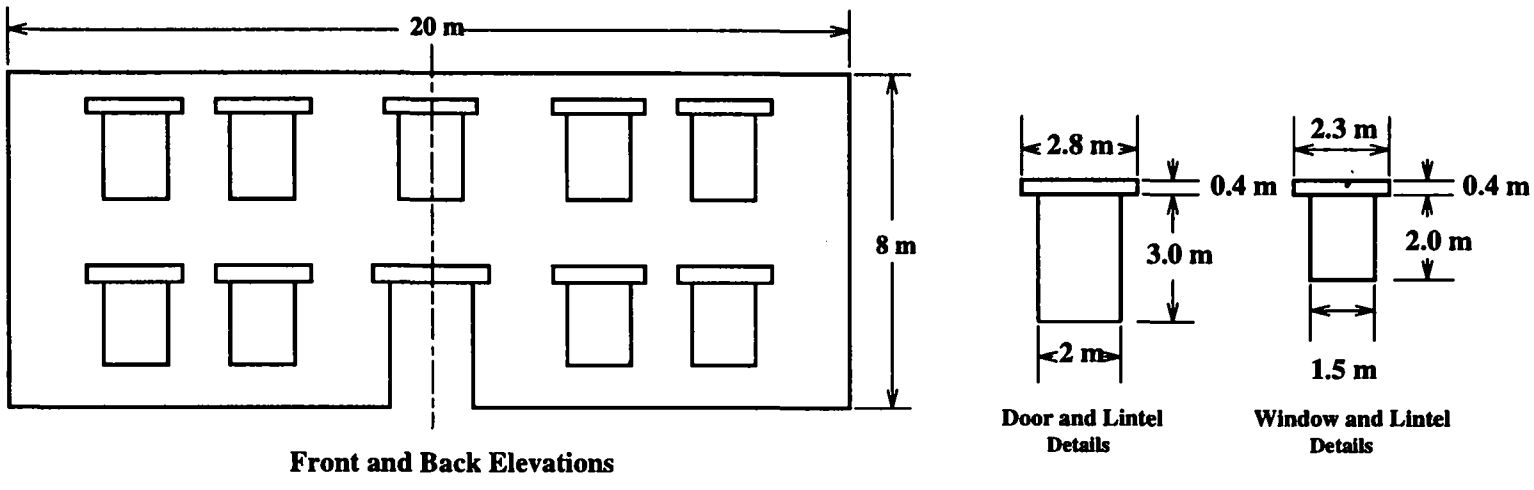


Figure 4.6: Facade Layout

shown in Table 4.2. The finite element mesh can be found in Figure 4.5 (only a half of the problem is modelled due to its symmetry).

4.2.2 Facade

A facade of the same size is also analysed in this study, representing the external wall of a two storey building. Its connection with the remainder of the building is neglected at this stage. The layout of openings in the facade is shown in Figure 4.6. The finite element model (Figure 4.7) includes lintels, whilst the frames of the door and windows are not simulated. When the facade is simulated using the masonry model, the lintels are kept elastic in order to avoid immediate failure above the openings. The elastic lintels have the same elastic modulus and Poisson's ratio as the masonry material.

4.2.3 Facade Box

A box consisting of two plain walls and two facades is shown in Figure 4.8. The front and back facades have the same layouts and meshes as the facade described before. Two end walls are plain walls which are modelled using the same mesh as shown in Figure 4.5. All

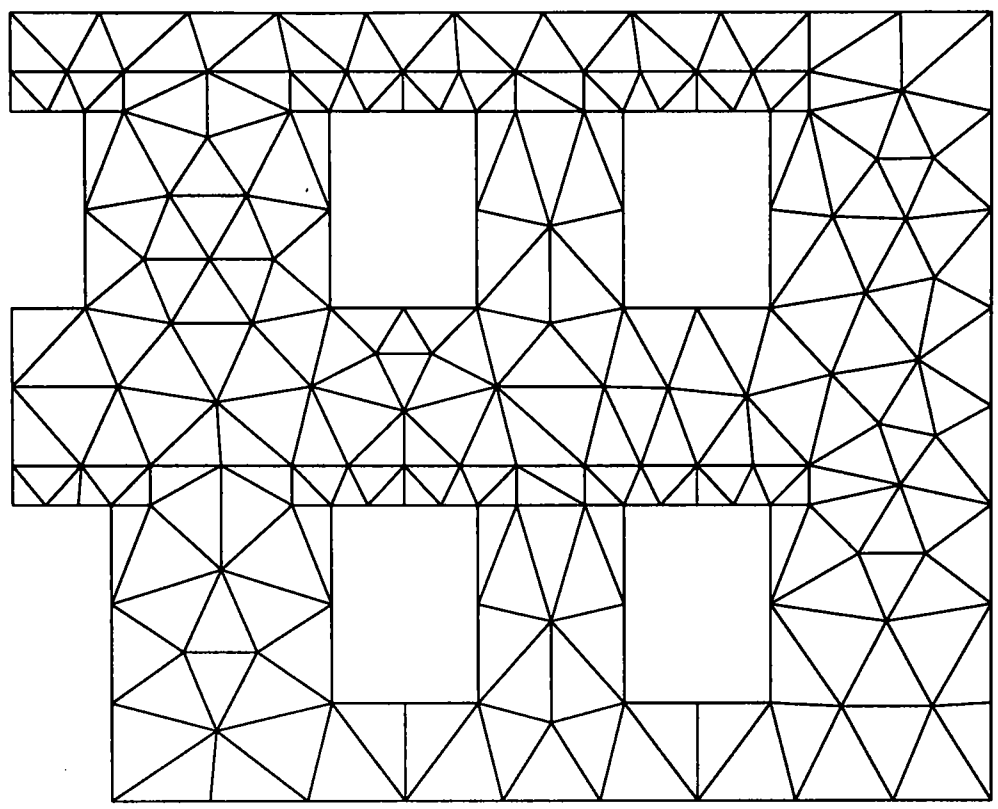


Figure 4.7: Finite Element Mesh for the Facade

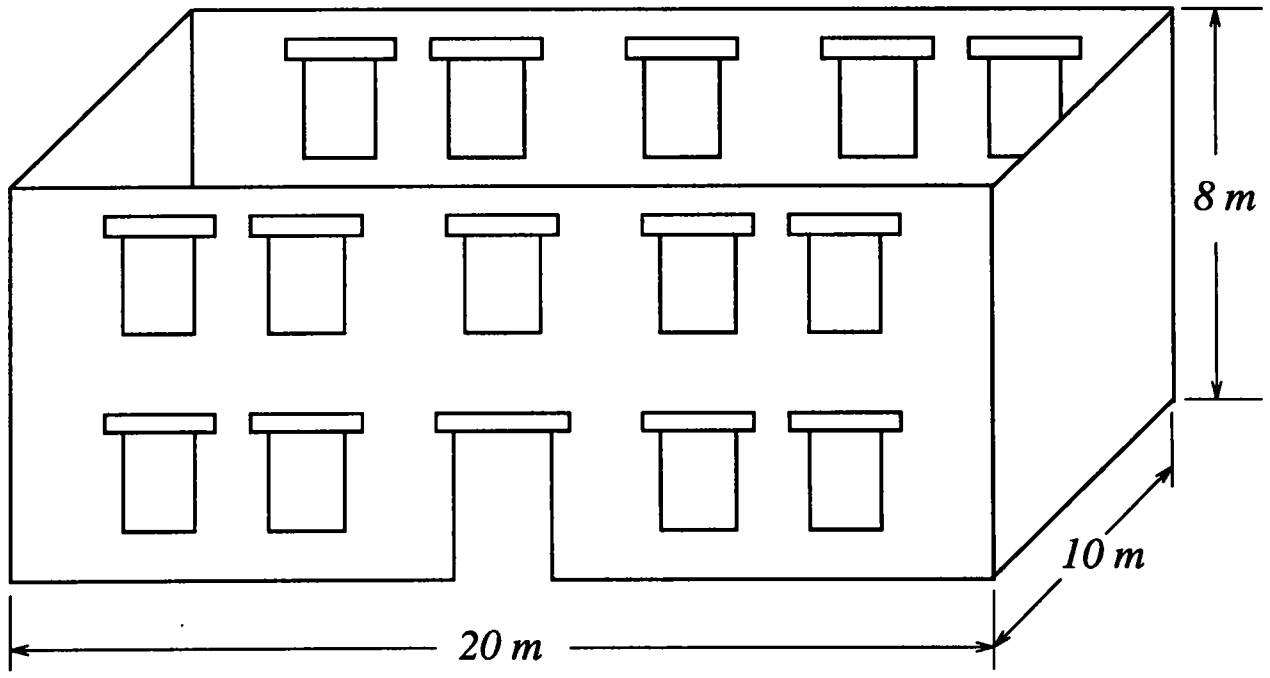


Figure 4.8: Facade Box

these walls are simulated by plane stress elements with the masonry material model. At the corners the ties which constrain relative vertical displacements are installed between the end walls and facades.

4.3 Presentation of Results

The main concern of this study is the strains induced by the tunnelling activities. Although the self weight of the building is applied before tunnelling commences, the corresponding deformation was reset to zero before the tunnelling starts, while the stresses were maintained. Thus all the crack patterns and strains shown in this study are caused by tunnelling induced settlement only.

4.3.1 State

Each Gauss point in the mesh has a "cracking state" variable which shows whether the material at the point is intact (0), singly (1) or doubly cracked (2) or healed (-1) (*i.e.* the crack has reclosed).

4.3.2 Cracking Strain

As mentioned in Chapter 2 a cracking strain ϵ^{cr} has been introduced to monitor the cracking-reclosure process. It is reasonable to use ϵ^{cr}, which excludes the elastic part of the deformation, rather than total strain to describe the degree of severity of settlement damage in masonry buildings. Instead of principal components, ϵ^{cr} can be resolved into three components: (1) ϵ_1^{cr} which represents the component normal to the first emerged crack, (2) ϵ_2^{cr} which represents the component normal to the second crack, if it exists, and (3) γ_{12}^{cr} which shows the shear deformation across the crack. Instead of using the total strain to determine the damage categories from Table 4.1, ϵ_1^{cr} and ϵ_2^{cr} are compared with Table 4.1. A possible relationship between the damage categories and γ_{12}^{cr} is a subject for future research.

The finite element analysis will give cracking strains at all Gauss points. The cracking damage will be presented by plotting contours either of the values of each component of ϵ^{cr} or the categories of damage in the wall or facade.

The cracking pattern will be represented by drawing short lines at each point where visible cracking occurs (*i.e.* the cracking strain is greater than 500 $\mu\epsilon$), the thickness of these lines indicating the magnitude of the cracking strains.

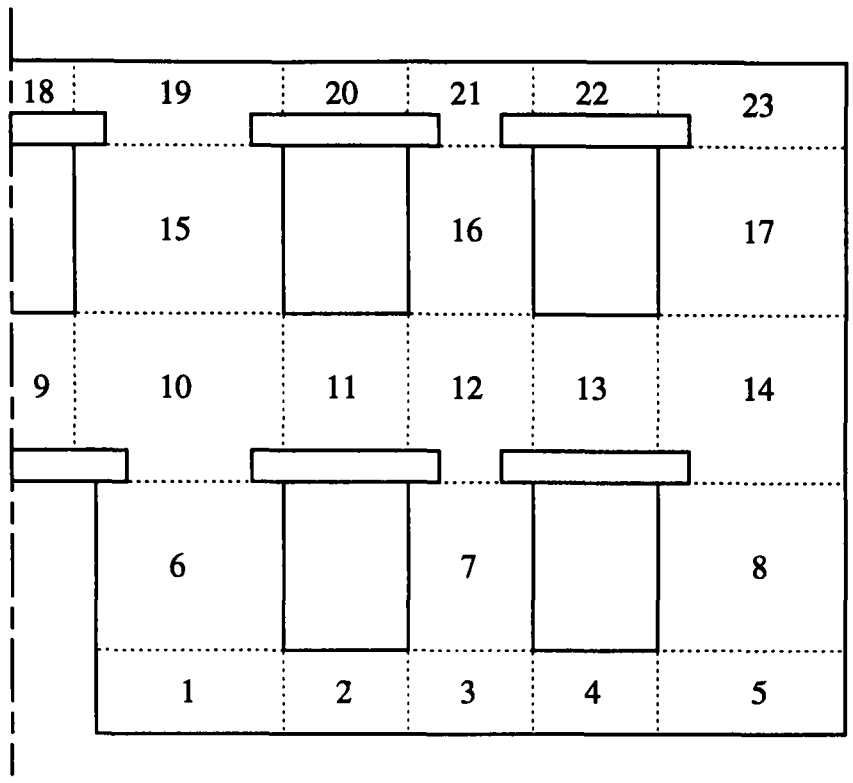


Figure 4.9: Averaging Zones for Facade

4.3.3 Average Cracking Strain

In the finite element analysis, cracked material has little stiffness in the direction normal to the cracks, so that the material can "float" within the cracked area. This may cause highly localised distribution of cracking strain, with two adjacent areas having unrealistically large and then small amounts of cracking strain. This could cause two problems. Firstly, the overall degree of severity of damage might be misinterpreted. Secondly, for comparison between different cases, simply comparing the maximum ϵ^{cr} value could be misleading. Thus an average ϵ^{cr} over a specific area would give a more practical estimate of the true value of ϵ^{cr}. The average cracking strain $\overline{\epsilon}^{cr}$ is defined as

$$\overline{\epsilon}^{cr} = \frac{\sum_i \epsilon^{cr} \Delta A_i}{A} \tag{4.9}$$

where the sum is over all Gauss points which fall in a particular area A and ΔA_i is the area related to a Gauss point.

The method of specifying the averaging zones depends on the application. However, in this study the facade is divided into 23 zones (Figure 4.9) for the purpose of comparison between different cases.

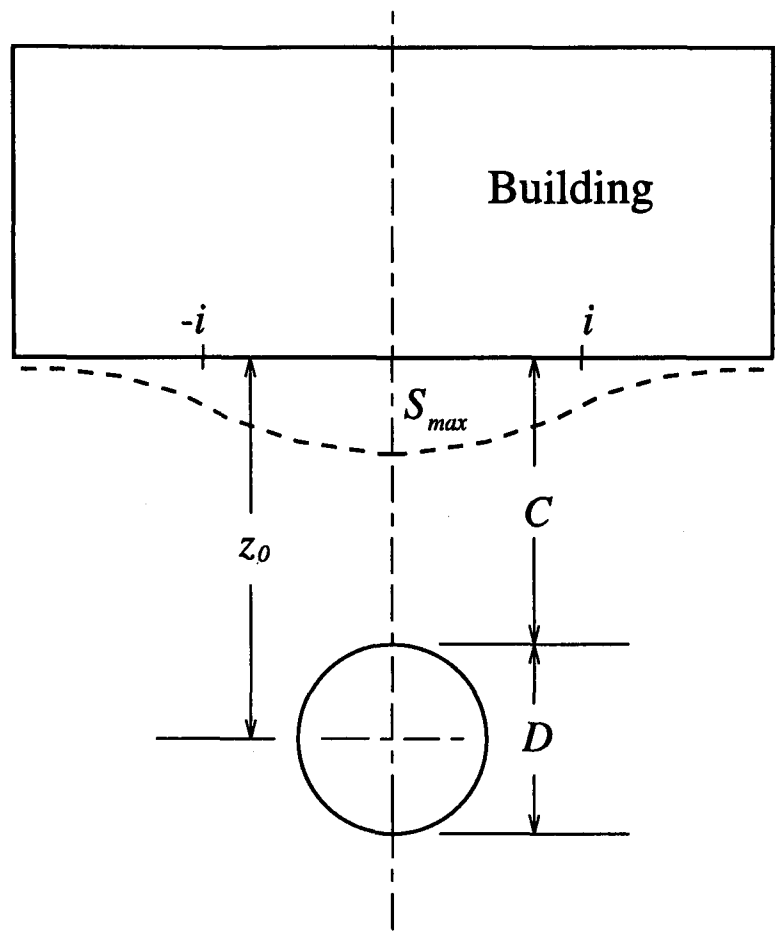


Figure 4.10: Tunnelling Scheme

4.3.4 Cracked Area Proportion

An alternative method to remove the "floating" effect is calculating the ratio of the cracked area over the total area. Since a large cracking strain may be concentrated at a few Gauss points, cracking strain at one or few Gauss points reaching the limit of a specific damage category does not necessarily reflect the real situation of cracking damage in the building. Thus the area of cracking which reaches a specific strain limit, divided by the total area, is used to judge the transfer between different categories. It can be assumed that if more than 0.5% of the total area has entered a certain damage category then this category of damage is applicable.

4.4 Plain Wall on Gaussian Curve

A plain wall as described before is located symmetrically above a circular tunnel of 5m diameter with tunnel axis at depth of 10m below the ground level in London clay (Figure 4.10). For such a configuration, the point of inflexion can be determined by

i(m)	2.5	5.0	12.5
Δ_s(mm)	9.84	9.84	6.85
L_s(m)	5.00	10.00	20.00
$\epsilon_b(\mu\epsilon)$	1849	1430	521
$\epsilon_d(\mu\epsilon)$	1775	686	125
Δ_h(mm)	6.88	1.16	
L_h(m)	7.50	5.00	
$\epsilon_b(\mu\epsilon)$	675	118	
$\epsilon_d(\mu\epsilon)$	865	227	
$\epsilon_{max}(\mu\epsilon)$	1849	1430	521
Damage Category	moderate	slight	very slight

Table 4.3: Calculation on Plain Wall Using Burland-Wroth Approach ($S_{max} = 25$mm)

Equation 4.3 as

$$i = Kz_0 = 0.5 \times 10.0 = 5.0\text{m}$$

For the range of $1-2\%$ of possible ground loss for tunnelling in London Clay, the range for the maximum settlement will vary from 16mm to 31mm. The S_{max} for this study has been chosen to be 25mm. Although ($S_{max} = 25$mm, $i = 5.0$m) are used as a standard load case, other values of i are also used in comparison analyses.

4.4.1 Burland-Wroth Method

Following the current practice, the maximum tensile strains in a plain wall located above the tunnel can be determined using the Burland-Wroth method. For the proposed tunnelling scheme ($i = 5.0m$, $S_{max} = 25$mm), the maximum tensile strain can be determined (Table 4.3). Two other cases, with $i = 2.5$m and 10.0m are also included as comparisons. All of these three cases show that the maximum tensile strains, which are the maximum bottom fibre bending strains, appear at the centrelines. As i increases with constant S_{max}, the damage category will be lower.

4.4.2 Finite Element Analysis: Elastic Wall

The analysis can be carried out using the finite element method. As the problem is symmetric, only half of the wall is analysed. The vertical displacements of the ground

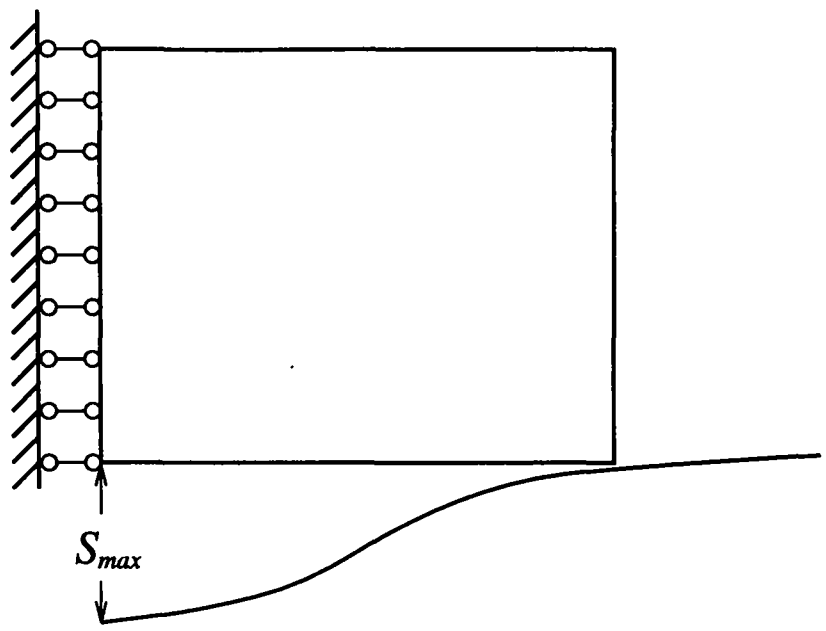


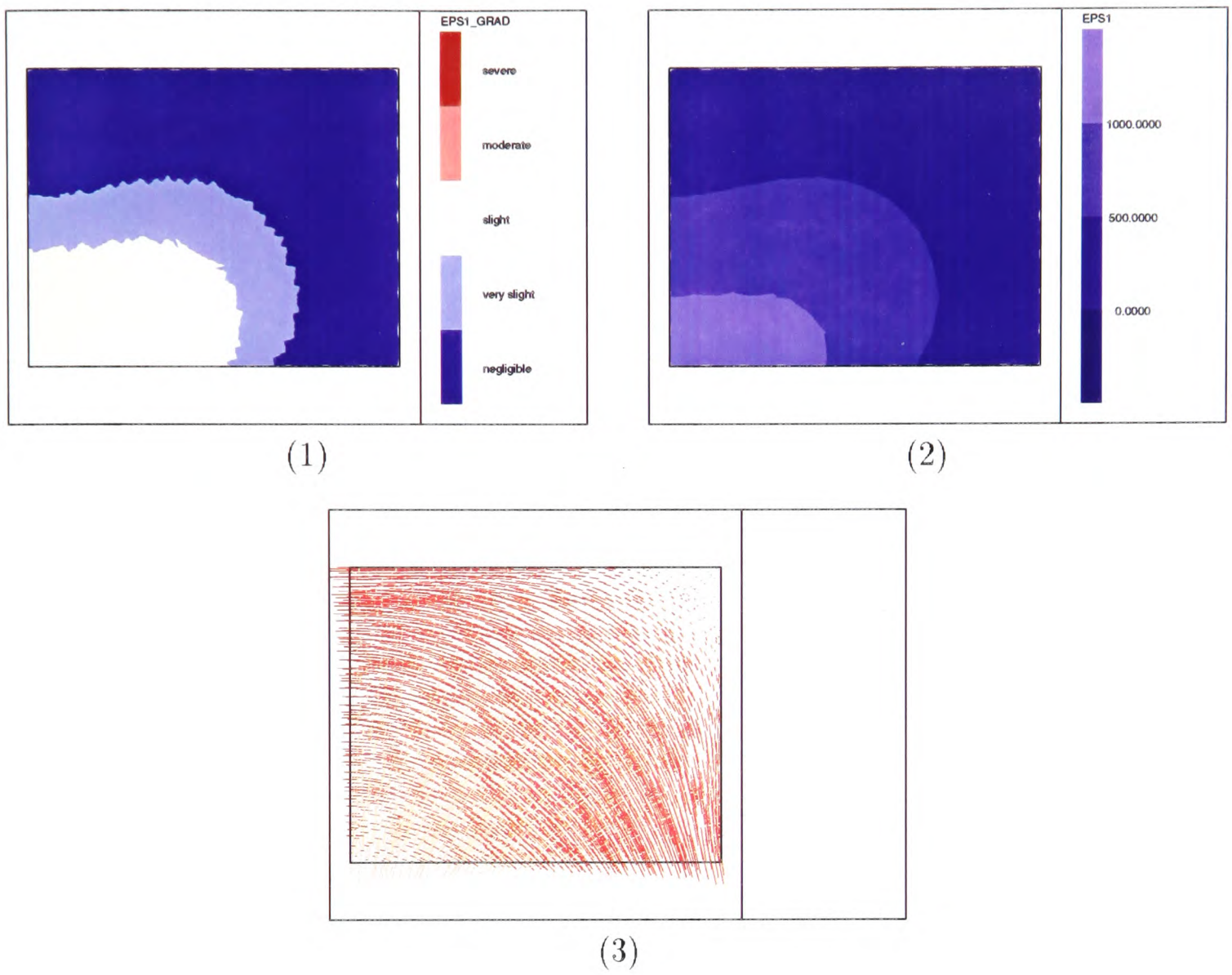
Figure 4.11: Boundary Condition for Finite Element Analysis

surface are applied to the bottom nodes of the wall (Figure 4.11). These nodes are restrained horizontally as it is unrealistic to impose the greenfield horizontal soil movement on the building.

The main results of the analysis can be found in Figure 4.12. Figure 4.12-(2) exhibits the contour of the major principal strains within the wall, while Figure 4.12-(1) shows the corresponding severity of the possible cracking. The highest grade in this case is moderate cracking. Figure 4.12-(3) is the strain trajectory which indicates the possible directions of these potential cracks.

Compared with the Burland-Wroth method, with the standard settlement trough, elastic analysis gives similar estimates for the maximum strain and the category of damage. The most severe cracking area emerges in the sagging area. However, according to the strain trajectory, the largest cracking is likely to be horizontal at the bottom of the mid-span of the wall. It is caused by pulling down by the ground rather than by the bending effect in this case.

Settlement troughs with the values of i equal to 2.5m and 12.5m were applied to the same elastic wall. The corresponding predictions of the major principal strains are shown in Figure 4.13. It is seen that the maximum principal strain for the case of $i = 2.5$m reaches $3500\mu\epsilon$, suggesting the onset of severe cracking and a more concentrated cracked area, compared with the case of $i = 5.0$m. In the case of $i = 12.5$m the wall does not experience any visible cracking. It can be concluded that as i is decreased while S_{max}



(1) (2)

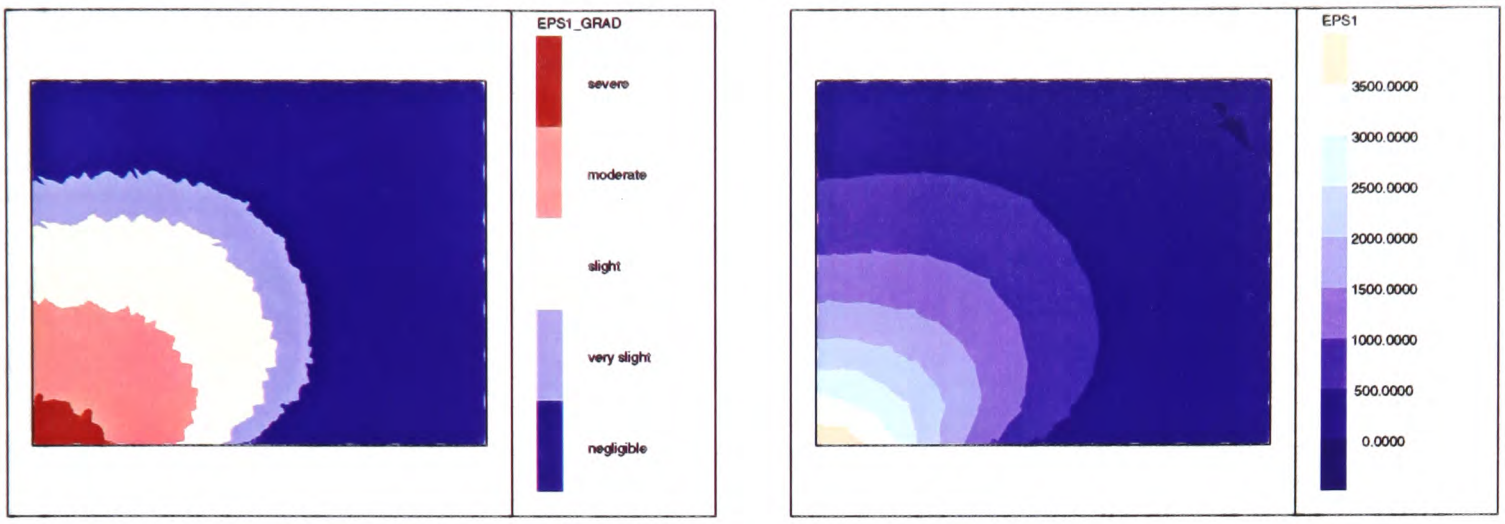
(3)

Figure 4.12: (1) Damage Grade, (2) Cracking Strain and (3) Strain Trajectory in Elastic Plain Wall (i=5.0m)

stays unchanged, the maximum tensile strain increases and the cracked area becomes more concentrated near the centreline for the elastic wall. This agrees with the results of the Burland-Wroth method. A larger i gives a flatter settlement trough and causes less cracking.

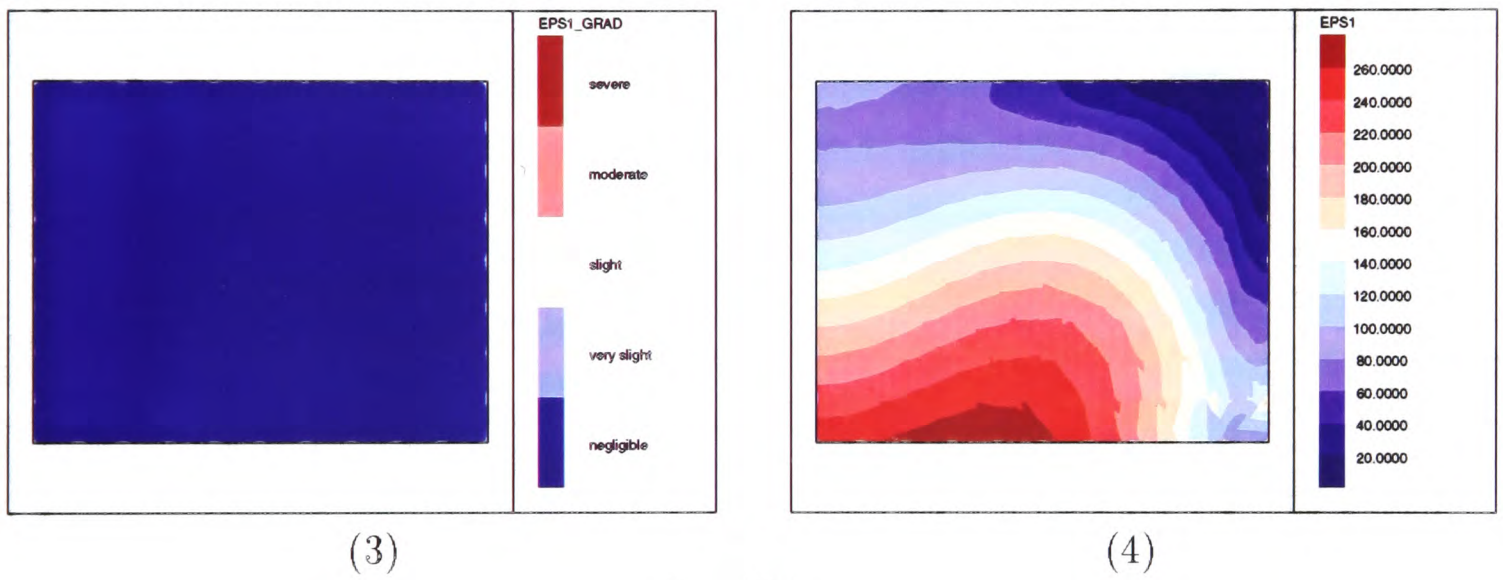
4.4.3 Finite Element Analysis: Masonry Wall

The same plain wall is analysed using the masonry material model. The damage induced by the same settlement trough is much more severe than in the elastic analysis. Figure 4.14 includes various presentations of the result. Instead of the principal total strain used in the elastic analysis, the relevant strain in the no tension model is the cracking strain, whose two components, ϵ_1^{cr} and γ_{12}^{cr}, are shown in Figures 4.14-(3,4) respectively. The



(1) (2)

i = 2.5m



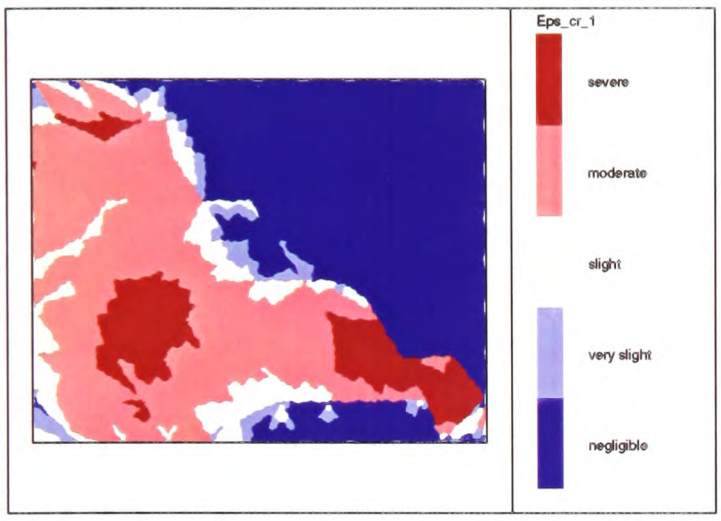
(3) (4)

i = 12.5m

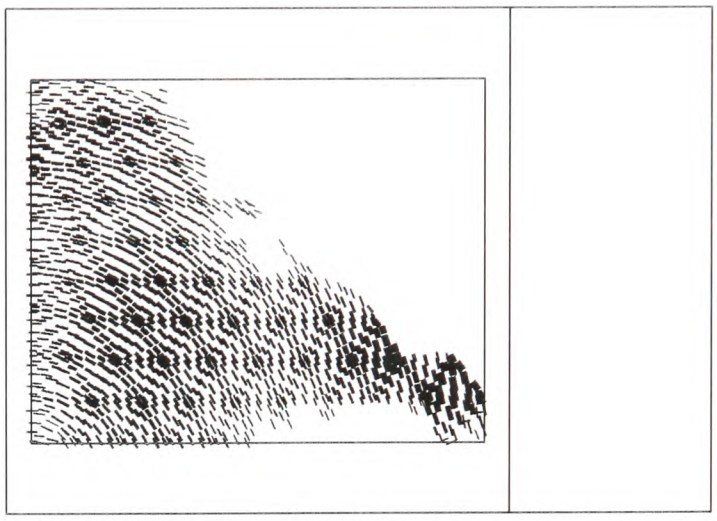
Figure 4.13: (1,3) Damage Grades, (2,4) Major Principal Strains in Elastic Plain Wall (i=2.5, 12.5m)

equivalent damage grade is displayed in Figure 4.14-(1) with severe cracks. The predicted visible cracking pattern is given in Figure 4.14-(2). In the sagging region serious cracking caused by shear deformation becomes a major source of damage. Severe damage also occurs near the bottom right corner. In addition to ϵ_1^{cr}, which is related with cracking opening, the masonry model shows high γ^{cr}, which represents sliding between cracked layers and cannot be exhibited in the elastic case.

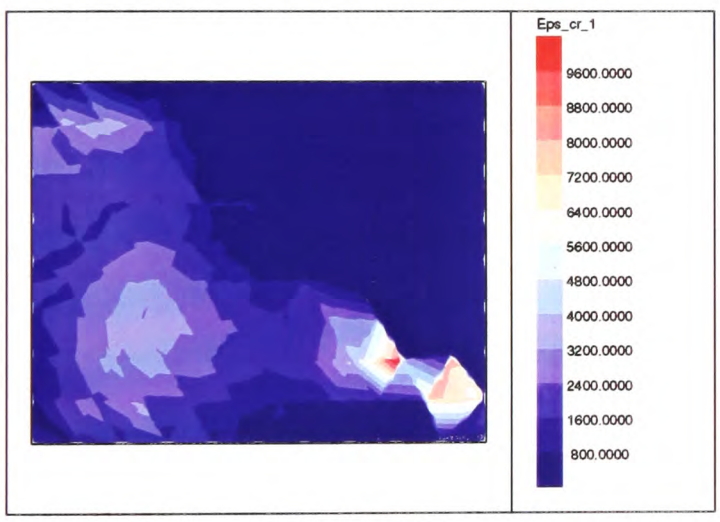
From Figure 4.14-(5) an arching effect is observed in the cracked wall. This arch supports the material above it and prevents it from further cracking, and even recloses some cracked areas, as shown by the state given in Figure 4.14-(6). However the material below the arch, particularly near the bottom right corner, experiences serious damage.



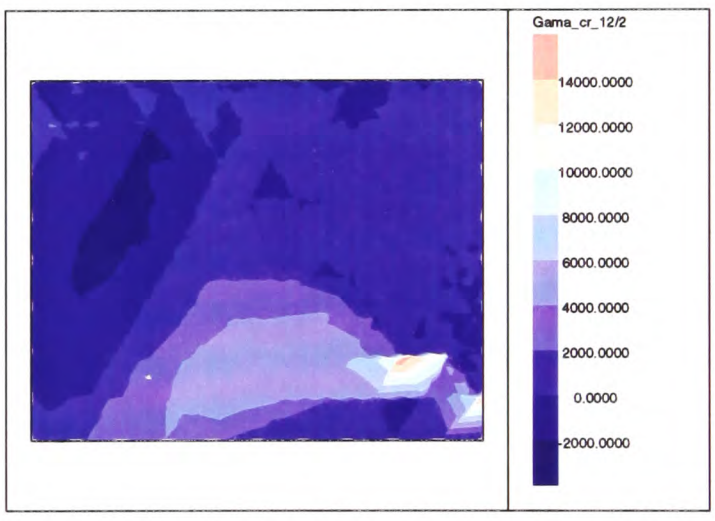
(1) Damage Grade



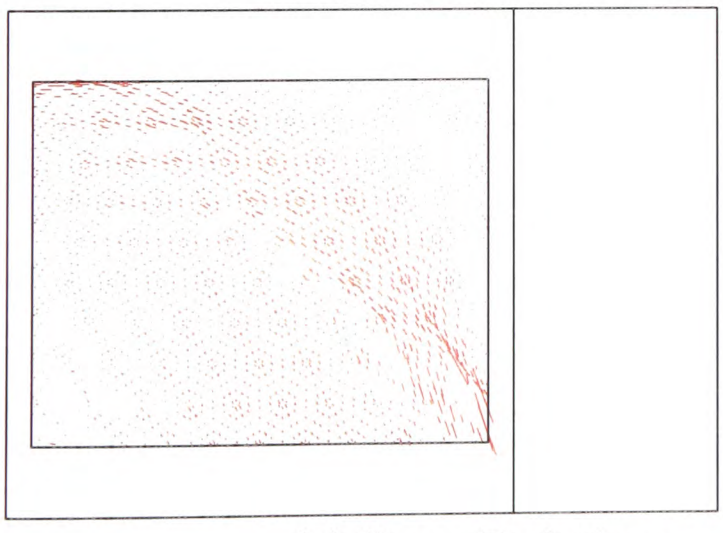
(2) Cracking Pattern



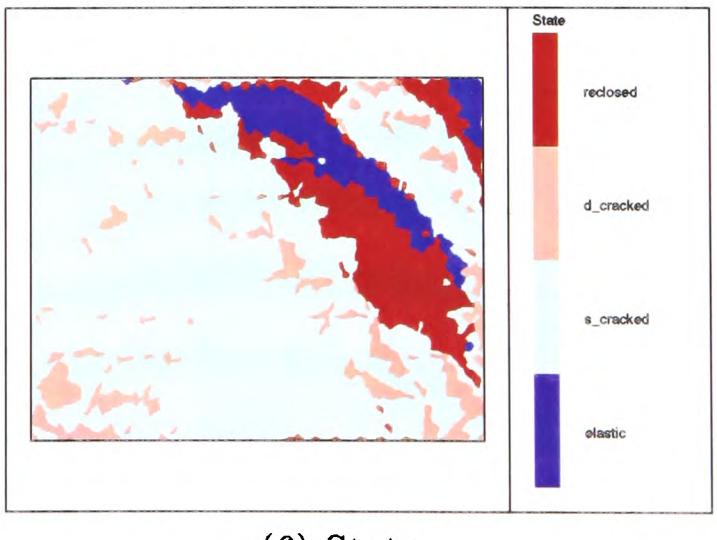
(3) Normal Cracking Strain



(4) Shear Cracking Strain



(5) Stress Trajectory



(6) State

Figure 4.14: Results of Masonry Plain Wall (i=5.0m)

By comparing the elastic and masonry wall, it is noticed that at the same diagonal cracking positions, the masonry model gives more cracks which are oriented closer to the vertical, but with large γ^{cr} than the potential cracks predicted in the elastic model. This is because the cracks in the no tension model appear as soon as tensile stress develops, rather than along the principal direction of the total tensile strain.

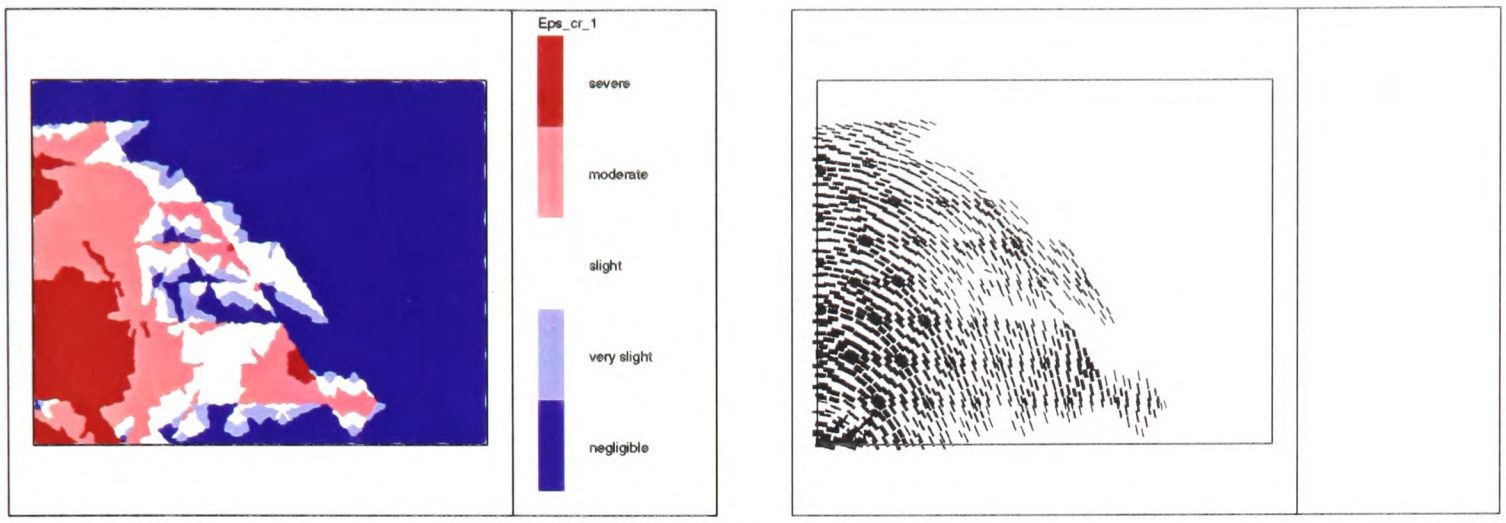
The cracking patterns and damage grades of the same masonry wall subject to the troughs with $i = 2.5, 12.5$m are given in Figure 4.15. In Figure 4.15-(1,2), the major cracked area in the case of $i = 2.5$m moves to the bottom at the centreline and there is no cracking near the bottom right corner. In the case of $i = 12.5$m the only major cracked area is near the right corner (Figure 4.15-(3,4)). Comparing the cracking grades and patterns, it is concluded that varying the i changes both the cracking pattern and the severity of cracking for the masonry model. Generally speaking, a smaller value of i will cause more concentrated damage, as seen in the analysis using the elastic model.

4.4.4 S_{max}-i Curves for Damage Grades

It is obvious that for a given i, the cracking becomes more severe when S_{max} increases. A particular damage grade occurs when the S_{max} reaches a specific value. Varying the value of i will form a curve which is the boundary between two adjacent damage categories in the S_{max}-i space. Thus there are four such curves for the various damage categories (slight, moderate *etc.*). The relationship between S_{max}, i and the damage grades can be graphically represented by such curves. Figure 4.16 illustrates the S_{max}-i curves for the plain wall analysed by the Burland-Wroth method, elastic and no tension models. For the masonry wall, a damage grade is considered to have been reached only when more than 0.5% of the total area of the wall experiences such cracking.

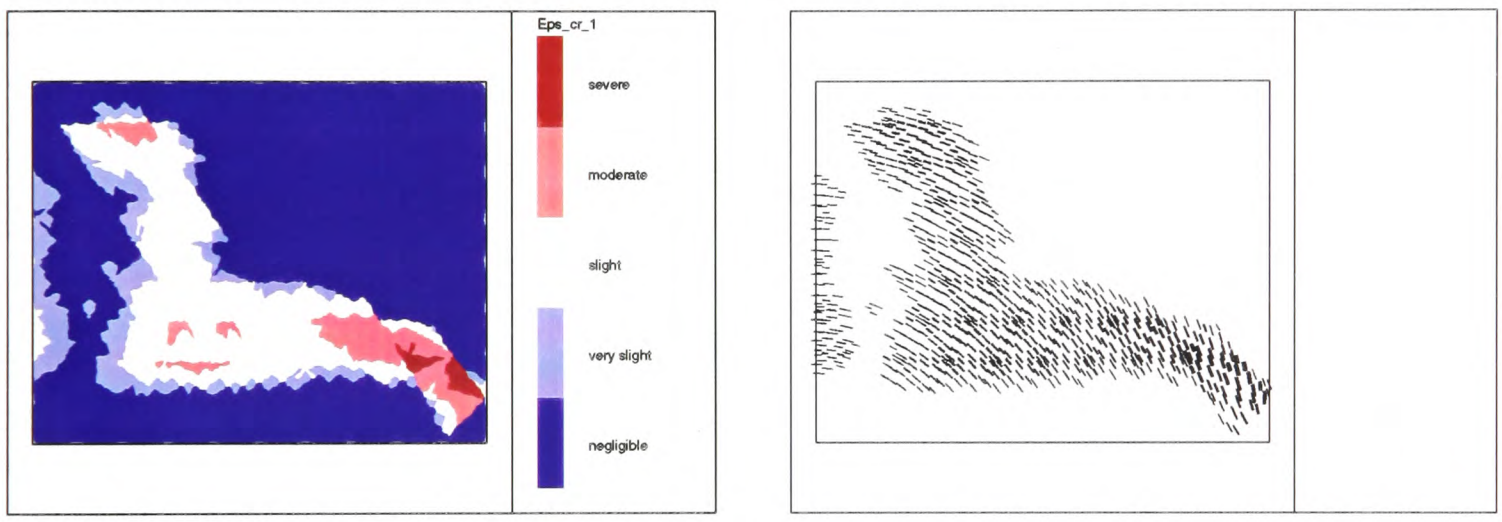
It is clear that for most cases either increasing S_{max} with a fixed i or decreasing i with a fixed S_{max} will increase the damage grade, *i.e.* cause wider cracks. In other words, a larger value i will cause less serious damage and have larger tolerable value of S_{max} for a given damage grade.

However, an exception exists for the masonry wall. When the value of i changes from 2.5m to 5.0m, the value of the S_{max} corresponding to the severe damage grade becomes



(1) (2)

i = 2.5m



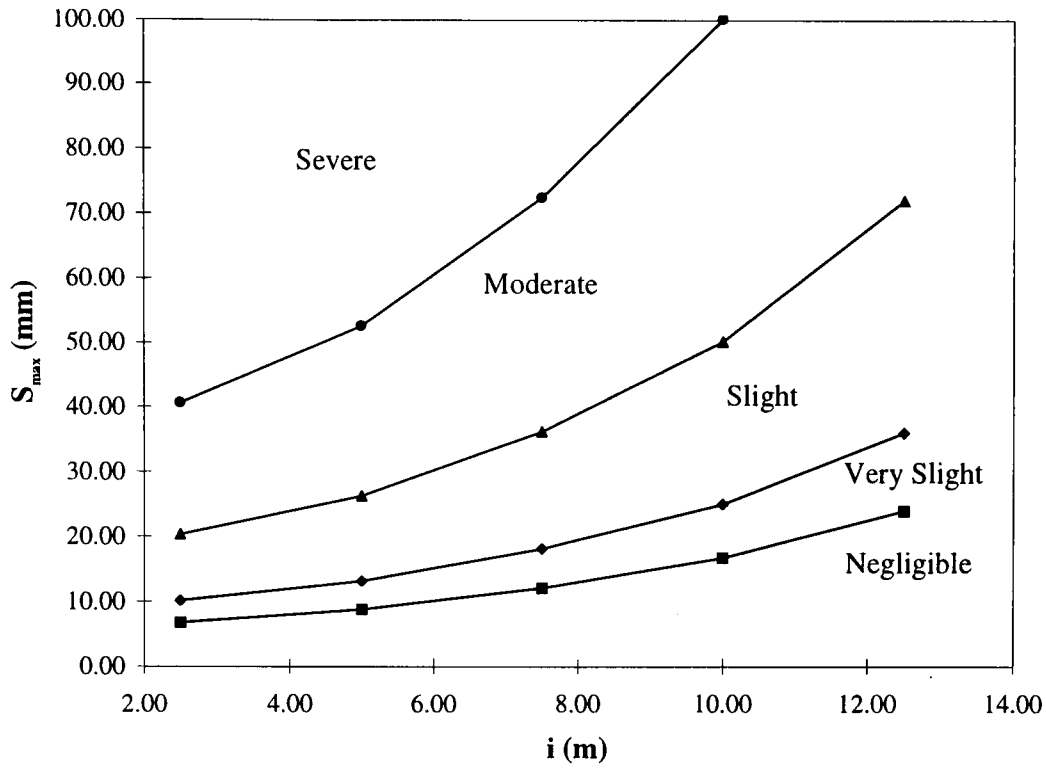
(3) (4)

i = 12.5m

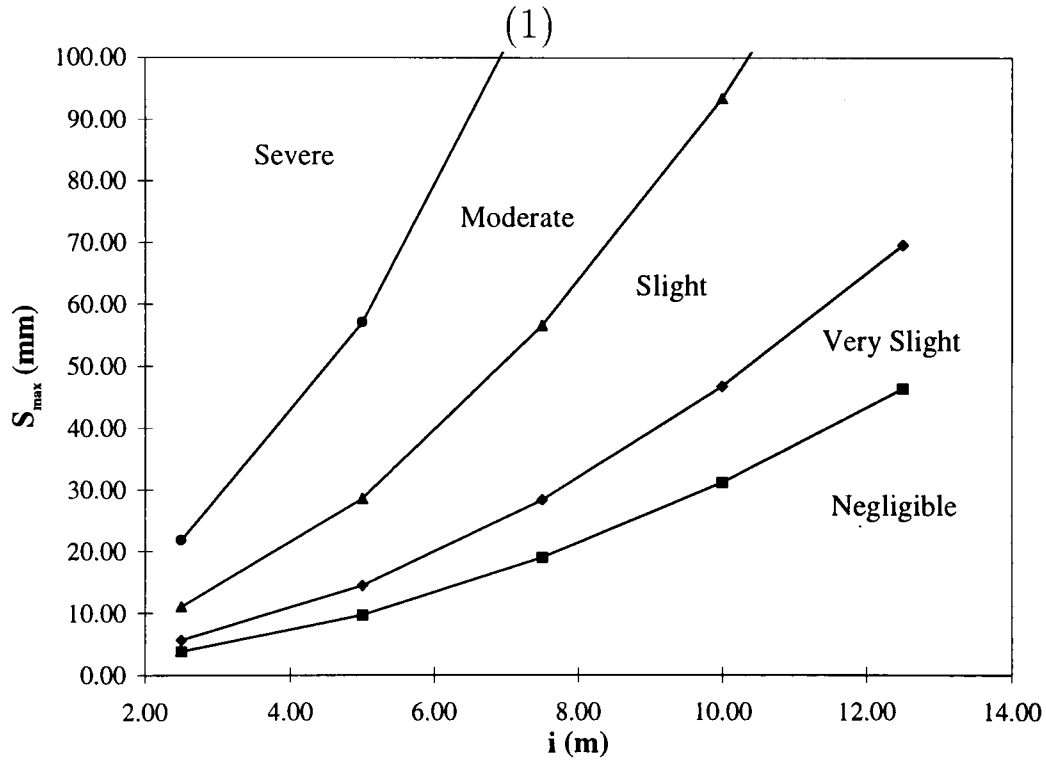
Figure 4.15: (1,3) Damage Grades and (2,4) Cracking Patterns in Masonry Plain Wall (i = 2.5, 12.5m)

lower, instead of rising as other curves. This exception may be explained by the change of the positions of the major cracked areas when the value of i changes.

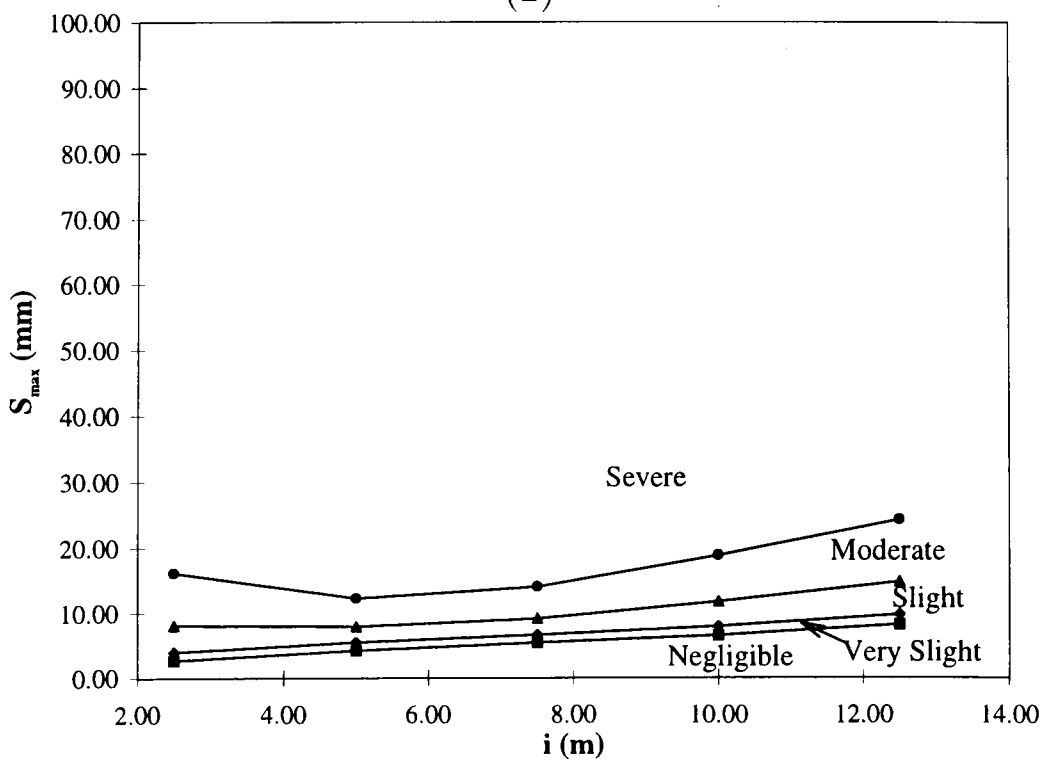
As discussed in the previous section, there are two cracking patterns in the plain masonry wall. In the first pattern, the major cracked area is at the bottom near the centreline. This pattern usually occurs when i is small and no strong arch is formed at the corner. When i is large, a strong stress arch is formed at the corner. The critical damage is caused by the cracks near the base of the arch. This second cracking pattern develops very quickly and reaches a severe grade at small values of S_{max}. For these two cracking patterns there actually are two different S_{max}-i relationships for the severe damage grade as illustrated in Figure 4.17. When i is smaller than a certain value, only



(1)



(2)



(3)

Figure 4.16: S_{max}-i Curves for Plain Wall, (1) Burland-Wroth Method, (2) Elastic Model and (3) No Tension Model

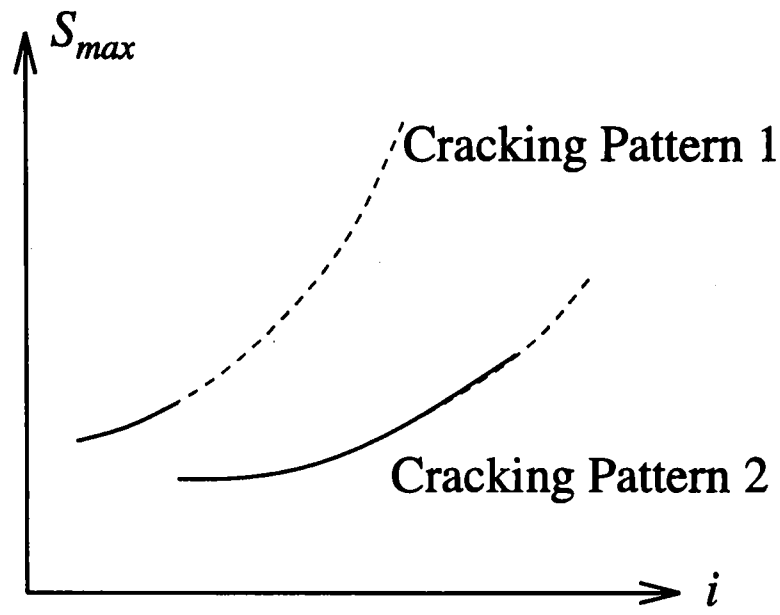


Figure 4.17: Schematic S_{max}-i Curves for Two Cracking Patterns in Masonry Plain Wall

the first type of cracking occurs and the second type of cracking is not present. When the value of i increases the critical pattern will switch from the first cracking pattern to the second, causing the exception in Figure 4.16.

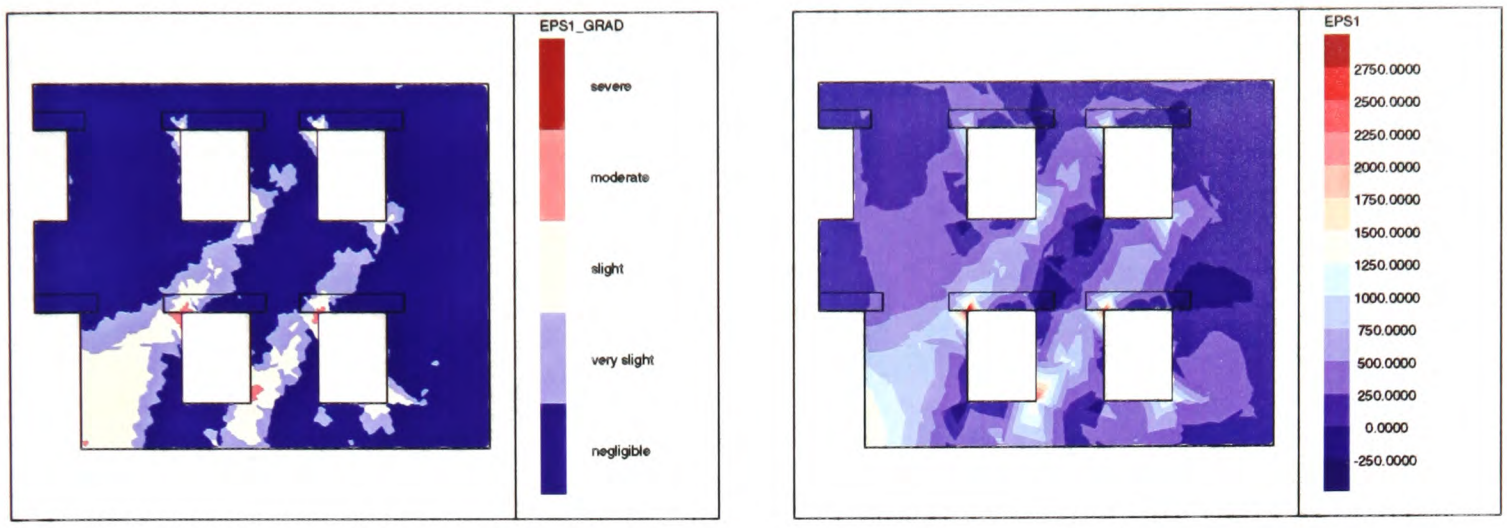
Compared with the Burland-Wroth approach and elastic model, the masonry wall is much more vulnerable. This is because the masonry material loses its stiffness once it is cracked, and thus the damage develops quickly.

4.5 Facade on Gaussian Curve

A facade with openings is analysed by applying the Gaussian curve settlement trough to it symmetrically, in an identical way as for the plain wall. The boundary conditions are the same as before.

4.5.1 Finite Element Analysis: Elastic Facade

The results for the elastic facade on the Gaussian curve settlement trough are shown in Figure 4.18. From the Figure 4.18-(2), the maximum principal strain in the facade is much higher than the equivalent case of the elastic plain wall (Figure 4.12). This phenomenon is due to the presence of the openings which cause stress concentration around their corners, leading to cracking and reducing the stiffness of the whole structure. Thus the facade experiences more serious damage (Figure 4.18-(1)). The directions of the



(1) (2)

(3)

Figure 4.18: (1) Damage Grade, (2) Major Principal Strain and (3) Strain Trajectory in Elastic Facade (i=5.0m)

potential cracks will coincide with the strain trajectory in Figure 4.18-(3). It is noticed that the main damage is confined to the portion on the ground floor between the door and the point of inflexion and at the corners of openings.

The comparison of the damage grades and the cracking patterns with $i = 2.5m, 12.5$m is given in Figure 4.19. The major principal strain for $i = 2.5$m (Figure 4.19-(2)) is almost two times that for $i = 5.0$ (Figure 4.18-(2)) and leads to the onset of severe damage near the centreline, while the facade in the case of $i = 12.5$ experiences less damage. This confirms that smaller values of i will cause more serious and concentrated damage in the elastic model.

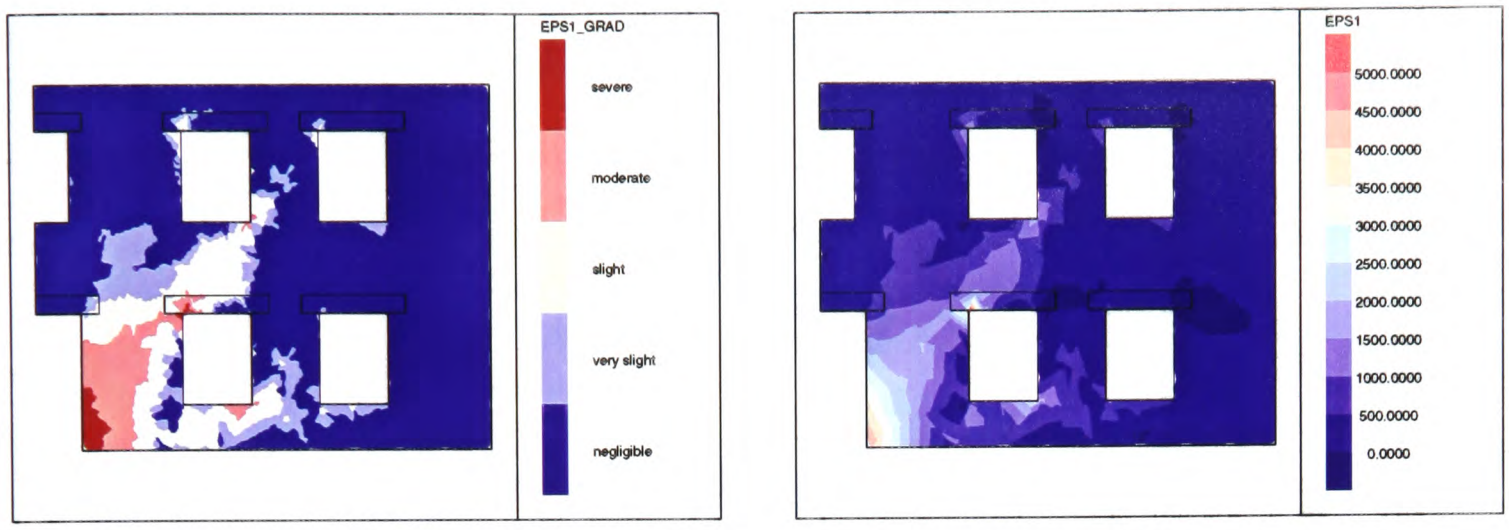
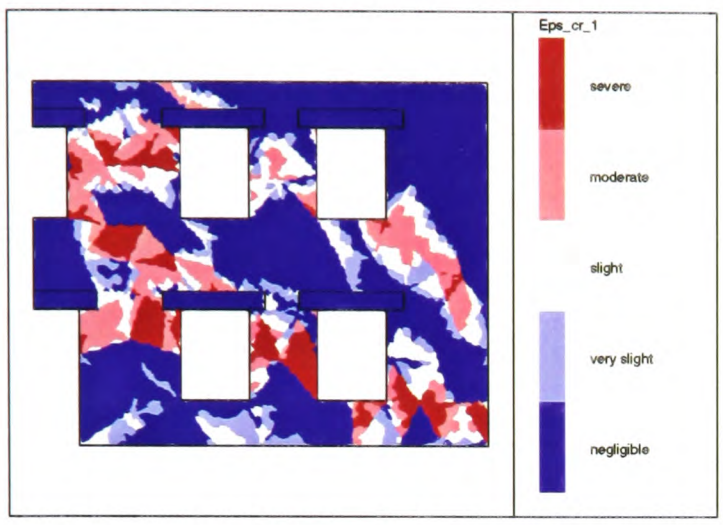


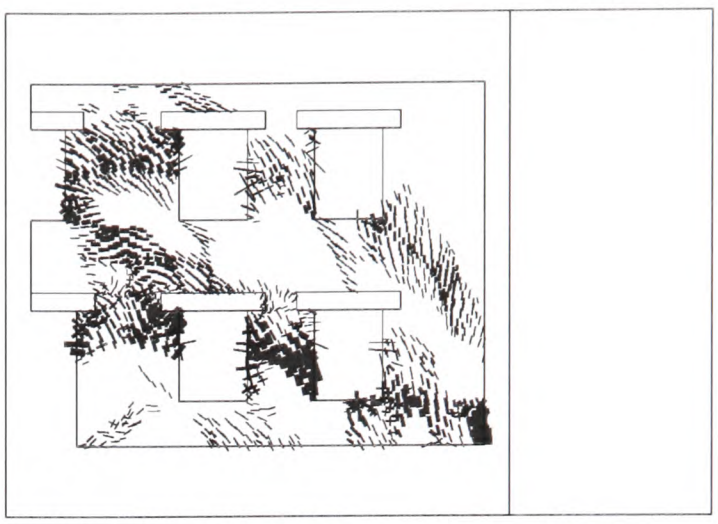
Figure 4.19: (1,3) Damage Grades and (2,4) Principal Strains in Elastic Facade (i=2.5, 12.5m)

4.5.2 Finite Element Analysis: Masonry Facade

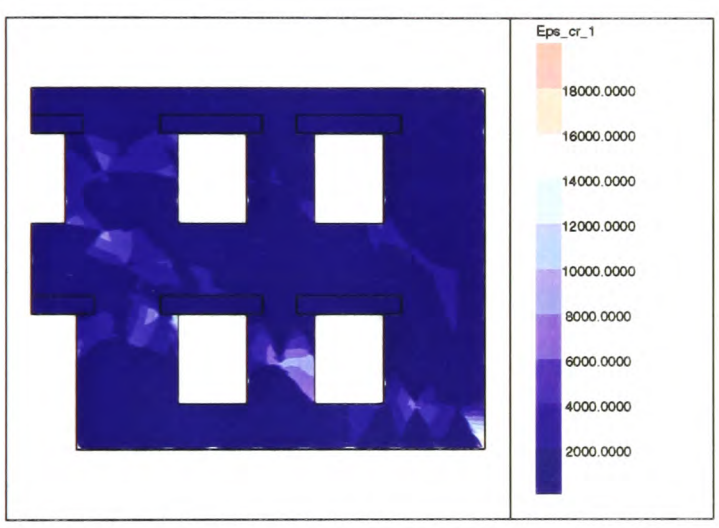
The use of the masonry model gives a different distribution of cracking on the same settlement trough (Figure 4.20), compared to the elastic model. Firstly, the cracking strains (Figure 4.20-(3)) are much higher than the principal strains in the elastic facade. This leads to more serious and widely distributed cracking damage in the masonry facade (Figure 4.20-(1)). Secondly, the damage pattern (Figure 4.20-(2)) has changed from one region originating from the door to several cracking bands under the stress arches (Figure 4.20-(5)) which separate the material above them from further severe damage. The masonry model also shows large shear deformation (Figure 4.20-(4)) within



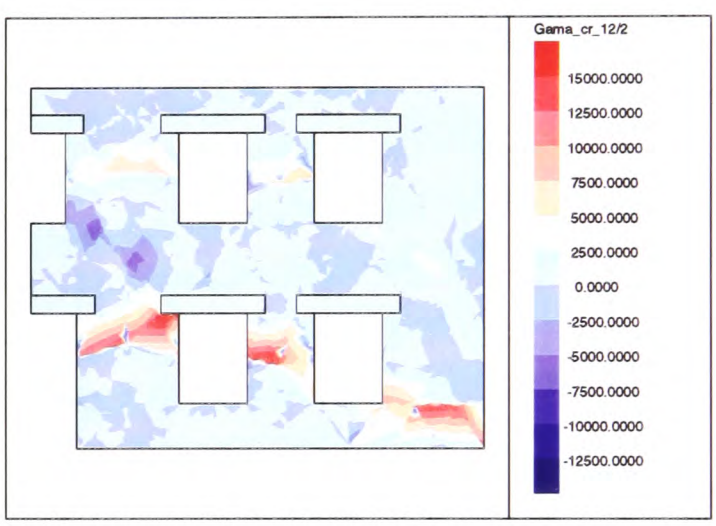
(1) Damage Grade



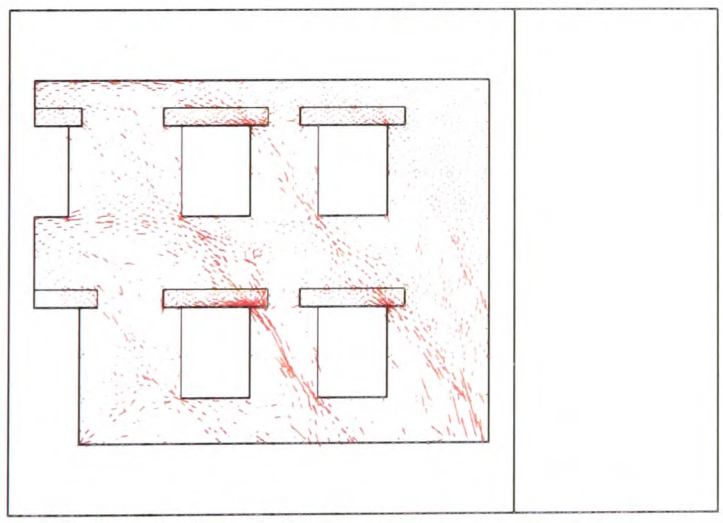
(2) Cracking Pattern



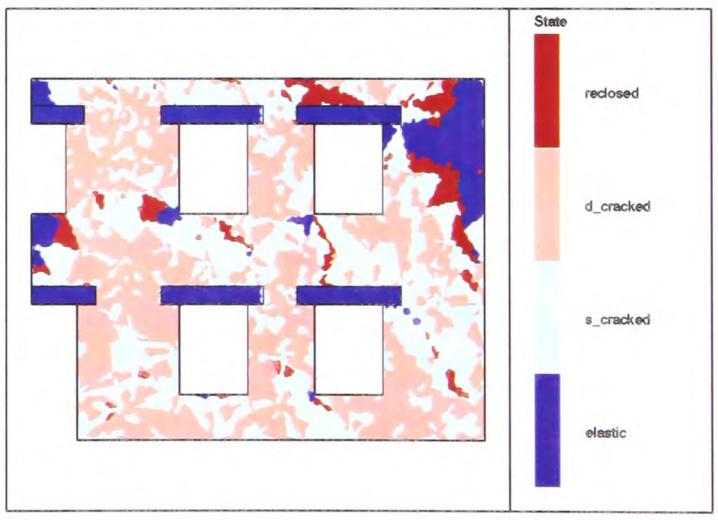
(3) Normal Cracking Strain



(4) Shear Cracking Strain



(5) Stress Trajectory

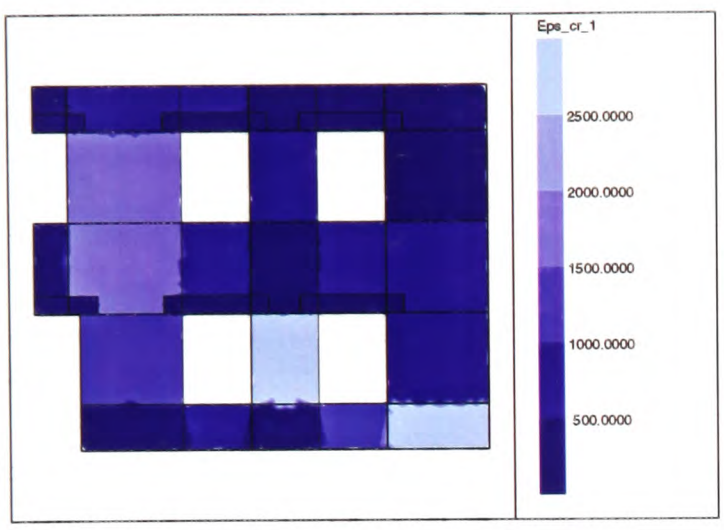


(6) State

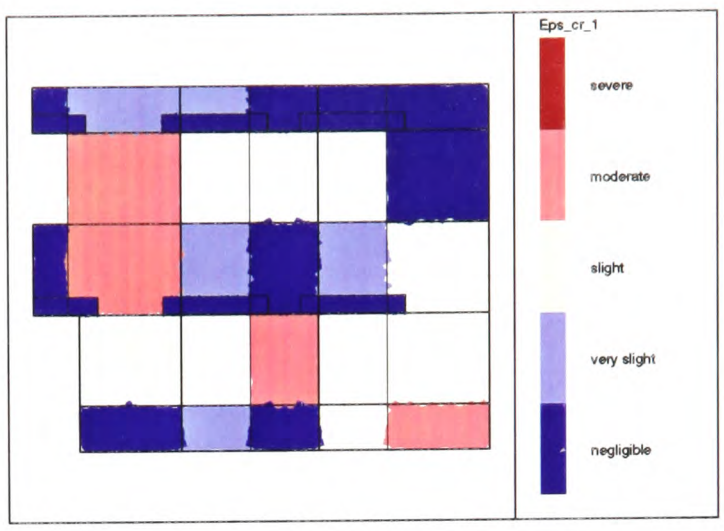
Figure 4.20: Results of Masonry Facade (i = 5.0m)

the seriously cracked areas.

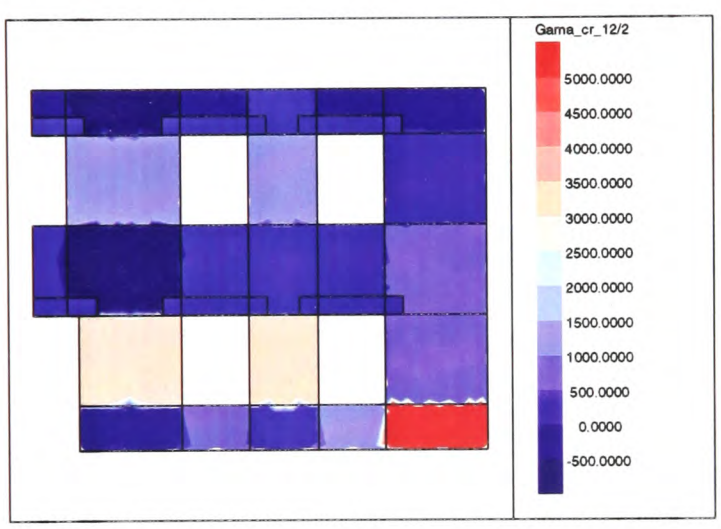
As mentioned before, the distribution of cracking strain is not smooth since the cracked material is able to "float". Some extremely large values might be false. The average cracking strains in the 23 averaging zones are given in Figure 4.21 and used to



(1)



(2)



(3)

Figure 4.21: Average Cracking Strains and Damage Categories in Masonry Facade (i = 5.0m)

compare quantitatively with other cases.

When $i = 5.0$m, the maximum ϵ_1^{cr} is greater than $18,000\mu\epsilon$ and occurs at the end corner of the facade (zone 5) which indicates that the facade experiences extremely severe damage. But this is not a good representation of the whole situation. Such a high cracking strain is unlikely to appear and it would happen at few points even if it were to be realistic. After averaging across each of the 23 zones, the overall damage is much more moderate (Figure 4.21). The highest damage category is moderate damage in zones 5, 7, 10 and 15.

Changing i will change the cracking pattern and severity as before. The averaged damage grades and the cracking patterns for $i = 2.5, 12.5$m are shown in Figure 4.15-

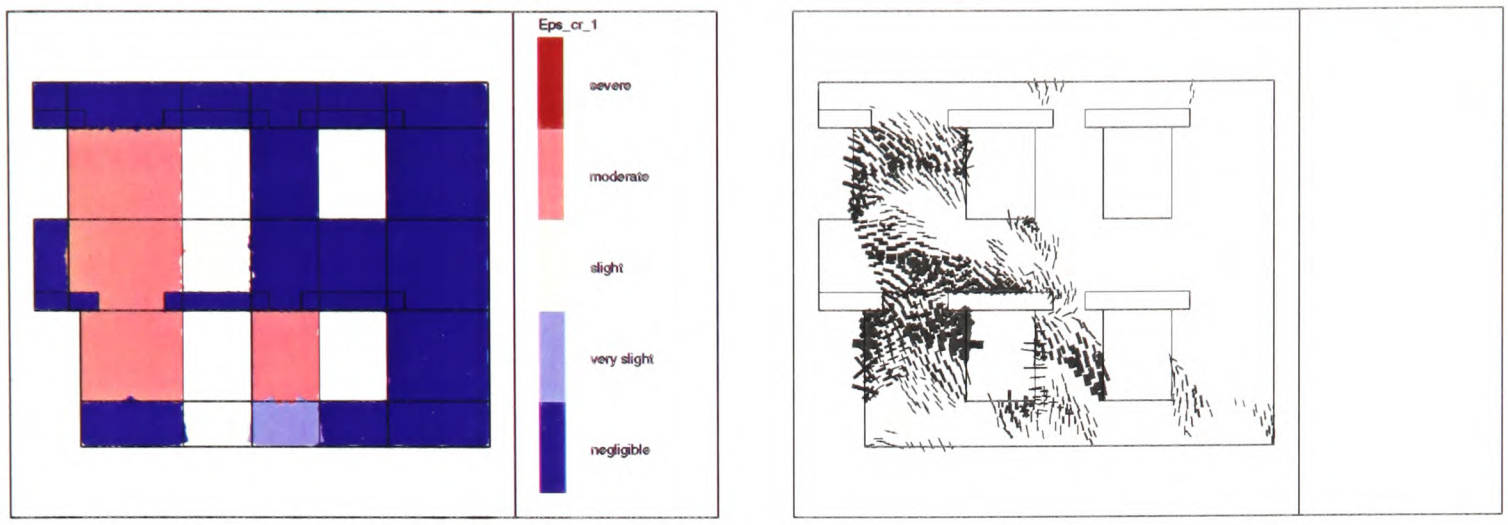
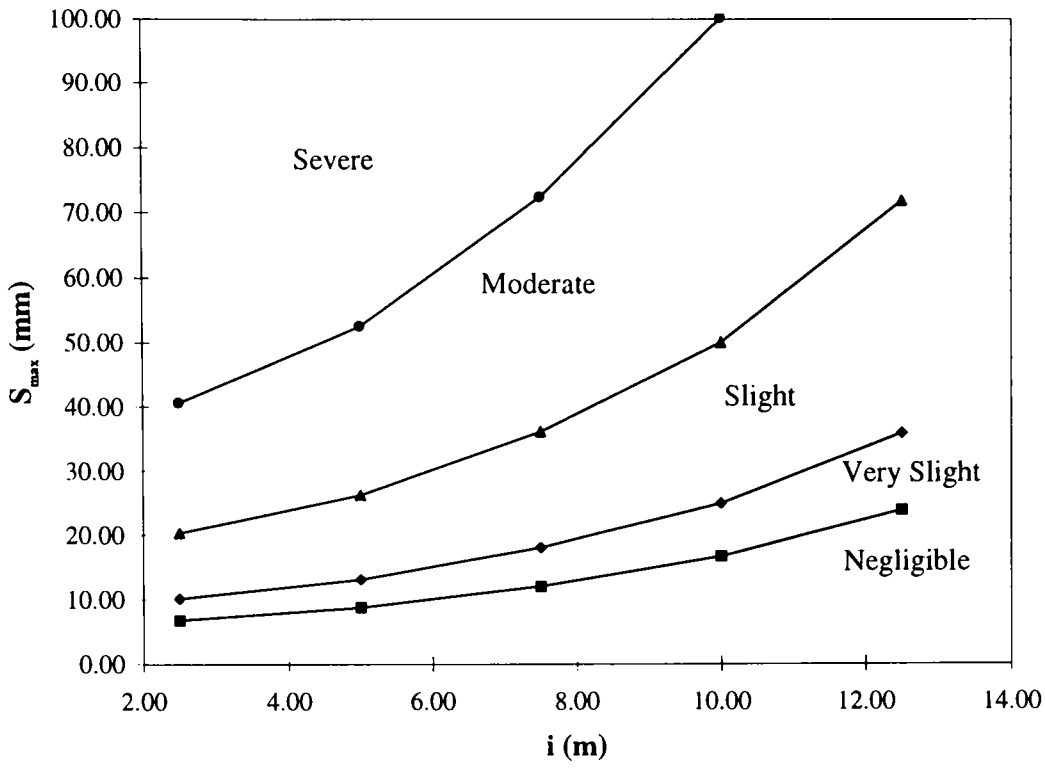


Figure 4.22: (1,3) Averaged Damage Grades and (2,4) Cracking Patterns in Masonry Facade (i=2.5, 12.5m)

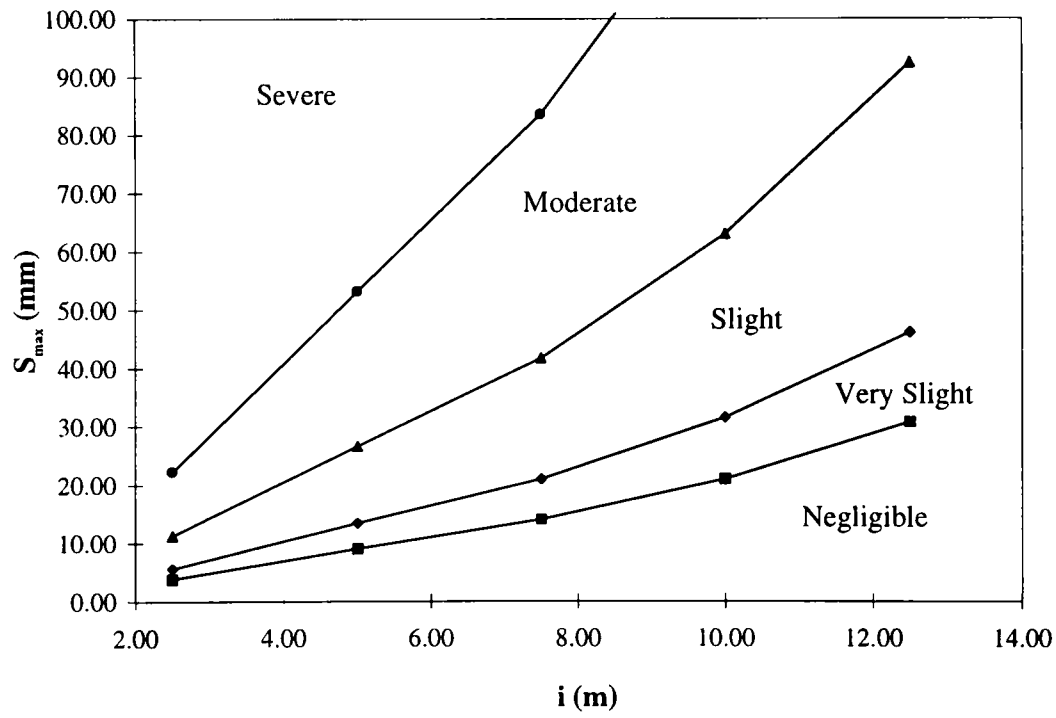
(1,2). The relationship between S_{max}, i and the damage grade is also presented by the S_{max}-i curves (Figure 4.23). The curves for the facade are very similar to those for the plain walls, except that the facades are more prone to cracking than the plain wall.

4.6 Masonry Facade Box on Greenfield Troughs

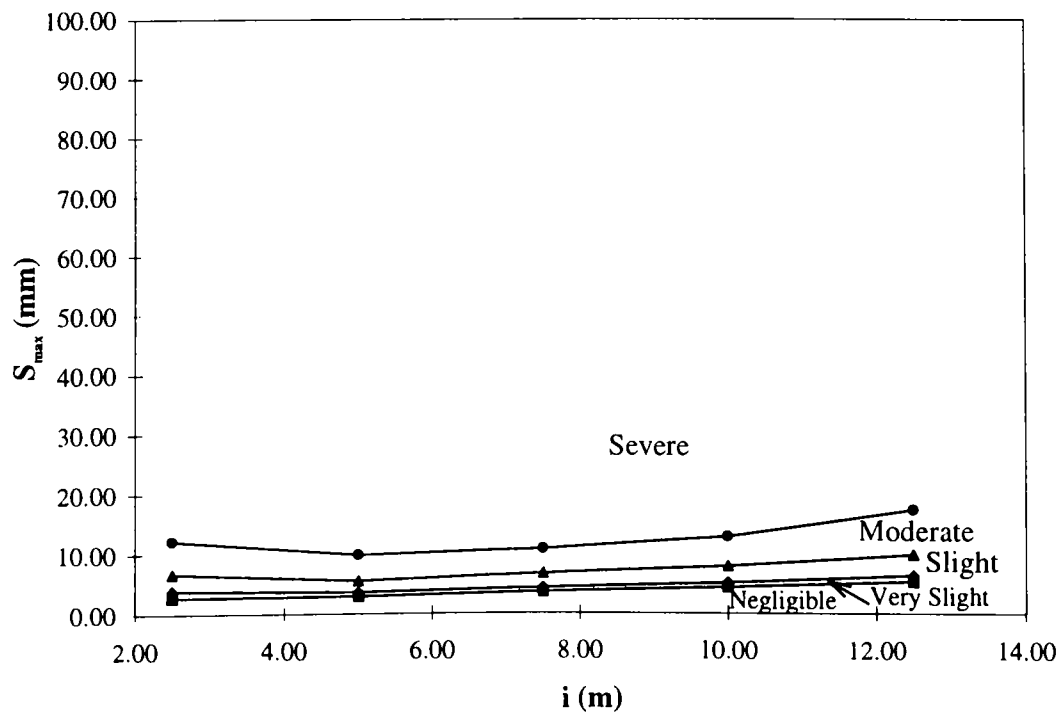
Two cases are analysed here (Figure 4.24). The first passes symmetrically under the the building along its centreline. The second case is the same tunnel but passing under the corner of the the building at a skew angle, causing a settlement trough that is a combination of the troughs in the transverse and longitudinal planes.



(1)

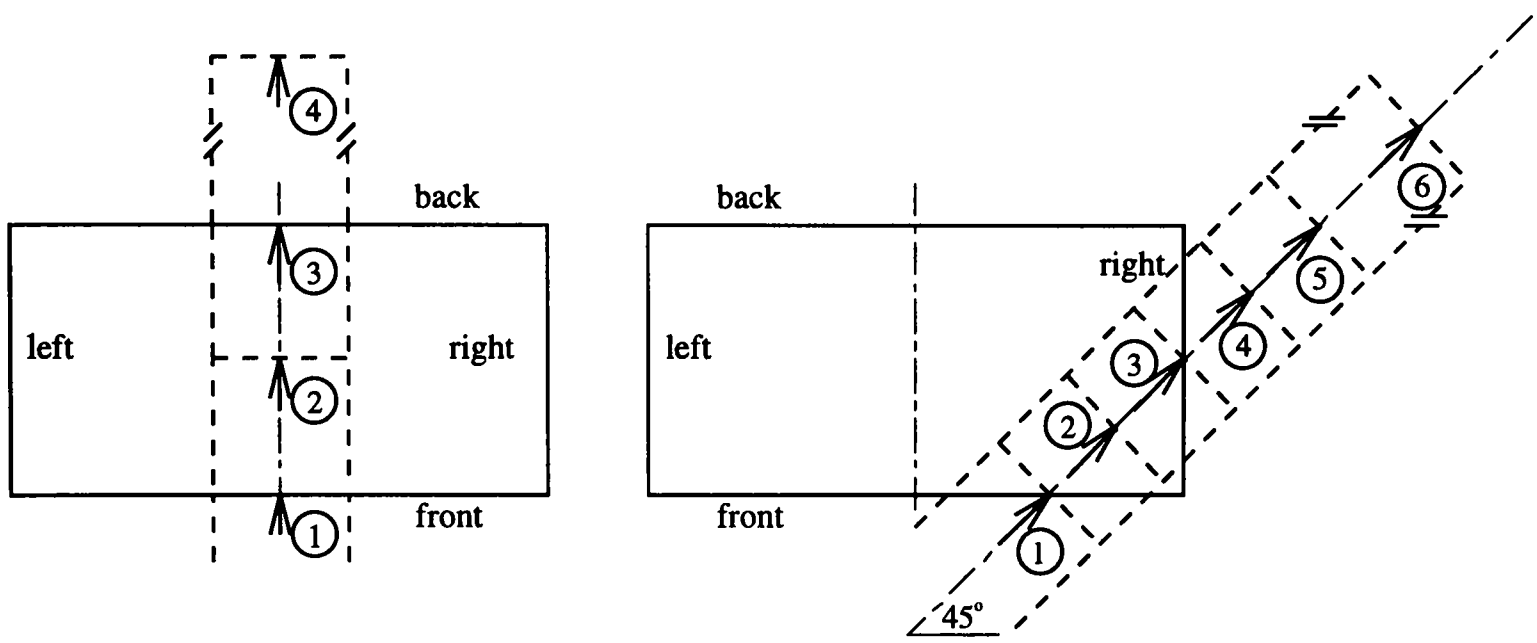


(2)



(3)

Figure 4.23: S_{max}-i Curves for Facade, (1) Burland-Wroth Method, (2) Elastic Model and (3) No Tension Model



(1) symmetric scheme (2) skew scheme

Figure 4.24: Tunnelling Schemes under the Facade Box

4.6.1 Masonry Facade Box on the Symmetrically Excavated Tunnel

The tunnel is excavated by four steps, the position of the tunnel face for each step can be found in Figure 4.24(1). As the tunnel advances, the shapes of settlement troughs beneath front and back facades are similar but with changing maximum values of settlement. The ultimate damage patterns in these two facades are almost identical to the single facade wall.

The shapes of settlement troughs along the end walls are changing when the tunnel advances, as they depend on the position of the tunnel face (Figure 4.25), with reversal from initial hogging to final sagging. Since their locations are far from the centreline, such a reversal does not cause visible cracking in the end walls, except that some cracks occur at the lower corners, caused by the shear forces transferred by the ties between facades and end walls.

4.6.2 Masonry Facade Box on the Skew Tunnel

The tunnelling scheme is progressed in six stages to monitor the settlement change during the advance (Figure 4.24-(2)). The combination of longitudinal and transverse settlement troughs causes a different behavioural response.

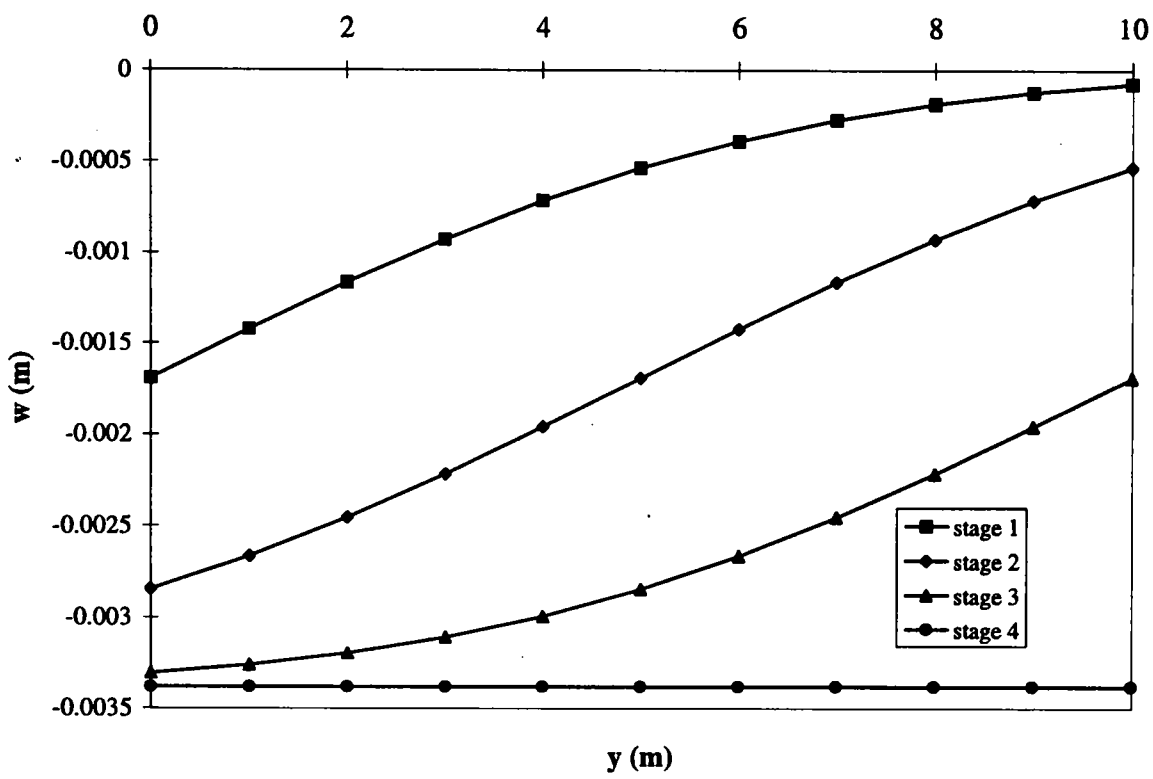


Figure 4.25: Settlement Trough along the Right End Wall, Symmetric Tunnel

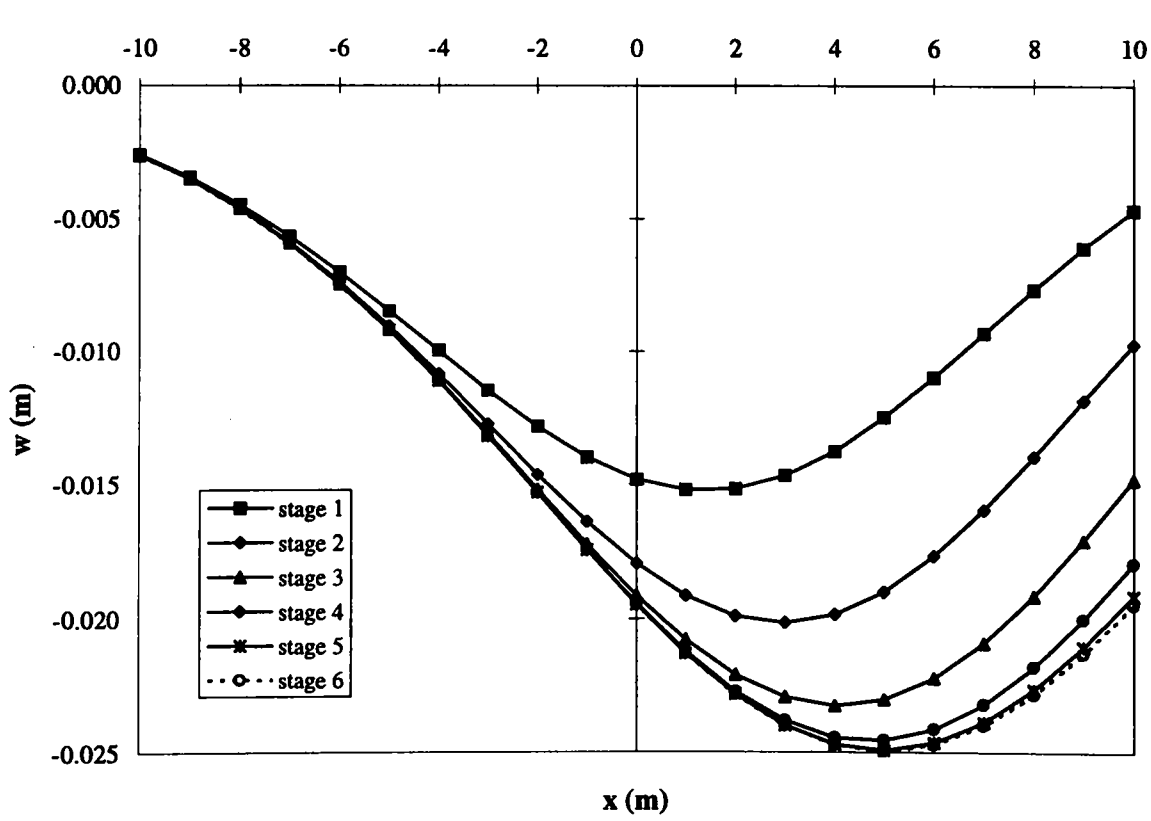


Figure 4.26: Settlement Trough along the Front Facade, Skew Tunnel

Front Facade

The majority of the front facade lies in the sagging area (Figure 4.26), but the point of maximum settlement moves from near the centreline of the facade to the centreline of

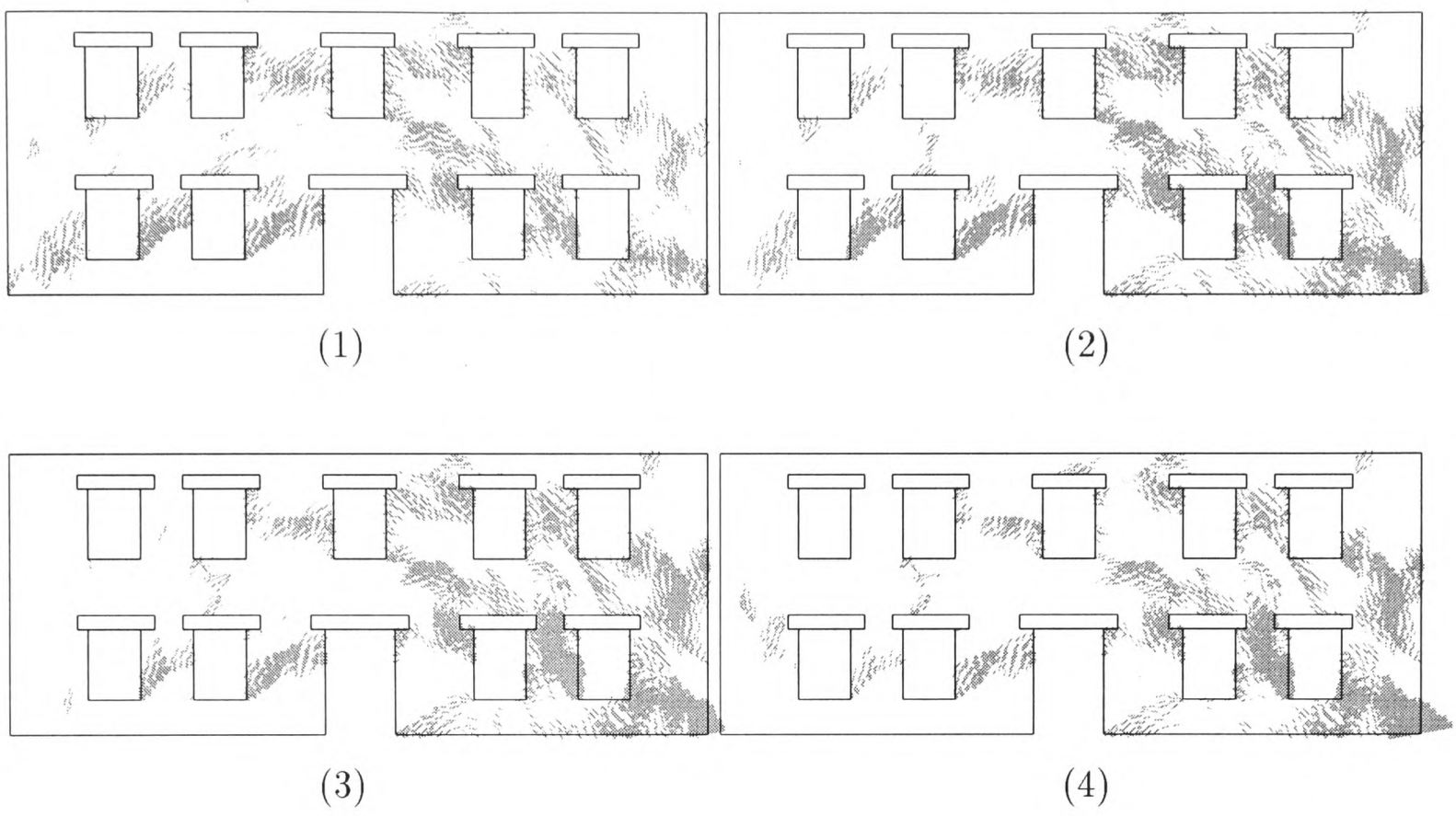


Figure 4.27: Cracking Patterns in Front Facade for Skew Tunnel. Stages 1,2,3 and 6.

the tunnel. The damaged area also moves from left to right. Some cracks occurring at early stages in the left part reclose while the cracks in the right part become progressively more serious (Figure 4.27).

Right End Wall

As the tunnel progresses under the corner, the settlement trough under the right end wall changes from hogging to sagging (Figure 4.28). Thus comparing with the previous case, the right end wall will experience more serious damage. The cracking develops from vertical near to the top, due to the hogging mode, to cracks corresponding to the sagging mode (Figure 4.29).

Back Facade

Due to its location, the back facade finishes mainly in the hogging region, thus it is expected that the ultimate cracking pattern will be vertical cracks from the top of the facade. However, at the early stage the left part of the trough is in the sagging

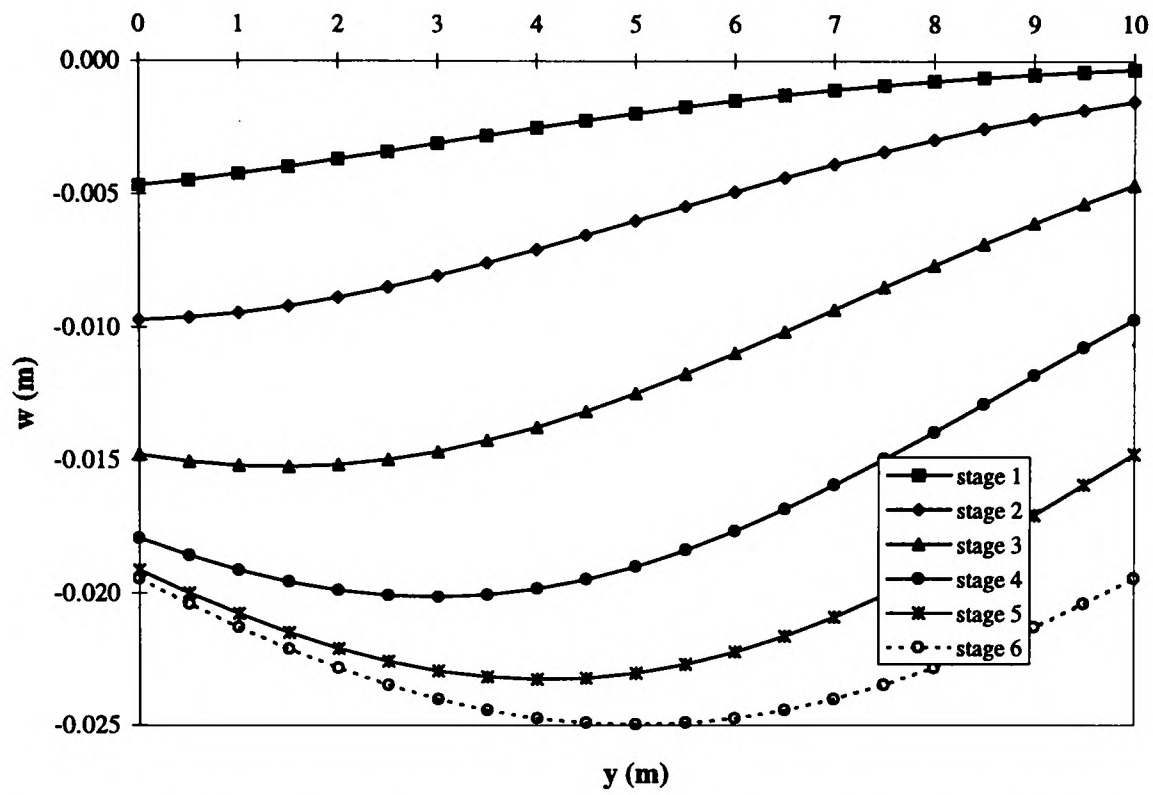
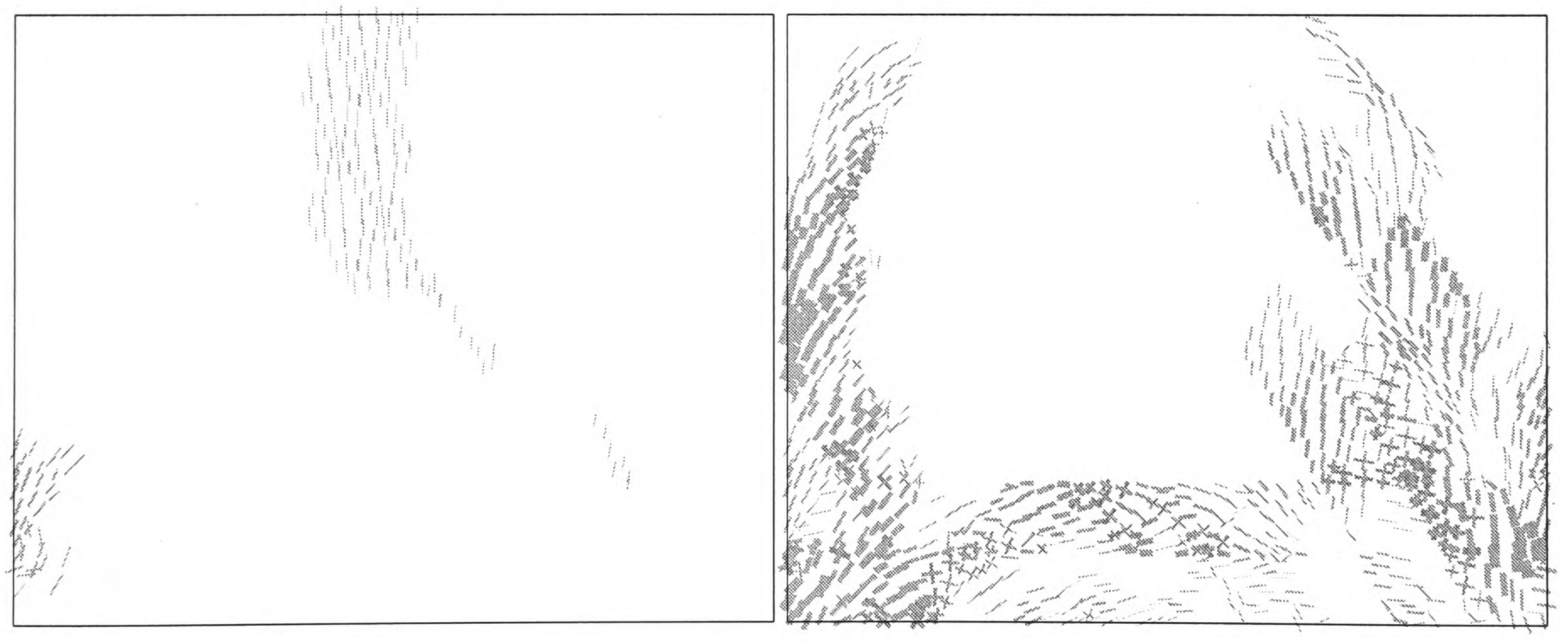


Figure 4.28: Settlement Trough along the Right End Wall, Skew Tunnel



(1) (2)

Figure 4.29: Cracking Patterns in the Right End Wall for Skew Tunnel, (1) Stage 1 and (2) Stage 6.

mode which leads to some damage corresponding sagging pattern occurring early, and reclosing later on (Figure 4.31).

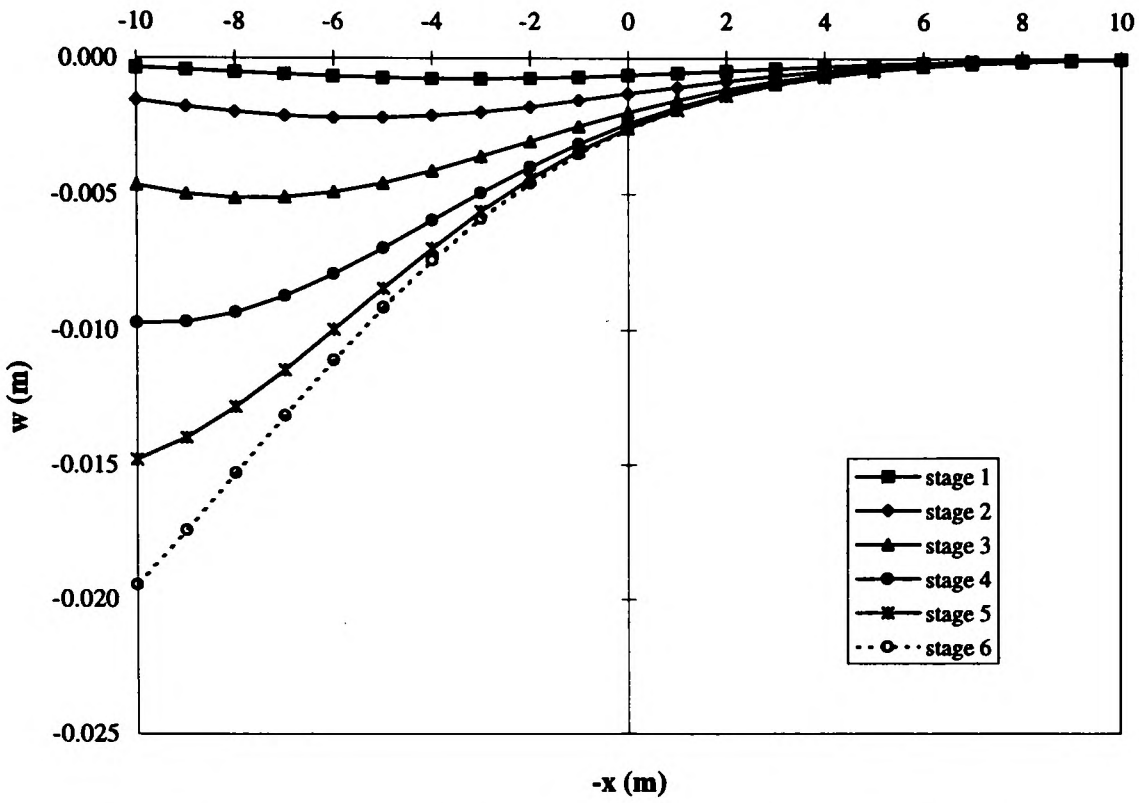
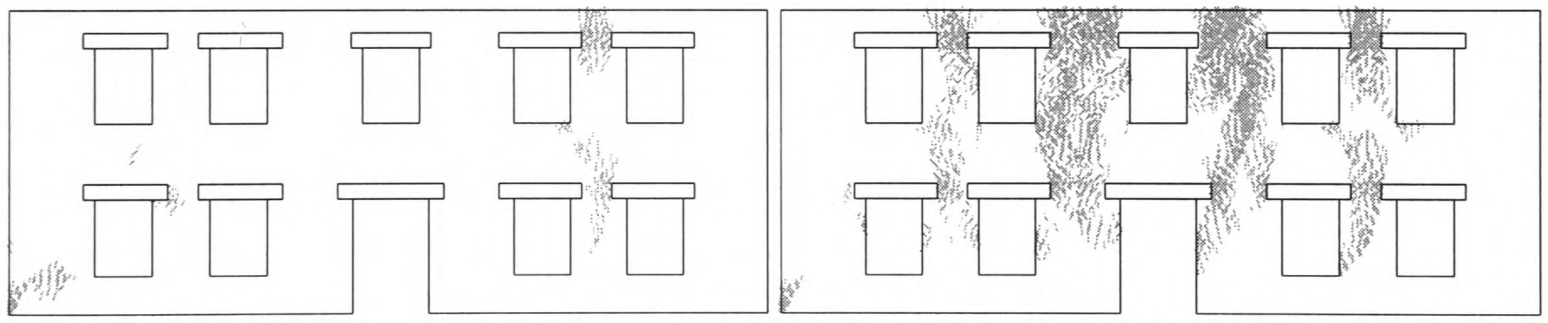


Figure 4.30: Settlement Trough along the Back Facade, Skew Tunnel



(1) (2)

Figure 4.31: Cracking Patterns in the Back Facade for Skew Tunnel, (1) Stage 3 and (2) Stage 6.

Left End Wall

The settlement along the left end wall stays in the hogging mode (Figure 4.32). Therefore its damage pattern is vertical cracking from the midpoint of the upper boundary, which is the typical hogging damage mode (Figure 4.33).

4.7 Effect of the Material Parameters

Along with the elastic modulus and Poisson's ratio, there are three more parameters used to define the masonry model, f, residual stiffness factor, c, residual tensile strength

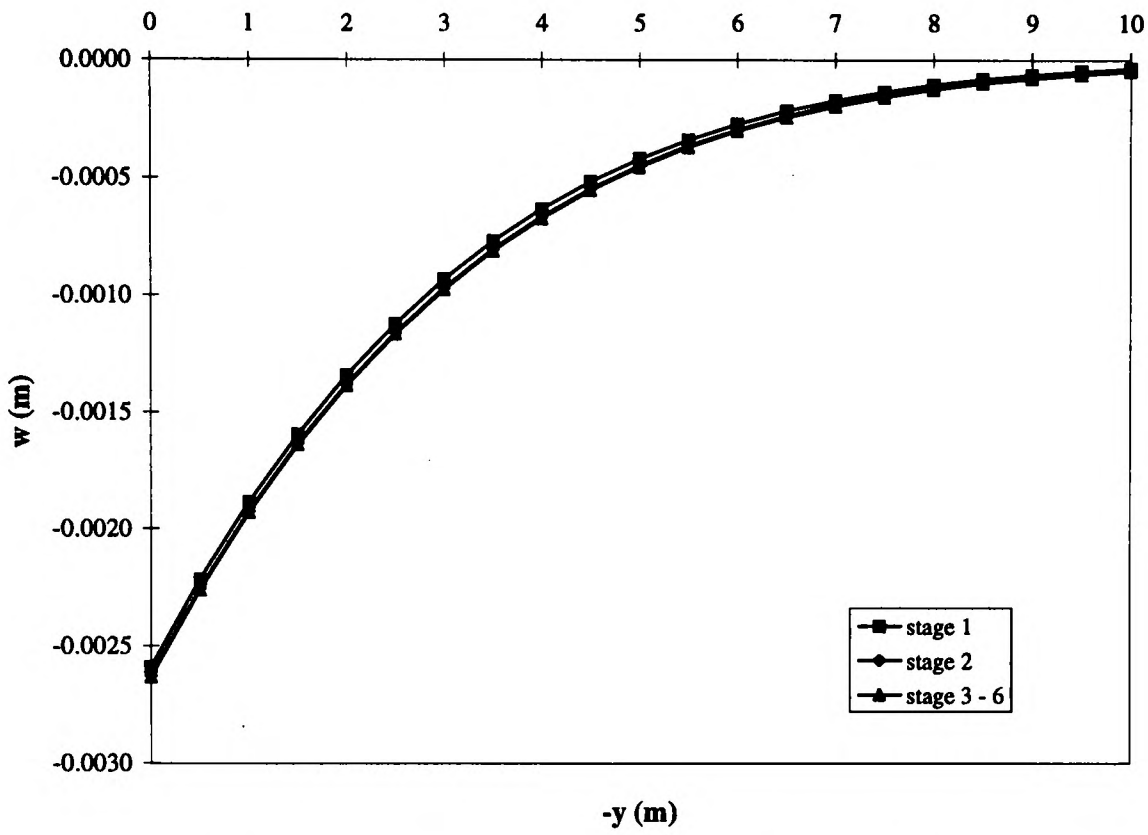


Figure 4.32: Settlement trough along the left end wall, skew tunnel

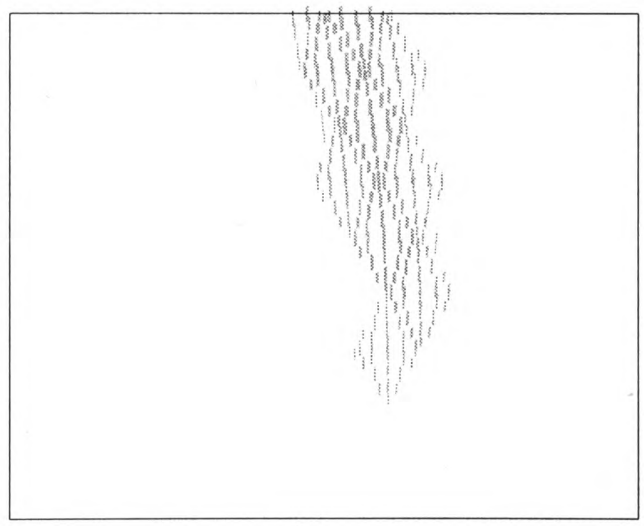
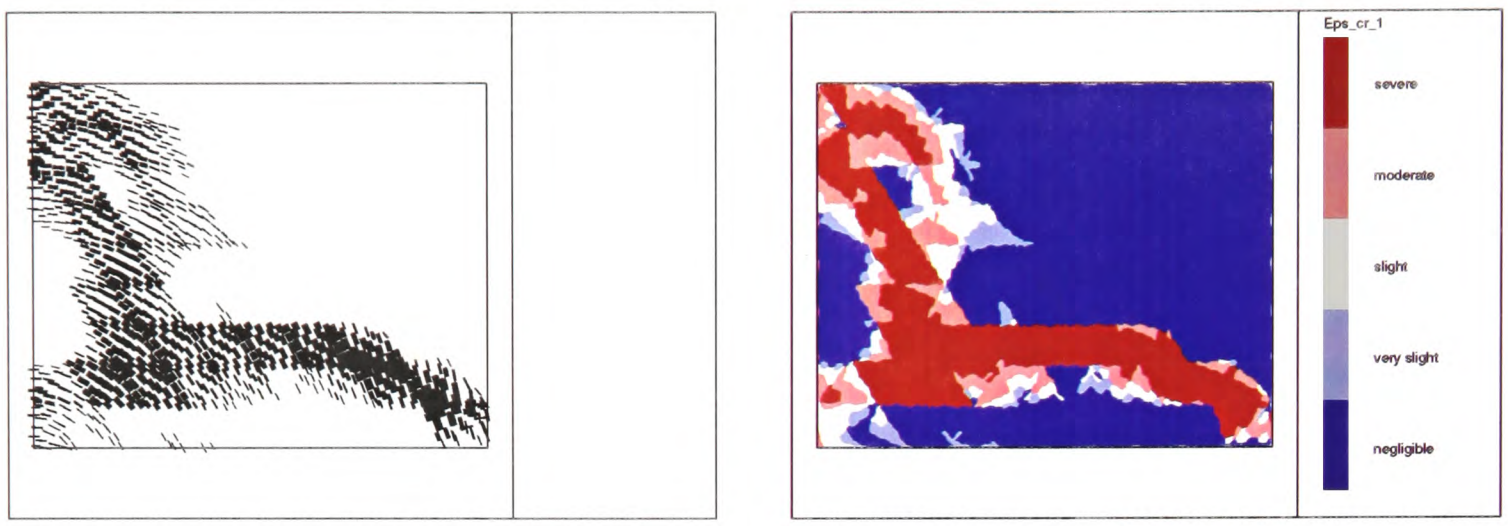


Figure 4.33: Cracking Pattern in the Left End Wall, Stage 6

and ϵ_0^{cr}, stiffness reduction rate parameter. These parameters will affect the predicted cracking patterns and damage categories, and their effects are tested and compared for the plain masonry wall subject to the standard Gaussian curve settlement trough as follows.

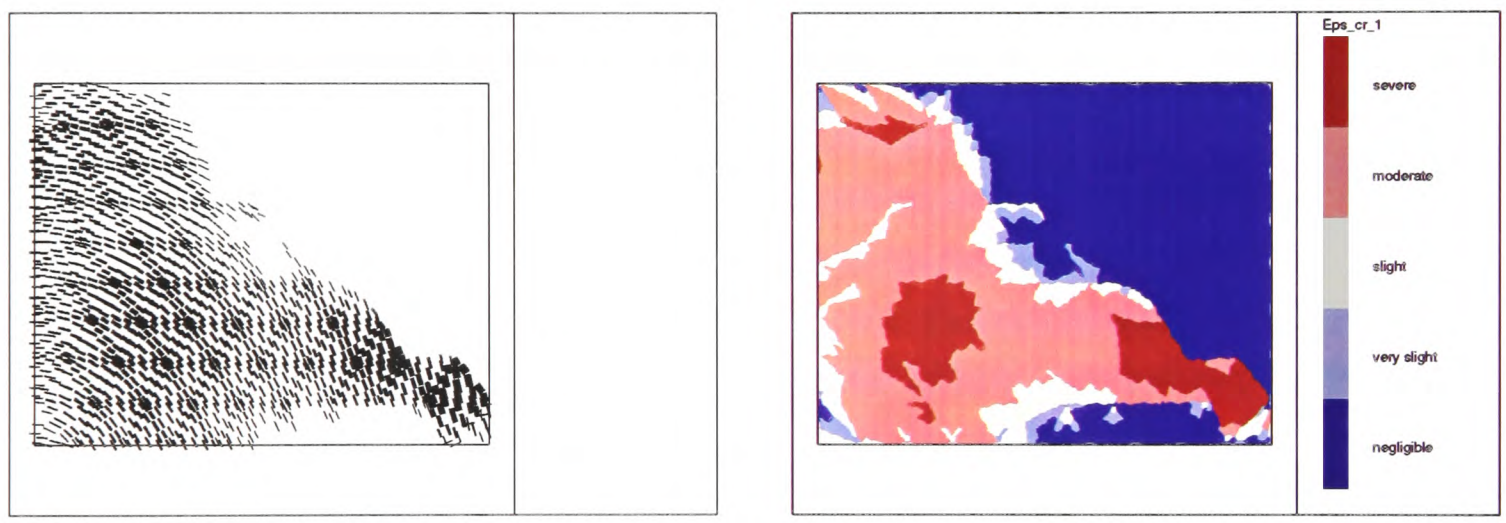
Residual Stiffness Factor f

The residual stiffness factor f changes the stiffness distribution and then deformation



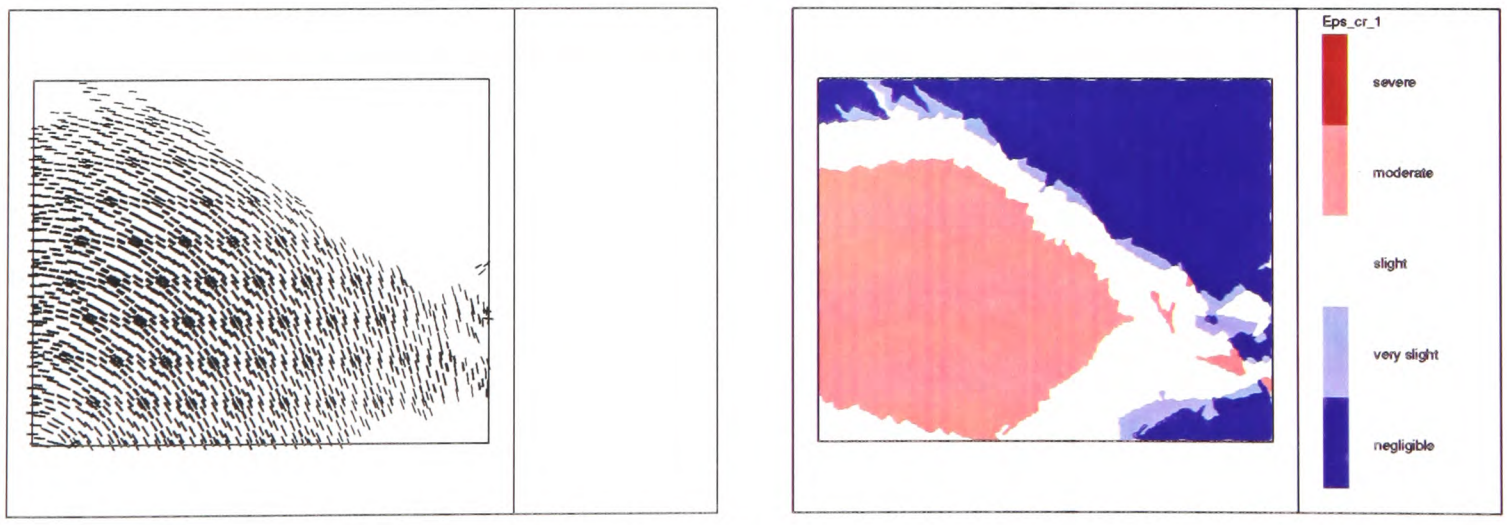
(1) (2)

(1) f = 0.001



(3) (4)

f = 0.01



(5) (6)

f = 0.1

Figure 4.34: Cracking Patterns and Damage Grades in Plain Masonry Wall for Different f: c = 10kPa, $\epsilon_0^{cr} = 4\mu\epsilon$

distribution within the wall and facade. The different values of 0.001, 0.01, 0.1 are used for the plain wall analysis while c and ϵ_0^{cr} remain at 10kPa and $4\mu\epsilon$. Although the cracking states are similar in three cases, the cracking patterns and the degrees of severity are very different. (Figure 4.34). A smaller value of f gives less stiffness in the cracked area and localises the severe cracking while a bigger value of f tends to spread the cracking with less damage. Since the extremely small f may cause unrealistic deformations due to ill-conditioning of the stiffness matrix, $f = 0.01$ was chosen to be used in the main analyses in this study.

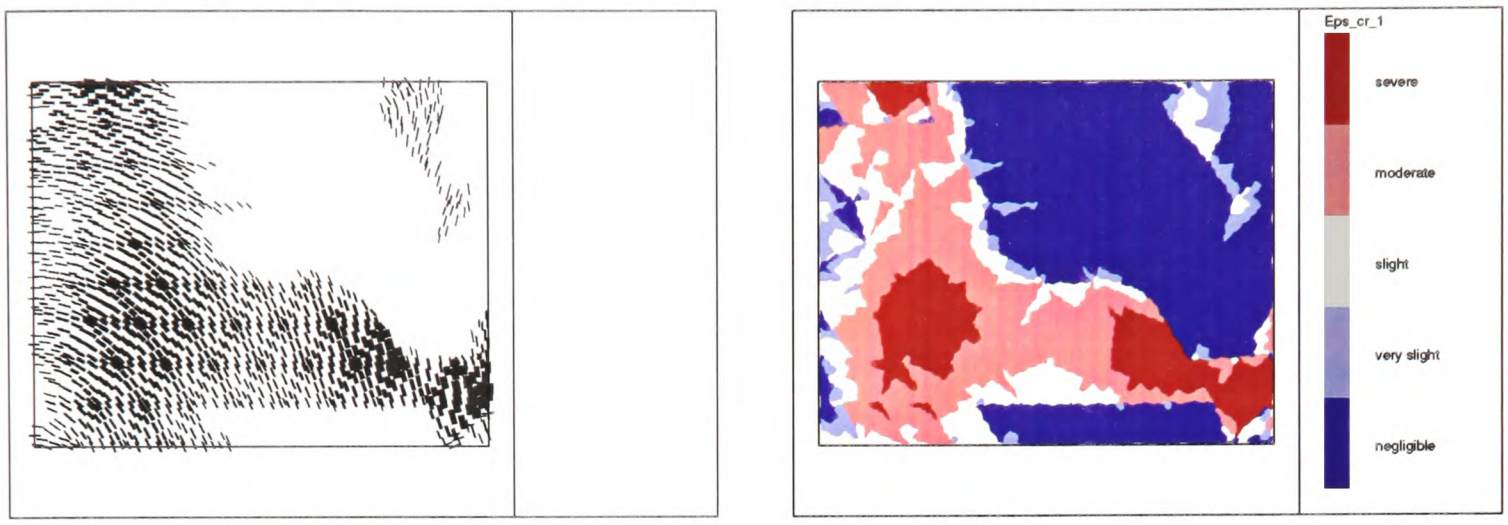
Residual Tensile Strength c

For the ideal no tension model, the residual tensile strength c should be zero, but that value predicts some unexpected or unrealistic cracking since the unloaded state could be considered as either safe or cracked.

The cracking patterns and damage grades for the three different values of c are given in Figure 4.35. Increasing c will make the material more elastic-plastic. For c less than 10kPa, the main predicted cracking patterns do not vary significantly (Figure 4.35). In fact, compared with typical compressive (20,000kPa) and tensile strength (500kPa) for masonry such a c value is negligible. Thus $c = 10$kPa was used in the main analyses throughout this study.

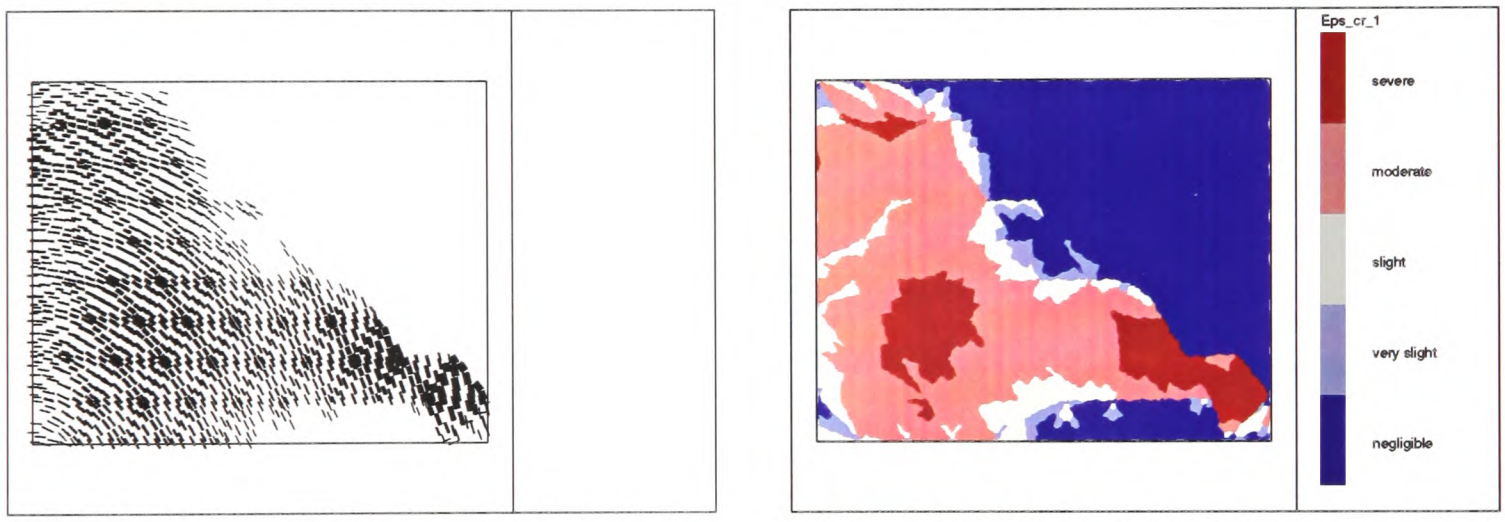
Stiffness Reduction Rate Parameter ϵ_0^{cr}

For the strict no tension model, ϵ_0^{cr} is zero, but this causes a problem with unrealistic reclosure in the material. Compared with the visible cracking strain limit of $500\mu\epsilon$, ϵ_0^{cr} of less then $10\mu\epsilon$ is reasonably small. The results for $\epsilon_0^{cr} = 2, 4, 8\mu\epsilon$ show there is little change in the cracking patterns (Figure 4.36). The value of ϵ_0^{cr} used in this study is $4\mu\epsilon$. It is obvious that a very large ϵ_0^{cr} would cause the material to behave elastically (Figure 4.37).



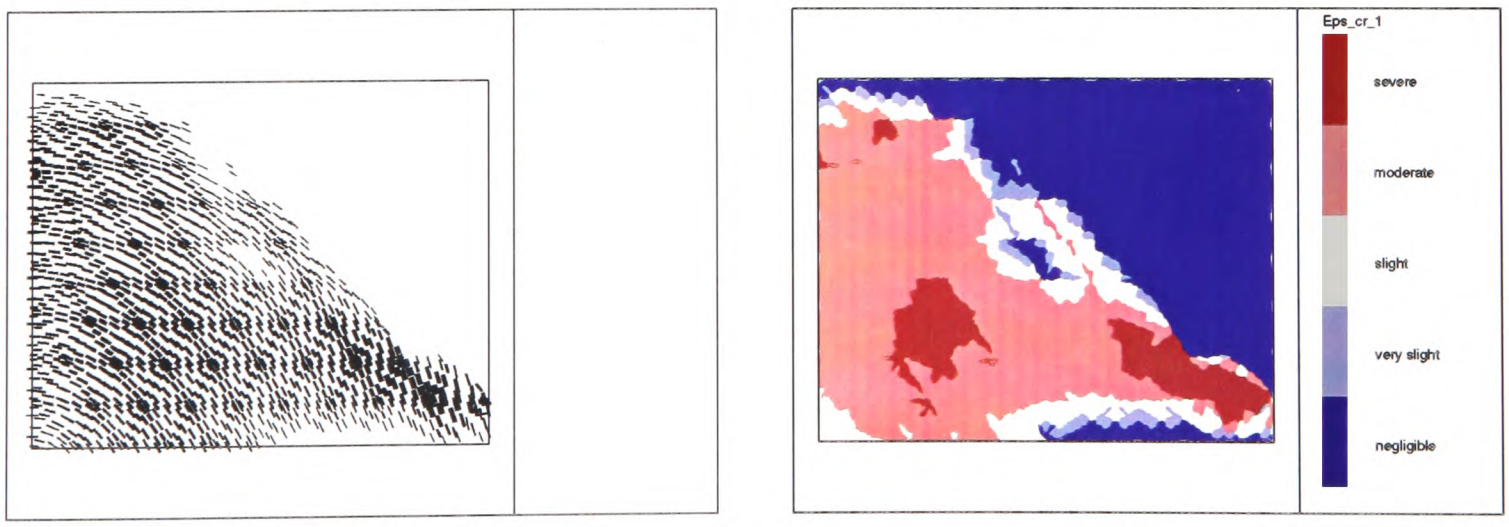
(1) (2)

c = 0 kPa



(3) (4)

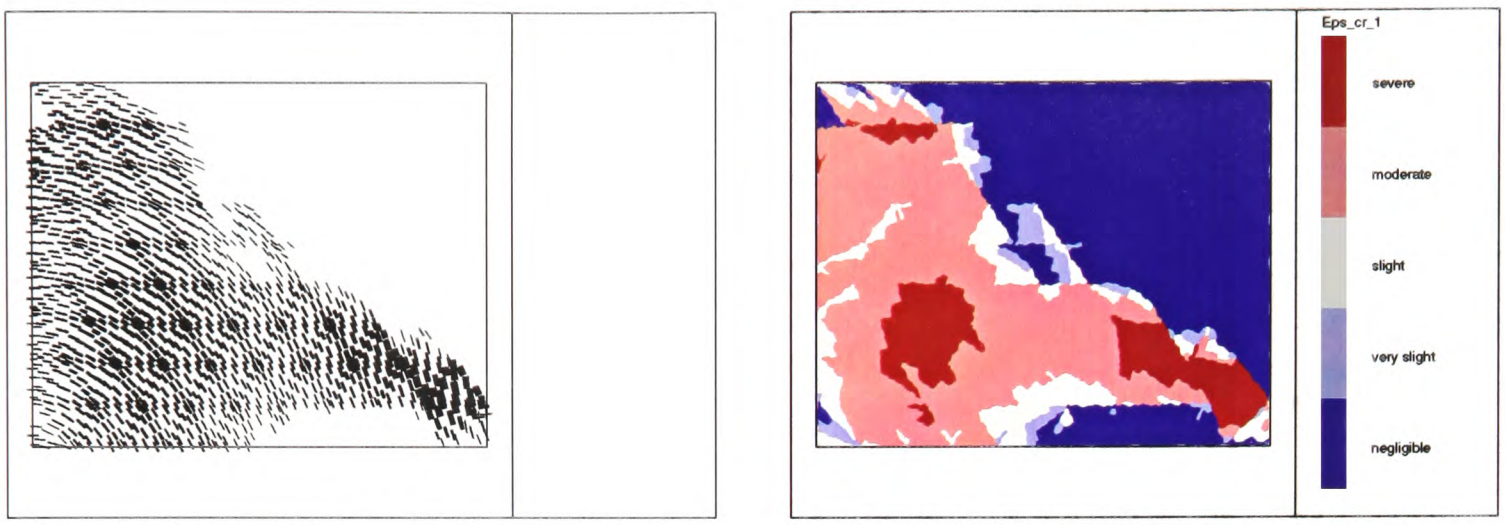
c = 10 kPa



(5) (6)

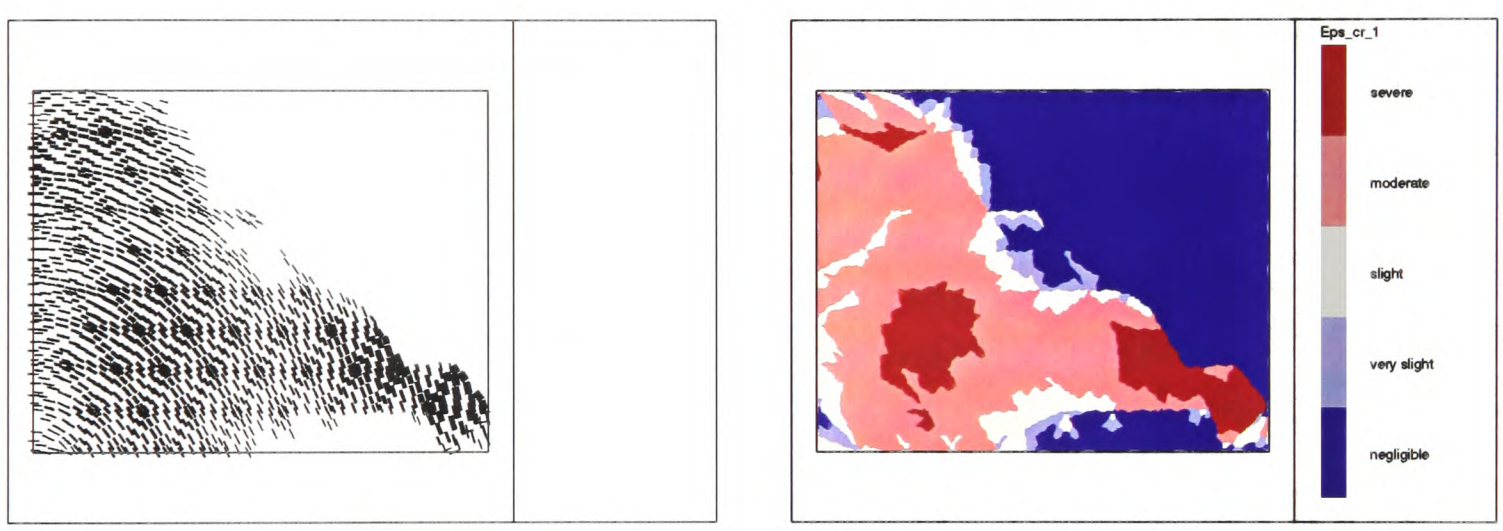
c = 20 kPa

Figure 4.35: Cracking Patterns and Damage Grades in Plain Masonry Wall for different c: f = 0.01, $\epsilon_0^{cr} = 4\mu\epsilon$



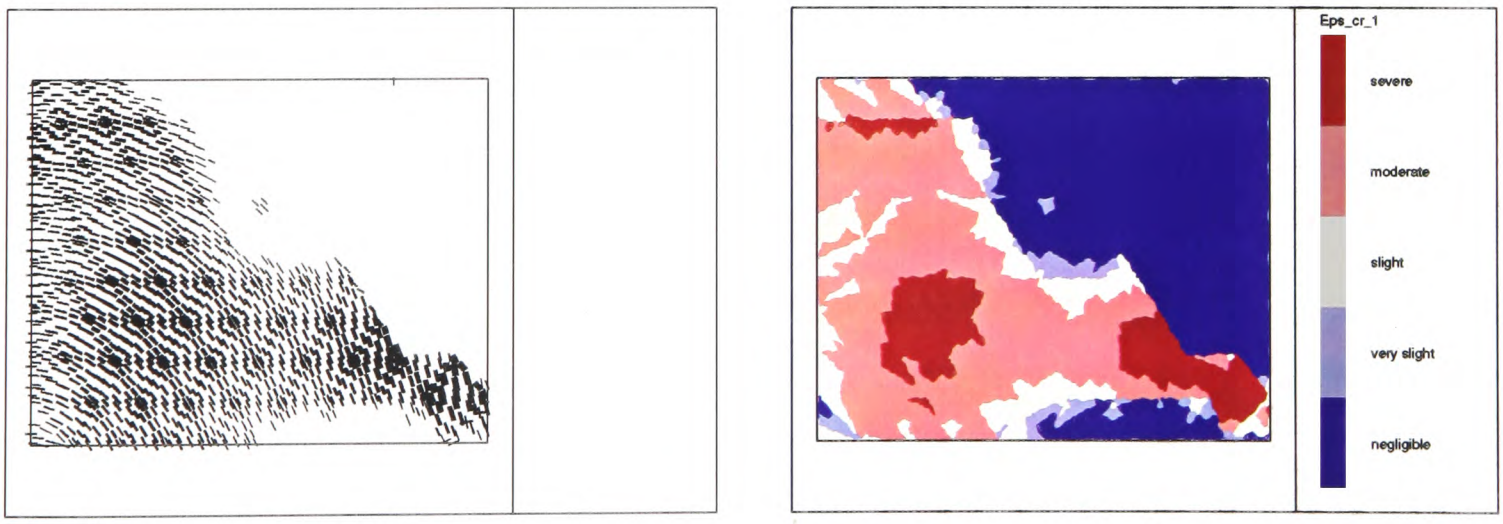
(1) (2)

$\epsilon_0^{cr} = 2\mu\epsilon$



(3) (4)

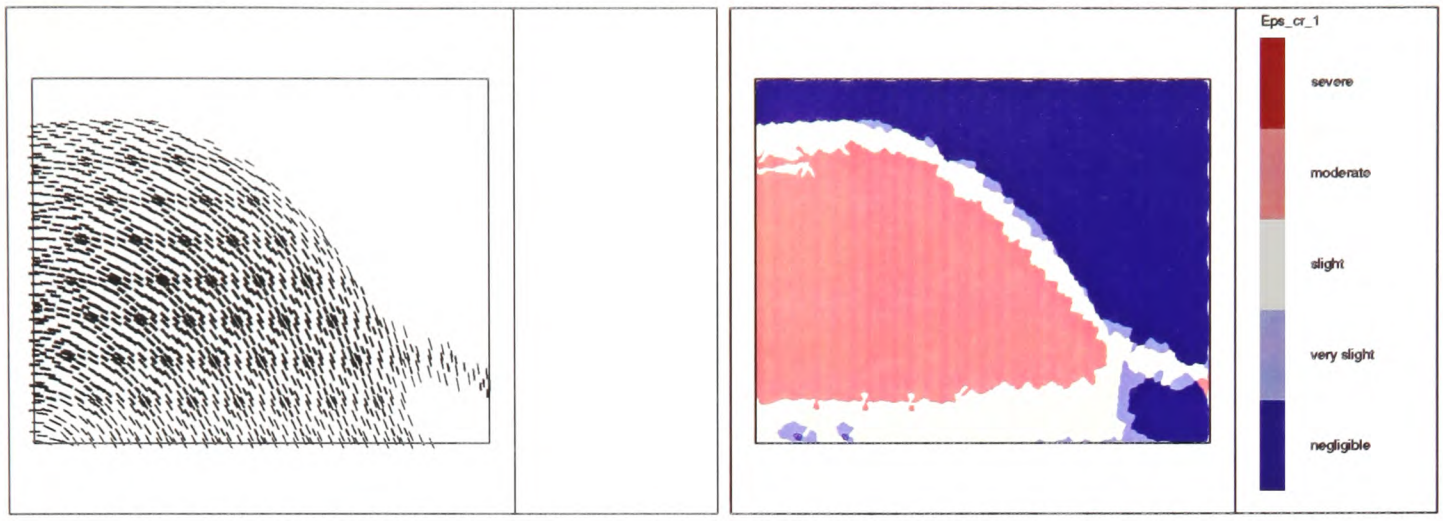
$\epsilon_0^{cr} = 4\mu\epsilon$



(5) (6)

$\epsilon_0^{cr} = 8\mu\epsilon$

Figure 4.36: Cracking Patterns and Damage Grades in Plain Masonry Wall for Different ϵ_0^{cr}: f = 0.01, c = 10kPa



(1) (2)

Figure 4.37: Cracking Pattern for $\epsilon_0^{cr} = 160\mu\epsilon$

4.8 Summary and Conclusions

A plain wall and a facade with openings have been analysed in this chapter by applying a Gaussian settlement trough to them, using elastic and masonry material models. The finite element results have been compared with the Burland-Wroth method which is the current practice in the industry. The results show that masonry buildings will behave very differently to elastic buildings when they experience the same settlement due to tunnelling. The masonry buildings will have different cracking patterns and more severe damage. Stress arches are formed in the masonry building and affect its post-cracked behaviour.

For the tunnel passing under the corner of the building, the advance of the tunnel will cause more serious cracking damage in the building than in the symmetric situation.

Some methods for presentation of the results of the analysis were also established in this chapter.

The parameters used in the masonry model affect the predictions and can be a means of adjusting the prediction when this model is applied in practical engineering projects.

5

2-D Analysis of the Settlement Damage Due to Tunnelling

In the previous chapter the response of a masonry facade to a Gaussian curve settlement profile induced by tunnelling was discussed. However, such a greenfield curve is unlikely to occur under a building, due to the interaction between the building and the ground. This interaction is to be analysed in this chapter using 2-D finite element analysis combining the building and the ground.

5.1 Soil Model and Tunnelling Simulation

To simulate the tunnelling process in the ground with the building, the first task is choosing a suitable soil model for London clay. Chow(1994) compared several soil models and pointed out that neither the linear elastic, non-linear elastic nor perfectly elastic-plastic models are able to predict the correct settlement trough, since they each give much wider or flatter and shallower troughs than Gaussian curves. The reason for the poor quality of these predictions was identified as being the elastic part of any of these constitutive models. The key to modelling the ground movements during tunnelling correctly is to capture the non-linearity and low stiffness of the soil at small strains

(Gunn, 1992) (Simpson, 1968). The nested yield surface model proposed by Chow(1994) and Houlsby(1997) has been proved to be able to reflect this feature of London clay.

5.1.1 Nested Yield Surface Model

The nested yield surface model includes several yield surfaces in the shape of von Mises yield surfaces in stress space. Each surface can be translated in the stress space by the stress point when the surfaces touch at the stress point. The outermost failure surface is represented by a von Mises yield surface which is fixed in the stress space. The sizes of the yield surfaces are governed by the stress-strain hardening law used in the model. The initial positions of the yield surfaces are set up on the basis of the past stress-strain history of the soil.

The properties are determined by the bulk elastic modulus K, the shear modulus G and the undrained shear strength c_u as usual for a von Mises surface. For a nested yield surface model consisting of n surfaces, the other $(n-1)$ surfaces require $(n-1)$ pairs of strength c_i and hardening parameter h_i $(i = 1, 2...n-1)$. They are usually described by dimensionless parameters $c_i' = c_i/c_u$, $h_i' = h_i/G$. The hardening parameters h_i' can be replaced by the more straightforward parameters $g_i' = G_i/G$ which are the dimensionless tangential shear stiffness after a specific surface is activated. A typical combination of c_i', g_i' for expression of a 'S' shaped curve of the shear modulus against the strain amplitude is chosen by Houlsby(1997) (Table 5.1).

5.1.2 Soil Properties

The properties of London clay from a site at Victoria Embankment, London, which was investigated by St John *et al.* (1992) , have been chosen to be used in this study.

The undrained shear strength c_u and shear modulus G increase linearly with the depth below the ground surface,

$$c_u = c_{u0}(1 + \rho)\, z = 60 + 60\, z \text{ kPa} \tag{5.1}$$

$$G = G_0\,(1 + \lambda)\, z = 30000 + 3000\, z \text{ kPa} \tag{5.2}$$

The ground water level is assumed at the depth of $z = 0$. The site investigation

Surface	c_i'	h_i'	g_i'
1	0.02	9	0.9
2	0.04	4.5	0.75
3	0.06	1.5	0.5
4	0.1	0.75	0.3
5	0.15	0.6	0.2
6	0.2	0.6	0.15
7	0.3	0.3	0.1
8	0.5	0.1	0.05
9	0.7	0.05	0.025

Table 5.1: Value of Constants in Nested Yield Surface Model

showed that K_0, the coefficient of earth pressure, varies from 1.0 to 1.5. Thus K_0 is assumed for simplicity to be 1.0 in this study. The self-weight of the clay is chosen as 20kN/m^3. Therefore the initial horizontal and vertical stresses are linearly increasing with depth.

With application of the chosen constants in Table 5.1, the nested yield surface model will represent a clay soil in which the stiffness reduces with increasing strain. For instance, for the soil at the depth of $z = -7.5\text{m}$, *i.e.* at the crown of the tunnel, the stiffness-strain relationship is shown in Figure 5.1.

5.1.3 Tunnelling Simulation

The ground is modelled by 2-D plane strain elements with the nested yield surface model described above. A block of ground of $30\text{m} \times 30\text{m}$ with unit thickness is analysed (Figure 5.2). The tunnelling is simulated by removing the elements in the area of the tunnel. Boundary conditions can be found in Figure 5.3. Lining of the tunnel is not considered, so that this study will give more conservative results than in a real case. The process is considered as an undrained process; long term consolidation effects are not taken into account.

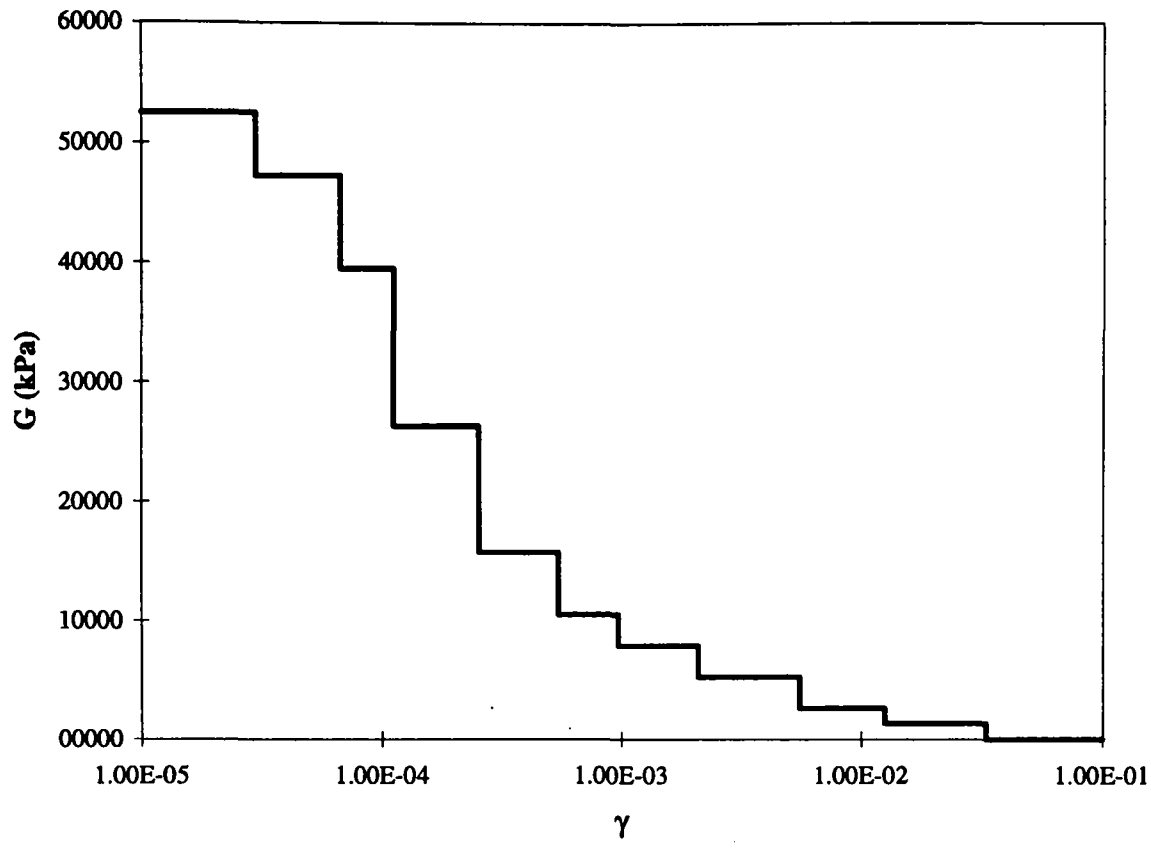
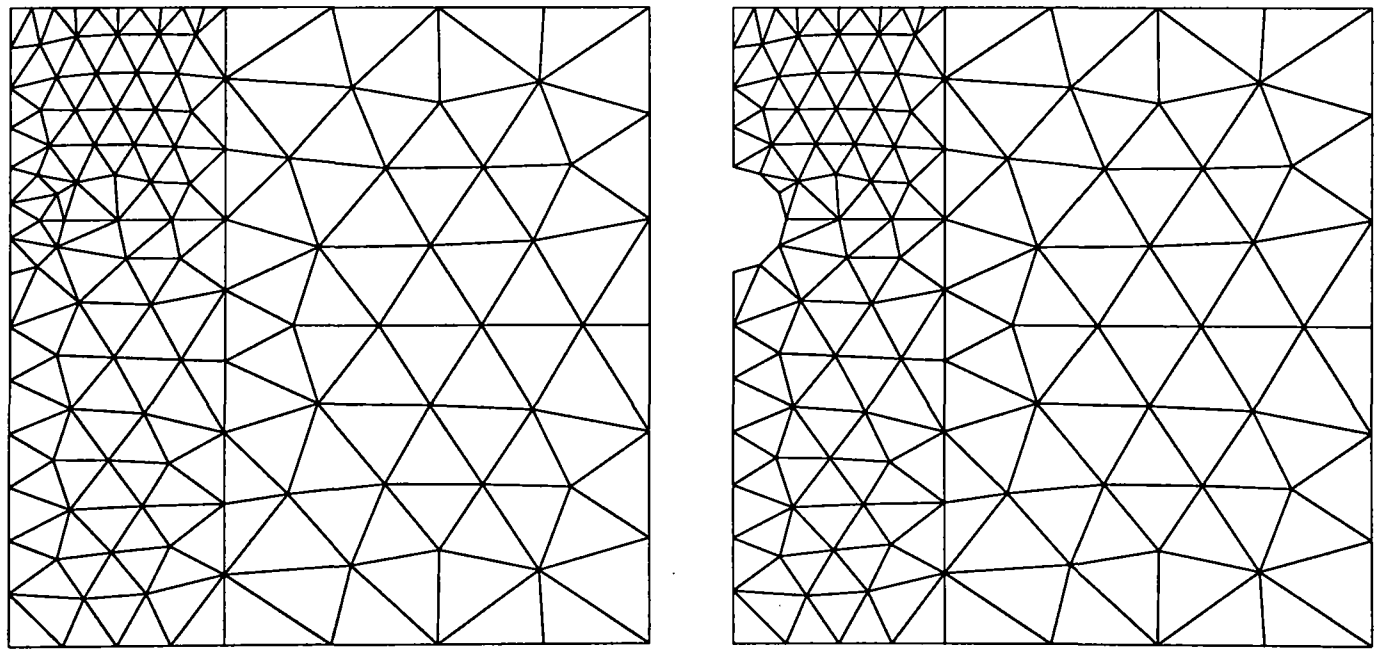


Figure 5.1: G-strain Curve for Soil at Tunnel Crown



(1) (2)

Figure 5.2: Finite Element Meshes before and after Excavation

5.2 Greenfield Trough by Finite Element Method

5.2.1 Settlement Trough

First, the greenfield settlement trough is calculated using the nested yield surface model with ten surfaces described above. The calculated settlement trough induced by the

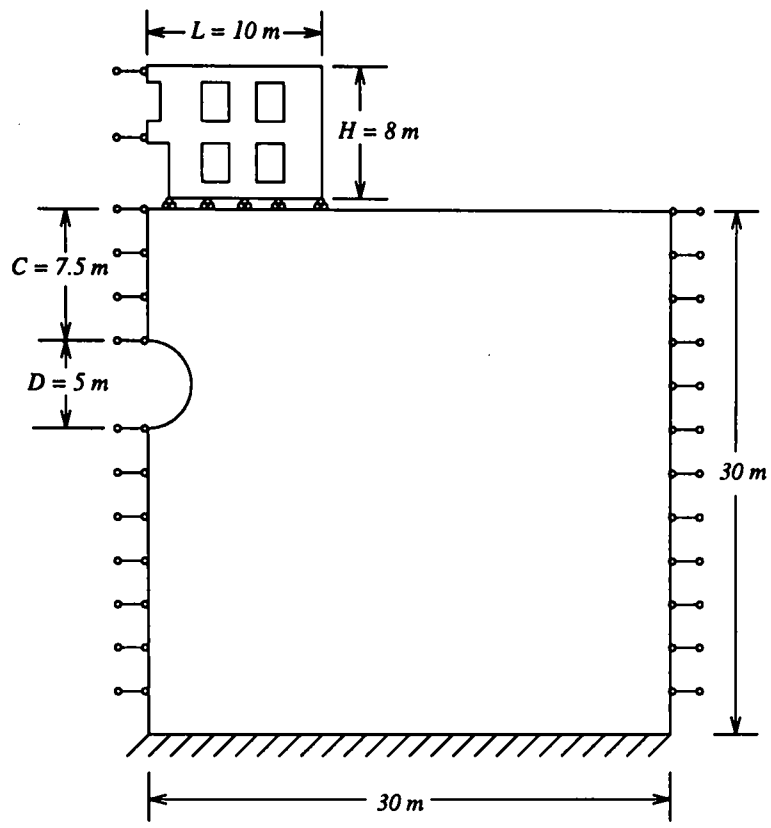


Figure 5.3: Boundary Conditions for the Ground and Facade

tunnelling scheme described in Chapter 4 is shown in Figure 5.4. Compared with $i = 5$m for the Gaussian curve, the finite element model gives a wider trough, the point of the inflexion being at the point $i = 7$m. The settlement is still appreciable remote from the tunnel. This may be due to the lack of vertical restraint at the side boundary.

The state number, *i.e.* the number of activated yield surfaces in the ground (Figure 5.5) shows the most highly non-linear area is located around the tunnel. At the ground surface, the non-linear area is limited to near the centreline of tunnelling, so that the most settlement happens within a narrow zone.

5.2.2 Masonry Facade on the Greenfield Trough

The calculated greenfield settlement trough is applied to the masonry facade which has the same layout and finite element mesh as in Chapter 4. The cracking pattern is shown in Figure 5.6-(1) and is very similar to the corresponding case in the previous chapter. The dominating cracking pattern is several crack bands along the stress arches, shown in Figure 5.6-(2).

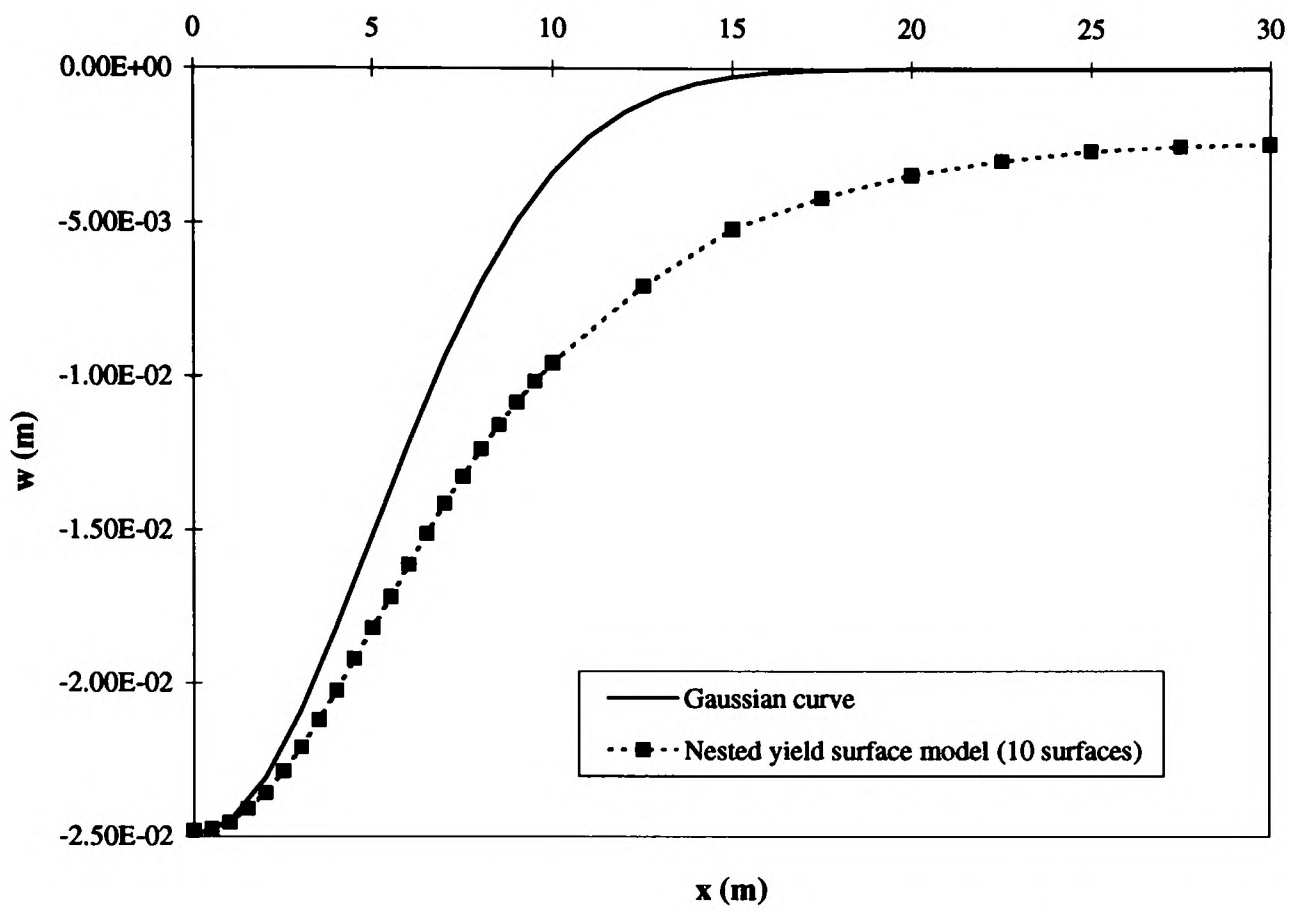


Figure 5.4: Ground Movements Predicted by Nested Model

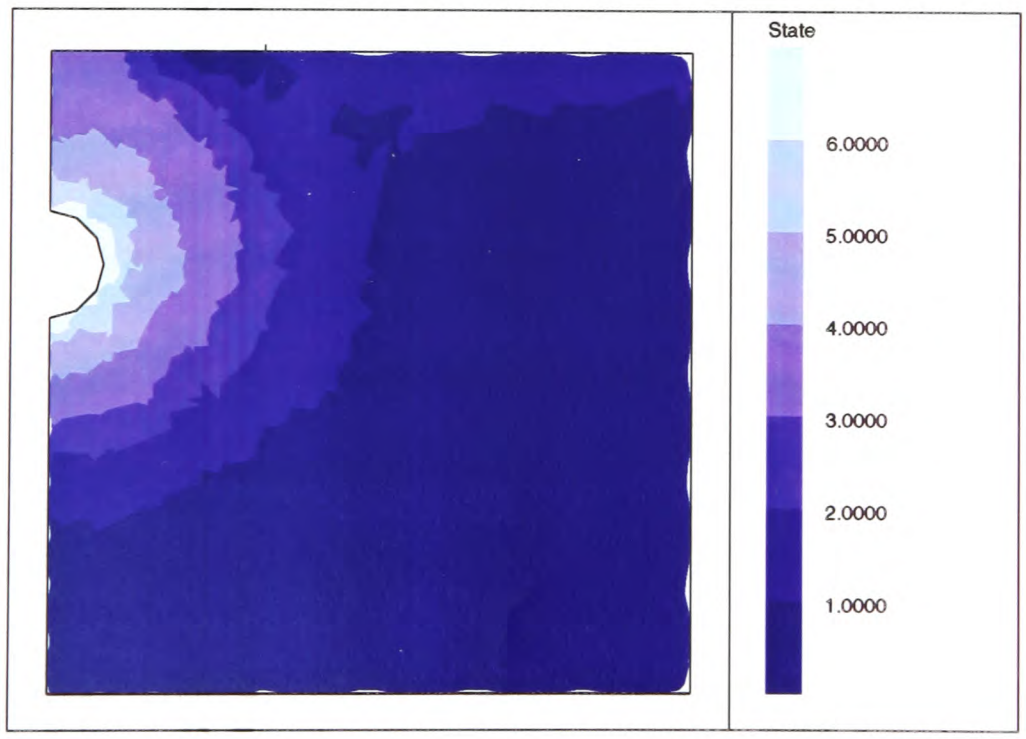
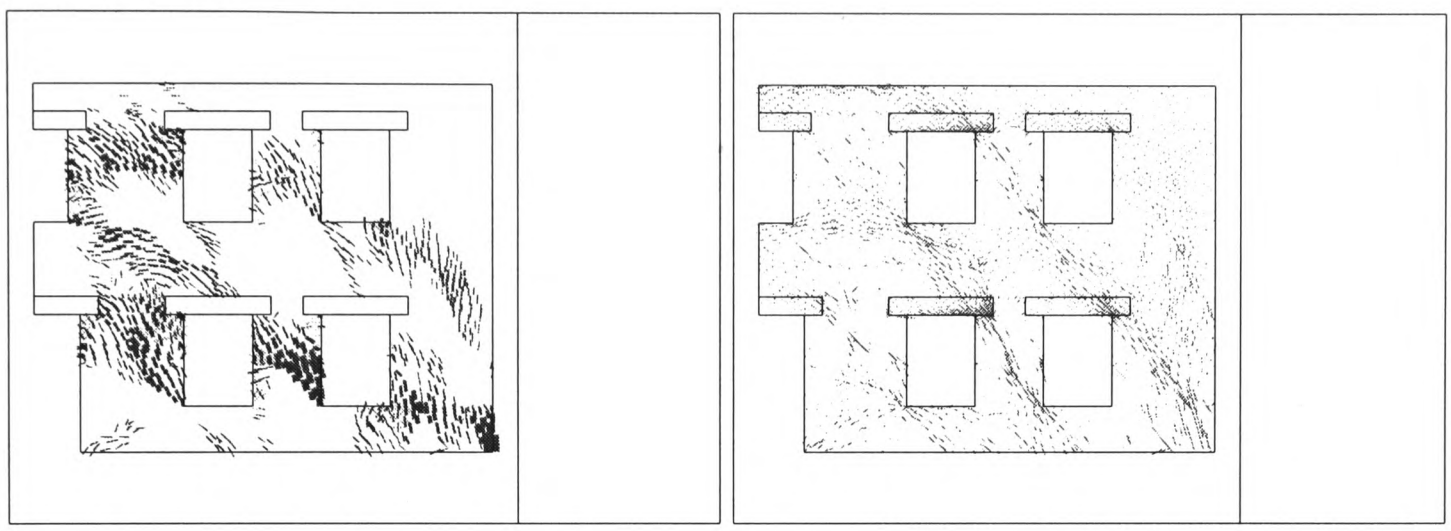


Figure 5.5: State Number in the Greenfield Ground

5.3 Combined Analysis

5.3.1 The Models

The ground model and facade model used before are used here for the combined analysis, both of them having unit thickness. Tie elements which connect the 2-D nodes in



(1) (2)

Figure 5.6: (1) Cracking Pattern and (2) Stress Trajectory for Greenfield Settlement

horizontal and vertical directions are installed between the facade and the ground to produce the combined system (Figure 5.3).

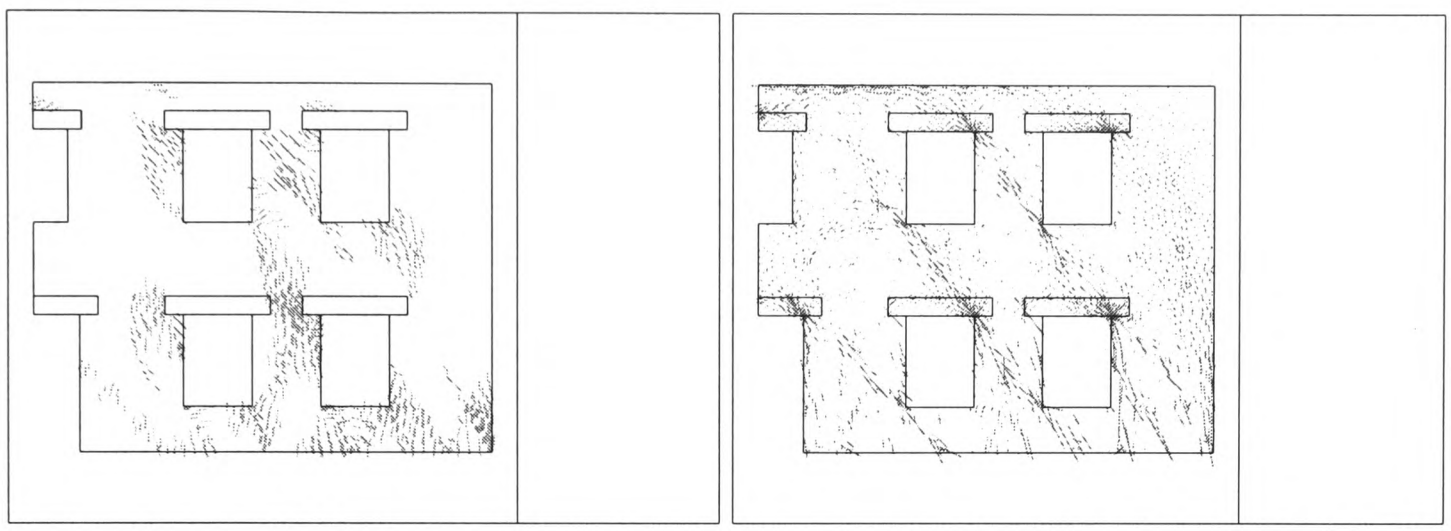
The self-weight of the soil is represented by the initial stresses in the ground. The self-weight of the building is applied first without the tunnel. Then the displacements in the ground and facade due to the self-weight are reset to zero before the excavation. The state variables are, however, kept unchanged. Thus the history of loading has been retained and all the displacements discussed in this chapter are due only to the excavation. Tunnelling without lining is simulated by removing the elements within the tunnel area. The process is assumed undrained.

5.3.2 Standard Facade on Standard Tunnel

Compared with the greenfield analysis, the combined analysis gives a different prediction of the settlement profiles and cracking damage in the facade.

Cracking Damage

The cracking pattern predicted by the combined analysis shows differences from the greenfield case (Figure 5.7). First, the combined analysis predicts less serious damage in the building, as expected. In addition, the cracking pattern is quite different to the greenfield analysis. On the first floor, the cracking pattern is similar to the greenfield case, with the cracks parallel to the stress arches. On the ground floor the dominant



(1) (2)

Figure 5.7: (1) Cracking Pattern and (2) Stress Trajectory in Facade, Combined Analysis

cracking pattern is vertical cracks which suggest the existence of tensile horizontal strain at the base. It should be noted that there are still some significant stress arches developing in the facade.

Ground Movements and State

The ground movements from the combined analysis are very different from the greenfield case too (Figure 5.8). The settlement beneath the building is much higher than in the greenfield. As the process is assumed to be undrained, the settlement outside the building is much less than in the greenfield; heave is even observed near the facade. The overall settlement trough underneath the facade is roughly divided into three flat steps. In contrast to the inward horizontal movement in the greenfield, the combined analysis shows outward horizontal movement beneath the building. This is because the building moves into the ground and pushes the soil away. The curve of the horizontal movement is also divided into three parts corresponding to the steps in the vertical settlement. The positions of the separating points coincide with the stress arches in the building. The distribution of the horizontal strain (Figure 5.9) at the base also shows that the horizontal movement is influenced by these arching forces which cause the soil to move out. Inside each of the arches, the ground is pulled out and has tensile strain. These horizontal tensile strains cause the vertical cracks in the facade. The arching effect will be discussed in detail later in this chapter.

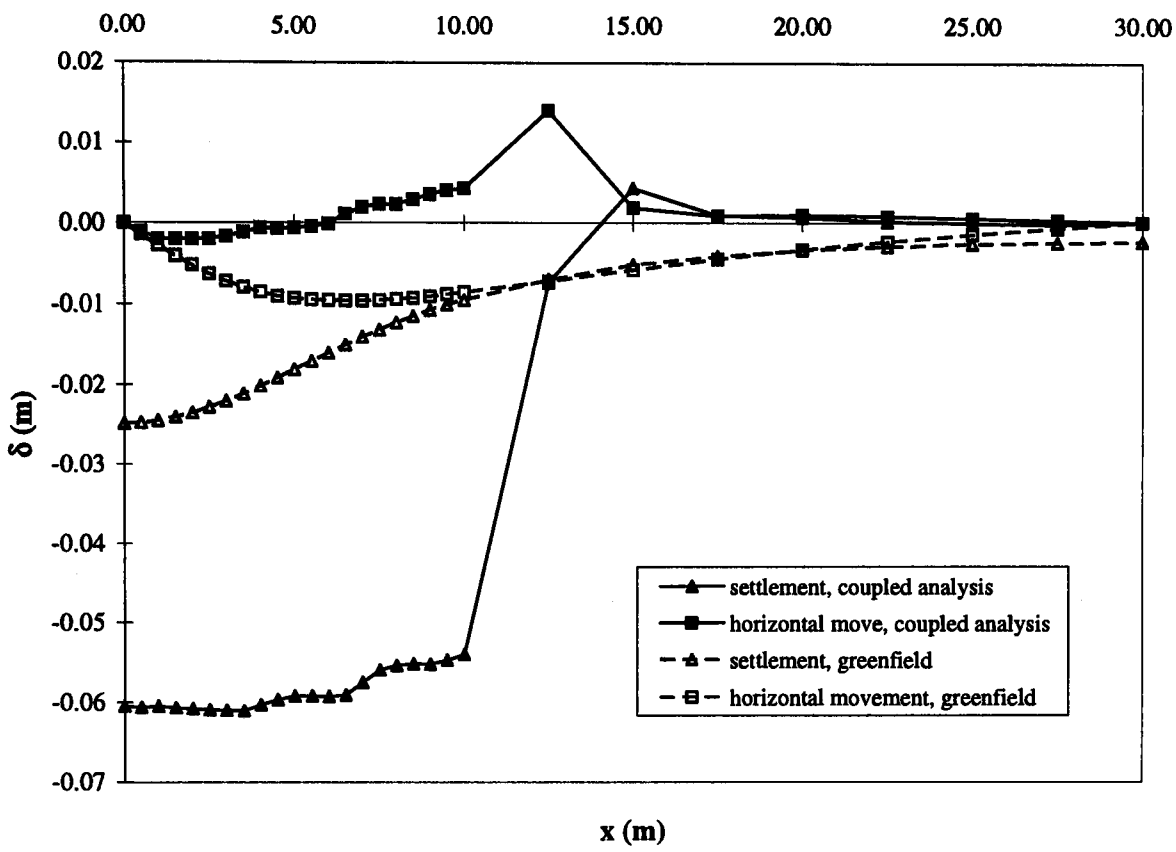


Figure 5.8: Ground Movements of Combined Analysis

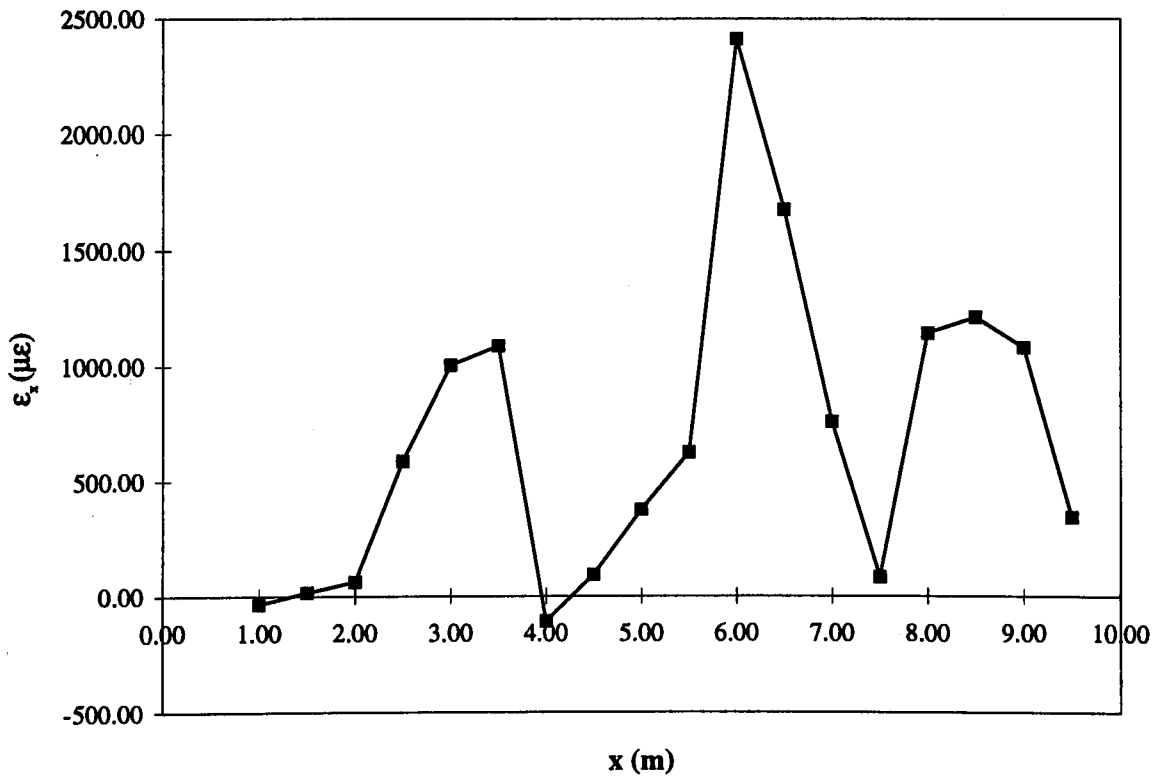
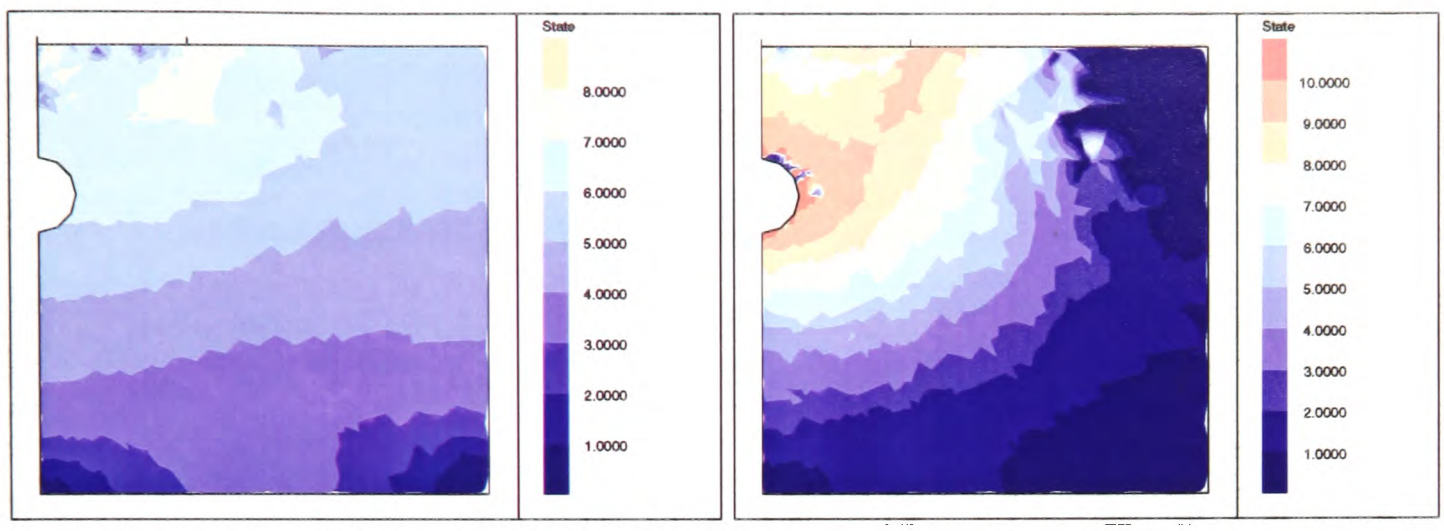


Figure 5.9: Horizontal Strain at the Base of Facade, Combined Analysis

What is happening in the ground can be seen through the number of activated yield surfaces. The states in the ground before and after the excavation are shown in Figure



(1) (2)

Figure 5.10: States in Ground (1) before and (2) after Excavation

5.10. It is seen that the ground under the building is initially in a non-linear state before excavation because of the self-weight of the building. After excavation, there are more yield surfaces activated around the tunnel than in the greenfield case. The other highly plastic area where 9 surfaces are activated is located around the corner of the facade.

These highly non-linear areas can explain the larger settlement in the combined analysis. Although the weight of the building has already been sustained by the ground before tunnelling commences, it has changed the state in the ground under the building. Because the strength or capacity of the soil depends on its state, its strength becomes lower than unloaded soil. Therefore, the soil enters a more highly non-linear state during tunnelling and has a lower stiffness and larger displacements than in the greenfield. Since there is a stress concentration around the corner of the facade, another highly non-linear area is likely to emerge there and develops towards the tunnel to form a possible failure surface. The stability of the tunnel needs therefore to be discussed.

5.3.3 Stability during Tunnelling

In Figure 5.10, two 9-surface areas are likely to join together. If the loading increases further, they may form a 10-surface band where the soil reaches the outermost surface, *i.e.* the von Mises failure surface. This failure band is actually a potential sliding surface. Thus the reduction of stability of tunnelling due to the weight of the facade becomes a concern.

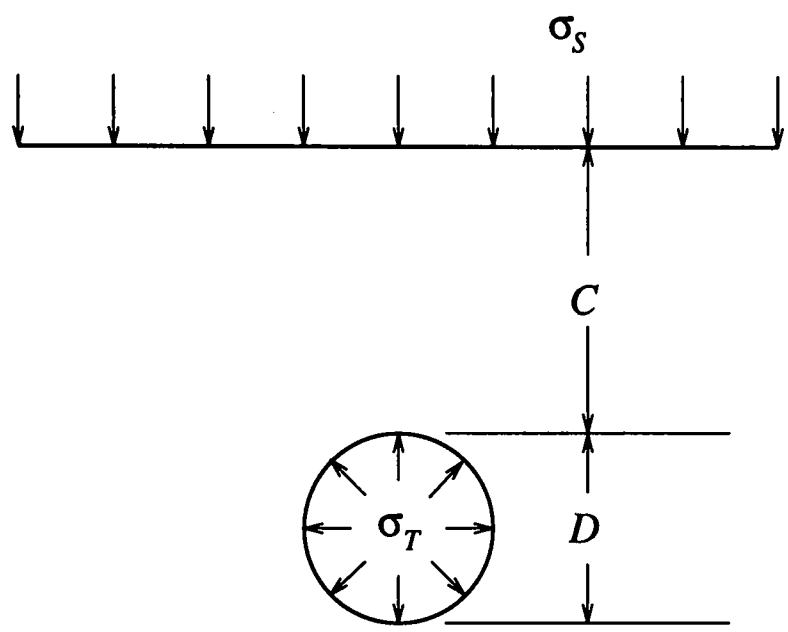


Figure 5.11: Definition of Stability Number

Davis *et al.* (1980) discussed the stability of shallow tunnels in cohesive material, using limit theorems and uniform perfectly elastic-plastic material models. The stability number

$$N = \frac{\sigma_s - \sigma_t + \gamma_s \left(C + \frac{D}{2}\right)}{c_u} \tag{5.3}$$

was used to indicate the stability of tunnelling as in Figure 5.11. They derived four failure mechanisms in the transverse plane depending on the tunnelling configurations (Figure 5.12). Then the upper and lower bound stability numbers for plane stain circular tunnels were derived (Figure 5.13).

The physical meaning of the stability number is that it is inversely related to a factor of safety. For soils whose properties are varying with depth, the stability number could be defined as

$$N = \frac{\sigma_s - \sigma_t + \gamma_s(C + \frac{D}{2})}{c_{u0}\left(1 + \rho(C + \frac{D}{2})\right)} \tag{5.4}$$

if it is assumed that the strength close to the springings of the tunnel dominates the calculation.

Now the stability number for the greenfield is

$$N_{ground} = \frac{\gamma_s(C + \frac{D}{2})}{c_{u0}\left(1 + \rho(C + \frac{D}{2})\right)} \tag{5.5}$$

Though the building weight is not spread over the whole ground surface, the nominal

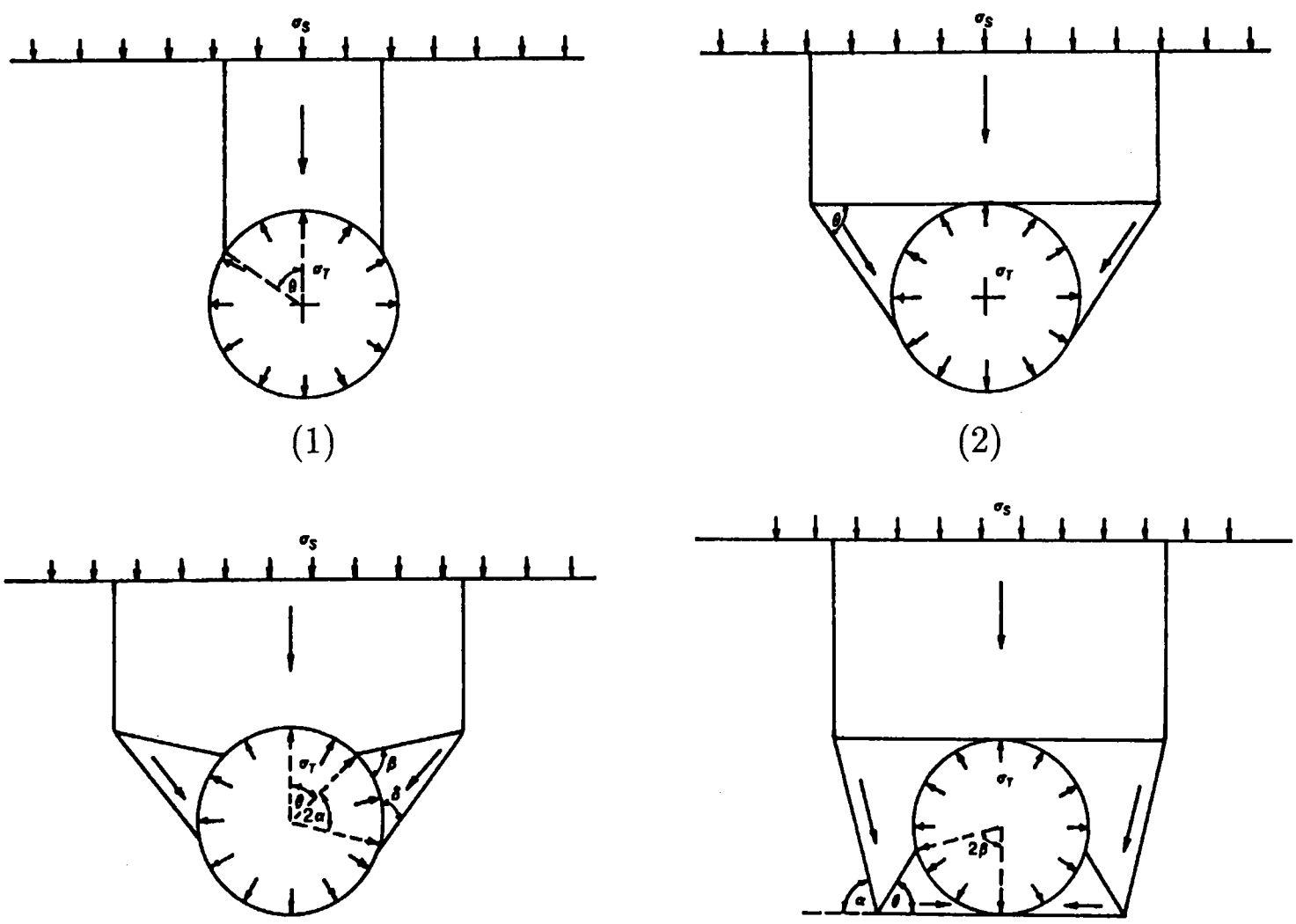


Figure 5.12: Mechanisms for Upper Bound Failure (Davis *et al.*, 1980)

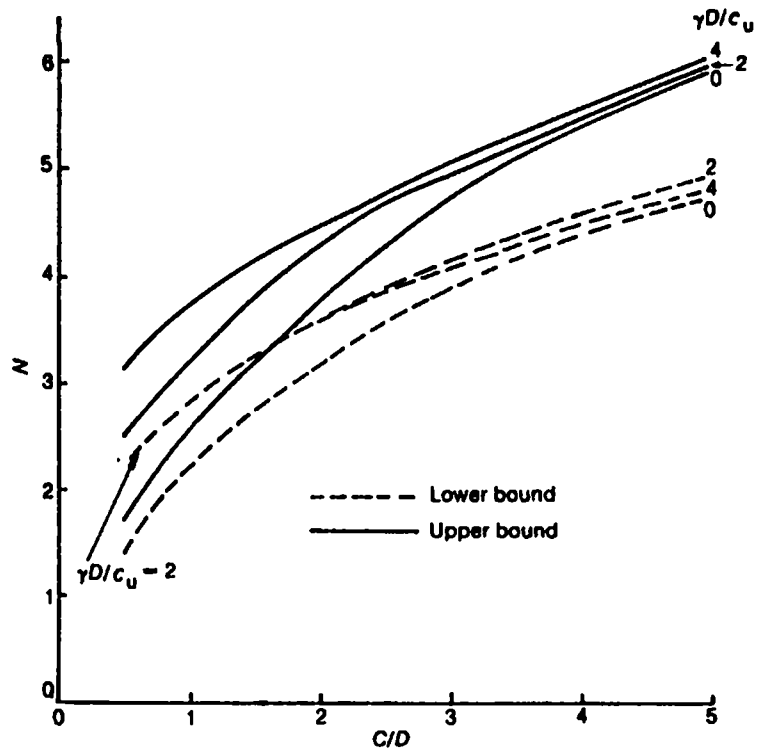


Figure 5.13: Upper and Lower Boundary Limits (Davis *et al.*, 1980)

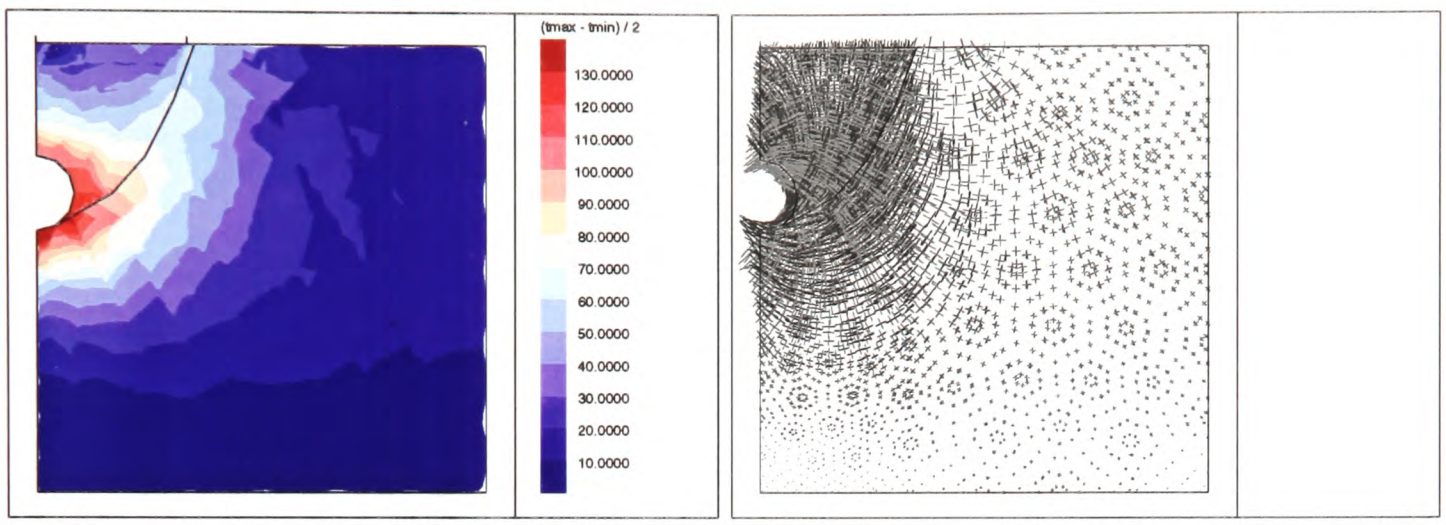
stability number used in this study is written as

$$N_{total} = \frac{\gamma_b t H + \gamma_s (C + \frac{D}{2})}{c_{u0}\left(1 + \rho(C + \frac{D}{2})\right)} \tag{5.6}$$

where H is the height of the facade, standing for the contribution from the building to the stability.

According to Davis *et al.* (1984), for the current tunnel with $\frac{C}{D} = 1.5$, the lower and upper limits for N are approximately 2.9 and 3.4. The stability number for the current greenfield case ($N_{ground} = 1.67$), is less than the lower limit and the tunnel is stable, while the stability number for the combined case ($N_{total} = 3.0$) is just above the lower limit which indicates the tunnel is near failure and may be expected to result in large settlement. The likely sliding plane here, which is a bit different from the mechanisms derived by Davis *et al.* (1984), is driven by both the tunnelling and the presence of the building, shown in Figure 5.14.

It should be pointed out that putting a 1m thick facade on a 1m thick block of the ground will overestimate the stresses in the ground. In addition the long-term consolidation after the building was built would be expected to reduce the stresses in the ground at the ends of the building. However this analysis gives the trend of the



(1) (2)

Figure 5.14: (1) Shear Stresses and (2) Maximum Shear Stress Plane in Ground, Combined Analysis

ground movements and shows the mechanism of the interaction between the building and ground due to tunnelling.

5.4 Parametric Study

As noticed before, the interaction between the building and the ground plays a key role in the ground settlement and the damage to the building. In addition to the stiffness and weight of the building, there are several other factors involved in the process. It is necessary to carry out a parametric study of these factors.

5.4.1 Selection and Normalisation of Parameters

It is obvious that the stiffness, size and weight of the building, the size and position of the tunnel, and the stiffness and strength of the soil will affect the interaction between the building and the ground. In addition to these explicit parameters, there are also some other implicit factors, such as the layout within the facade and the constants used to define the nested yield surface model and masonry model. These implicit factors will be kept unchanged here. The rate of change of the ground strength and stiffness with depth are also unchanged. The parameters with which we are concerned and their dimensions are summarised in Table 5.2.

From these nine parameters the following six normalised parameters can be derived.

Parameter	δ	L	Et	$\gamma_b t$	C	D	G_0	γ_s	c_{u0}
Dimension	L	L	F/L/L	F/L/L	L	L	F/L/L	F/L/L/L	F/L/L

Table 5.2: Concerned Parameters of Interaction

There are listed here:

$$\delta' = \frac{\delta}{D}\frac{G_0}{\gamma_s D},$$

$$L' = \frac{L}{D} \qquad (Et)' = \frac{Et}{G_0 D}, \qquad (\gamma_b t)' = \frac{\gamma_b t}{c_{u0}}$$

$$C' = \frac{C}{D}, \qquad \gamma_s{}' = \frac{\gamma_s\left(C+\frac{D}{2}\right)}{c_{u0}+\rho\left(C+\frac{D}{2}\right)}.$$

The parameter $\gamma_s{}'$ is actually the stability number of the tunnel in the greenfield.

The geometric parameters L' and C' are not changed in this study, therefore the dimensionless settlement will be a function as

$$\delta' = f\left((Et)', (\gamma_b t)', (\gamma_s)'\right) \tag{5.7}$$

The parametric study will investigate the effects of these three factors.

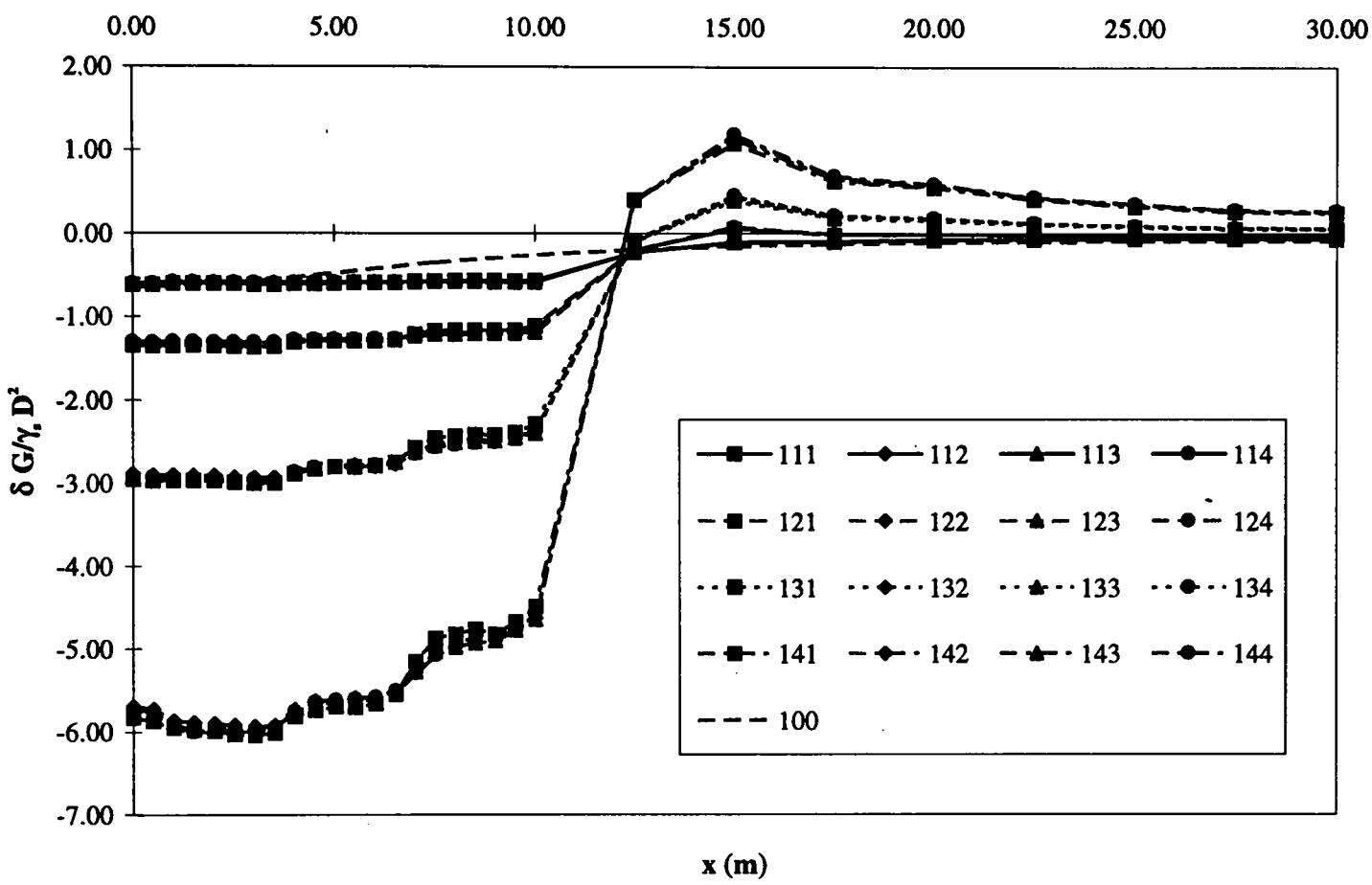
5.4.2 Test Problems

Test problems are summarised in Table 5.3. The number of a test consists of three digits. The first digit (1,2,3) refers to the three different values of γ_s', and second (1,2,3,4) and third (1,2,3,4) digits stand for the four different values of $(\gamma_b t)'$ and $(Et)'$ respectively. Tests 100, 200, 300 are greenfield analyses whilst other problems are combined analyses. According to this numbering method, the previous greenfield and combined runs are 200 and 233.

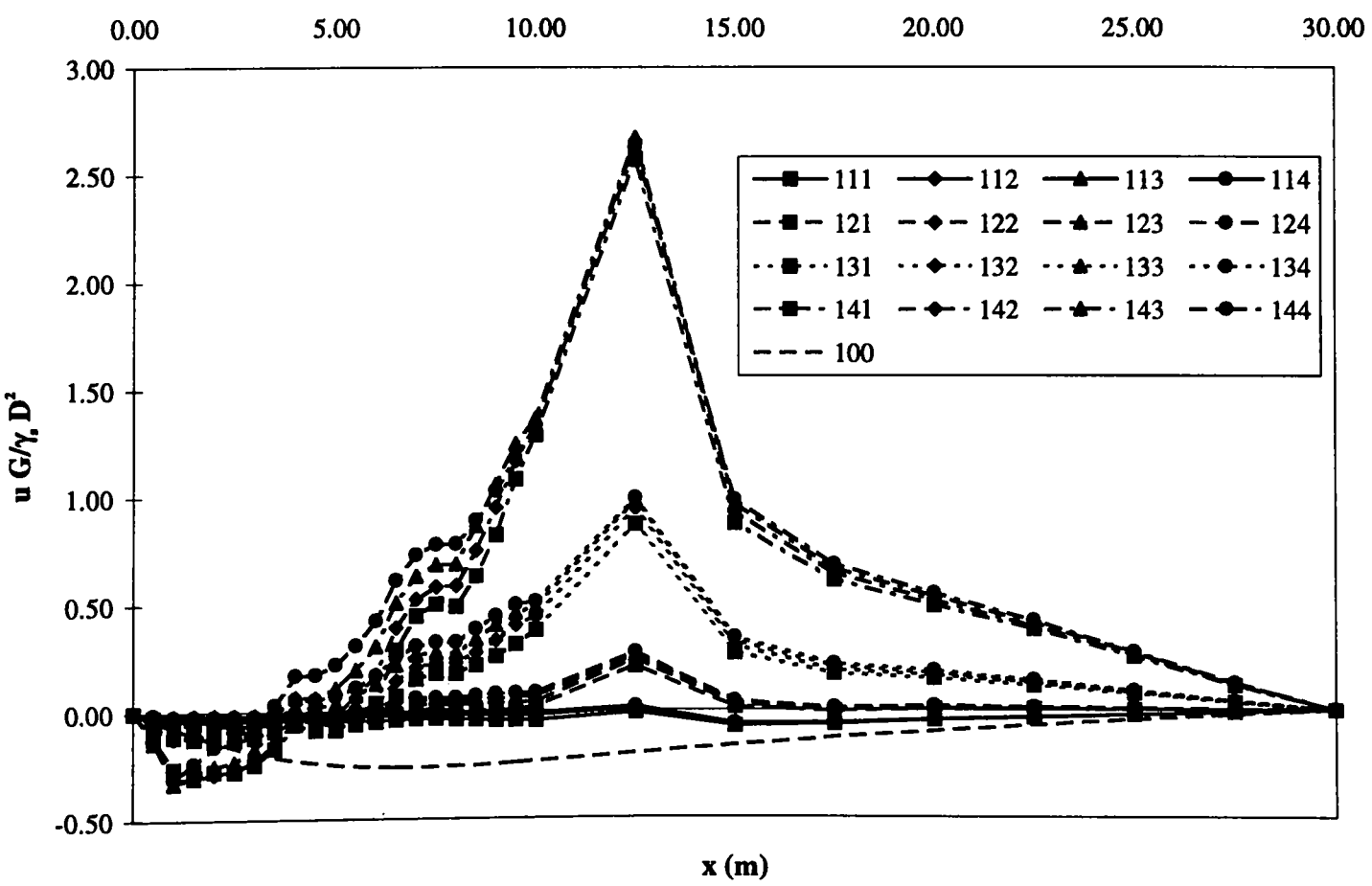
All the settlement troughs of these test problems are shown in Figures 5.15, 5.16 and 5.17. The effects of all parameters are discussed below.

No.	γ_s	$(\gamma_s)'$	$\gamma_b t$	$(\gamma_b t)'$	Et	(Et)'	N_{grnd}	N_{total}	δ_{max}	δ_i
100	10	0.8333333	0	0	0	0	0.8333333	0.8333333	0.642	0.378
111	10	0.8333333	3	0.05	1.50E+06	10	0.8333333	1.0333333	0.616	0.584
112	10	0.8333333	3	0.05	5.00E+06	33.333333	0.8333333	1.0333333	0.601	0.585
113	10	0.8333333	3	0.05	1.00E+07	66.666667	0.8333333	1.0333333	0.601	0.586
114	10	0.8333333	3	0.05	1.50E+07	100	0.8333333	1.0333333	0.602	0.583
121	10	0.8333333	10	0.1666667	1.50E+06	10	0.8333333	1.5	1.36	1.21
122	10	0.8333333	10	0.1666667	5.00E+06	33.333333	0.8333333	1.5	1.31	1.22
123	10	0.8333333	10	0.1666667	1.00E+07	66.666667	0.8333333	1.5	1.31	1.23
124	10	0.8333333	10	0.1666667	1.50E+07	100	0.8333333	1.5	1.31	1.23
131	10	0.8333333	20	0.3333333	1.50E+06	10	0.8333333	2.1666667	3	2.57
132	10	0.8333333	20	0.3333333	5.00E+06	33.333333	0.8333333	2.1666667	2.94	2.63
133	10	0.8333333	20	0.3333333	1.00E+07	66.666667	0.8333333	2.1666667	2.95	2.63
134	10	0.8333333	20	0.3333333	1.50E+07	100	0.8333333	2.1666667	2.97	2.64
141	10	0.8333333	30	0.5	1.50E+06	10	0.8333333	2.8333333	6.04	5.16
142	10	0.8333333	30	0.5	5.00E+06	33.333333	0.8333333	2.8333333	5.94	5.28
143	10	0.8333333	30	0.5	1.00E+07	66.666667	0.8333333	2.8333333	5.97	5.27
144	10	0.8333333	30	0.5	1.50E+07	100	0.8333333	2.8333333	6.01	5.29
200	20	1.6666667	0	0	0	0	1.6666667	1.6666667	1.49	0.848
201	20	1.6666667	0	0	1.50E+06	10	1.6666667	1.6666667	1.27	0.808
202	20	1.6666667	0	0	5.00E+06	33.333333	1.6666667	1.6666667	1.17	0.809
203	20	1.6666667	0	0	1.00E+07	66.666667	1.6666667	1.6666667	1.09	0.815
204	20	1.6666667	0	0	1.50E+07	100	1.6666667	1.6666667	1.04	0.82
211	20	1.6666667	3	0.05	1.50E+06	10	1.6666667	1.8666667	1.33	1.08
212	20	1.6666667	3	0.05	5.00E+06	33.333333	1.6666667	1.8666667	1.24	1.09
213	20	1.6666667	3	0.05	1.00E+07	66.666667	1.6666667	1.8666667	1.19	1.09
214	20	1.6666667	3	0.05	1.50E+07	100	1.6666667	1.8666667	1.16	1.09
221	20	1.6666667	10	0.1666667	1.50E+06	10	1.6666667	2.3333333	1.94	1.78
222	20	1.6666667	10	0.1666667	5.00E+06	33.333333	1.6666667	2.3333333	1.92	1.81
223	20	1.6666667	10	0.1666667	1.00E+07	66.666667	1.6666667	2.3333333	1.84	1.77
224	20	1.6666667	10	0.1666667	1.50E+07	100	1.6666667	2.3333333	1.83	1.78
231	20	1.6666667	20	0.3333333	1.50E+06	10	1.6666667	3	3.84	3.42
232	20	1.6666667	20	0.3333333	5.00E+06	33.333333	1.6666667	3	3.72	3.49
233	20	1.6666667	20	0.3333333	1.00E+07	66.666667	1.6666667	3	3.67	3.45
234	20	1.6666667	20	0.3333333	1.50E+07	100	1.6666667	3	3.65	3.46
241	20	1.6666667	30	0.5	1.50E+06	10	1.6666667	3.6666667	9.25	8.1
242	20	1.6666667	30	0.5	5.00E+06	33.333333	1.6666667	3.6666667	8.67	8.05
243	20	1.6666667	30	0.5	1.00E+07	66.666667	1.6666667	3.6666667	8.42	7.91
244	20	1.6666667	30	0.5	1.50E+07	100	1.6666667	3.6666667	8.4	7.88
300	30	2.5	0	0	0	0	2.5	2.5	3.63	1.82
311	30	2.5	3	0.05	1.50E+06	10	2.5	2.7	2.9	2.02
312	30	2.5	3	0.05	5.00E+06	33.333333	2.5	2.7	2.51	2.01
313	30	2.5	3	0.05	1.00E+07	66.666667	2.5	2.7	2.32	2
314	30	2.5	3	0.05	1.50E+07	100	2.5	2.7	2.24	1.99
321	30	2.5	10	0.1666667	1.50E+06	10	2.5	3.1666667	3.99	3.5
322	30	2.5	10	0.1666667	5.00E+06	33.333333	2.5	3.1666667	3.64	3.43
323	30	2.5	10	0.1666667	1.00E+07	66.666667	2.5	3.1666667	3.54	3.39
324	30	2.5	10	0.1666667	1.50E+07	100	2.5	3.1666667	3.5	3.37
331	30	2.5	20	0.3333333	1.50E+06	10	2.5	3.8333333	12.6	11.5
332	30	2.5	20	0.3333333	5.00E+06	33.333333	2.5	3.8333333	11.7	11.2
333	30	2.5	20	0.3333333	1.00E+07	66.666667	2.5	3.8333333	11.4	11
334	30	2.5	20	0.3333333	1.50E+07	100	2.5	3.8333333	11.3	11.1
341	30	2.5	30	0.5	1.50E+06	10	2.5	4.5	fail	fail
342	30	2.5	30	0.5	5.00E+06	33.333333	2.5	4.5	fail	fail
343	30	2.5	30	0.5	1.00E+07	66.666667	2.5	4.5	fail	fail
344	30	2.5	30	0.5	1.50E+07	100	2.5	4.5	fail	fail

Table 5.3: Summary of the Test Problems

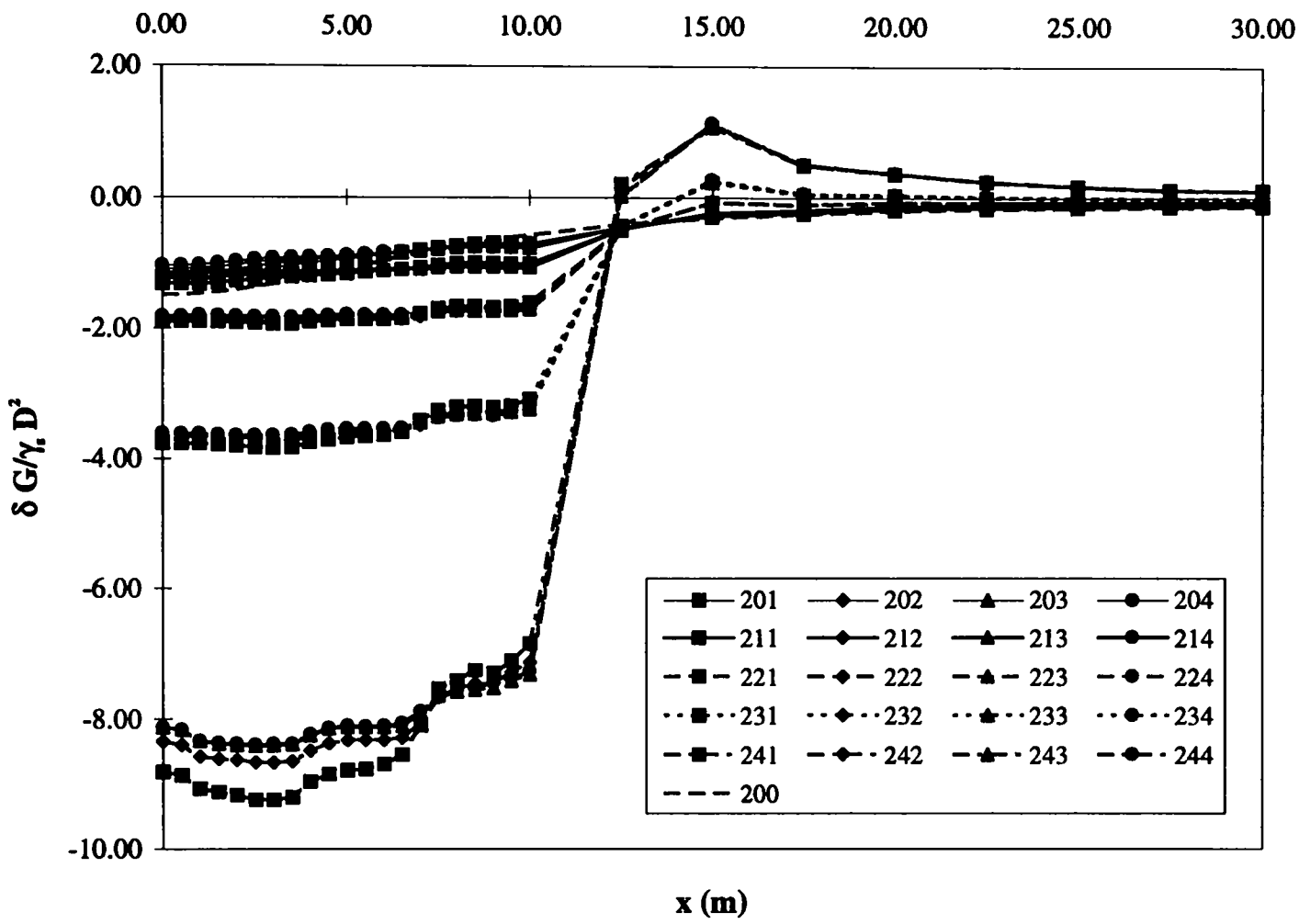


(1) Settlements

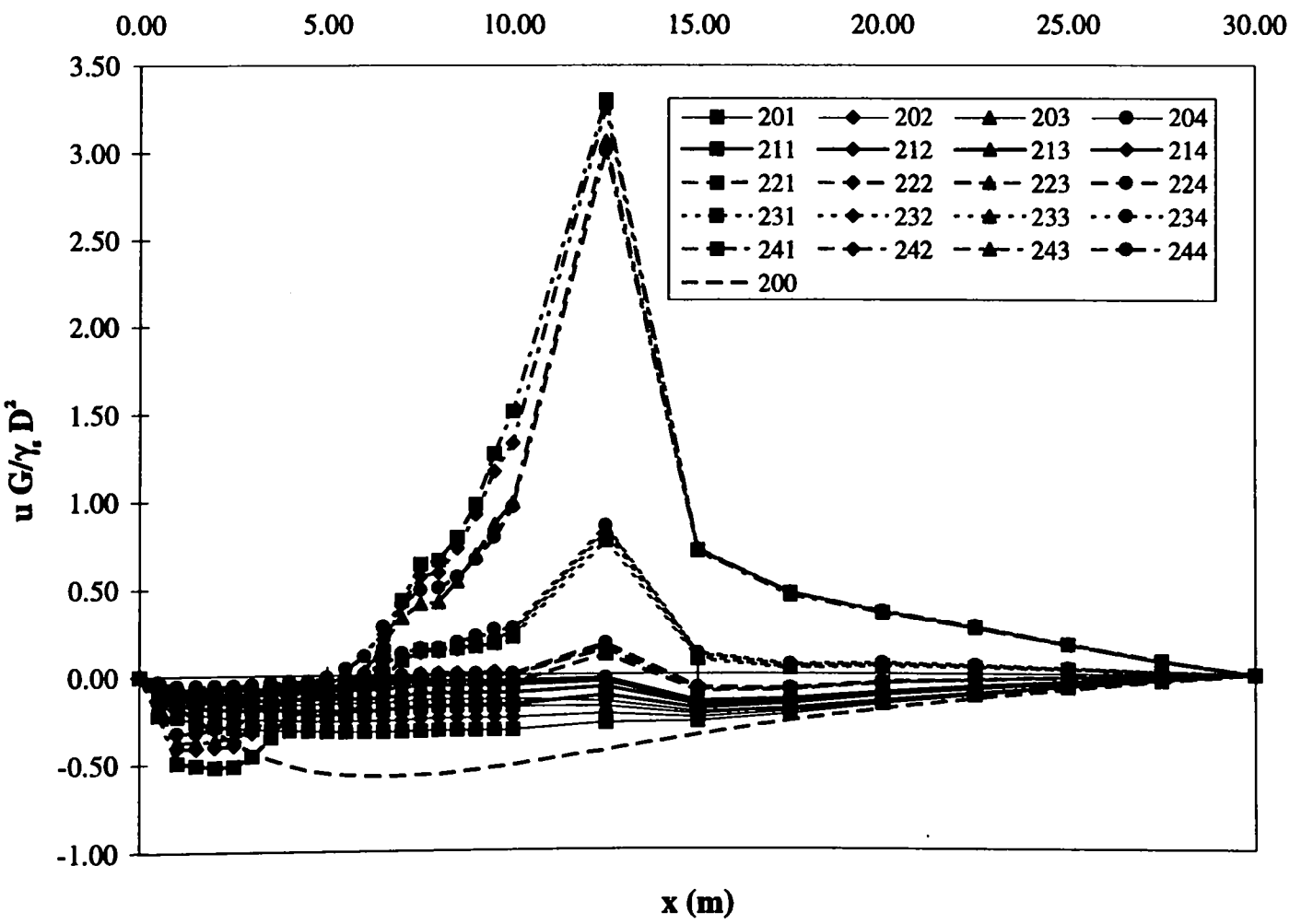


(2) Horizontal Movements

Figure 5.15: Ground Movements, γ'_s=0.833

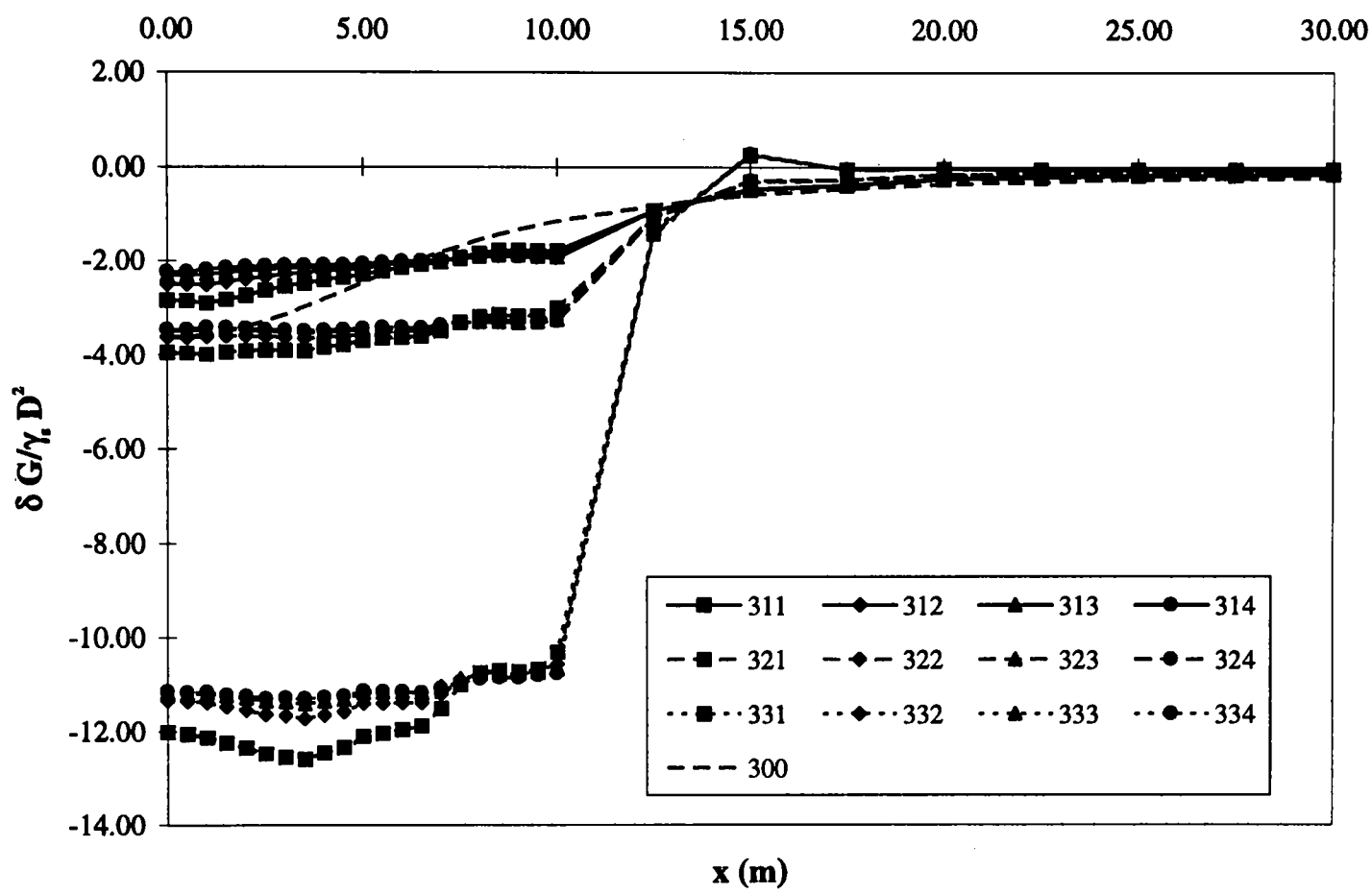


(1) Settlements

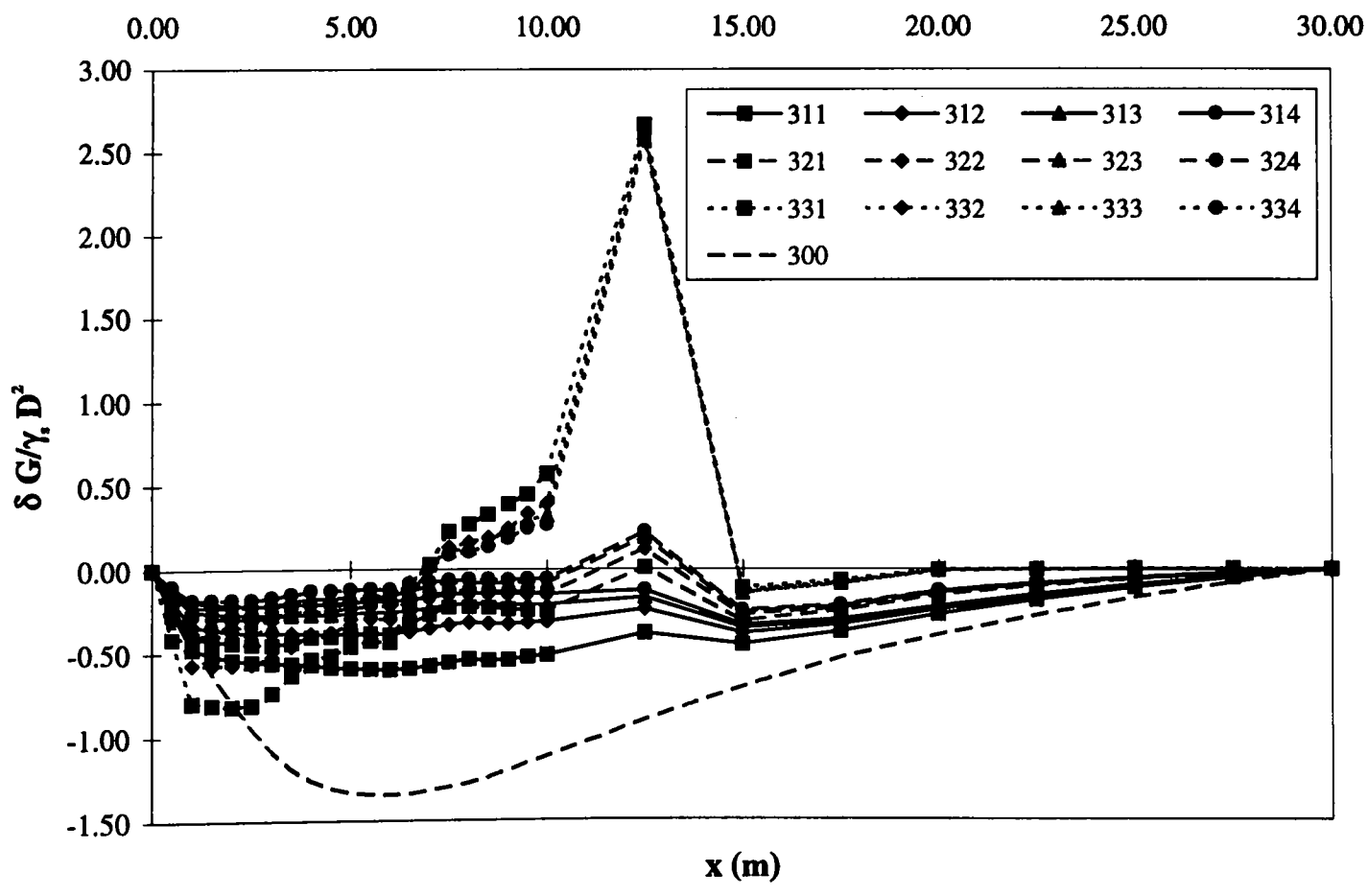


(2) Horizontal Movements

Figure 5.16: Ground Movements,γ_s'=1.667



(1) Settlements



(2) Horizontal Movements

Figure 5.17: Ground Movements,γ'_s=2.50

5.4.3 Discussion of Results

Arching Effects

All the tests exhibit three major stress arches in the facade which are roughly located at the same places as previous Run 233, around $x = 4.5, 7.0, 10.0$m. Some typical arches can be found in Figure 5.20. The middle arch is about at the point of inflexion and the outermost one at the end of the facade. The presence of the arches can be explained by the fact that when the ground moves during excavation, it tends to form a Gaussian curve settlement. This tendency causes the redistribution of the masonry material in the facade and forms several arches.

However the effects of these arches are not only limited to within the facade. They play an important role in the interaction between the building and the ground (Figure 5.18). First the arching effect is the mechanism of the influence of the masonry building on the settlement trough. Due to the presence of these arches, the pressure on the ground from the building is also redistributed. The pressure around the arches will increase. Since the weight of the building has been already sustained by the soil before excavation, the net extra load between building and the ground should be zero. Thus the pressure on the ground not under the arches will be reduced. In consequence, the soil under the arches will settle more than that not under under the arches. This process leads to a flatter settlement trough. The arching process is consistent with cracking along the arches as seen before.

Second, the horizontal component of the arching forces will push the soil outwards and cause horizontal tensile strain and vertical cracks in the facade.

In addition, the large force will cause a stress concentration near the arch supports in the ground. This may cause the local failure of the soil close to the foundation.

The effect of $(\gamma_b t)'$

From Figures 5.15, 5.16 and 5.17 it is clear that the weight of the building has the most significant effect on the overall settlement trough under the facade.

A smaller $(\gamma_b t)'$, *i.e.* a lighter building will reduce the settlement trough beneath

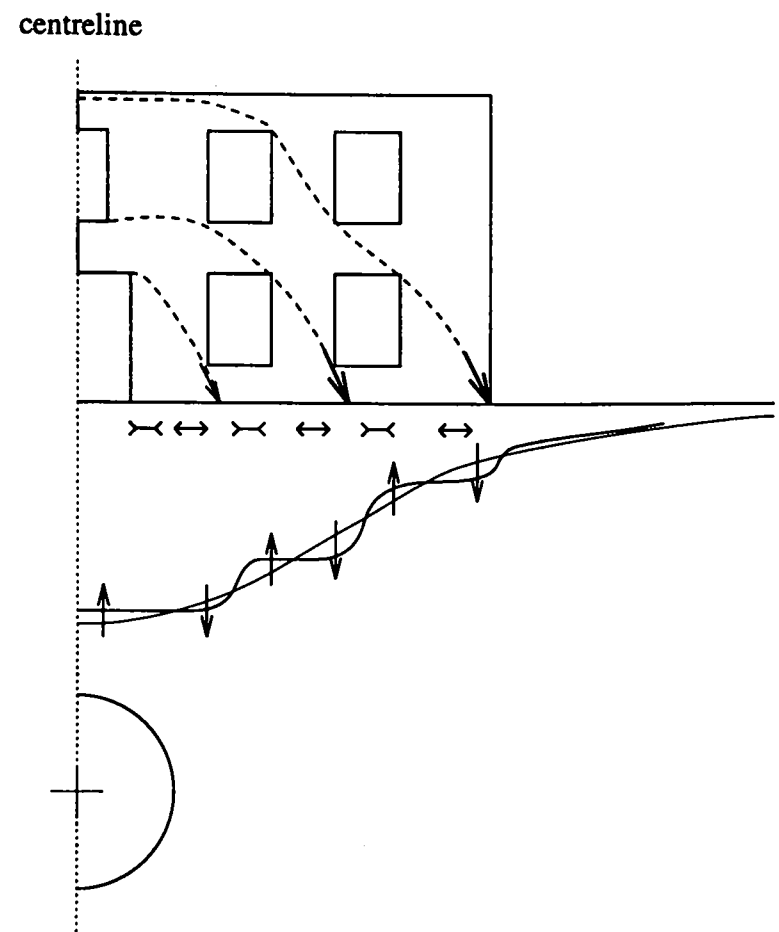


Figure 5.18: Arching Effect and Ground Movements

the facade. When $(\gamma_b t)'$ increases, it results in a more non-linear state in the ground which produces large settlements. Also, the heavy building will cause larger arching forces when its weight is redistributed. Both aspects give larger settlement, and even tend to cause the failure. This can be seen in Figure 5.19 which includes the states in the ground of Runs 213, 223, 233 and 243 with the different values of $(\gamma_b t)'$.

As far as the facade is concerned, different weights generate different shapes of the arches (Figure 5.20). In Run 213, the middle and outermost arches are rather lower than in other runs with larger values of $(\gamma_b t)'$. The low arches confine the cracked area mainly within the ground floor and leave the upper part of the facade intact.

As the building becomes heavier, the strong low arch will disappear since it could not support the material above it. The cracked area will expand. In addition, the horizontal components of the arching forces will increase, and the consequent vertical cracks which emerge become more critical. Figure 5.21 shows cracking patterns of Runs 213 to 243 demonstrating such a process.

As a comparison, a limit condition of a weightless building is also analysed (Runs

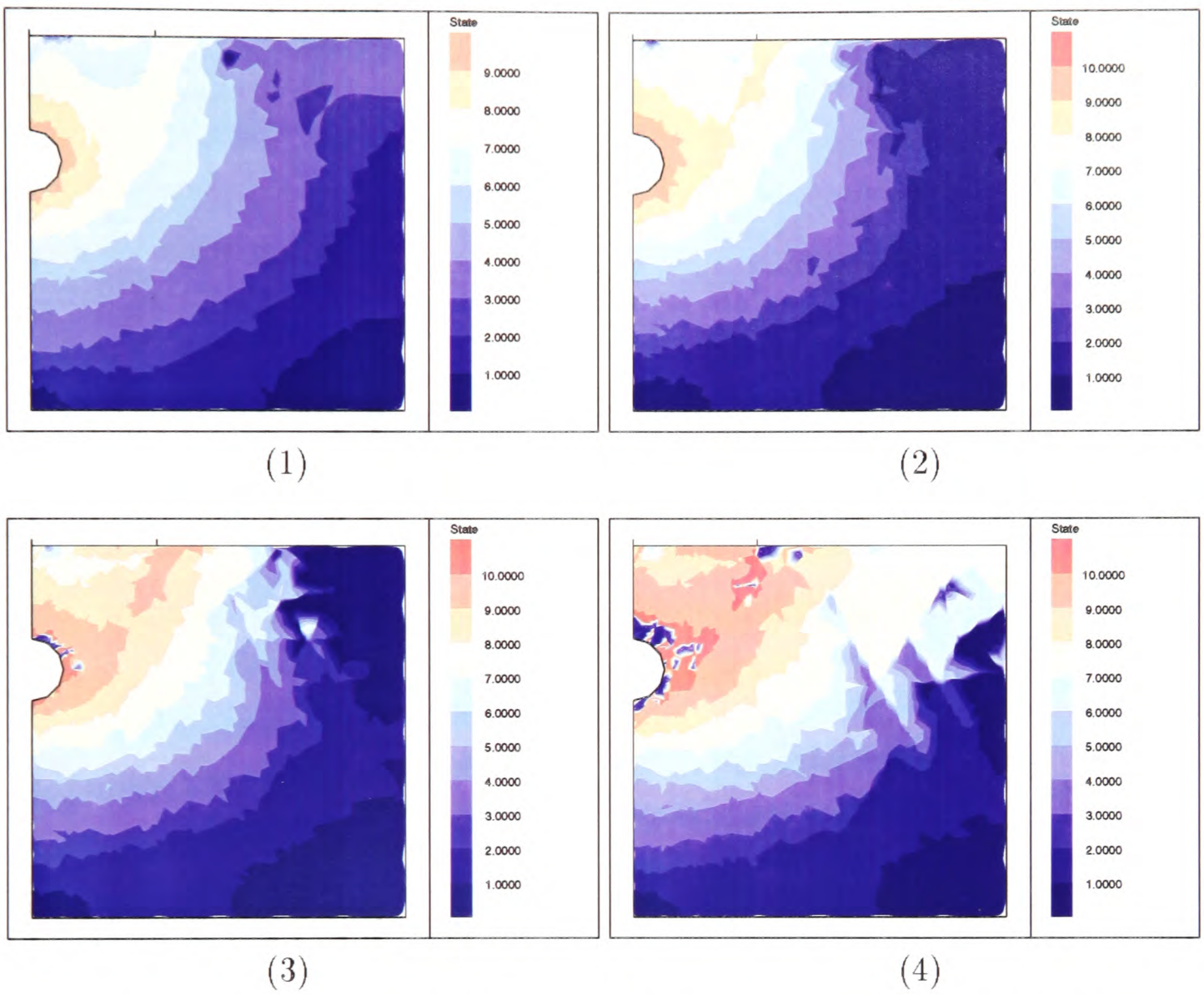
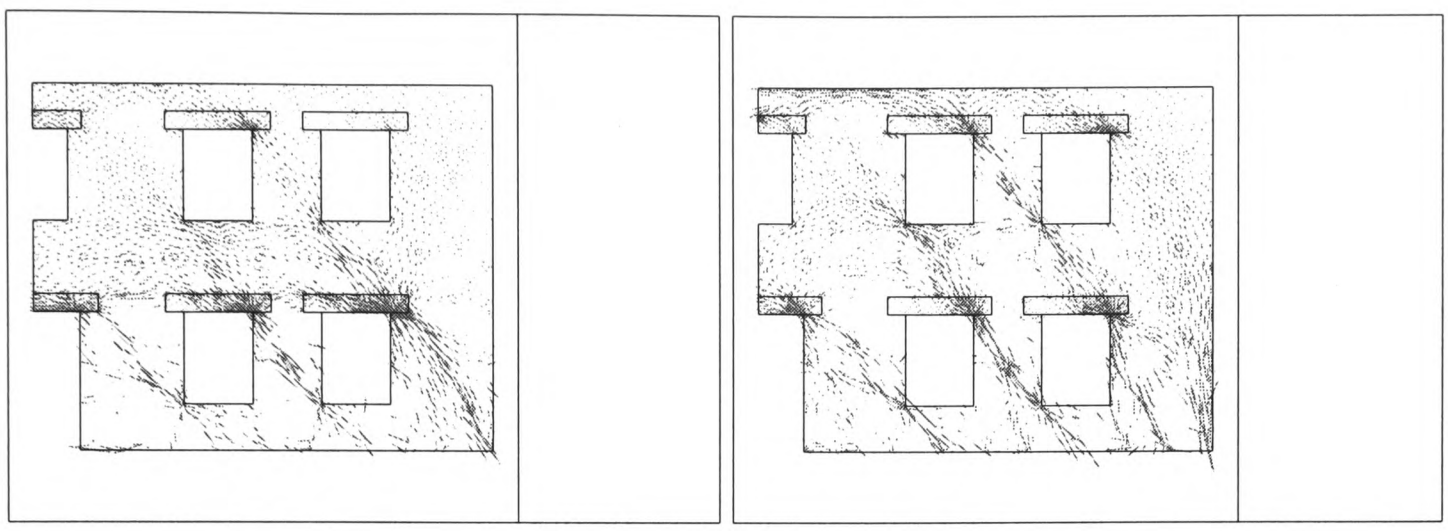


Figure 5.19: Comparison of States in Ground Different $(\gamma_b t)'$, Runs (1) 213, (2) 223, (3) 233, (4) 243

201, 202, 203 and 204 for different stiffness values). Figure 5.22 shows the cracking patterns and stress trajectories of a typical weightless case Run 203. Since a weightless facade cannot form strong stress arches, the settlement trough beneath it nearly follows the greenfield profile. It should be pointed out that in reality separation between the building and the ground surface may occur under an extremely light building. Since the models used in this study are not able to simulate such separation, the analysis may result in unrealistically large horizontal cracks at the bottom of the facade.

The effect of γ_s'

It is obvious that increase of γ_s' will lead to an increase of the stability number and therefore cause larger settlement, δ', when the other parameters remain unchanged.



(1) (2)

(3) (4)

Figure 5.20: Comparison of Arches in Facades for Different $(\gamma_b t)'$, Runs (1) 213, (2) 223, (3) 233, (4) 243

This agrees with the change of the state in the ground. Compared with Run 223 with $\gamma_s' = 1.667$, Run 123 with $\gamma_s' = 0.833$ shows no serious failure occurring in the ground after excavation, while Run 323 with $\gamma_s' = 2.5$ exhibits a large failure area, with a sliding failure mechanism almost forming (Figure 5.23). Therefore the tests of larger γ_s' show more serious damage induced by the vertical settlements, as also seen in the cracking patterns in Figure 5.23.

On the other hand, the horizontal movements displayed in Figures 5.15, 5.16 and 5.17 exhibit a general trend that an increase of γ_s' reduces the outward horizontal movement beneath the facade. It can be explained by the fact that a larger γ_s' imposes larger horizontal initial stresses which will hold the ground and the building together, and support the arches formed in the facade.

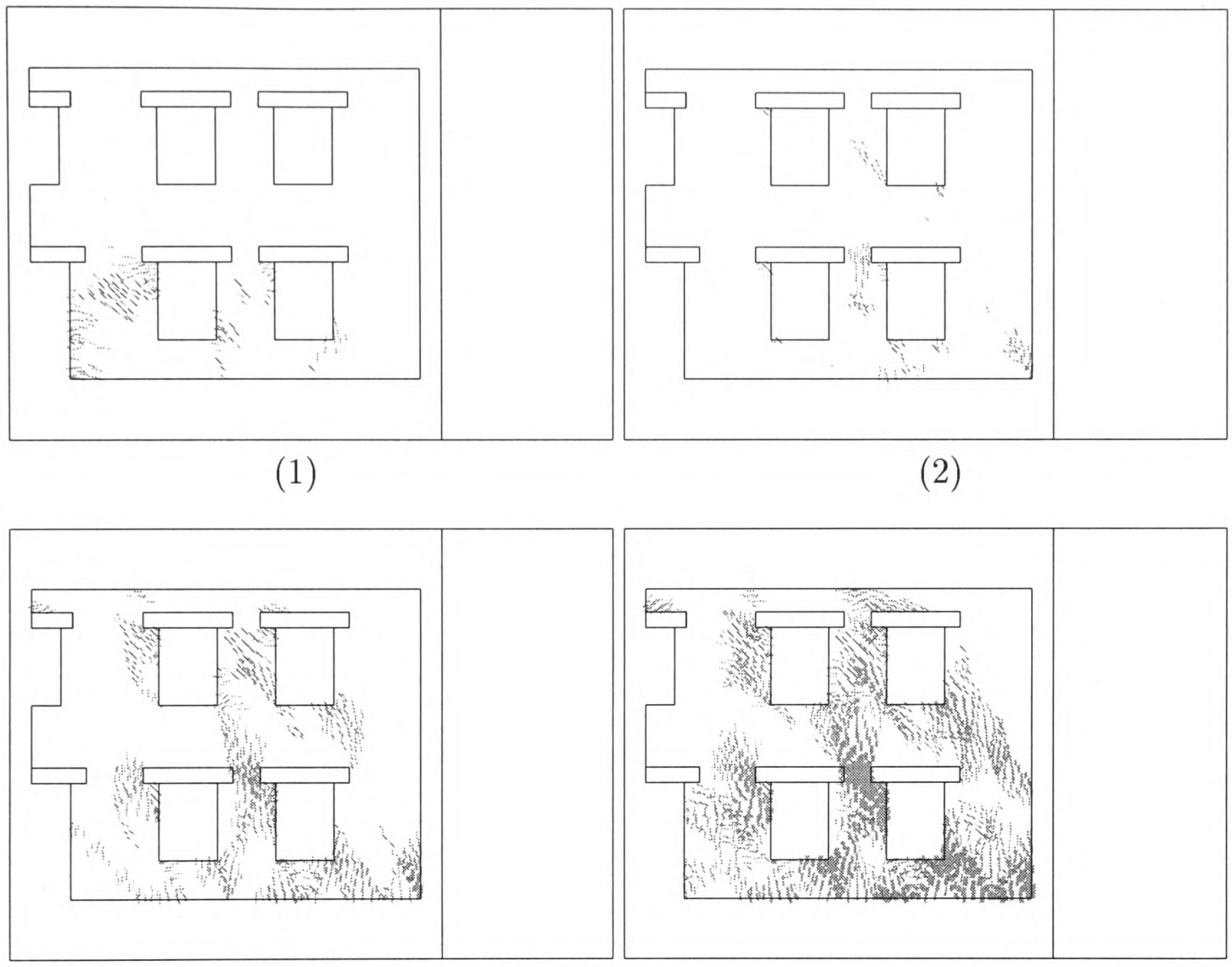


Figure 5.21: Comparison of Cracking Patterns in Facade for Different $(\gamma_b t)'$, Runs (1) 213, (2) 223, (3) 233, (4) 243

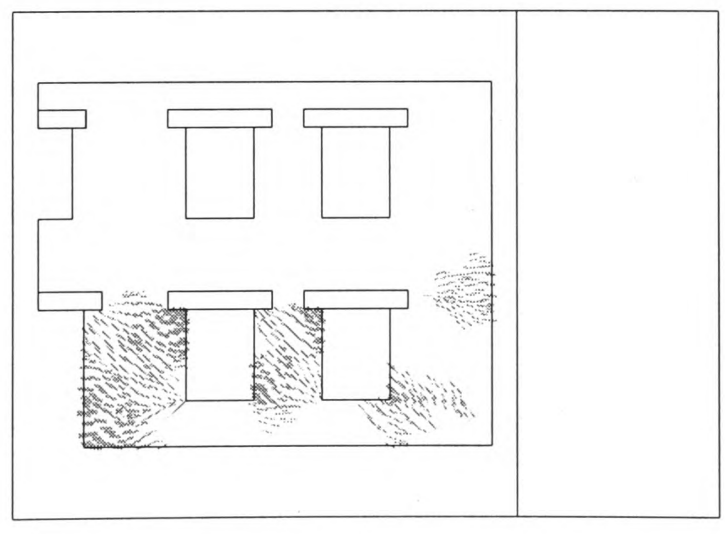
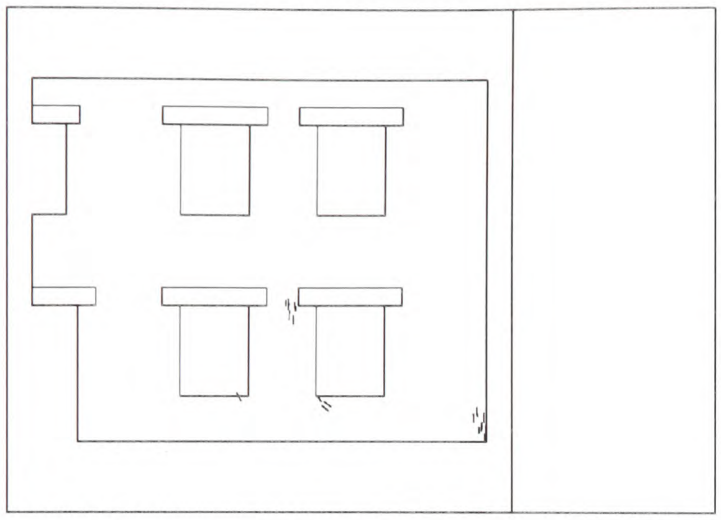


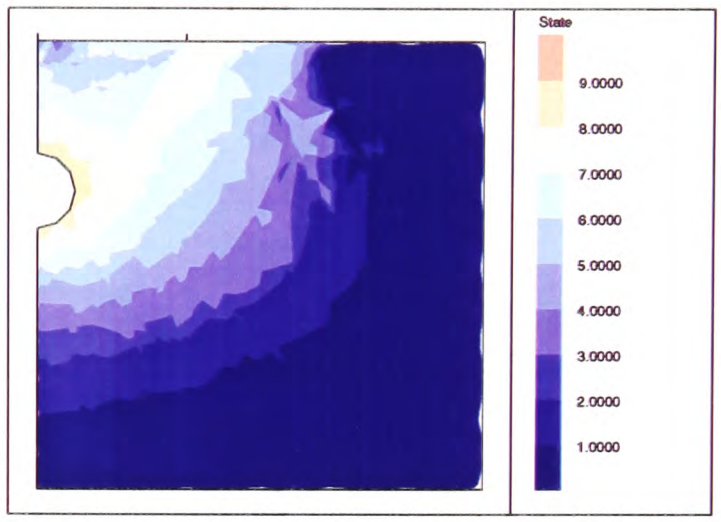
Figure 5.22: Cracking Pattern of Weightless Facade, Run 203

The effect of $(Et)'$

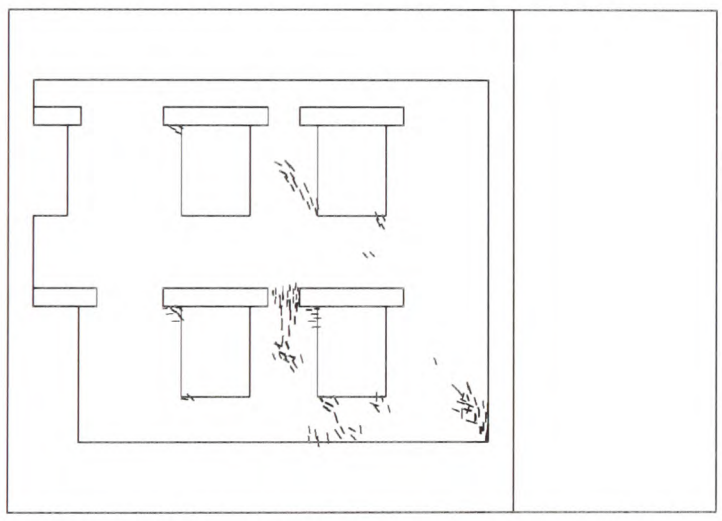
It can be seen from Figures 5.15, 5.16 and 5.17 that the value of $(Et)'$ does not govern the overall shape of the settlement troughs, but has influence on the local shape beneath the



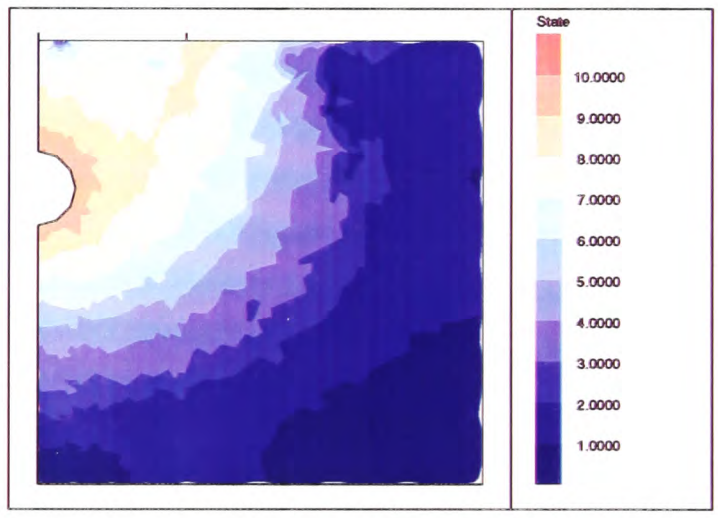
(1)



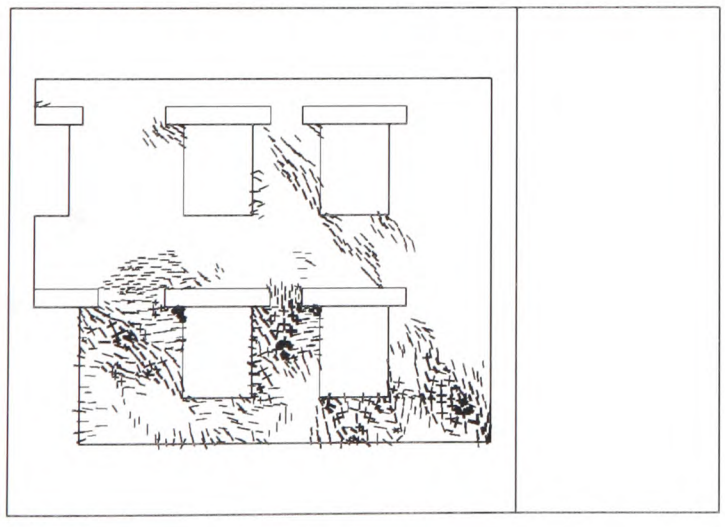
(2)



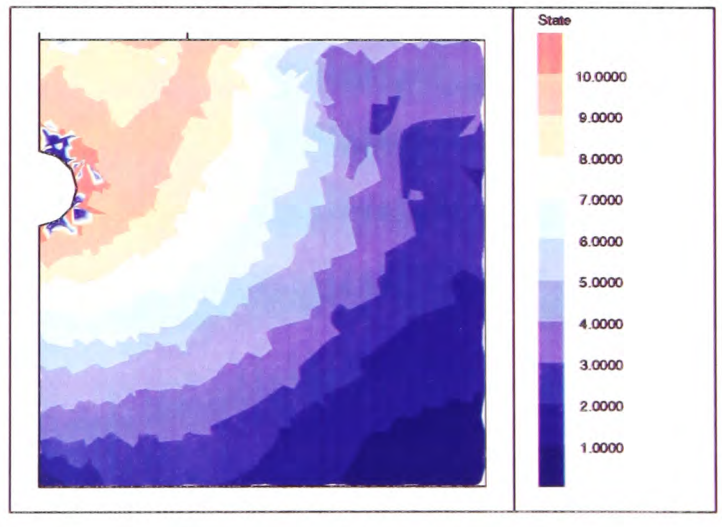
(3)



(4)

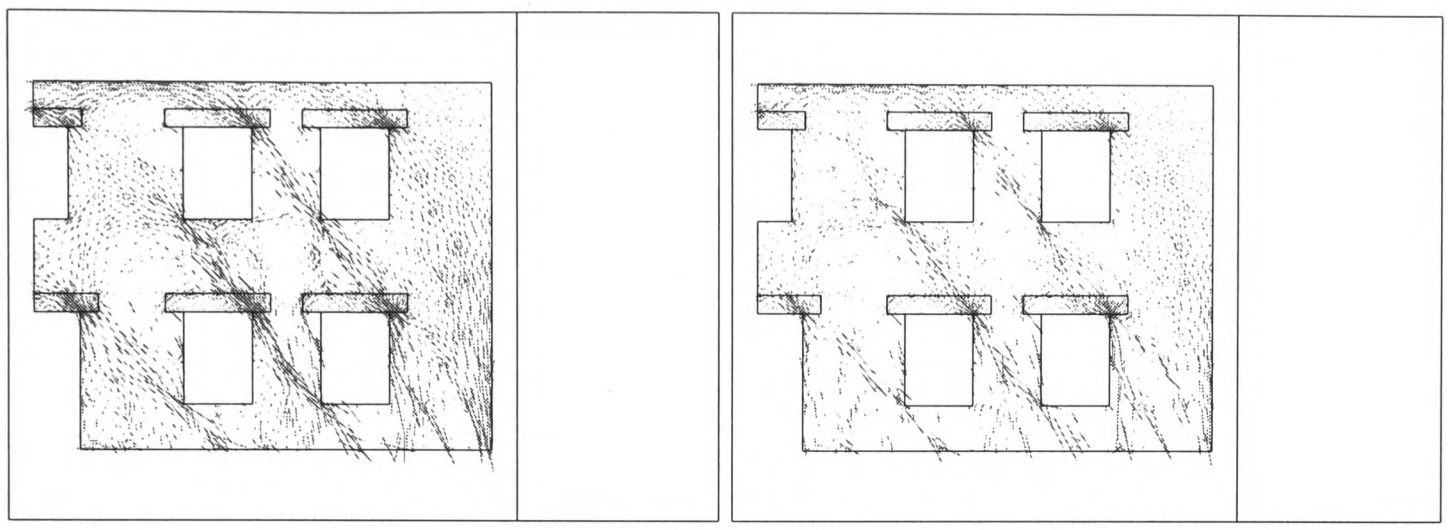


(5)



(6)

Figure 5.23: Cracking Patterns in Facade and States in Ground, Runs (1,2) 123, (3,4) 223, (5,6) 323



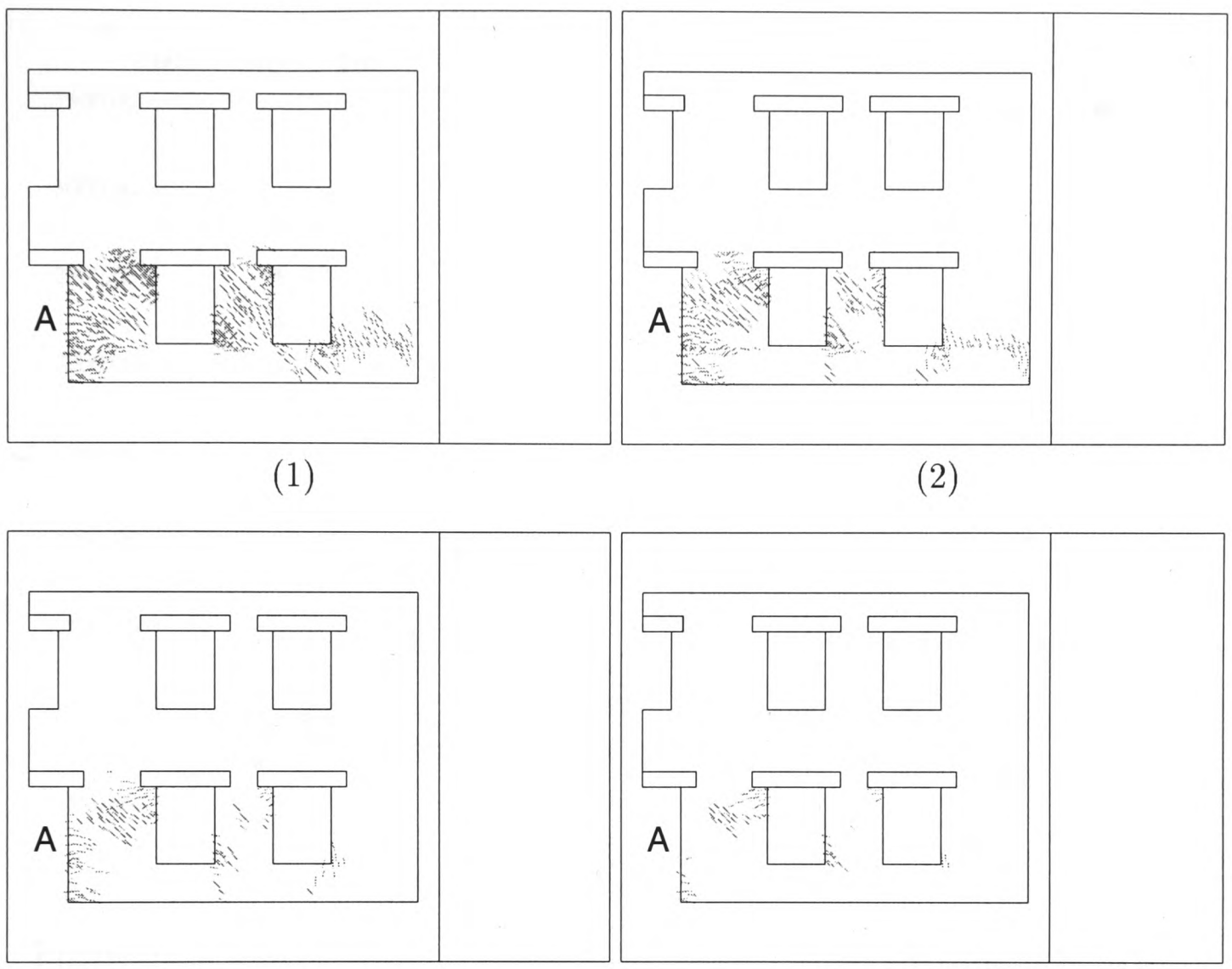
(1) (2)

Figure 5.24: Stress Trajectory in Facades with Different $(Et)'$, Runs (1) 231, (2) 233

facade. This can be explained by the relationship between the stiffness of the building and the formation of arches.

The test problems show that the smaller the value of $(Et)'$ is, the more uniform is the pressure between the facade and the ground, as would be expected. For instance, the stress trajectory of Run 233 with $(Et)' = 66.67$ in Figure 5.24 shows that the stresses are more concentrated around the arches than in Run 231 with $(Et)' = 10.0$. Imagining the situation where a building without stiffness collapses and spreads all its weight uniformly on the ground will help to understand this trend. In consequence, lower stiffness will reduce the arching effect and allow the ground to settle freely, producing larger differential displacements. Therefore the facade will experience more serious damage. This trend can be clearly seen in Runs 211 to 214, the cracking patterns of which are included in Figure 5.25, with $(Et)'$ varying from 10 to 100. The cracking damage in the area near A is due to the settlement and reduced by the increasing $(Et)'$ appreciably.

The value of $(Et)'$ has appreciable effects on the horizontal movement as well. Large values of $(Et)'$ will reduce the horizontal movement in most cases. This effect is stronger for the compressive strain area than the tensile strain area (Figure 5.26). However it does not reduce the vertical cracks induced by such horizontal movement very much, typically in Runs 231 to 234 in Figure 5.27. Although the damage in the areas near A and B which is due to the settlement is reduced by the increasing stiffness, the cracks near C are almost not affected since they are caused by the horizontal movements.



(1) (2)

(3) (4)

Figure 5.25: Comparison of Cracking Patterns with various $(Et)'$, Runs (1) 211, (2) 212, (3) 213, (4) 214

Comparison with Two Limit Conditions

Some additional runs have been carried out using the same parameters as Runs $2xx$ but with the elastic model for the facade. They are named as $e2xx$ (Table 5.4).

Another limit condition tested is the situation without facade stiffness. This situation is modelled by spreading the weight of the building uniformly as a surcharge over the ground block (but with no facade) within the extent of the facade. Four runs were carried out for $(\gamma_b t)' = 0.05, 0.167, 0.33, 0.5$, each with the γ_s' of 1.667. These runs were named as 210, 220, 230.

In the elastic runs, the settlements are still governed by the weight of the building (Figure 5.28). The heavy building will experience large settlement. For the stiffness used here, the troughs are almost flat. As the stiffness increases, the settlement troughs

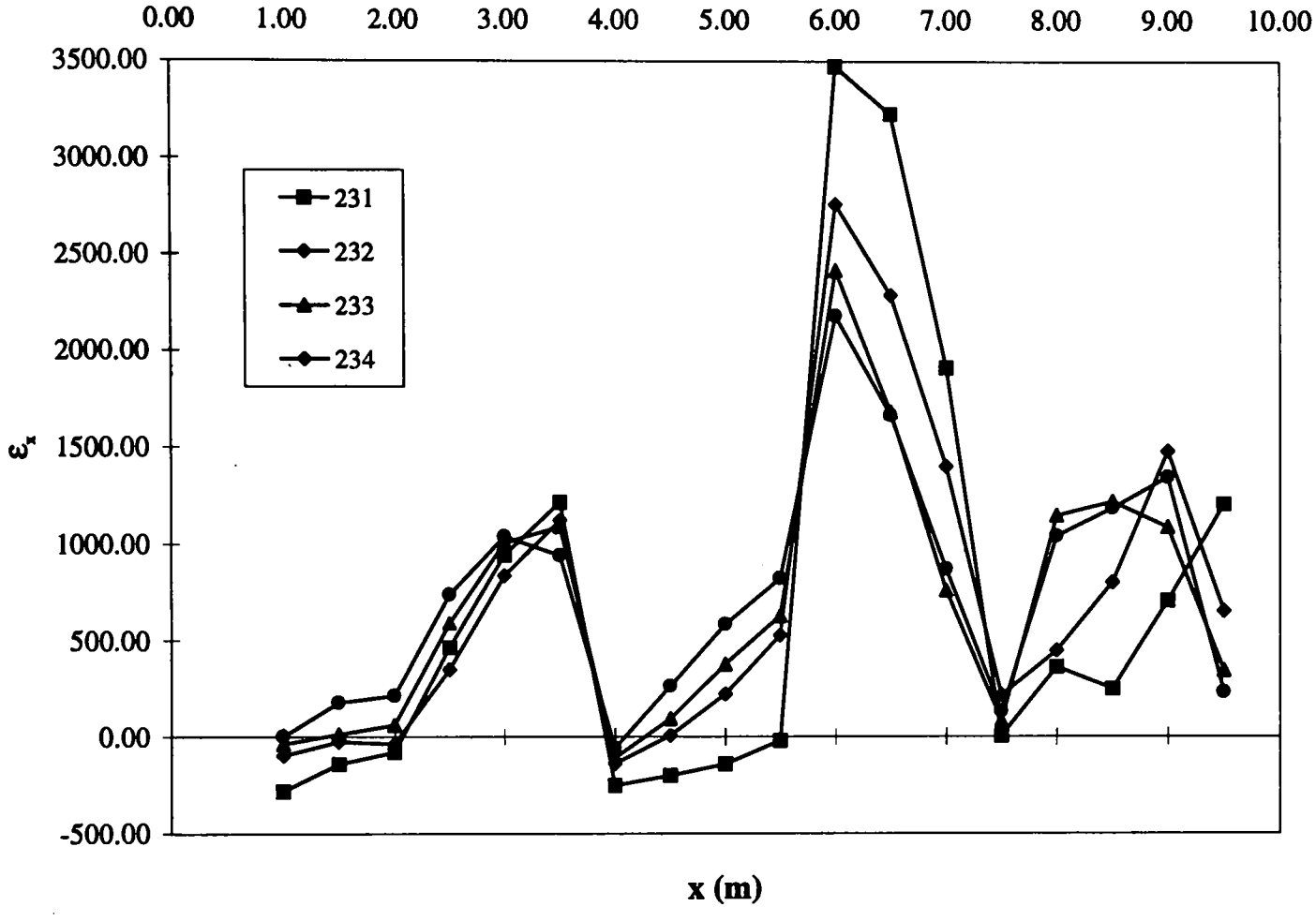


Figure 5.26: Ground Strains beneath the Facade, Runs 231, 232, 233, 234.)

become flatter, but such an effect is very small within the range of the stiffness values considered here (Figure 5.29). The horizontal movements beneath the elastic building are inward and very small.

In the elastic facade, a strong arching effect is still observed. In a similar way to a stress arch formed by the trajectory of large compressive stresses, a stress cable is described by the trajectory of large tensile stresses. In addition to the arches in the elastic facade, some cable effect is also exhibited, which "lifts up" the ground. Both arch and cable resist the ground movement induced by the tunnelling and give a flat trough (Figure 5.30).

In the zero stiffness runs, the settlement troughs are very similar to the greenfield results but with settlements increasing with the values of the surcharge.

Comparing the settlement troughs of elastic, masonry facades and the greenfield cases with surcharge, all shown in Figure 5.28, it can be seen that for the same weight

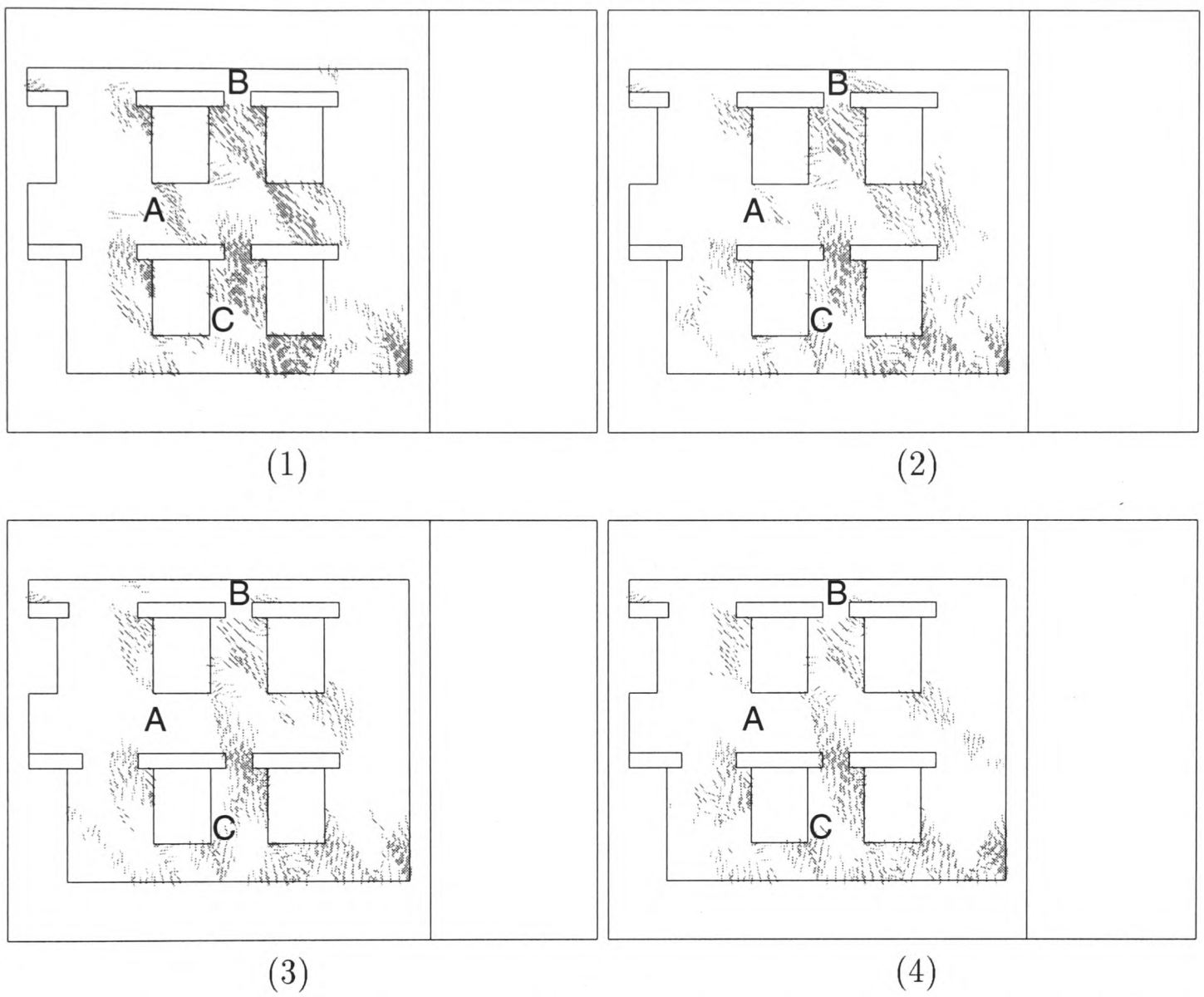


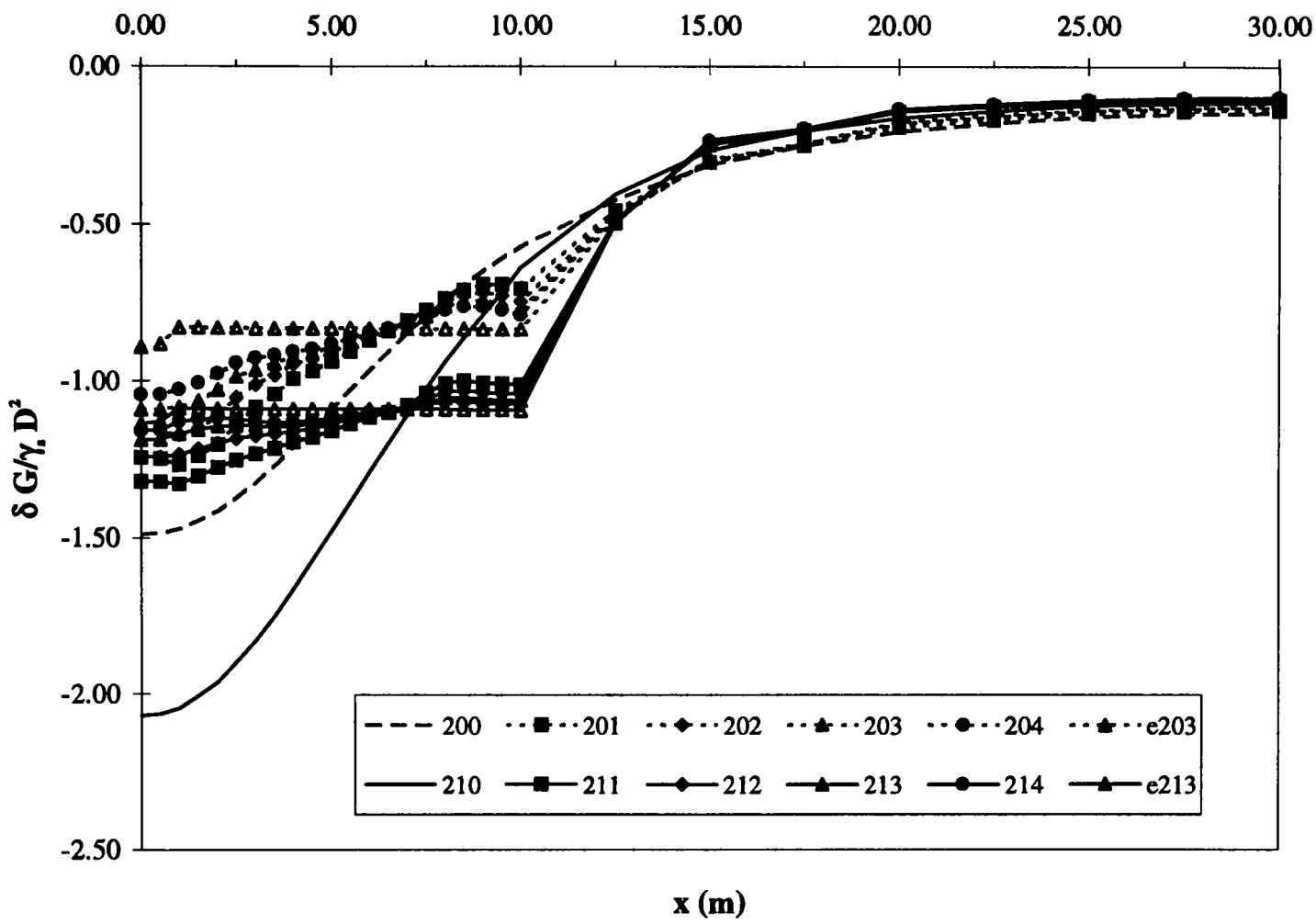
Figure 5.27: Comparison of Cracking Patterns with various $(Et)'$, Runs (1) 231, (2) 232, (3) 233, (4) 234

of building, all of them except for Run 230 give the same values of settlement roughly at the point of inflexion. The stiffness of the building can change the shape of the trough under the building locally, but does not change the settlement at the point of inflexion, which is mainly controlled by the weight of the building.

In the exceptional case, Run 230, the stability number is above the lower boundary of 2.9 and the state in ground also shows a large area of failure (Figure 5.31).

Figure 5.32 could be used to illustrate the settlement process approximately.

The facade can be seen as a beam supported at the points of inflexion. The settlement at the points of inflexion, δ_i, is determined by the weight of the building because the weight of building has previously caused the soil under it to yield partially. Even without the interaction of the building, the greenfield with this partially yielded soil will give a



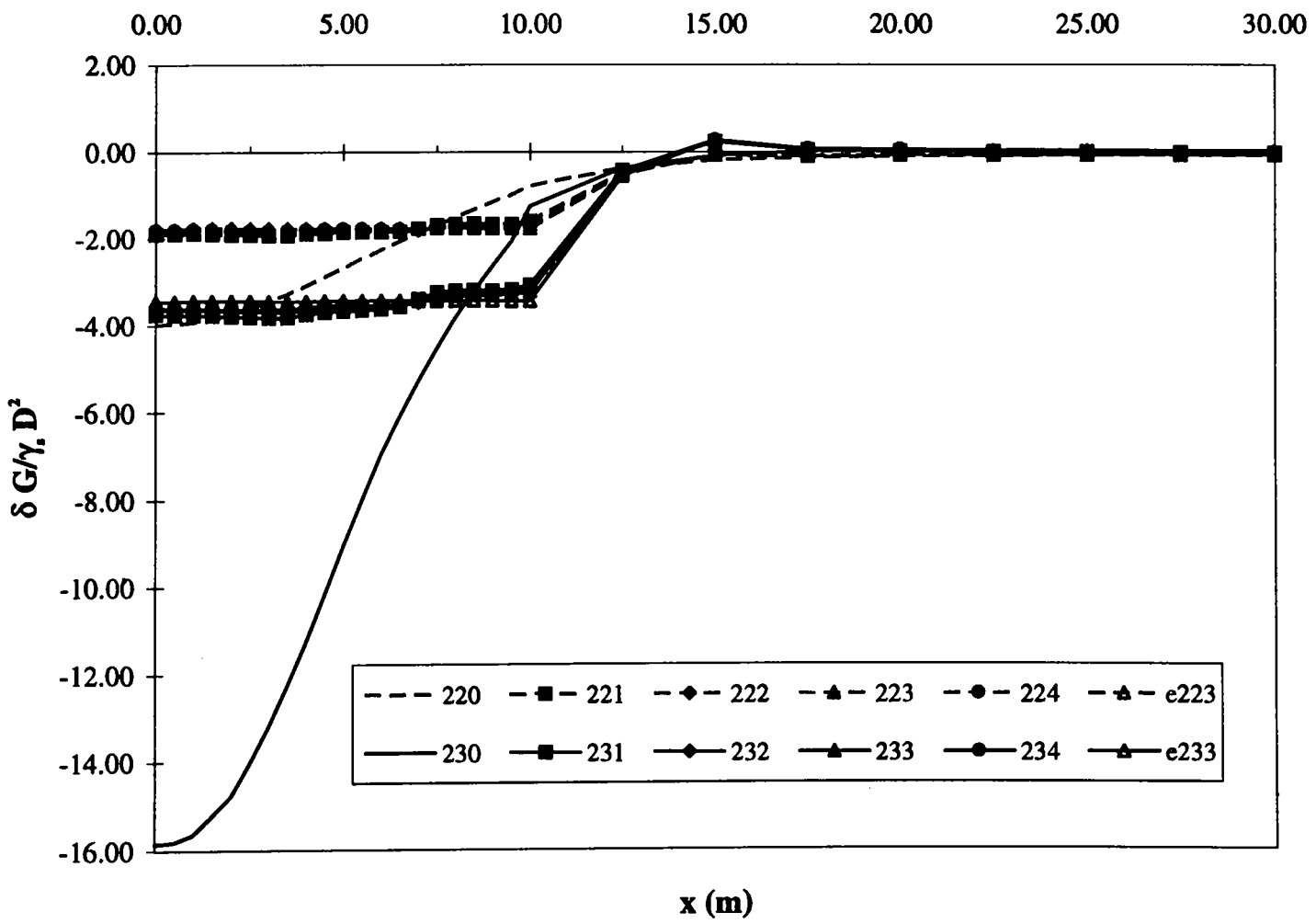


Figure 5.28: Ground Movements of Elastic Facade, Compared with Masonry Facades, γ_s'=2.50

No.	γ_s	$(\gamma_s)'$	$\gamma_b t$	$(\gamma_b t)'$	Et	(Et)'	N_{gmd}	N_{total}	δ_{max}	δ_i
210	20	1.6666667	3	0.05	0	0	1.6666667	1.8666667	2.07	1.11
220	20	1.6666667	10	0.1666667	0	0	1.6666667	2.3333333	3.99	1.88
230	20	1.6666667	20	0.3333333	0	0	1.6666667	3	15.9	5.3
240	20	1.6666667	30	0.5	0	0	1.6666667	3.6666667	fail	fail
e201	20	1.6666667	0	0	1.50E+06	10	1.6666667	1.6666667	0.839	0.834
e202	20	1.6666667	0	0	5.00E+06	33.333333	1.6666667	1.6666667	0.839	0.834
e203	20	1.6666667	0	0	1.00E+07	66.666667	1.6666667	1.6666667	0.837	0.834
e204	20	1.6666667	0	0	1.50E+07	100	1.6666667	1.6666667	0.836	0.834
e211	20	1.6666667	3	0.05	1.50E+06	10	1.6666667	1.8666667	1.1	1.09
e212	20	1.6666667	3	0.05	5.00E+06	33.333333	1.6666667	1.8666667	1.1	1.09
e213	20	1.6666667	3	0.05	1.00E+07	66.666667	1.6666667	1.8666667	1.09	1.09
e214	20	1.6666667	3	0.05	1.50E+07	100	1.6666667	1.8666667	1.09	1.09
e221	20	1.6666667	10	0.1666667	1.50E+06	10	1.6666667	2.3333333	1.79	1.77
e222	20	1.6666667	10	0.1666667	5.00E+06	33.333333	1.6666667	2.3333333	1.77	1.77
e223	20	1.6666667	10	0.1666667	1.00E+07	66.666667	1.6666667	2.3333333	1.77	1.77
e224	20	1.6666667	10	0.1666667	1.50E+07	100	1.6666667	2.3333333	1.77	1.77
e231	20	1.6666667	20	0.3333333	1.50E+06	10	1.6666667	3	3.48	3.44
e232	20	1.6666667	20	0.3333333	5.00E+06	33.333333	1.6666667	3	3.45	3.45
e233	20	1.6666667	20	0.3333333	1.00E+07	66.666667	1.6666667	3	3.45	3.45
e234	20	1.6666667	20	0.3333333	1.50E+07	100	1.6666667	3	3.45	3.45
e241	20	1.6666667	30	0.5	1.50E+06	10	1.6666667	3.6666667	7.79	7.75
e242	20	1.6666667	30	0.5	5.00E+06	33.333333	1.6666667	3.6666667	7.76	7.76
e243	20	1.6666667	30	0.5	1.00E+07	66.666667	1.6666667	3.6666667	7.77	7.76
e244	20	1.6666667	30	0.5	1.50E+07	100	1.6666667	3.6666667	7.76	7.76

Table 5.4: Summary of the Additional Test Problems

deep trough which has δ_i at its points of inflexion. However, the stiffness of the building will resist such a greenfield curve with partially yielded soil and give a flatter ultimate trough.

Thus, the settlement trough under a masonry facade with the size considered, symmetrically located above the tunnel, can be estimated by the following procedure when the tunnel remains stable. First, applying a surcharge equivalent to the weight of the building to the greenfield will produce a settlement trough. Plotting a horizontal line within the extent of building at the positions of the points of inflexion will be a good estimate to the settlement trough beneath the elastic facade. The settlement troughs produced by a masonry facade will vary between the elastic and the greenfield troughs, depending on the stiffness and the weight of the building.

Stability Number Charts

The results of settlement troughs of all the test problems can be summarised by the stability number - maximum settlement charts (Figure 5.33). The thick solid line

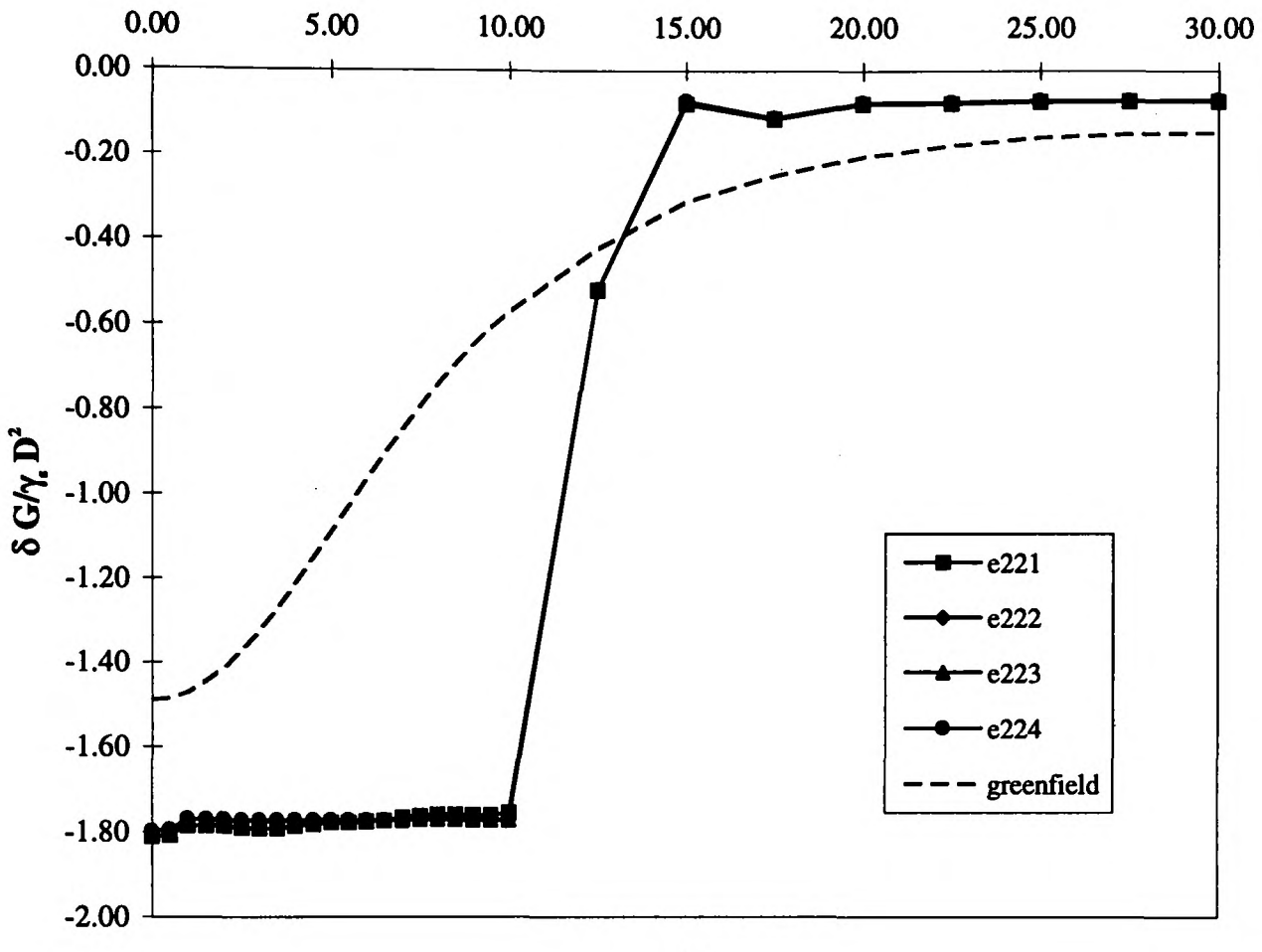


Figure 5.29: Settlements of Various Values of Stiffness, Runs e231, e232, e233 and e234

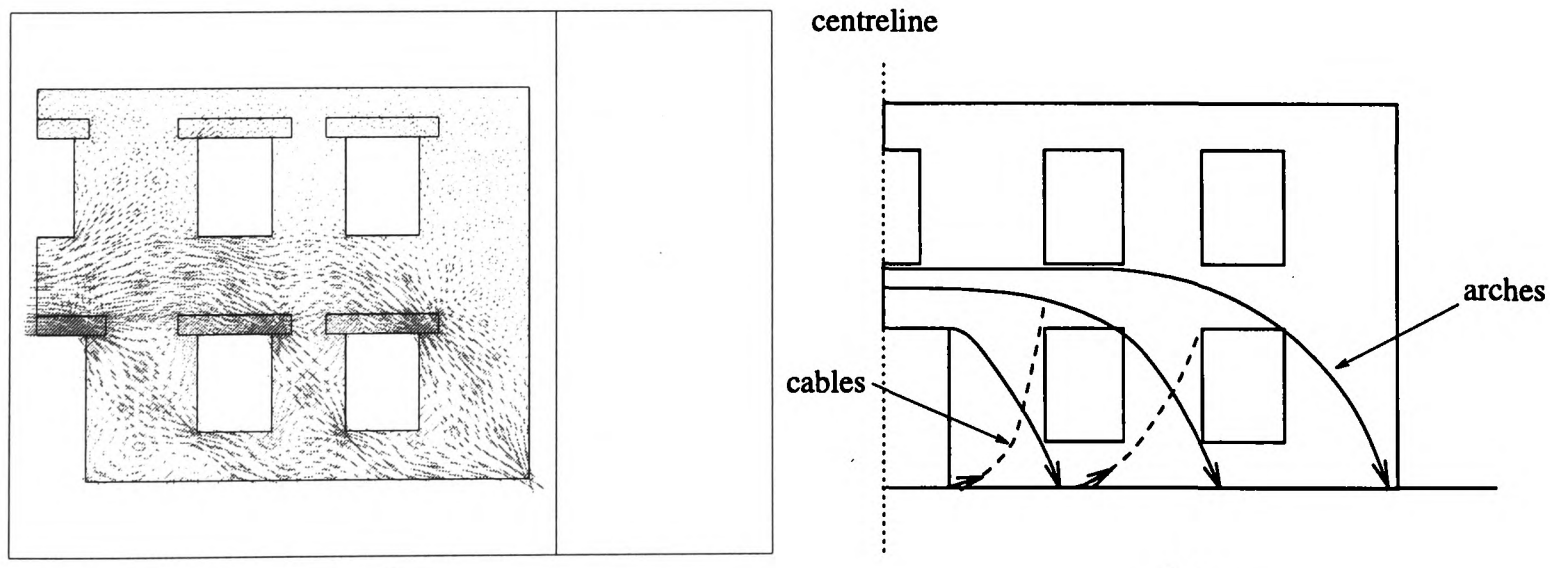


Figure 5.30: Arching and Cable Effects in Elastic Facade

refers to the greenfield case. When γ_s' rises, *i.e.* the stability number increases, the dimensionless settlement also increases. When the stability number approaches about 2.9, the curve raises sharply which means the tunnel is about collapse.

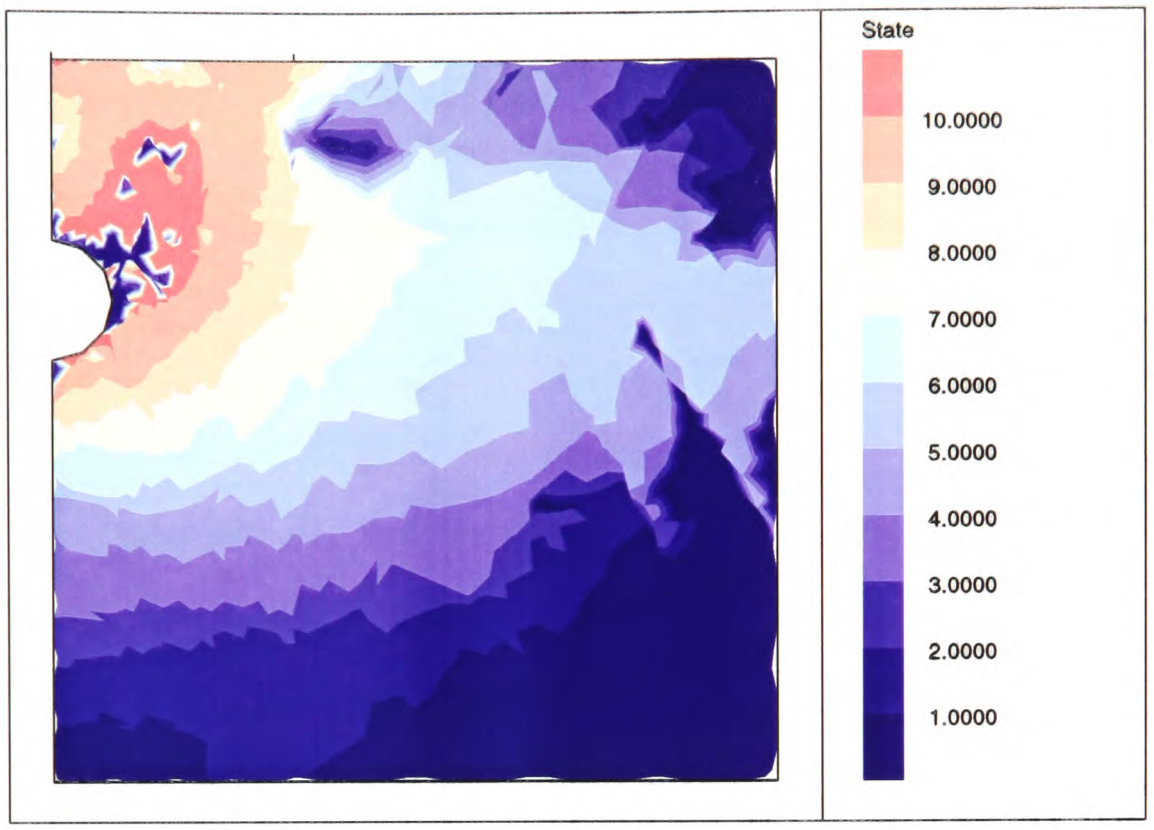


Figure 5.31: State in the Ground with Surcharge Equivalent to $(\gamma_b t)'$

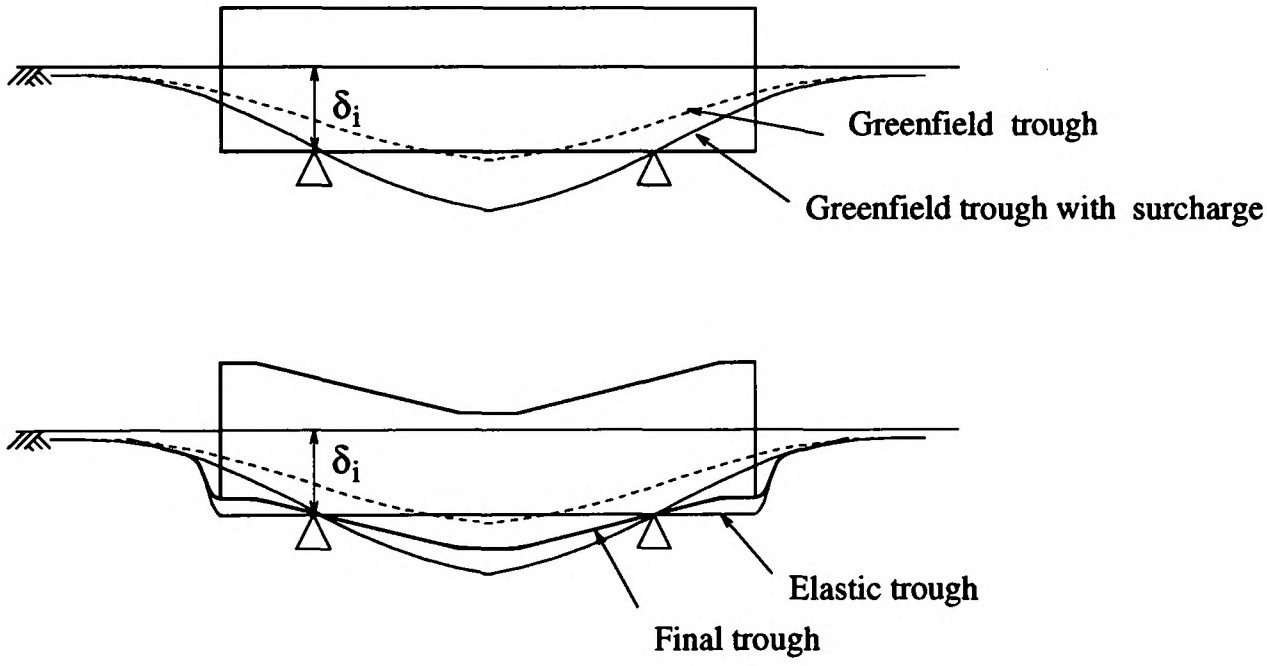


Figure 5.32: Effects of Weight and Stiffness of Building

The dotted lines are for the ground with a building. It is clear that the presence of a building will increase the stability number. It is also clear that the effect of the building is not necessarily to reduce the settlement. Only the light buildings are able to reduce the settlement. When the building becomes heavy, it will drive the ground to instability. A tunnel with a large stability number in a greenfield is more sensitive to the building. It is important to pay attention to heavy buildings when tunnelling in soft ground.

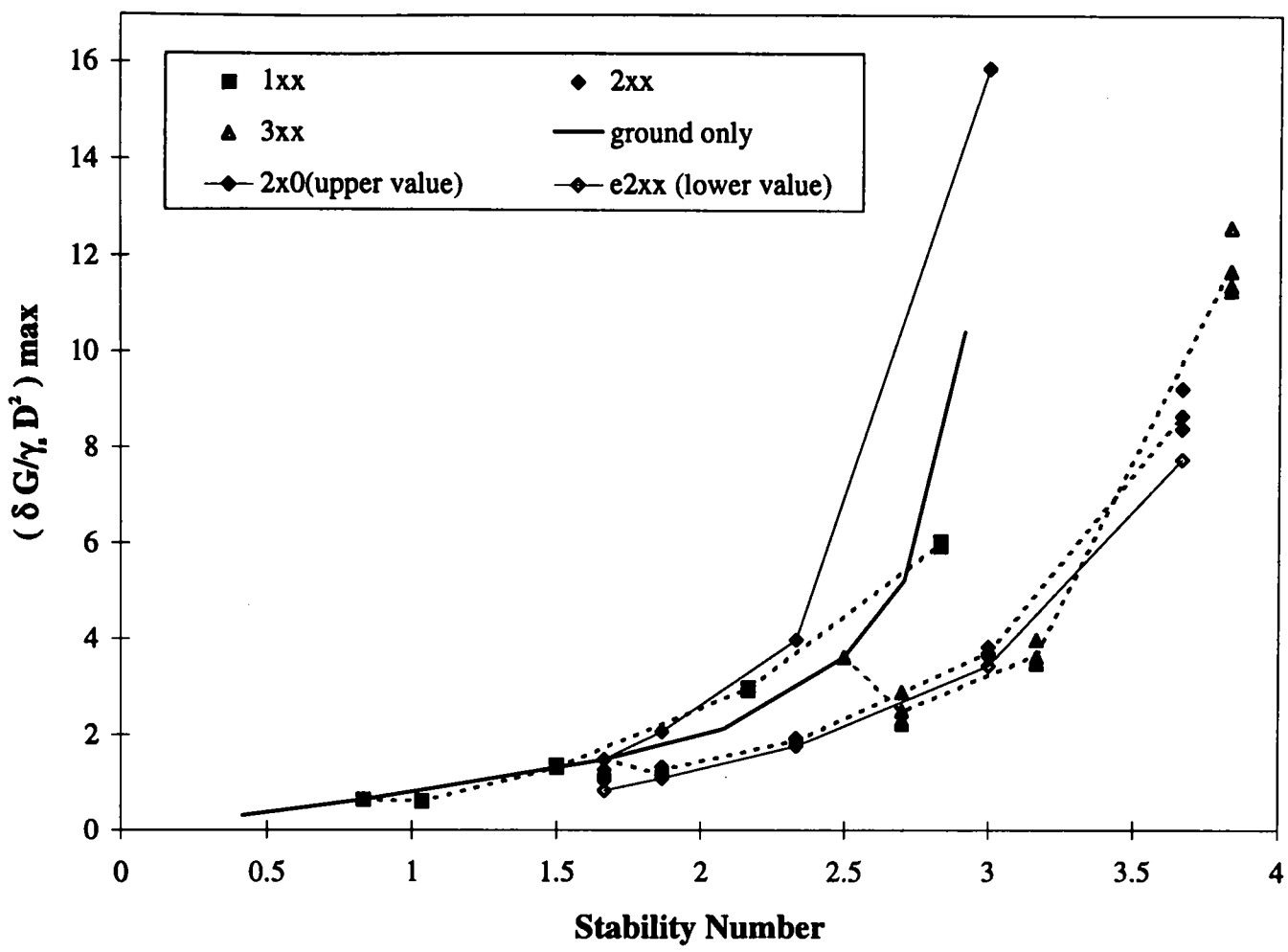


Figure 5.33: Stability Number Charts of All Tests

Since the buildings with the same weight on the same ground condition have the same value of the stability number, the test points of these buildings are distributed vertically due to the values of the building stiffness. A less stiff building will have a higher settlement. For the facades on the ground with the stability number of 1.667 in the greenfield condition, the upper limit of the combined cases is the thin solid line with solid diamond marks representing the facade without stiffness. The lower limit is the other thin solid line standing for the stiff elastic facade. For any facade with a different stiffness, the settlements will fall in the area between these two lines.

5.5 A Study on the Position of the Facade

In the above 2-D combined analyses, the effect of varying the position of the masonry building was not included. In this section, this effect is investigated.

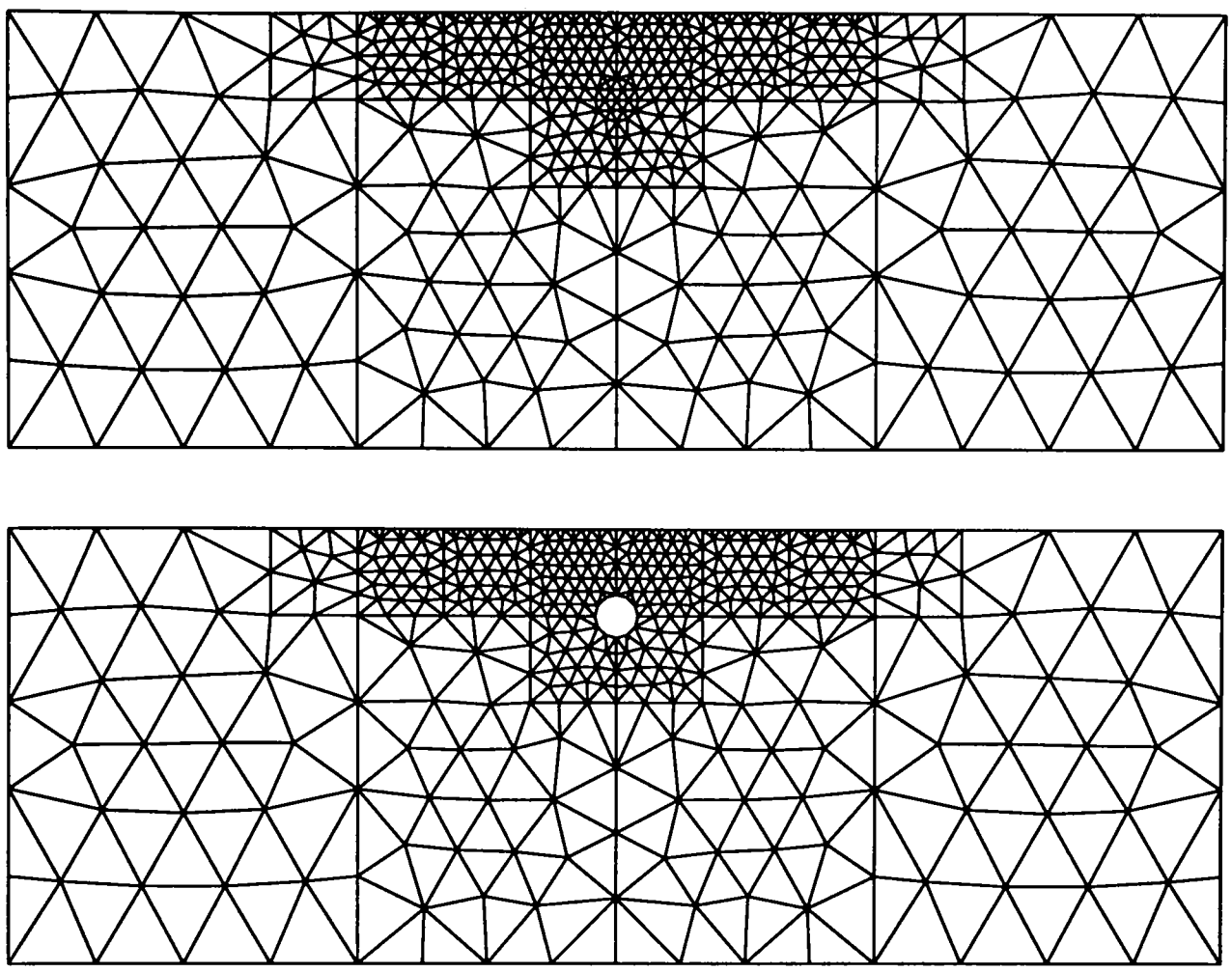


Figure 5.34: The Meshes for the Ground (1) before and (2) after Excavation

5.5.1 The Models

The Building

The same masonry facade as described in the previous analyses is used here. However, due to the asymmetry of the problem it is necessary to model the whole facade.

The Ground

A 140m $\times$ 50m block of ground with unit thickness is used. The meshes of the soil block before and after the excavation are shown in Figure 5.34.

The excavated tunnel is the same as discussed before, and simulated by removing the elements within the tunnel area, without installation of lining. The soil parameters are as described previously and the unit weight of the soil is $\gamma_s = 20\text{kPa}$.

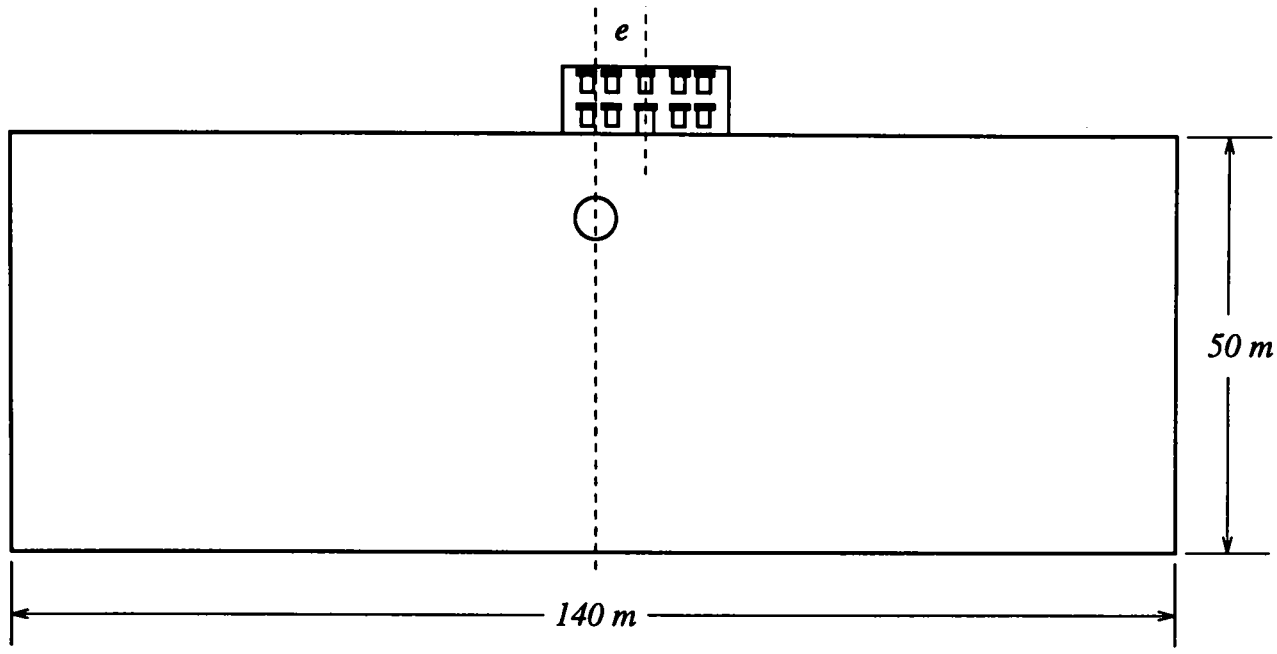


Figure 5.35: The Layout of the Model

	γ_s(kPa)	γ_bt(kPa m)	Et(kPa m)	e(m)	δ_{max}(cm)	position(m)
u200	20	0	0	0	2.35	0.0
u223a	20	10	1.00E+07	0	3.21	0.0
u223a1	20	10	1.00E+07	5	5.41	-5.0
u223b	20	10	1.00E+07	10	4.68	0.0
u223b1	20	10	1.00E+07	15	2.51	5.0
u223c	20	10	1.00E+07	20	1.94	1.0
u233a	20	20	1.00E+07	0	7.08	3.5, -3.5
u233a1	20	20	1.00E+07	5	14.3	-5.0
u233b	20	20	1.00E+07	10	9.67	0.0
u233b1	20	20	1.00E+07	15	4.25	5.0
u233c	20	20	1.00E+07	20	2.23	15.0

Table 5.5: Summary of the Test Problems with Different Positions of the Facade

The Position of the Facade

The position of the facade is described by its eccentricity e which is defined as the distance between the centrelines of the facade and the tunnel (Figure 5.35).

The Test Problems

A total of 11 cases are analysed in this section. Two values of the self-weight of the facade and five values of the eccentricity are considered along with the greenfield case. The numbering and the parameters are summarised in Table 5.5.

5.5.2 Discussion of the Results

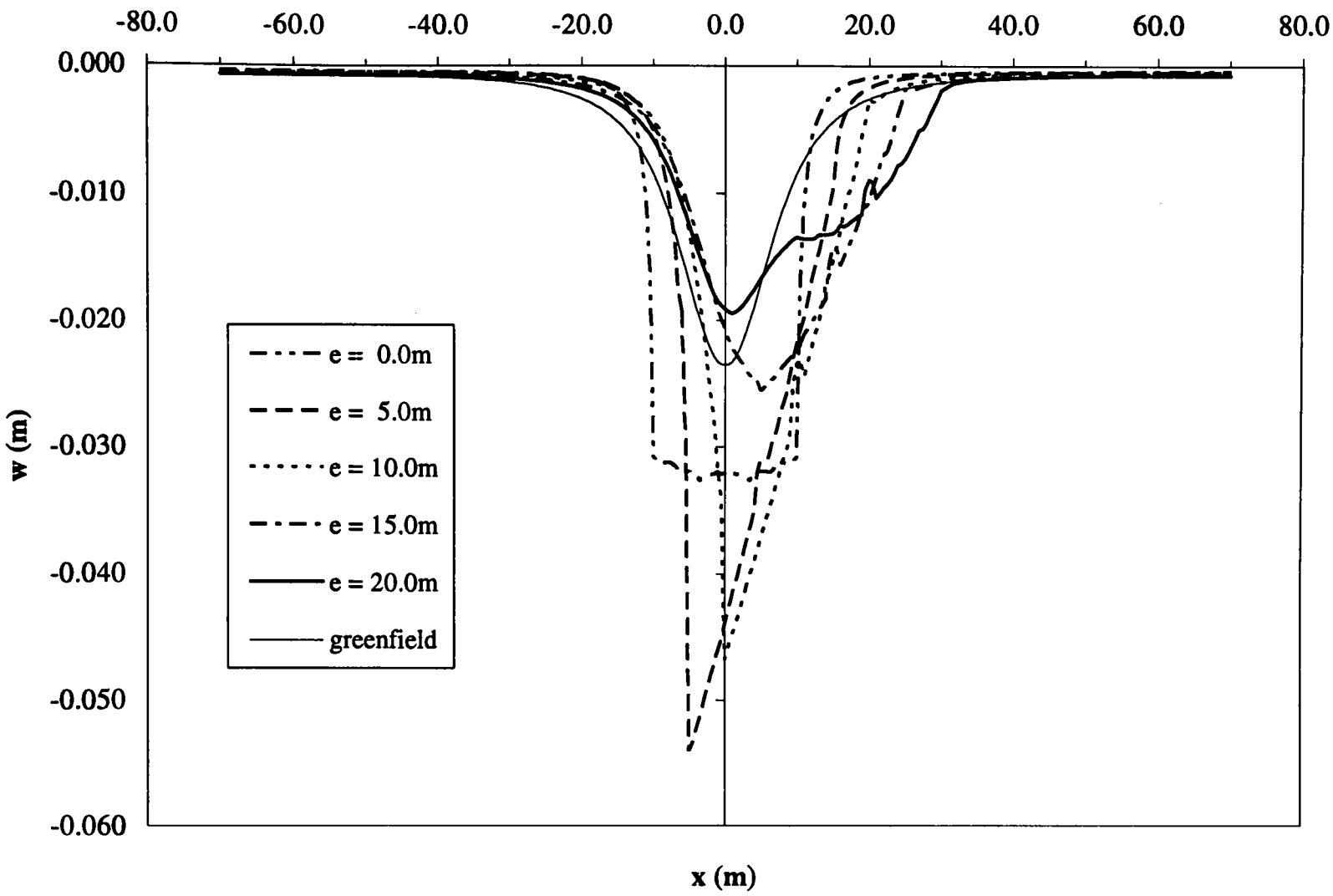
Ground Movements

The ground movements of all the tests are given in Figures 5.36 and 5.37. For both values of the self-weight of the facade, the settlement troughs under the facades have some similar features.

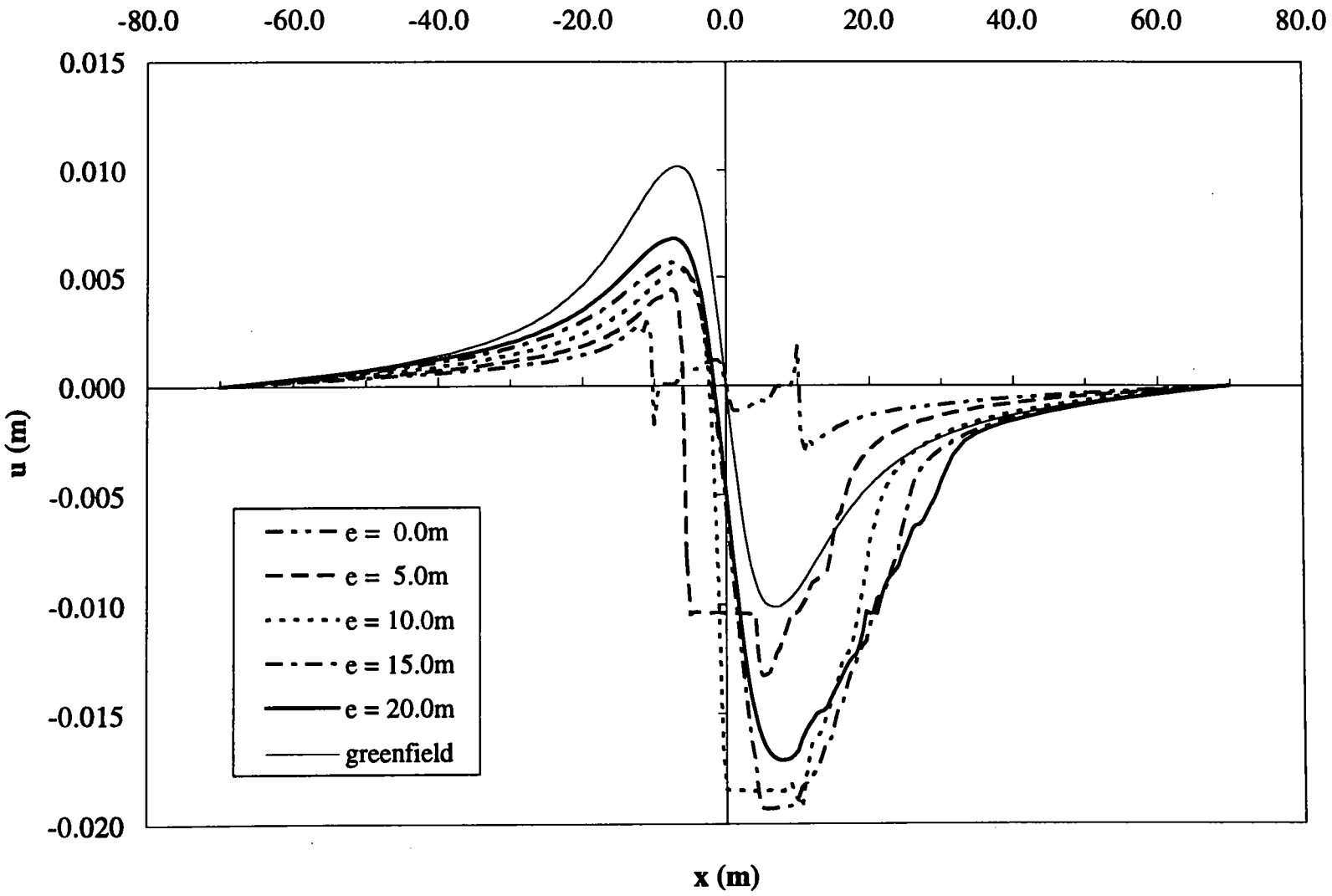
First, when a facade moves away from the symmetric location ($e = 0$), the maximum settlement beneath the facade also moves from the centre point of the facade to one end and the settlement increases dramatically. When $e = 5$m, the maximum settlement reaches 0.054 and 0.14m, which are 1.69 and 2.02 times that in the symmetric case. In addition considerable tilts of 2.2:1000 and 6.5:1000 are also observed at $e = 5$m for the two values of the self-weight of the building. This is consistent with the states observed in the ground. The typical state numbers of the tests $u223xx$ are shown in Figures 5.38 and 5.39. It can be seen that when $e = 5$m, a highly non-linear band extents from the tunnel to the left edge of the facade. Since the state number along this band reaches 9, a potential failure plane develops.

These observations can be explained with reference to the possible mechanism for upper bound failure discussed in Section 5.3.3 (Figure 5.12). It might be expected that when one edge of the facade coincides approximately with one failure surface of a possible upper bound failure mechanism of the ground alone, the effect of the building would be greatly to increase the tendency of the ground to fail along such a mechanism, leading to large settlement and tilt of the building. When e approaches 10m, the value of the maximum settlement is reduced but is still greater than that in the symmetric case.

When the facade lies entirely to one side of the centreline of the tunnel, the settlement under the facade is considerably decreased, becoming less than that in the symmetric case. Beyond the point of inflexion, the greenfield trough shows a hogging region. However, the trough under the facade always exhibits a sagging mode, even in this hogging area. This can be explained by the fact that the stress induced by the self-weight of the building controls the ground movements underneath it in the area far from the tunnel centreline. This effect is local for the light buildings, as the overall trough is still con-

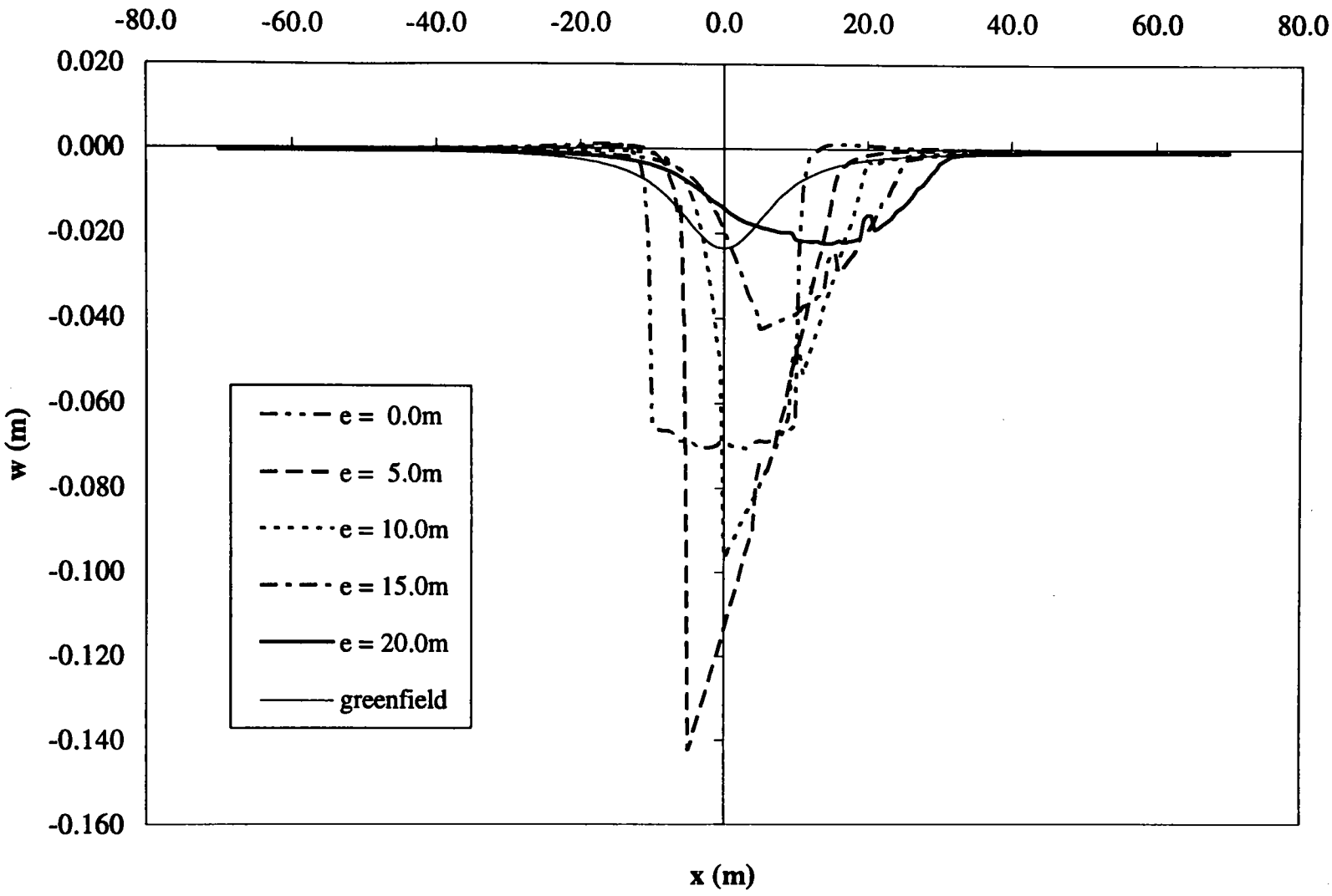


(1) Settlements

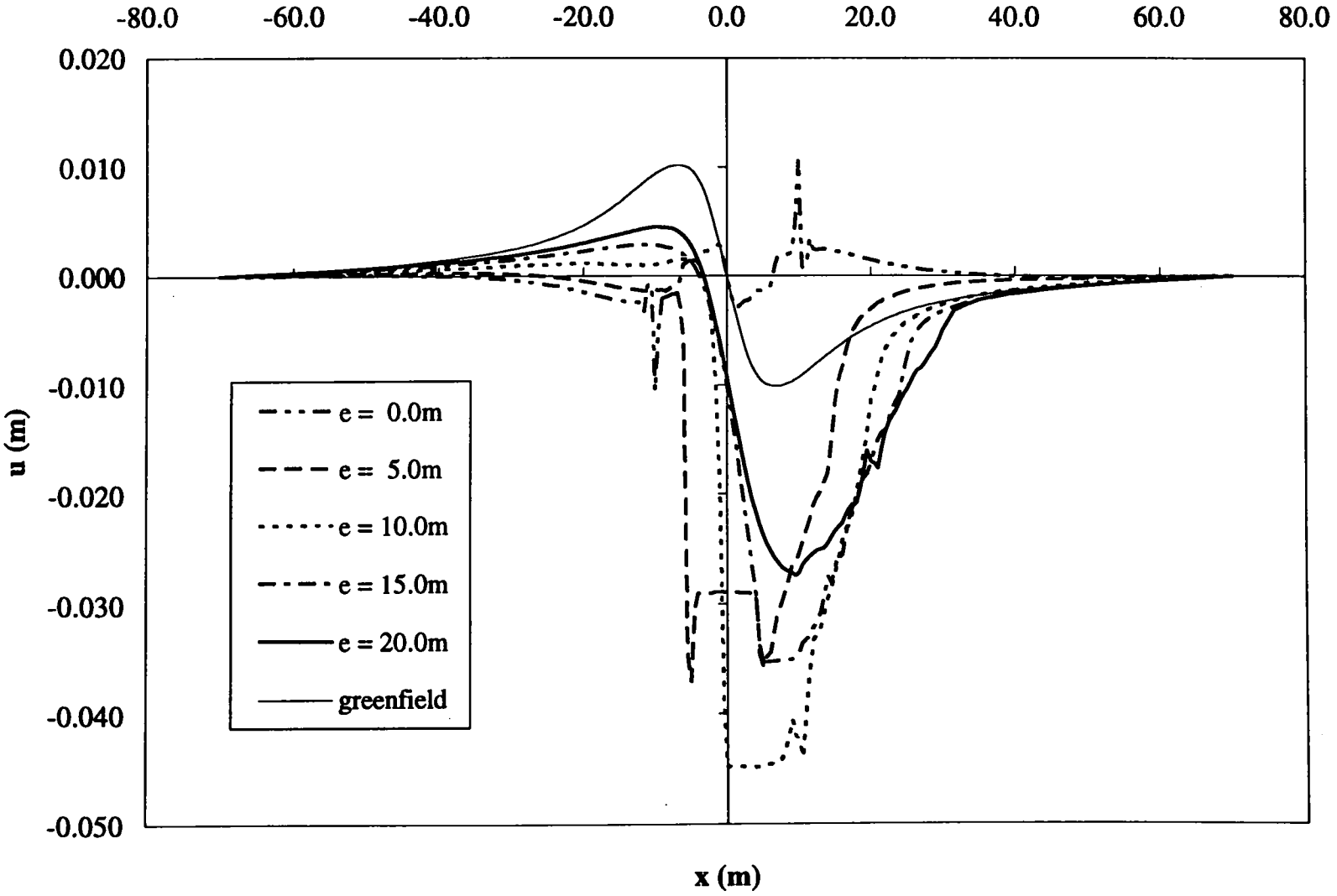


(2) Horizontal Movements

Figure 5.36: Ground Movements under Moving Facade, $\gamma_b t = 10.0\text{kN/m}^2$ (u223xx)

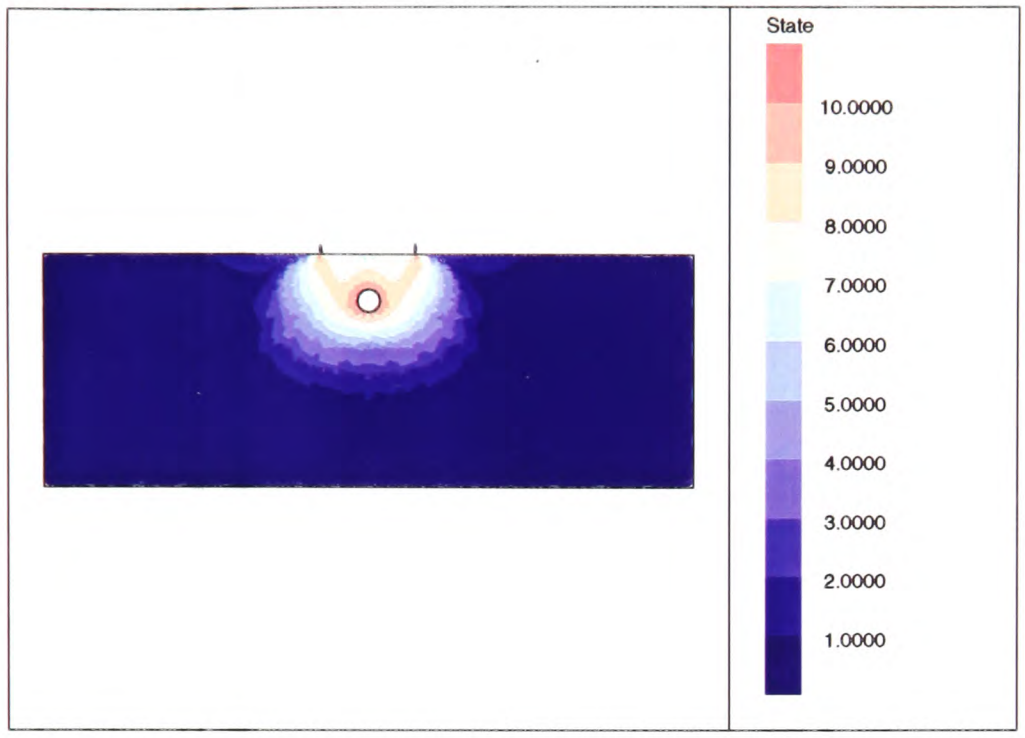


(1) Settlements

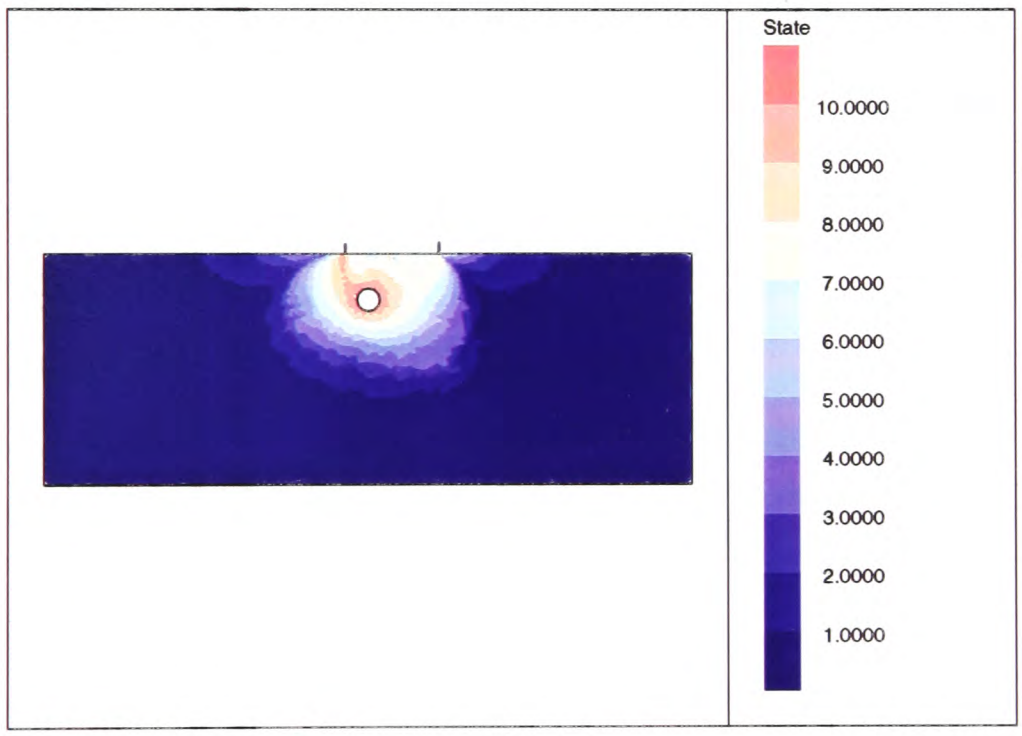


(2) Horizontal Movements

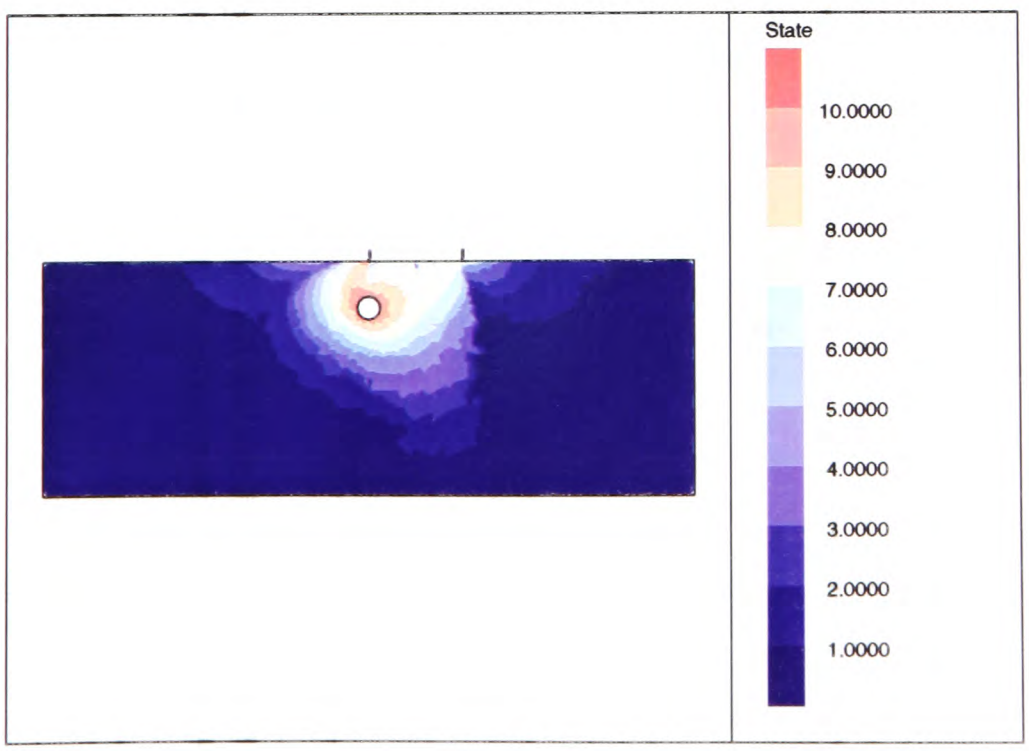
Figure 5.37: Ground Movements under Moving Facade, $\gamma_b t = 20.0\text{kN/m}^2$ (u233xx)



(1)

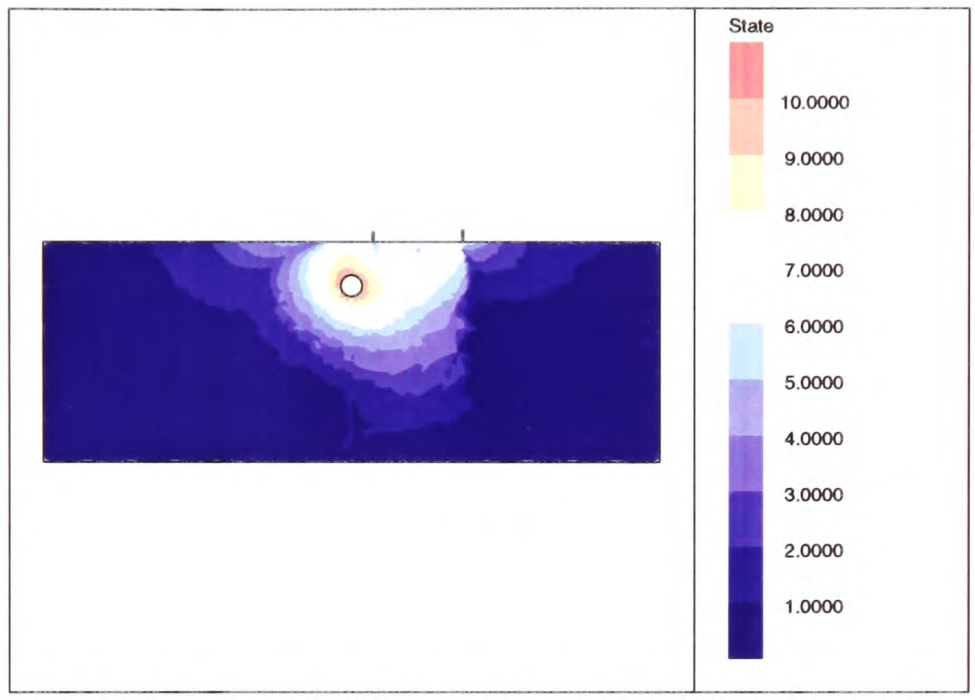


(2)

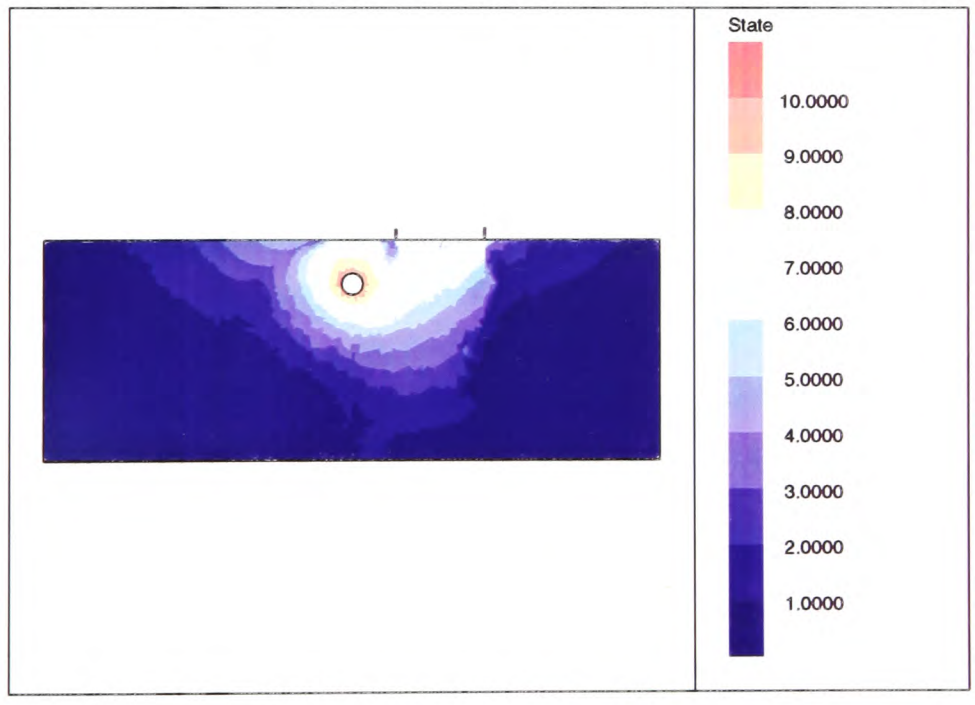


(3)

Figure 5.38: State Numbers Corresponding to e = (1) 0, (2) 5, (3) 10m (u223xx)



(1)



(2)

Figure 5.39: State Numbers Corresponding to e = (1) 15, (2) 20m (u223xx)

trolled by the excavation (Figure 5.36-(1)), whilst for the heavy building, the weight has the dominant effect (Figure 5.37-(1)).

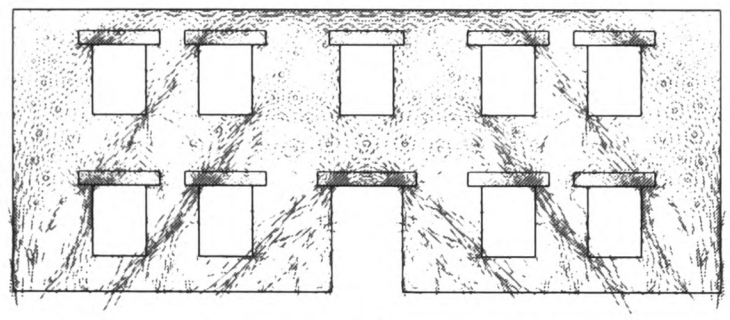
The different values of e also affect the horizontal movement in the ground beneath the facade. In the symmetric case ($e = 0$), most of the facade falls in the area where the ground tends to impose a compressive horizontal movement. This movement is reduced by the facade considerably, although some local tensile areas exist due to the arch forces, as discussed in Section 5.4.3. When e is 5 to 10m, the left part of the facade is still in the compressive area and able to resist the ground movement, whilst the right part follows the tensile ground horizontal movement since it does not have tensile stiffness. When e is 15 to 20m, the whole facade moves into the tensile area and translates with the ground horizontally.

Building Behaviour

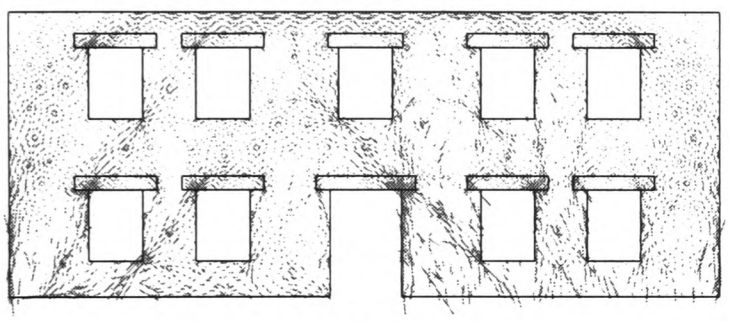
Stress arches are formed when the facade is symmetrically located over the tunnel. As the facade moves to one side, the stress arches gradually disappear, though the facade is always in the sagging mode. This process is illustrated by Figure 5.40. The stress arches cannot be formed in the tensile horizontal movement area since there is no support for the arches at the base.

In consequence, the cracking patterns change from those along the stress arches to the vertical cracks developed from the bottom of the facade due to the tensile horizontal strains. The cracking patterns of all tests in this section can be found in Figures 5.41 and 5.42 and show this process. As the facade moves to the right, the vertical cracked area moves from the right part of the facade to the left. When the facade is located remote from the tunnel, it will not experience cracking damage induced by the excavation.

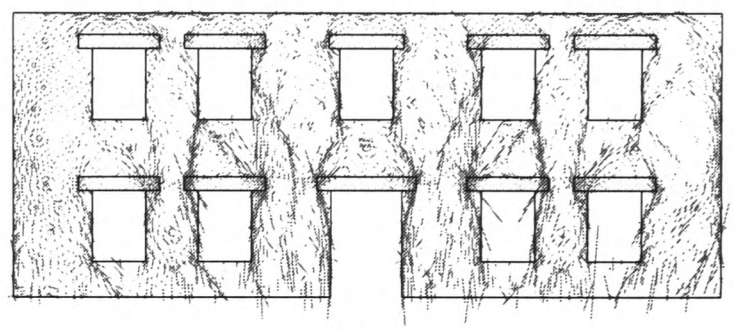
The no tension facade behaves approximately like a beam with its neutral axis near the top in this local sagging but horizontally tensile area.



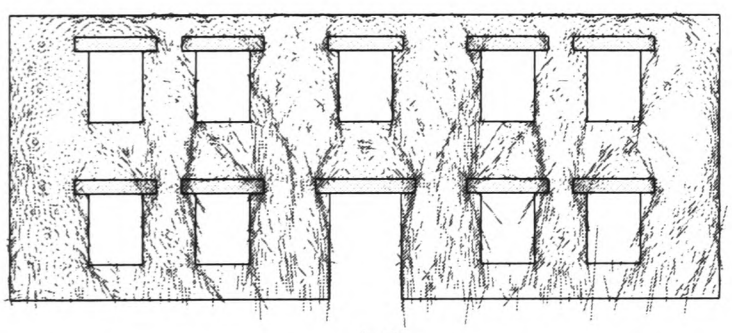
(1)



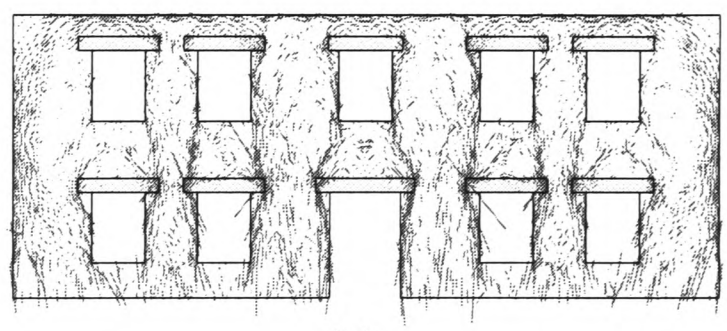
(2)



(3)



(4)



(5)

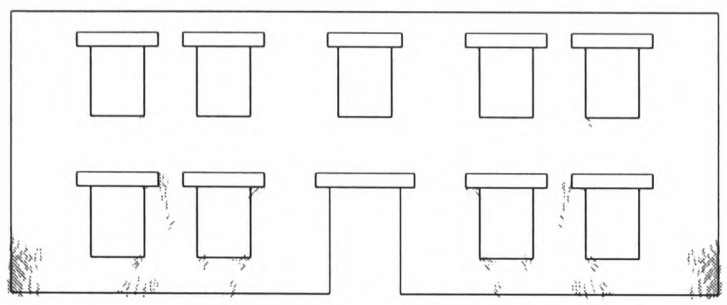
Figure 5.40: Stress Trajectory Plots Corresponding to e = 0, 5, 10, 15, 20m, $\gamma_b t$ = 10.0kPa(u223xx)

5.6 Summary and Conclusion

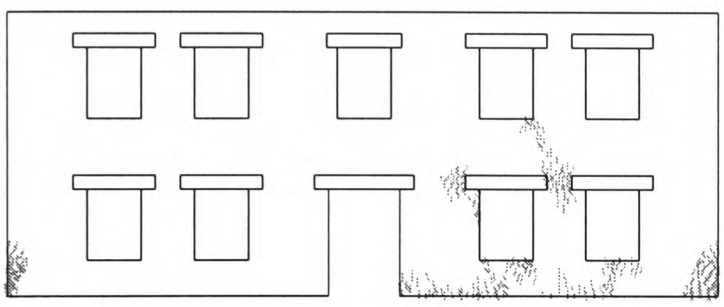
In this chapter the ground and masonry facade are analysed together in two dimensions. Soil is modelled by a nested yield surface model and the masonry facade by the elastic no tension model. Plane stress and strain elements are used for building and ground respectively. The two parts are connected by the tie elements developed in Chapter 3.

The weight of the building is applied first without the tunnel. Then the displacements in ground and facade due to the weight are reset to zero before the excavation but the state variables are kept unchanged. Tunnelling without a lining is simulated by removing the elements within the tunnel area. The process is assumed undrained.

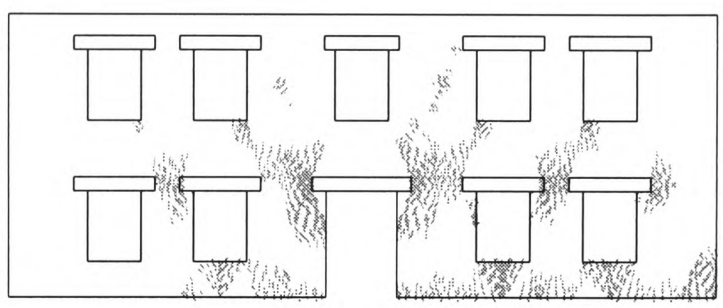
The combined analyses show that the weight of the building is a key factor in con-



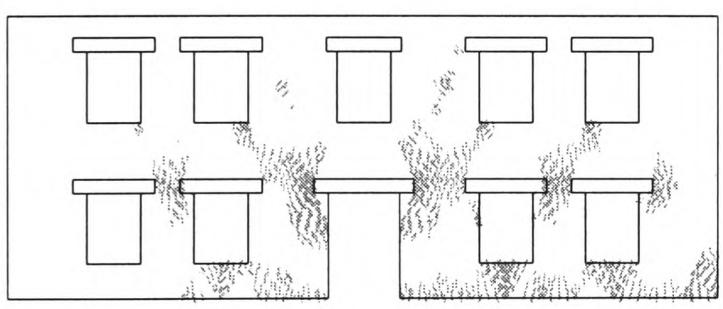
(1)



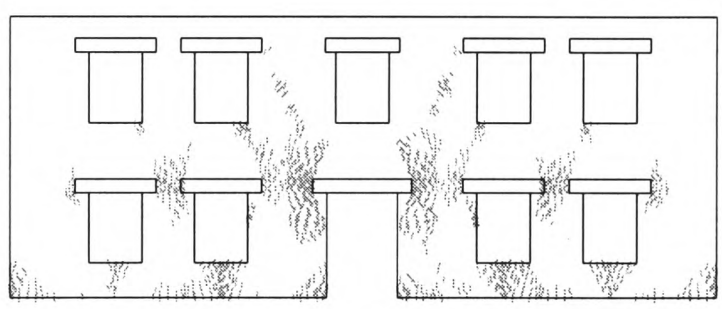
(2)



(3)



(4)

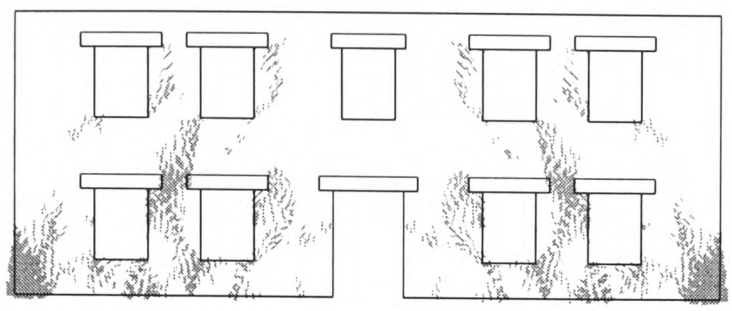


(5)

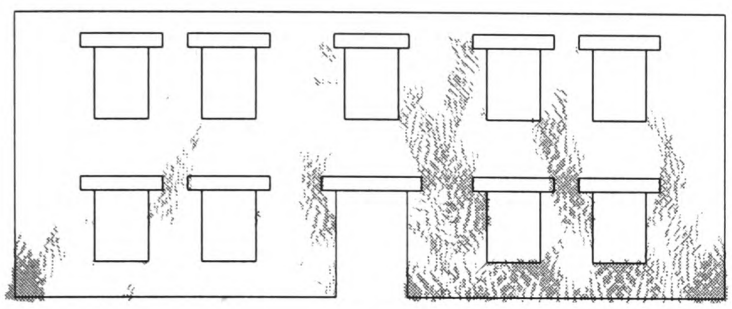
Figure 5.41: Cracking Patterns Corresponding to e = 0, 5, 10, 15, 20m, $\gamma_b t$ = 10.0kPa(u223xx)

trolling the average settlement under the building. When the facade is symmetrically located over the tunnel, the soil under the self-weight of the building has been previously partially yielded, so that it gives a larger average settlement than in the greenfield. Strong arching effects are observed in the masonry facade, which cause redistribution of the weight of the building and change the shape of the settlement trough. For a given weight of building, its stiffness will change the shape of the trough locally beneath it. When stiffness increases, the settlement trough becomes flatter.

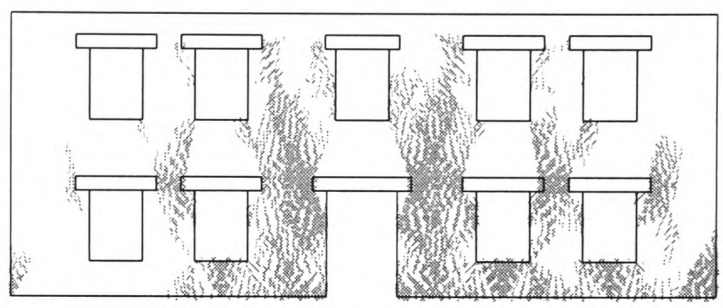
For a building of normal weight, the combined analysis gives less damage than applying the greenfield trough to the building. However, the large arching force may cause the ground to move outwards horizontally and impose tensile strain at the base of the facade, causing vertical cracks. When the building becomes heavy, it will drive the ground



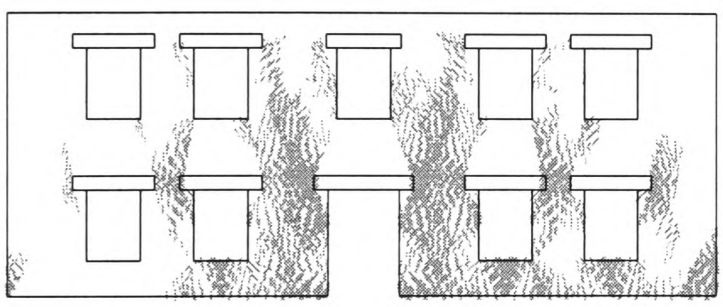
(1)



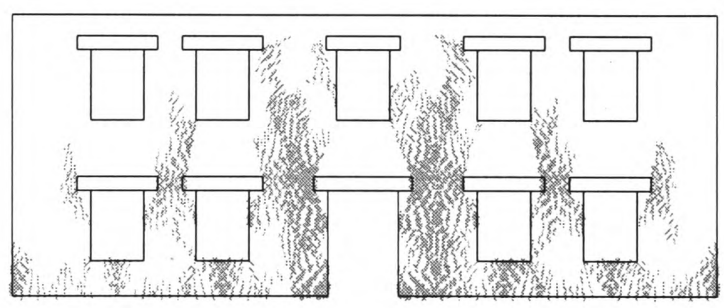
(2)



(3)



(4)



(5)

Figure 5.42: Cracking Patterns Corresponding to e = 0, 5, 10, 15, 20m, $\gamma_b t$ = 20.0kPa(u233xx)

to instability and large horizontal movements will occur and the facade will experience more serious damage.

In addition, the position of the masonry facade is another critical factor affecting the ground movements in the combined analysis. When the facade is located partially over the tunnel, it causes larger settlement at the corner near the tunnel than when symmetrically located. It also leads to an appreciable tilt.

When the facade is positioned in the overall hogging area, the self-weight may change the hogging mode beneath the facade to a local sagging. However, the ground beneath is in horizontal tensile strain, and this prevents the formation of stress arches within the building but instead causes vertical cracks to develop from the base of the facade.

It should be pointed out that consolidation after the building was built but before

tunnelling would be expected to change the stress distribution in the ground and increase the strength of the soil under the building. The undrained assumption in this chapter may overestimate the instability of the ground.

Putting a facade of unit thickness on a block of ground of same thickness also overestimates the stress in the ground, since the real stress distribution in the ground under a facade is a 3-D problem. In addition, skew tunnelling cannot be analysed by the 2-D method used in this chapter. Therefore, 3-D analyses are reported in the next chapter.

6

3-D Analysis of Settlement Damage Due to Tunnelling

6.1 Introduction

When a tunnel is excavated in the ground, a three dimensional stress and displacement distribution will be formed around the front face of the tunnel. At the ground surface, a wave of 3-D displacements and strains will advance while the tunnelling progresses until the ground reaches a final plane strain state (Lee and Rowe, 1990a,b) . Thus the settlement, and its effects on the buildings when calculated using plane strain conditions do not reflect the whole situation. This problem becomes more critical if the building is not symmetrically located with respect to the tunnel, in which case the plane strain approximation will be even less appropriate. Thus 3-D analysis is necessary for settlement and damage prediction.

Furthermore, the stress distribution beneath the building in the ground is also three dimensional, particularly in cohesive ground, since the adjacent soil gives vertical support. From this point of view, a 3-D analysis is also required.

Although the importance of 3-D analysis has been recognised for a long time, very few 3-D analyses have been performed due to the extensive computation time and mem-

No.	Description	Nodes	Elements	CPU time	Elapsed Time	Machine
SG	Symmetric greenfield	3658	2166	547647 s	157:22 h	Sun Sparc 10
SHN	Symmetric run with standard building, no tension model	5189	2923	951537 s	297:40 h	Sun Sparc 10
SHE	Symmetric run with standard building, elastic model	5189	2923		313:43 h	Sun Sparc 10
SLN	Symmetric run with light building, no tension model	5189	2923	1004930 s	314:03 h	Sun Sparc 10
SLE	Symmetric run with light building, elastic model	5189	2923	1003199 s	313:34 h	Sun Sparc 10
UG	unsymmetric greenfield	3541	2243	339325 s	94:48 h	Sun Ultrasparc 2
UHN	unsymmetric run with standard building, no tension model	5423	3133	736773 s	205:22 h	Sun Ultrasparc 2

Table 6.1: 3-D analyses

ory demand required. Almost all the previous 3-D analyses focus on the behaviour of the tunnel itself and greenfield settlements (Katzenbach and Breth, 1981), rarely involving the interaction between the buildings and the ground. Because of the extensive time and memory demand, 3-D analyses used to be run on supercomputers (Lee and Rowe, 1990a). Modern workstations are now sufficiently powerful to carry out these analyses. However only seven 3-D runs were done for this thesis due to the limitation of computer resources (Table 6.1).

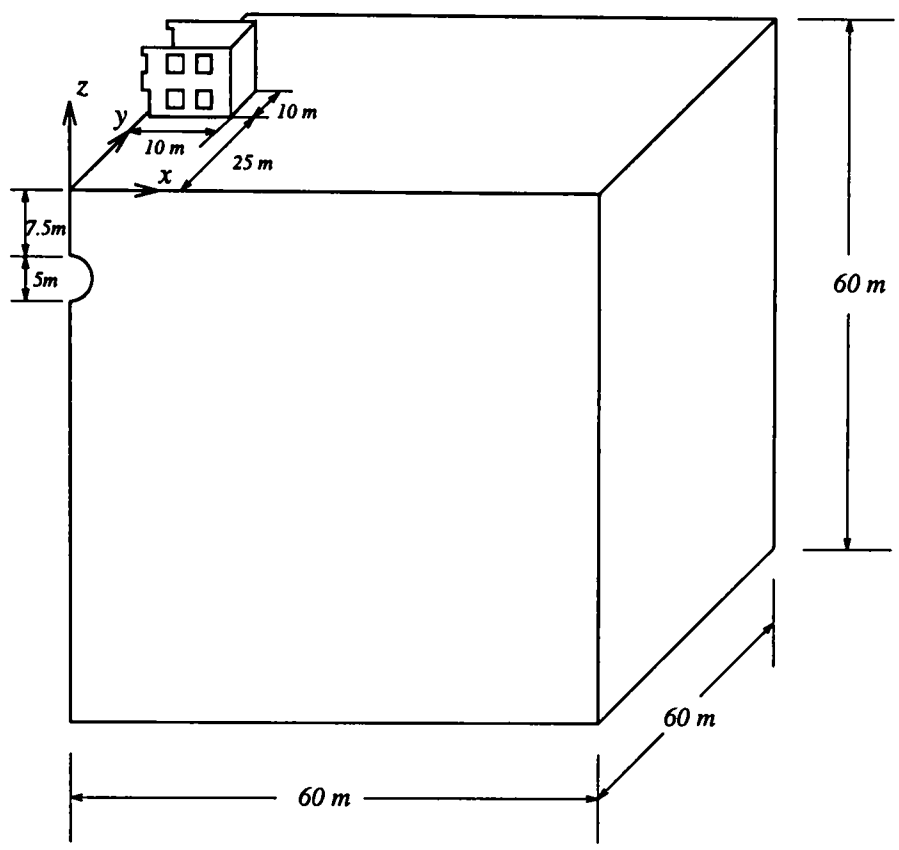


Figure 6.1: Ground Block with Building

6.2 Model used in Symmetric Runs

A 120m × 60m × 60m block of ground and a 20m × 10m × 8m facade box consisting of two facades and two plain end walls with thickness t = 1m are combined together to be analysed using the 3-D finite element method. A tunnel is excavated symmetrically under the building. Due to the symmetry of the problem, only half of the ground block and half of the facade box were analysed (Figure 6.1).

6.2.1 Building

The detailed layout and finite element meshes of the front and back facades are the same as used in previous chapters and can be found in Figures 4.6 and 4.7.

The size and mesh for the end wall are the same as the plain wall used in Chapter 4.

The material parameters are also the same as those in the previous analyses, except that the unit weight is 20kN/m^3 for the the standard building and 3kN/m^3 for the light building.

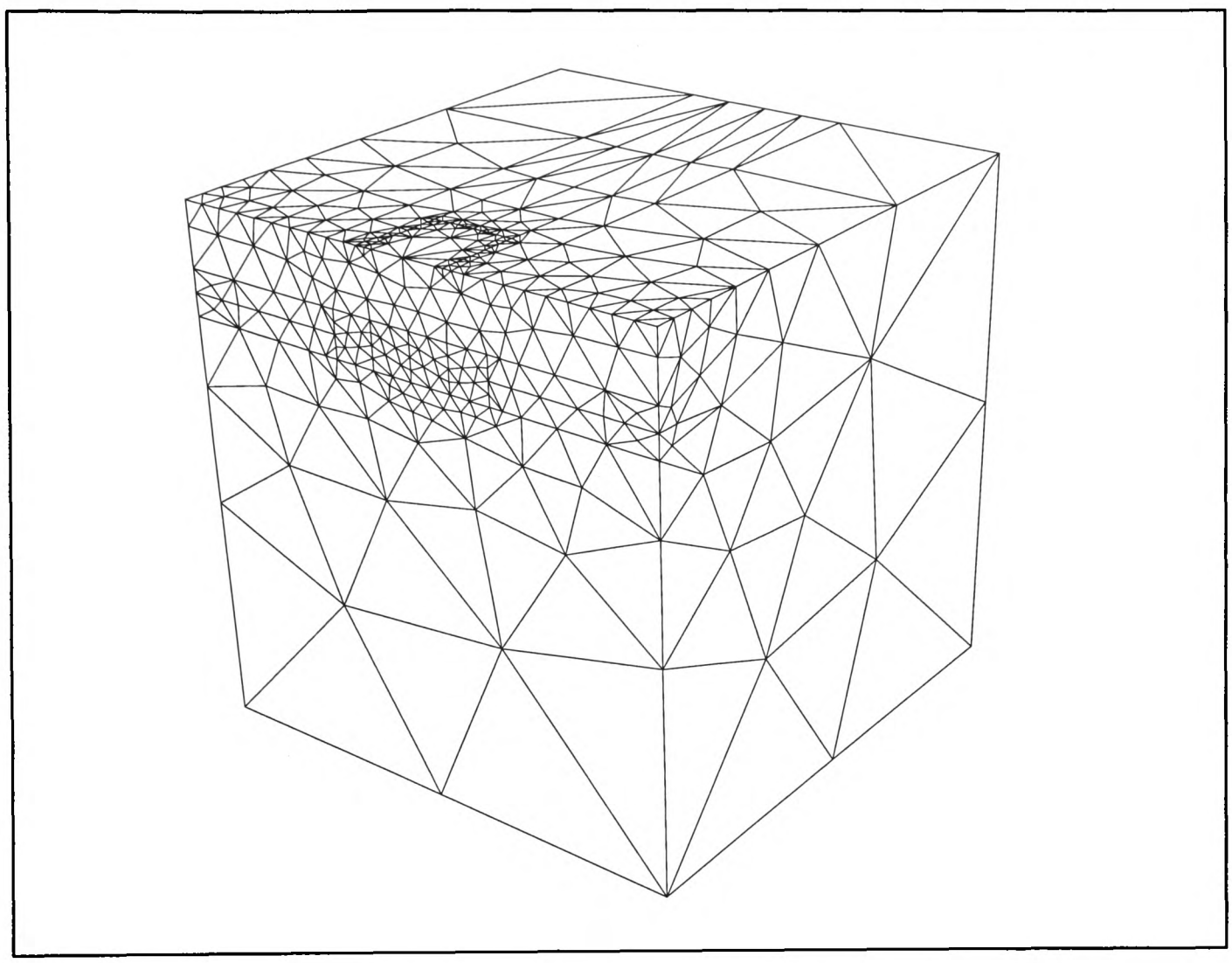


Figure 6.2: 3-D Finite Element Mesh for Ground in Symmetric Runs

6.2.2 Ground

The mesh for the ground (Figure 6.2) was generated using the computer-aided design package I-DEAS (Augarde, 1997). It consists of 2166 ten-noded tetrahedral solid elements. The building and ground meshes are combined by the tie elements developed in Chapter 3 which connect 2-D and 3-D nodes. It should be pointed out that the internal details of the mesh are not strictly symmetric about the plane $y = 30$m.

The nested yield surface model used in 2-D analysis was used in the 3-D analysis. The properties of the soil are as described in Chapter 5.

6.2.3 Boundary Condition

On all the side surfaces of the ground block, the nodes are constrained with a zero out-of-plane displacement condition but the faces are treated as smooth. On the bottom

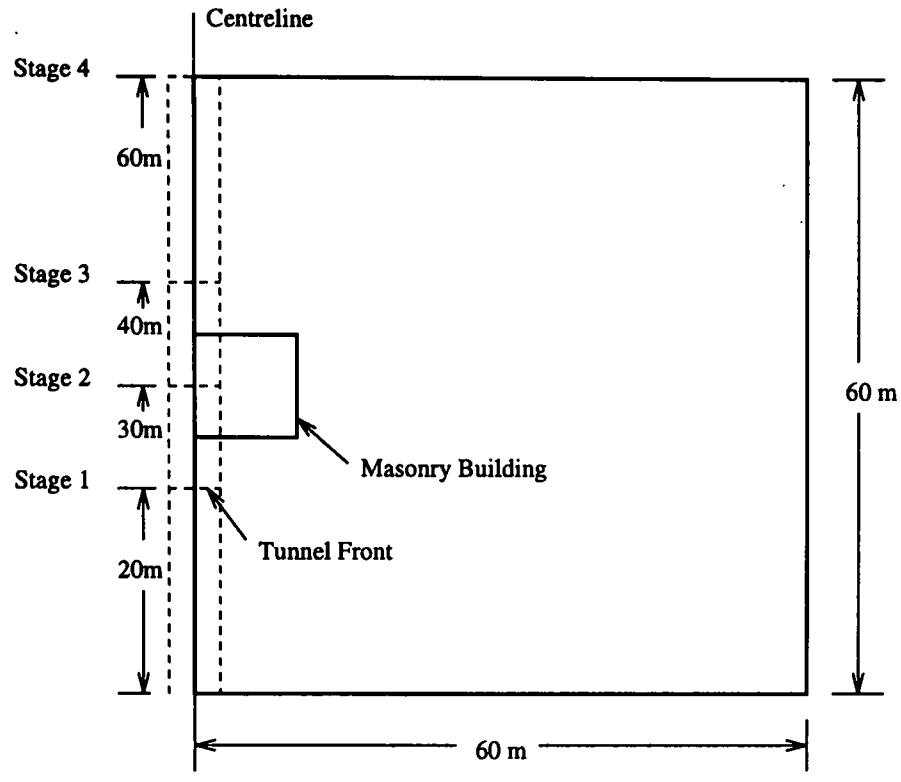


Figure 6.3: Positions of Tunnel Front in Symmetric Runs

plane, all the nodes are fully fixed.

In addition, the nodes in the facades along the centreline are not allowed to move horizontally because of the symmetry.

6.2.4 Loading Process

The excavation is simulated by removing the elements within the tunnel area. The process is divided into four stages, when the tunnel face reaches $\frac{1}{3}$, $\frac{1}{2}$, $\frac{2}{3}$ and the whole length (Figure 6.3).

At each stage the nodal forces representing the excavation are applied in 40 increments. Although more excavation stages and more increments would be advantageous for the accuracy of the solution, computation time limits the application of large numbers of stages and increments.

The self-weight of the soil is simulated by applying the corresponding initial stresses in the ground. In the combined analysis, the self-weight of the building is applied to the system before the excavation of the tunnel. Afterwards the displacements and strains caused by the weight of the building are reset to zero before the excavation commences, but the stresses in both building and ground are kept unchanged to record the loading

history in the ground. The cracking strain in the building is reset to zero as well, so that the cracking damage reported here is only that due to the tunnelling process.

6.3 Symmetric Runs

6.3.1 Greenfield, Run SG

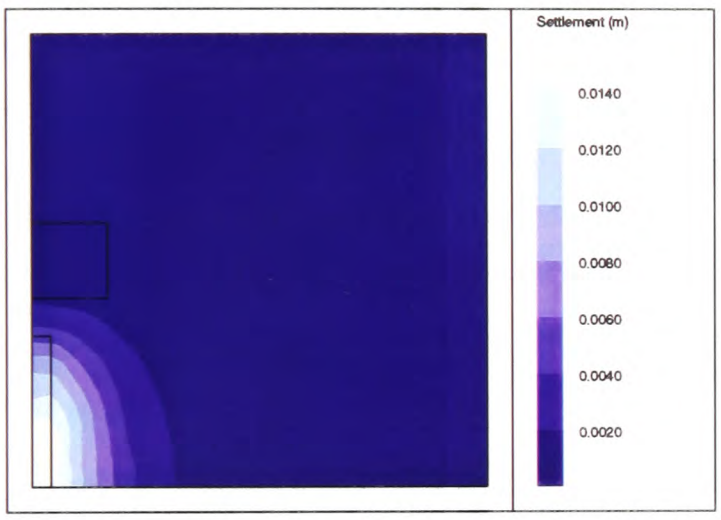
Excavation in the greenfield results in a settlement distribution on the ground surface similar to a Gaussian curve. As the tunnel advances, the settlement wave can be clearly seen in Figure 6.4. After the excavation is completed, the settlement along the y-axis should be uniform. However, since the ground is not evenly meshed, a slightly non-uniform distribution is observed. Figure 6.5 shows the settlement and horizontal movements at $y = 25$m, where the front facade will be located in the combined analyses. The position of the point of inflexion is at 7.0m from the centreline of the tunnel at the completion of excavation. This final settlement trough is very similar to the 2-D greenfield results. Thus the front and back facades on such settlement troughs will experience similar cracking damage, and this is shown in Figure 6.6.

The ground movements beneath the end wall (Figure 6.7) are also similar to the empirical shape of the settlement trough in the longitudinal direction as discussed in Chapter 4. The trough changes from hogging to sagging and then finally to a horizontal flat line. In response, the end wall has vertical cracks at early stages, which reclose later when the settlement trough becomes a horizontal line (Figure 6.8).

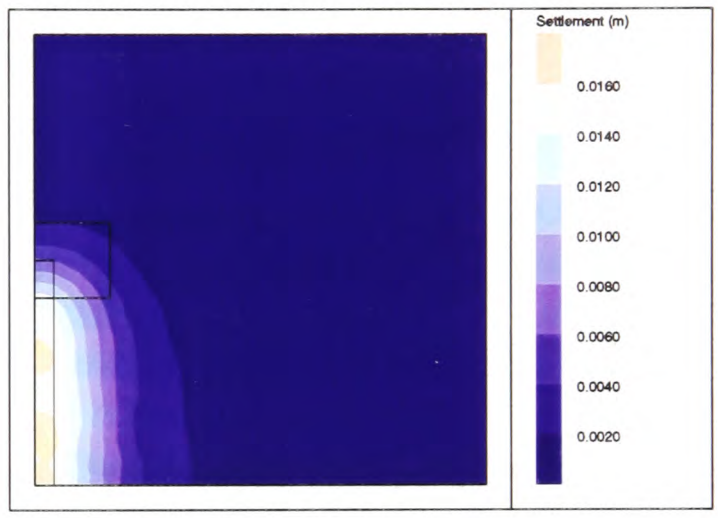
6.3.2 Combined Analysis with Building of Standard Weight

No Tension Model, Run SHN

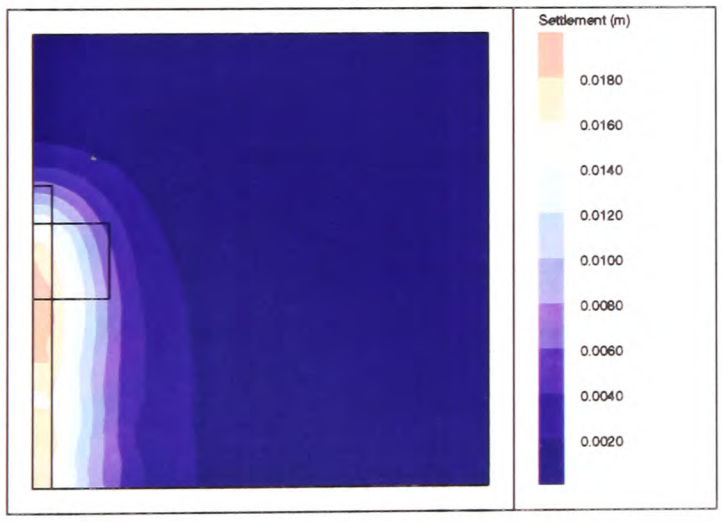
The elastic no tension masonry facade box was combined with the block of ground to simulate a complete ground-structure system. The presence of the building changed the ground movements. Figure 6.9 shows the plan views of the settlement on the ground surface. It can be seen that the combined analysis predicts larger average settlement beneath the facades and end walls than the greenfield results. This can be seen more clearly in Figures 6.10, 6.11 and 6.12 which show the settlement troughs beneath the



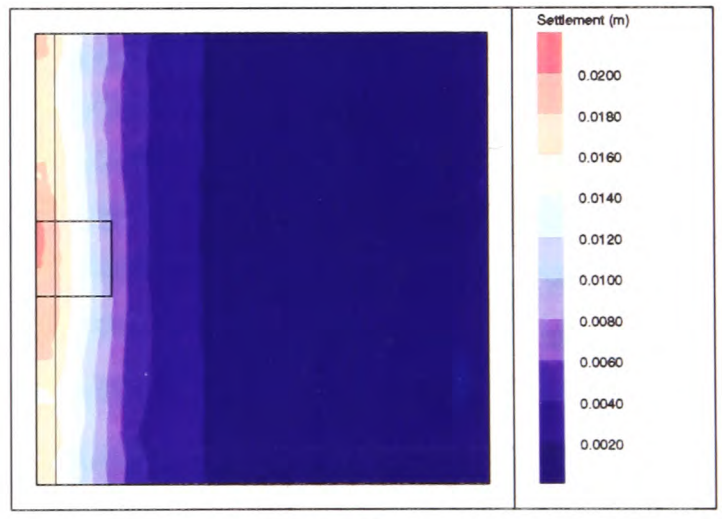
(1)



(2)

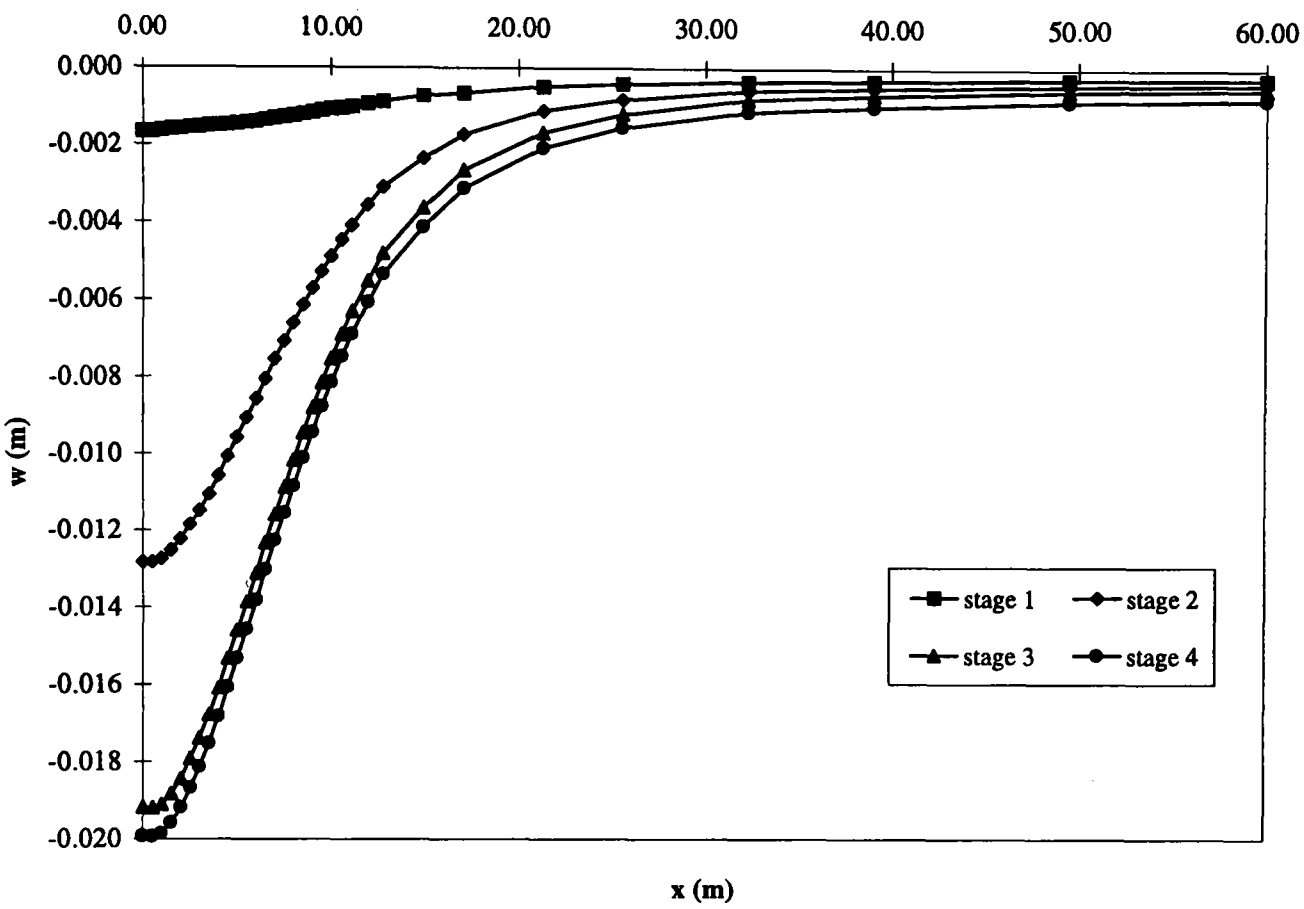


(3)

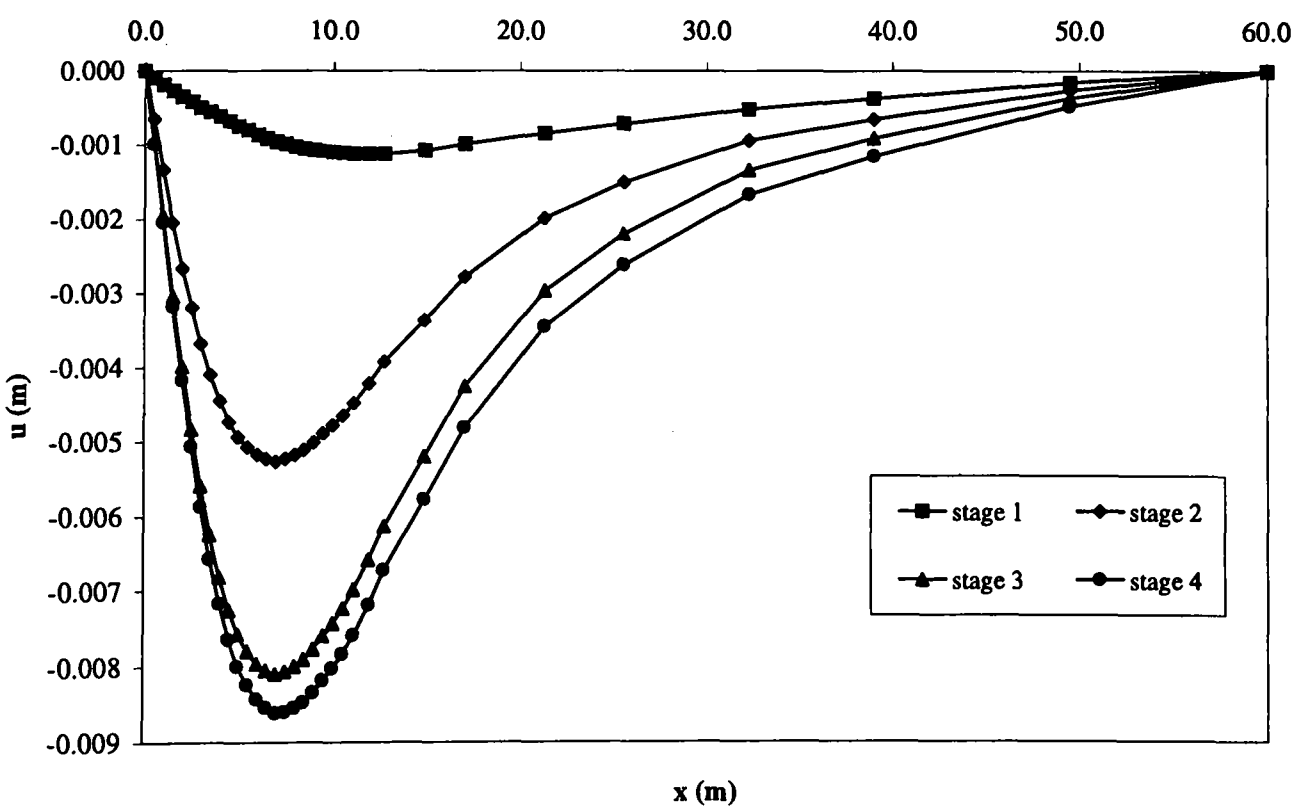


(4)

Figure 6.4: Settlement Wave in at Stages 1 to 4, the Symmetric Greenfield(SG)

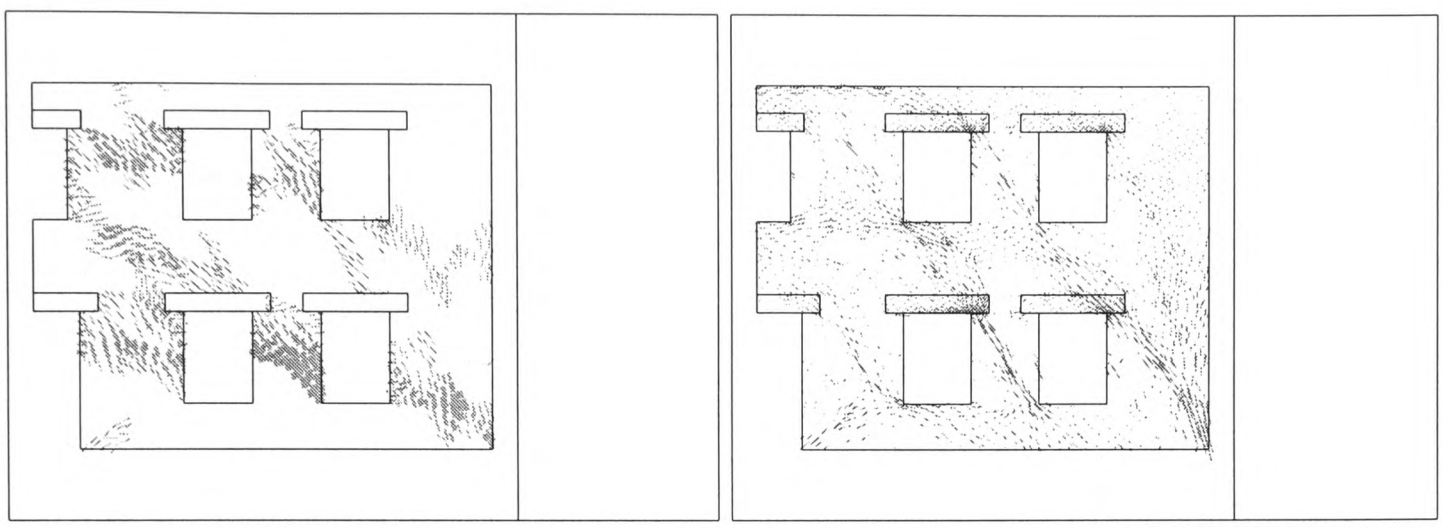


(1) Settlements



(2) Horizontal Movements

Figure 6.5: Ground Movements at y = 25 m, Symmetric Greenfield(SG)



(1) (2)

Figure 6.6: (1) Cracking Pattern and (2) Stress Trajectory in Front Facade, Symmetric Greenfield(SG)

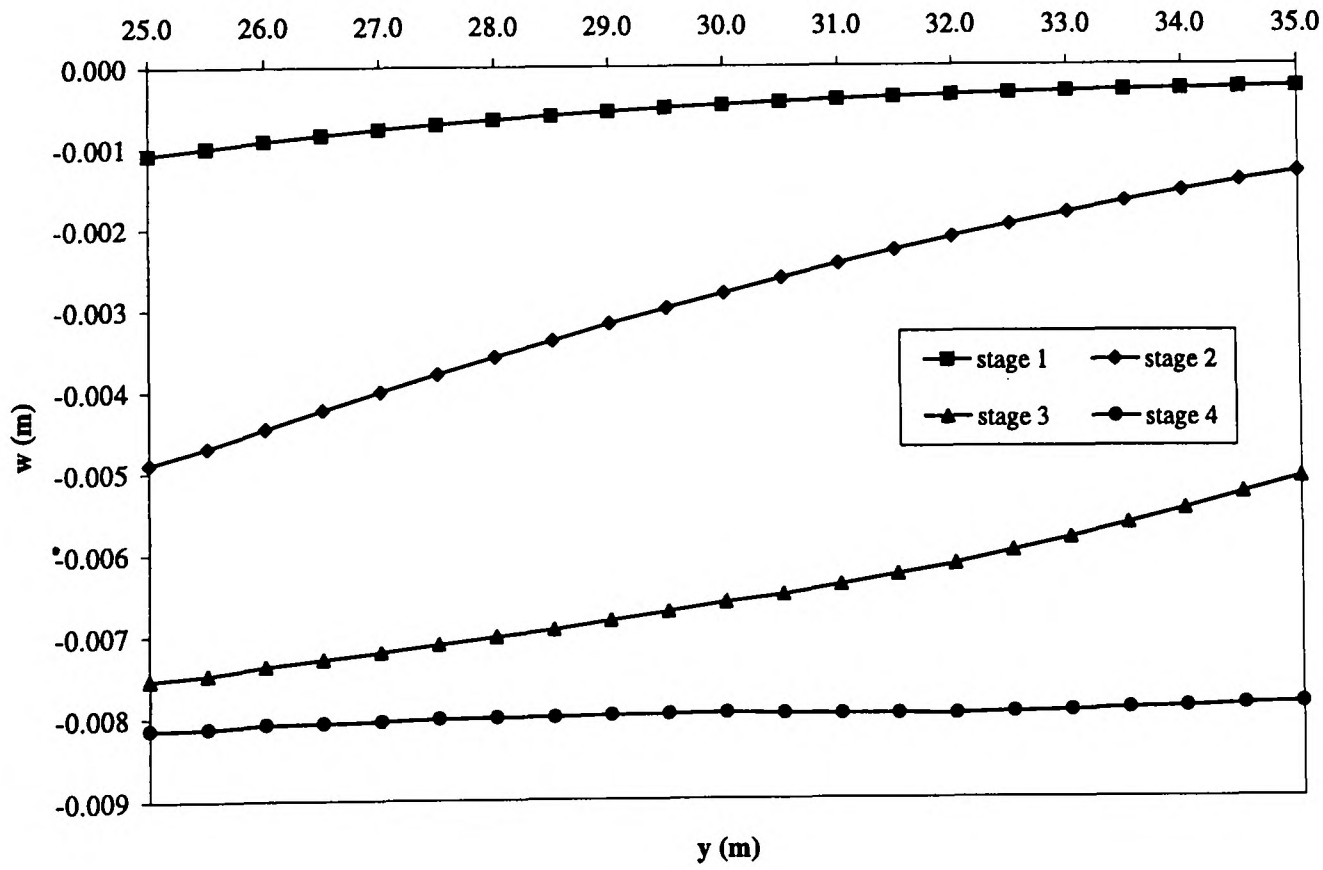
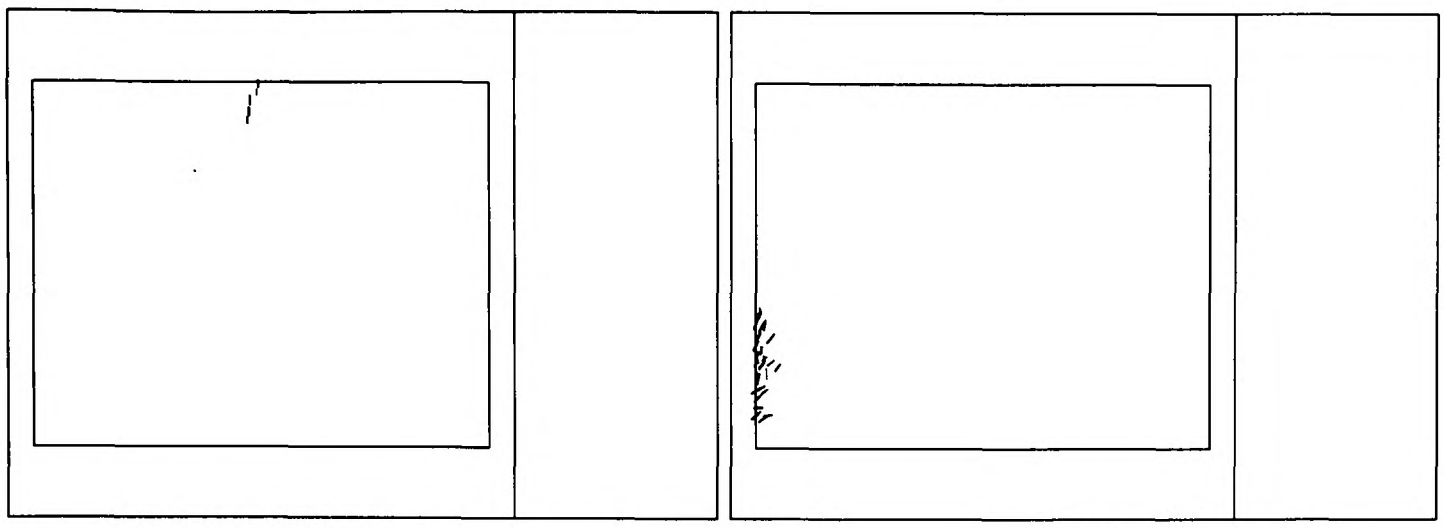


Figure 6.7: Settlement under End Wall, Symmetric Greenfield(SG)



(1) (2)

Figure 6.8: Cracking Patterns in Side End wall (1) at Stage 1 and (2) at Stage 4, Symmetric Greenfield(SG)

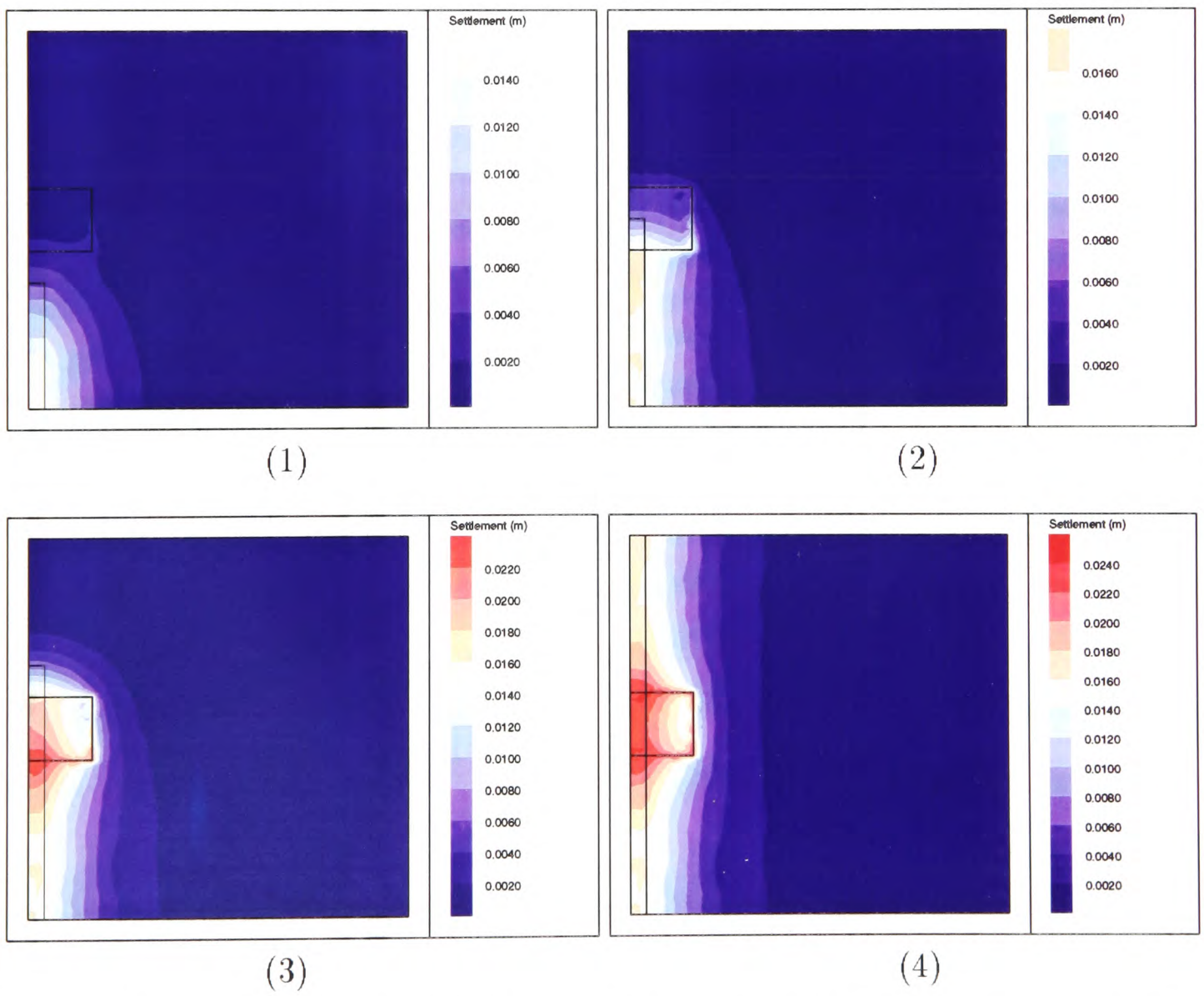


Figure 6.9: Settlement Wave in All Stages, the Symmetric Combined Analysis with No Tension Standard Building(SHN)

front, and back facades and the end wall.

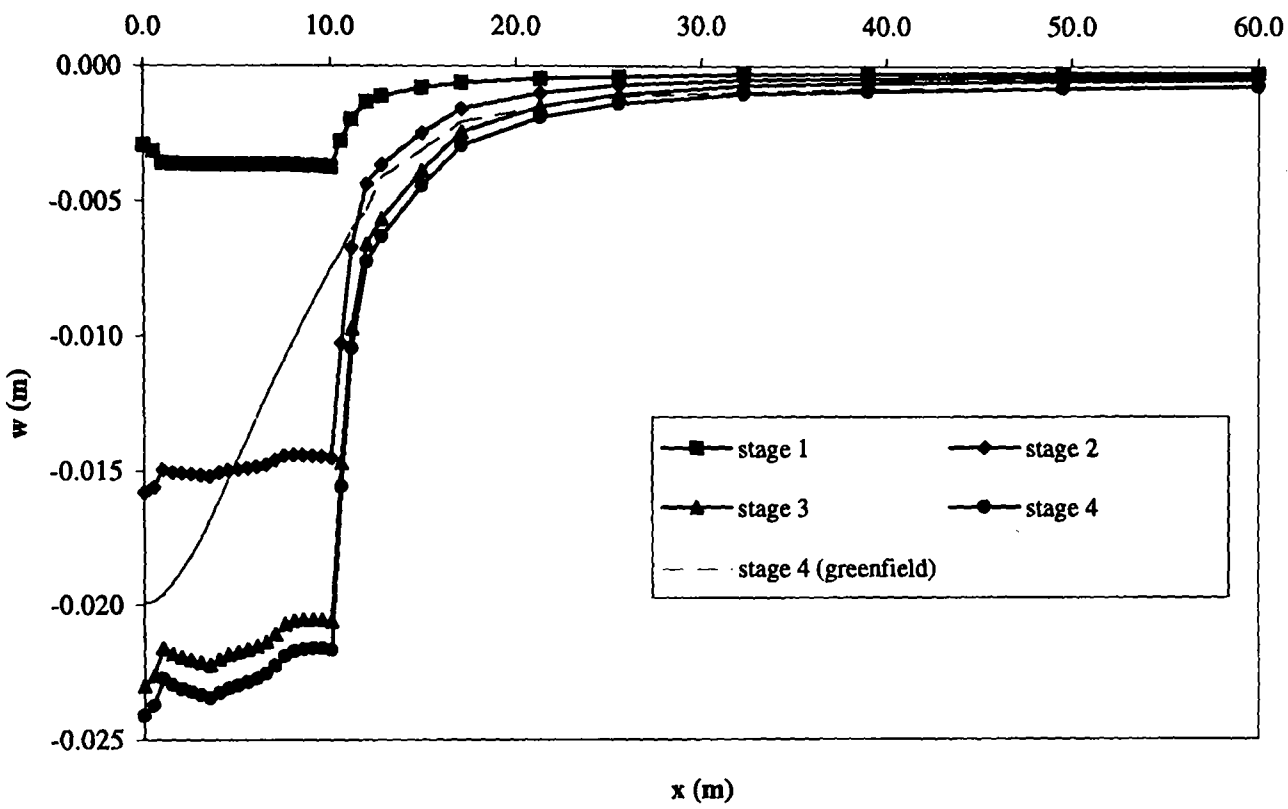
The settlement troughs underneath the facades (Figure 6.10-(1) for the front facade and Figure 6.11-(1) for back facade) are much flatter than in the greenfield case. Although the locations of the front and back facades are symmetric about the line of $y = 30$m, they experienced different settlement waves and were influenced by the interaction from the end wall, thus giving slightly different settlement troughs. As observed in the 2-D analysis, the settlement troughs underneath the facades are divided into three parts, corresponding to the stress arches developed in the masonry.

The horizontal displacements beneath the facades are much smaller (Figures 6.10-(2) and 6.11-(2)) than in the greenfield due to the resistance of the building. At most stages the horizontal movements are inward towards the centreline of the tunnel, as compared with 2-D analyses where large outward horizontal displacements were observed.

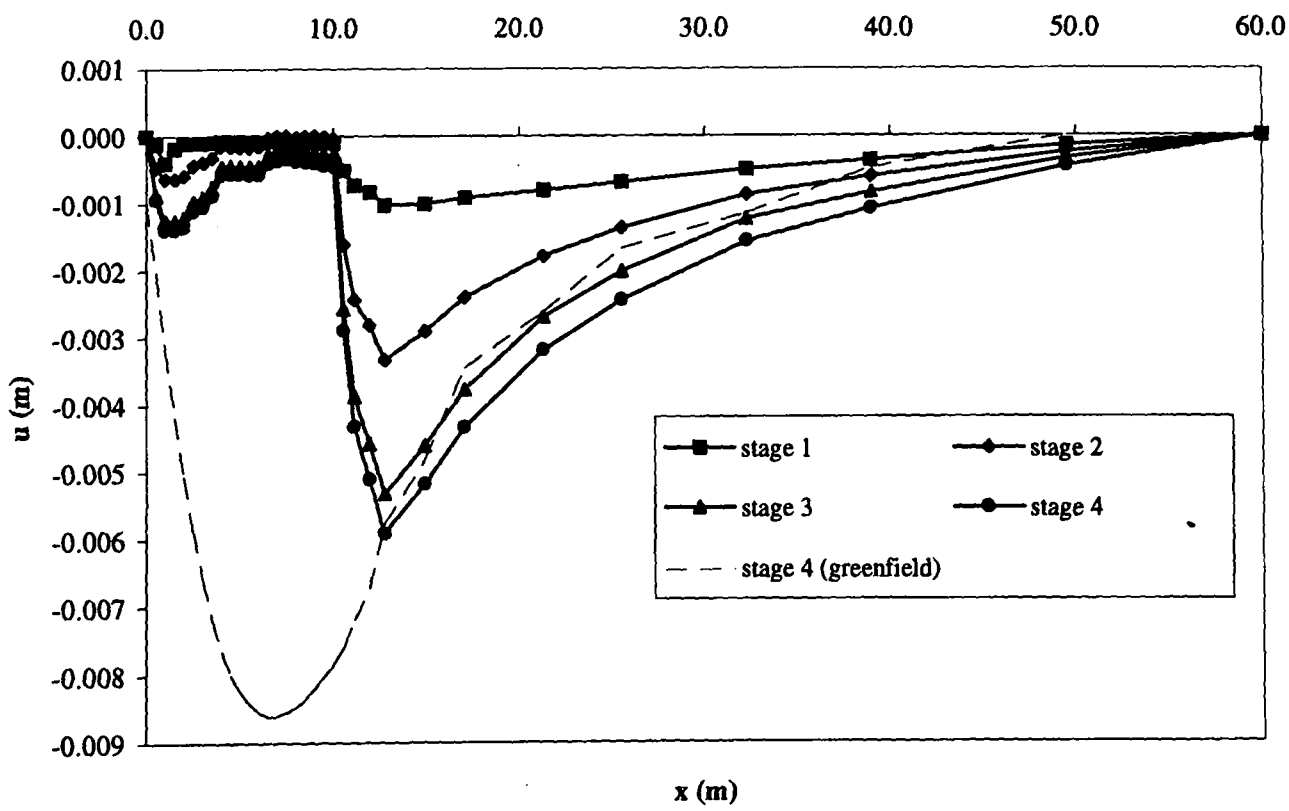
Under the end wall (Figure 6.12), the trough predicted by the combined analysis is similar to the greenfield prediction. However, the settlement increases at the two corners, which follow the large settlement of the front and back facades. Horizontal tensile strains also appear at the two ends (Figure 6.12). These tensile strains are due to the opposite horizontal movements of the two corners of the end wall within its plane. This phenomenon can be explained by the effect of soil tending to move around the corner.

In general, the excavation of the tunnel causes the ground to move towards the tunnel face. The movement vectors have two components, u and v, along the x- and y-axes parallel to the facades and the end wall respectively. When the soil reaches a corner between the facades and the end wall, it is blocked by the facade along the x-direction, since the facades have high compressive stiffness, especially when arches are formed. Because the mass translation must be continuous, the flow of soil changes direction in order to avoid the stiffness of the facades. This gives rise to components of soil movement in the y direction which cause tension in the end wall at the corners. This corner effect is well illustrated by Figure 6.13 which shows the total ground movement vectors around the end wall at the ground surface, at the completion of the excavation in the greenfield and in the combined analysis.

In a similar way to the 2-D analysis, the influence area of the building is small.

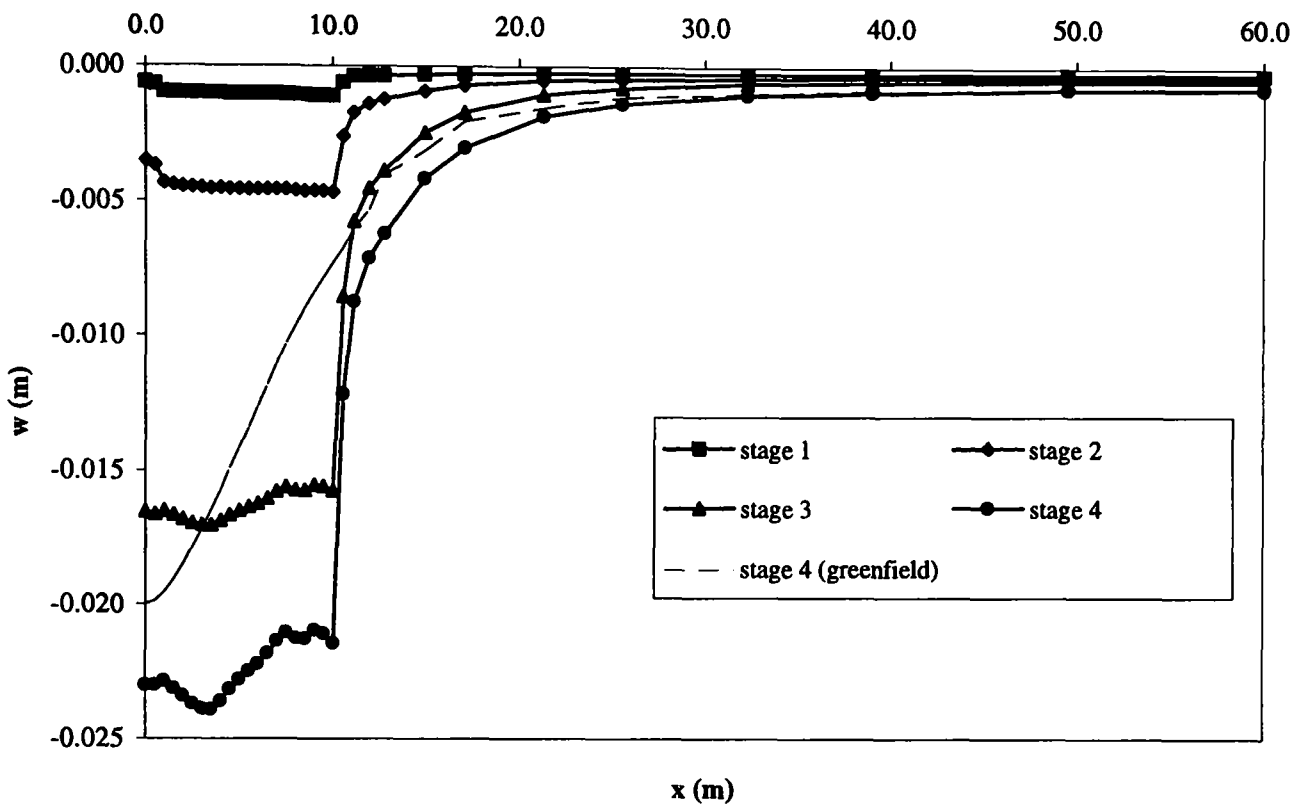


(1) Settlements

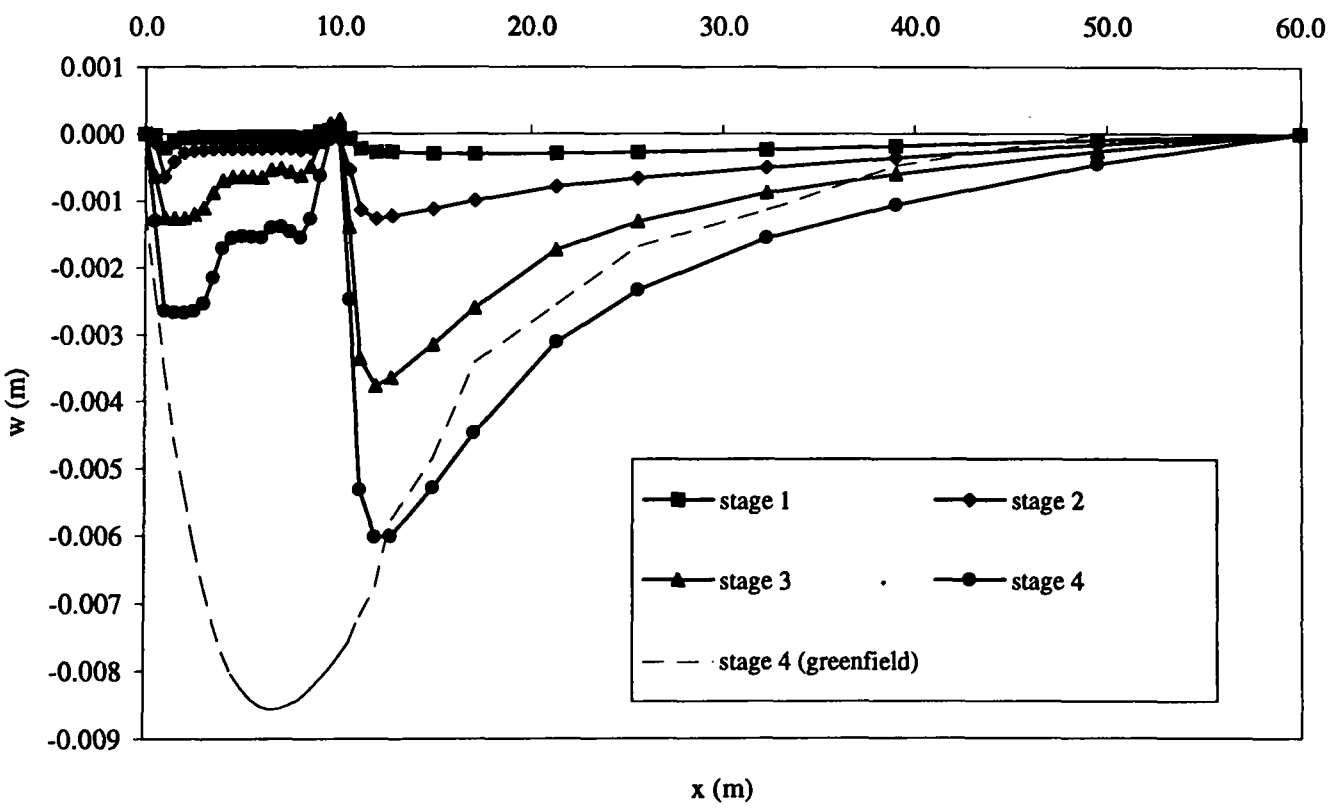


(2) Horizontal Movements

Figure 6.10: Ground Movements at y = 25 m, Symmetric Combined Run with No Tension Standard Building(SHN)

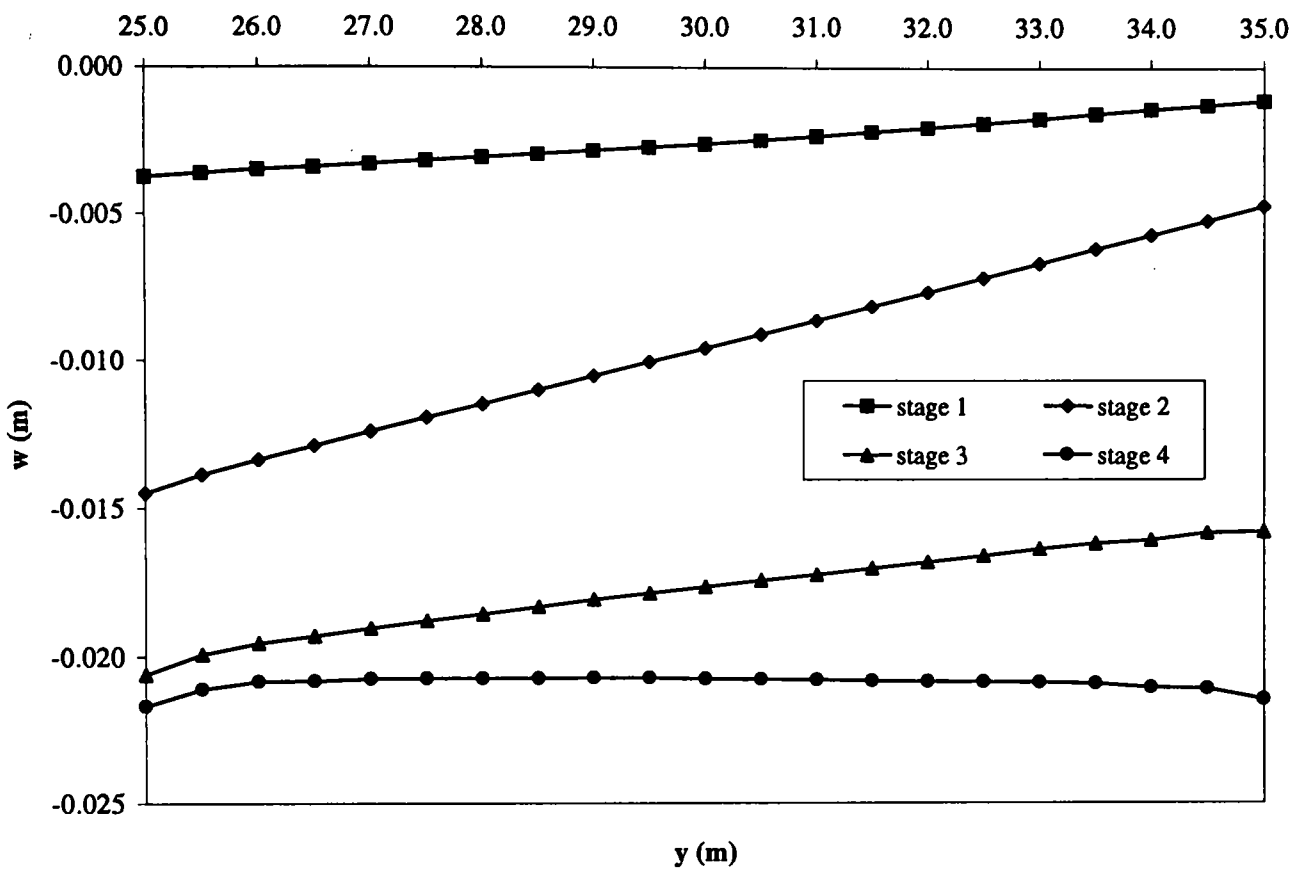


(1) Settlements

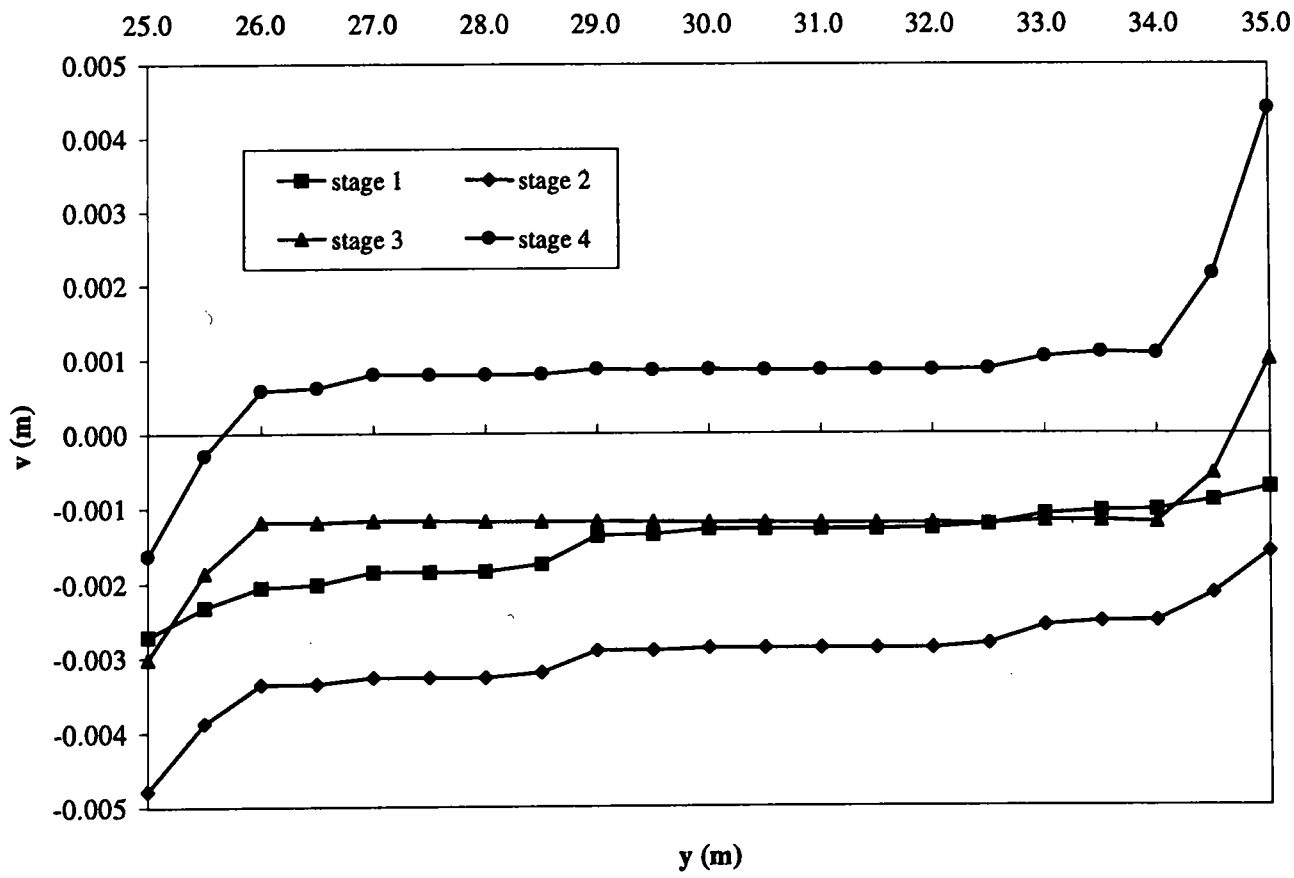


(2) Horizontal Movements

Figure 6.11: Ground Movements at y = 35 m, Symmetric Combined Run with No Tension Standard Building(SHN)

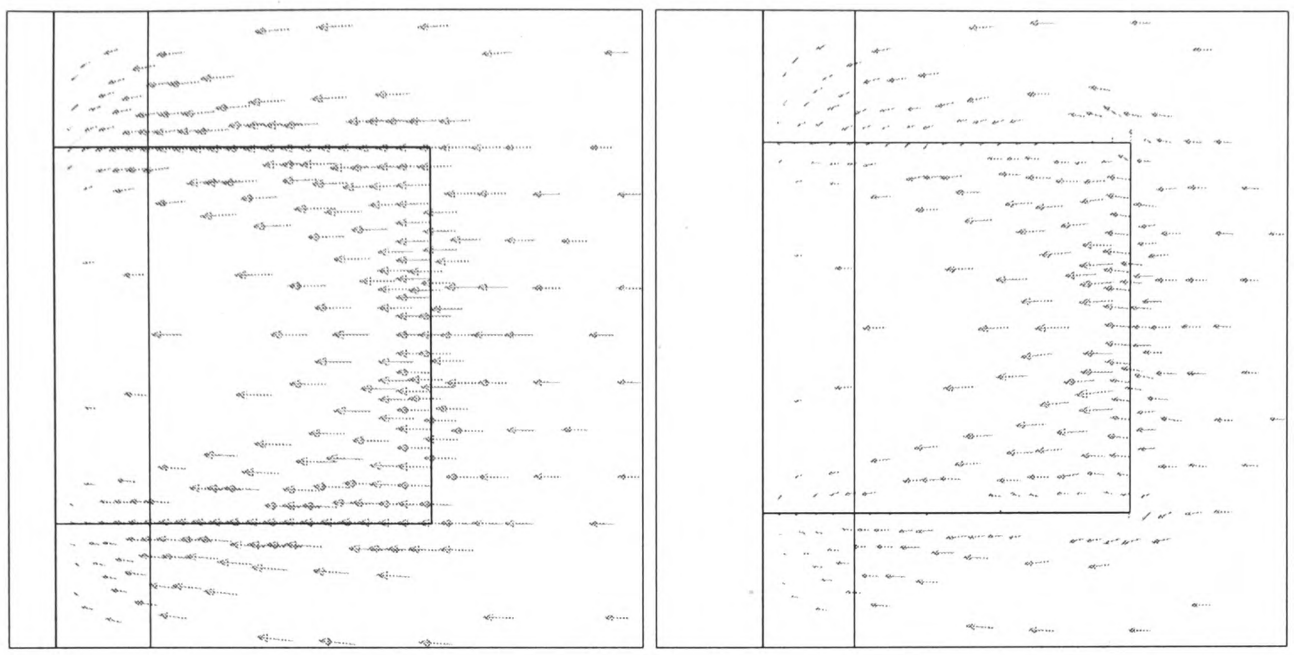


(1) Settlements



(2) Horizontal Movements

Figure 6.12: Ground Movements at x = 10 m, Symmetric Combined Run with No Tension Standard Building(SHN)



(1) (2)

Figure 6.13: Soil Movement Vector Plots around Building, at Stage 4, (1) Greenfield (SG), (2) Combined Analysis (SHN).

Figure 6.14 exhibits the ratio of the settlements of the combined analysis against that of the greenfield. The ratio under the facade is greater than 1.0 since the building sinks into the ground. It reduces rapidly outside of the facade. When $x = 15.0$, the difference between the analyses is less than 10%.

Serious damage is not observed in the building in the combined analysis. In the front facade (Figure 6.15), the cracks are located along the stress arches in the middle of the facade in the sagging mode. Near the corner, where the ground is in hogging and tensile horizontal strain occurs, some cracks are vertically oriented. The most serious cracking happens in the ground floor between the windows and the far end corner.

In the back facade (Figure 6.16), the final cracking pattern is similar to the front facade but has some minor differences due to the different troughs.

The combined analysis shows that there is not very serious damage in the end wall, except for two major cracking areas around the corners (Figure 6.17) which correspond to the horizontal tensile strains in the ground caused by the corner effect. Such a local damage can only be predicted by the 3-D analysis. At the early stages, the horizontal movement along the end wall also causes tensile strain at the base and leads to the onset of some vertical cracks in the middle of the end walls (Figure 6.17(1)).

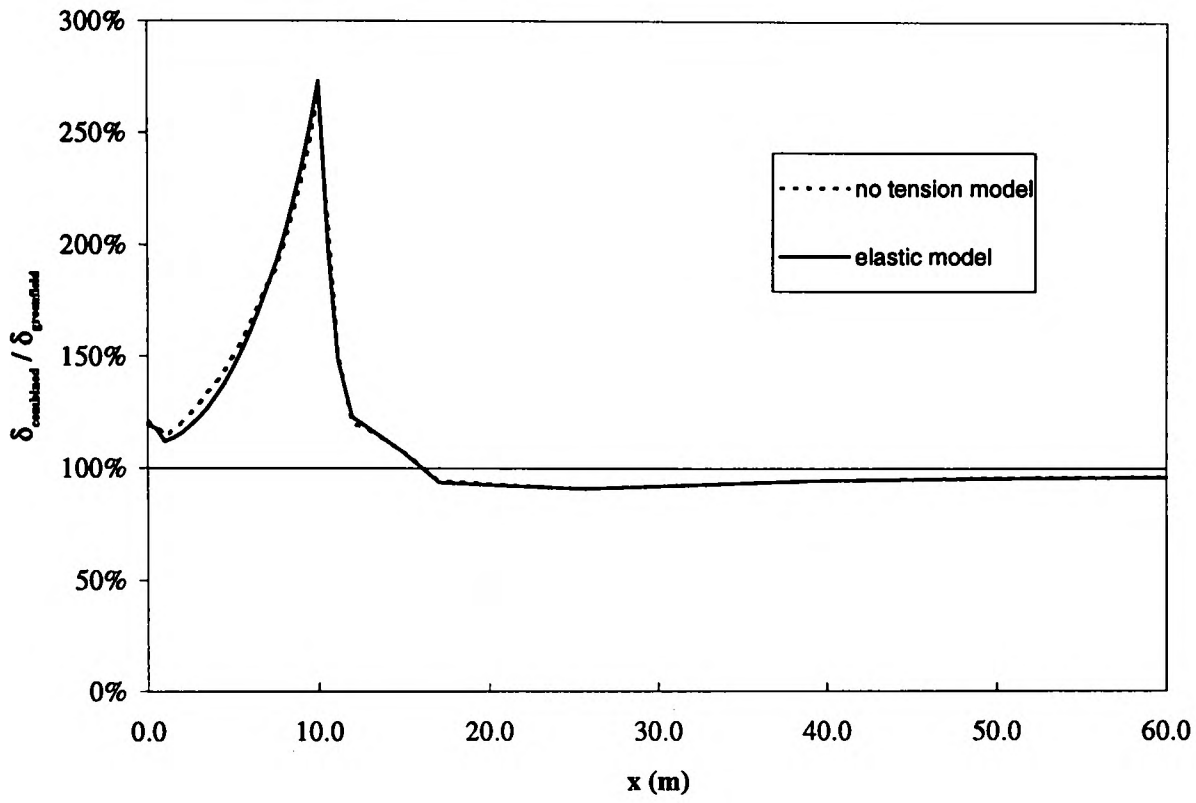


Figure 6.14: Ratio of Settlements under Facade against Greenfield(SHN)

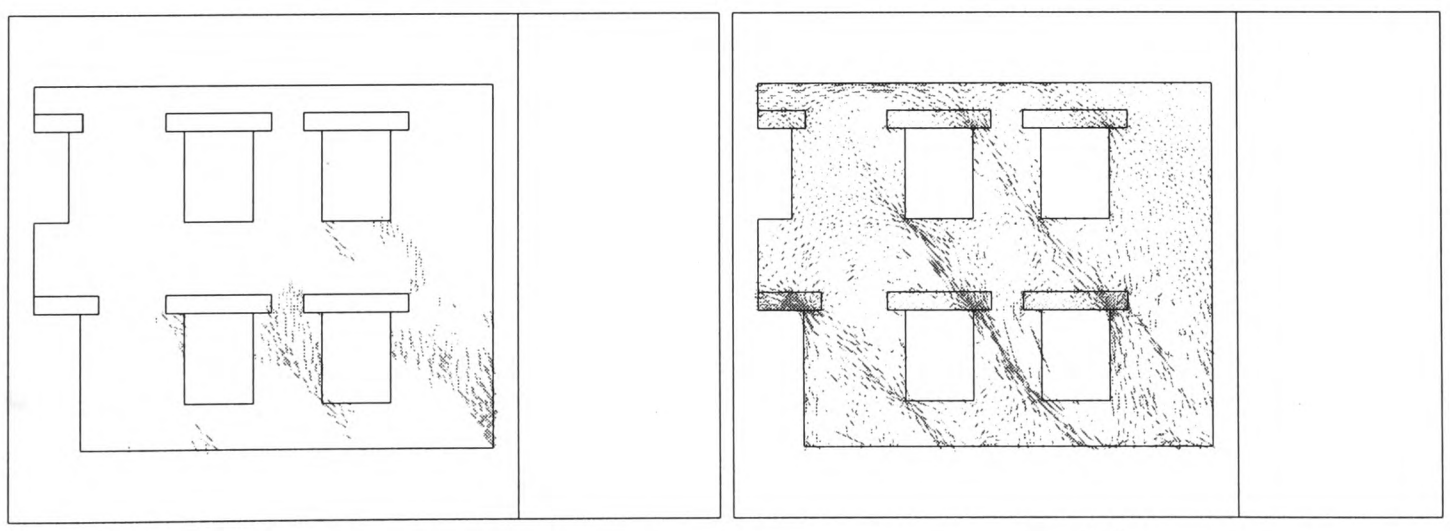
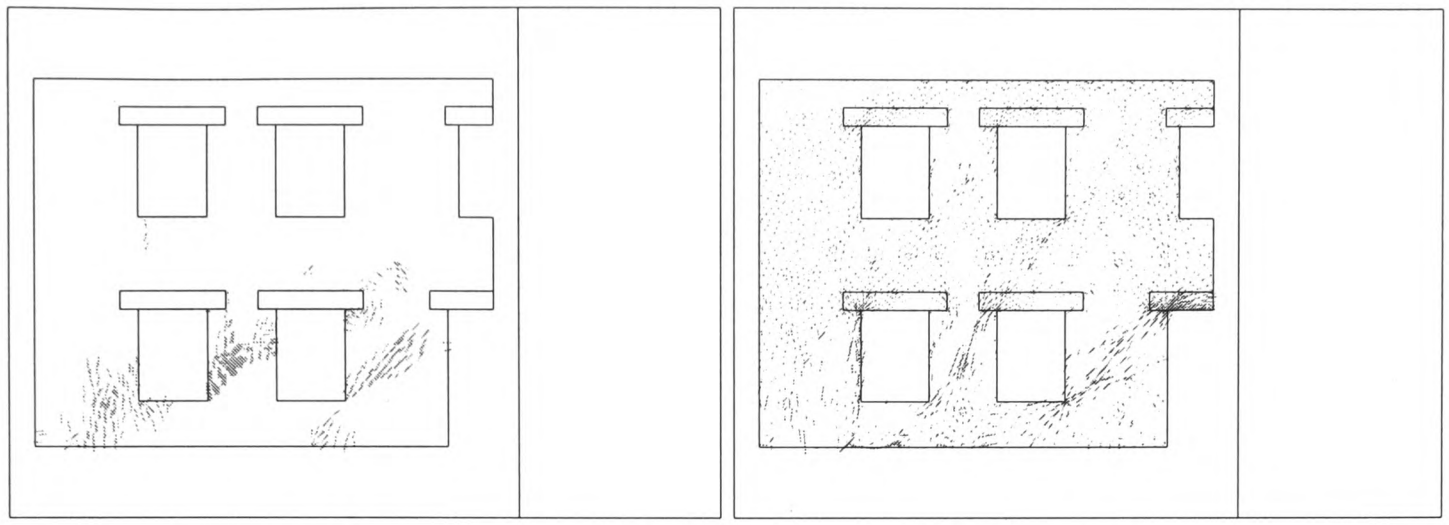


Figure 6.15: (1) Cracking Pattern and (2) Stress Trajectory in Front Facade at Stage 4, Symmetric Run Combined with Standard Facade, No Tension Model(SHN)

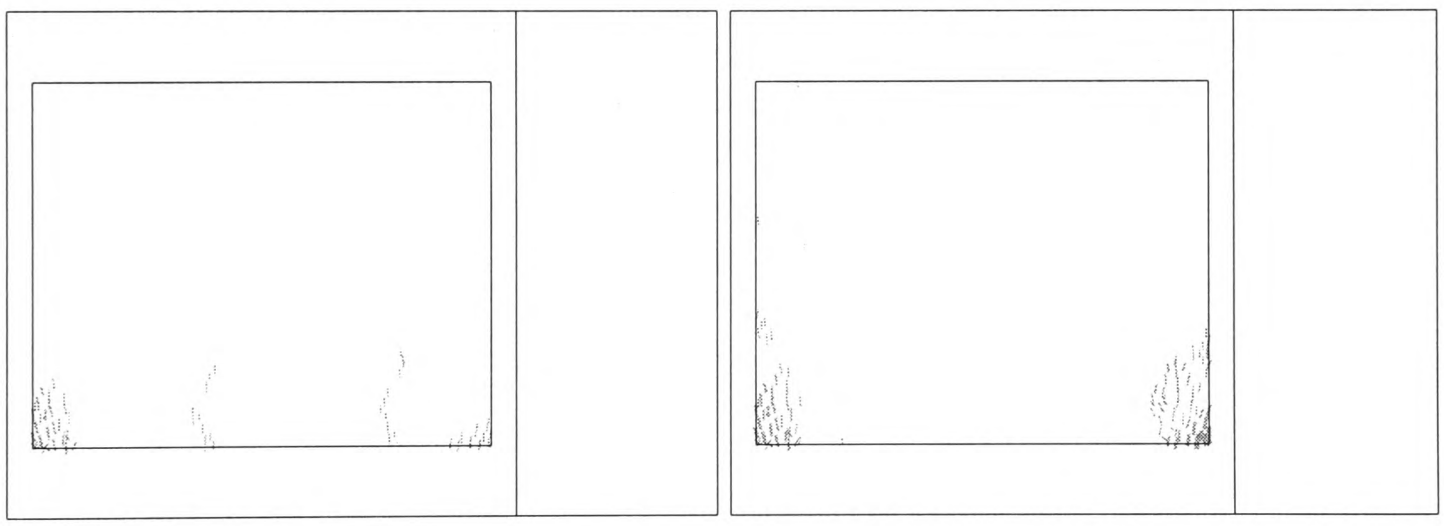
Elastic Building, Run SHE

The same problem was reanalysed using the elastic building model. The settlement trough and the horizontal movement under the front facade is shown in Figure 6.18. It



(1) (2)

Figure 6.16: (1) Cracking Pattern and (2) Stress Trajectory in Back Facade at Stage 4, Symmetric Run Combined with Standard Facade, No Tension Model(SHN)

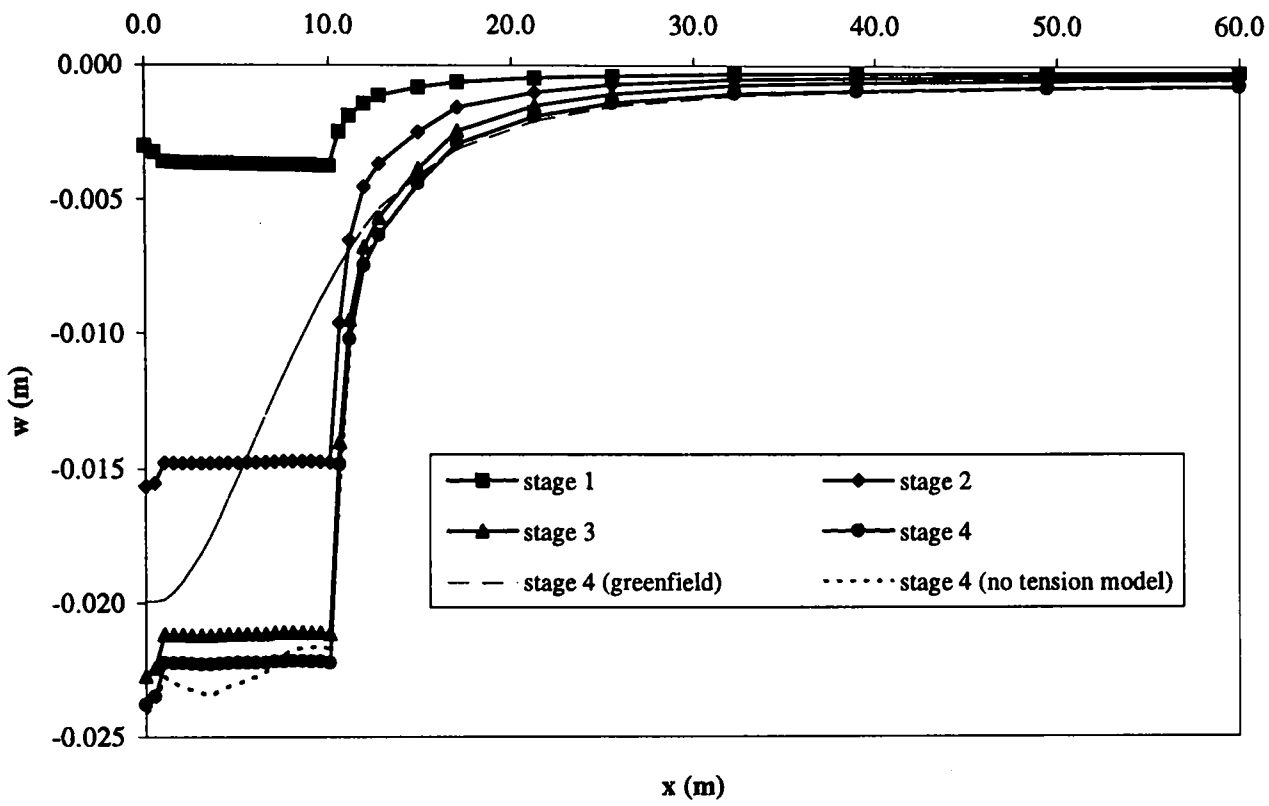


(1) (2)

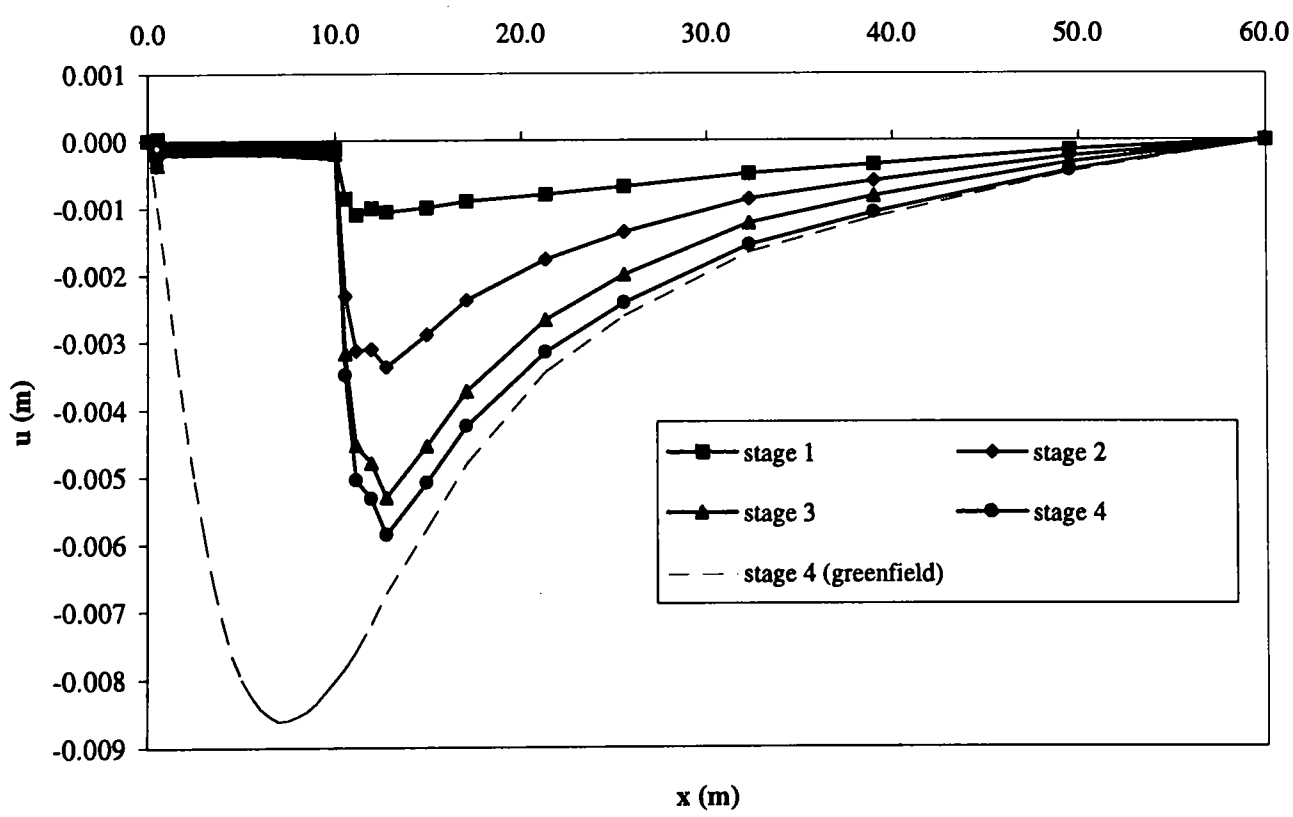
Figure 6.17: Cracking Patterns in Side End wall at (1) Stage 2 and (2) Stage 4, Symmetric Run Combined with Standard Facade, No Tension Model(SHN)

is seen that the settlement is greater than the greenfield, but much flatter than for the masonry model. As observed in the 2-D analysis, the settlements of the no tension and elastic models are about the same at the point of inflexion.

In the same way as the masonry model, the elastic model analysis shows the small area of influence of the building (Figure 6.14). As concluded in Chapter 5, the settlement value at the point of inflexion is representative of the effect of the weight of the building. At the point of inflexion, the ratio of $\delta_{combined}/\delta_{greenfield}$ is 1.83. The value of the same ratio for Runs e223 and 200 in 2-D analysis is 2.08. In Run e223 the weight of the facade is $\gamma_b t$ = 10.0kPa, while the $\gamma_b t$ is equal to 20.0kPa in this section. This implies that



(1) Settlements



(2) Horizontal Movements

Figure 6.18: Ground Movements at y = 25 m, Symmetric Combined Run with Elastic Standard Building(SHE)

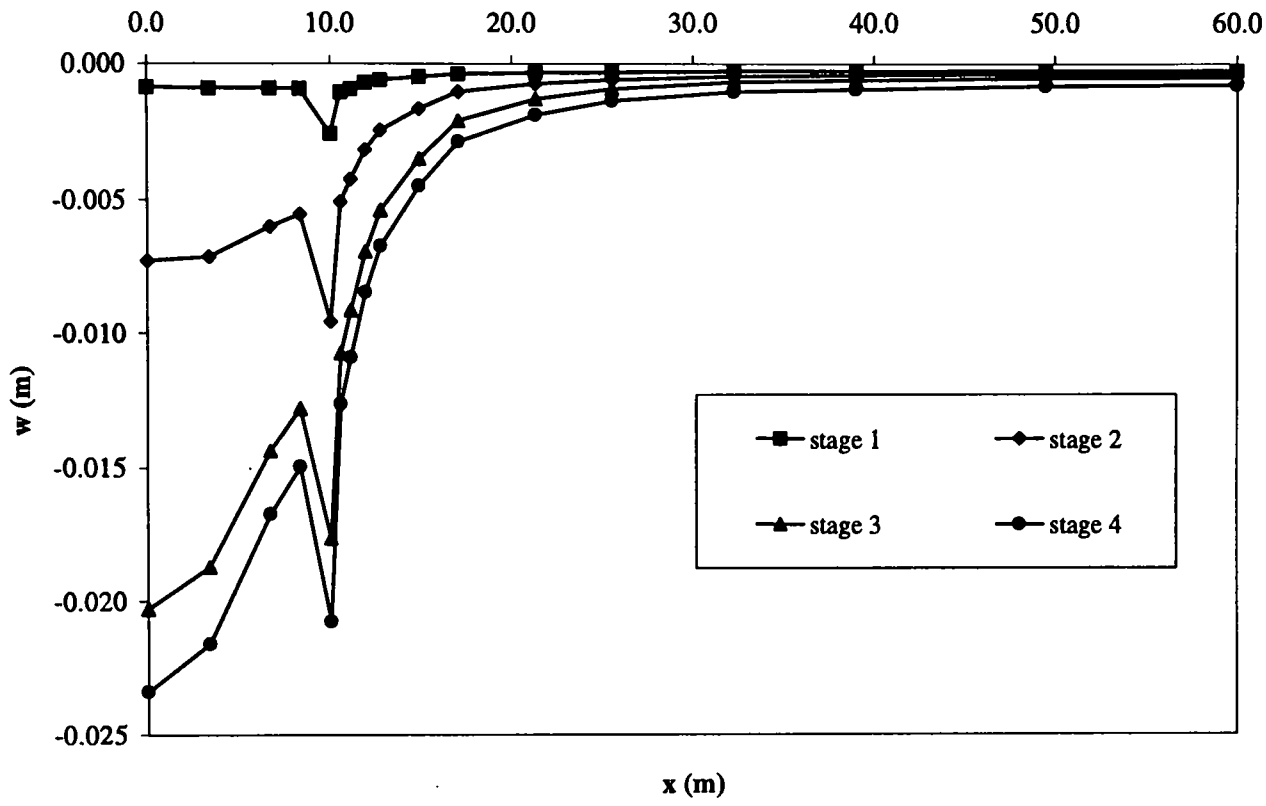


Figure 6.19: Settlement along the Line y=30m, Run SIIN

if a 2-D analysis is to be used to calculate the stress distribution in the ground under the facade, the thickness of the ground block must be more than two times that of the facade.

Indentation Effect

From the plan view of the settlement at the ground surface, it is seen that the facade box tends to indent into the ground. The typical situation can be seen in Figure 6.19 which shows the settlement trough along $y = 30$m. At $x = 10$m, where the end wall is, the settlement is large under the end wall. This is because the soil under the facades and end wall is already partially yielded and weaker compared with the surrounding ground. The line load on the ground from the facades and the end wall may still overestimate the real stress in the ground, especially near the base of the building. More accurate modelling of the interface between the base and the ground (*i.e.* a modelling of more realistic foundation conditions) would be needed in future work.

6.3.3 Combined Analysis with Light Weight Building

In the previous sections the masonry and elastic buildings on the ground exhibit very similar resistance to the ground movement. Both of them cause the ground to settle more than in the greenfield, but reduce the differential settlement. As observed in 2-D analyses, when the weight of the building reduces, the elastic building will keep the settlement trough flat while the masonry building tends to follow the Gaussian curve since the arch forces are not large enough to suppress the ground movements. A masonry building and an elastic building with $\gamma_b t = 3$kPa were analysed in 3-D to confirm this trend.

Light Masonry Building, Run SLN

A light masonry facade box was analysed with the ground. The settlement on the ground surface can be found in Figure 6.20, which shows that the ground settlement is not affected very much by the presence of the light masonry building. It can be seen more clearly in Figure 6.21 where the settlement troughs for combined analyses are almost the same as the greenfield curve, although slightly more linear under the facades. The horizontal movement also follows the greenfield curve.

In the front facade, the cracking damage is concentrated within the ground floor since low arches occur (Figure 6.22). The facade is split into two parts. Whilst the upper part remains undamaged, the lower part moves following the ground, in both vertical and horizontal directions. The horizontal cracking near the door may indicate the onset of the separation between the building and the ground.

Since the building is light, there is no deep indentation beneath the facades, so that the final trough under the end wall is nearly flat. Because the facades also move horizontally following the ground, the corner effect is not strong and does not cause visible cracking in the end wall.

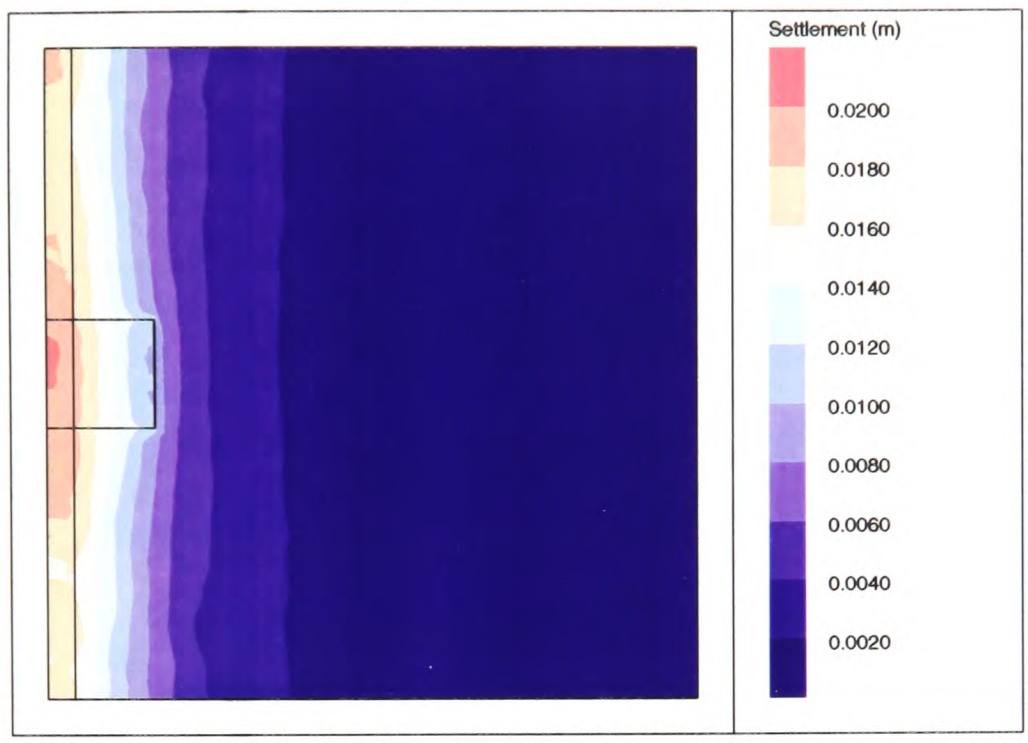


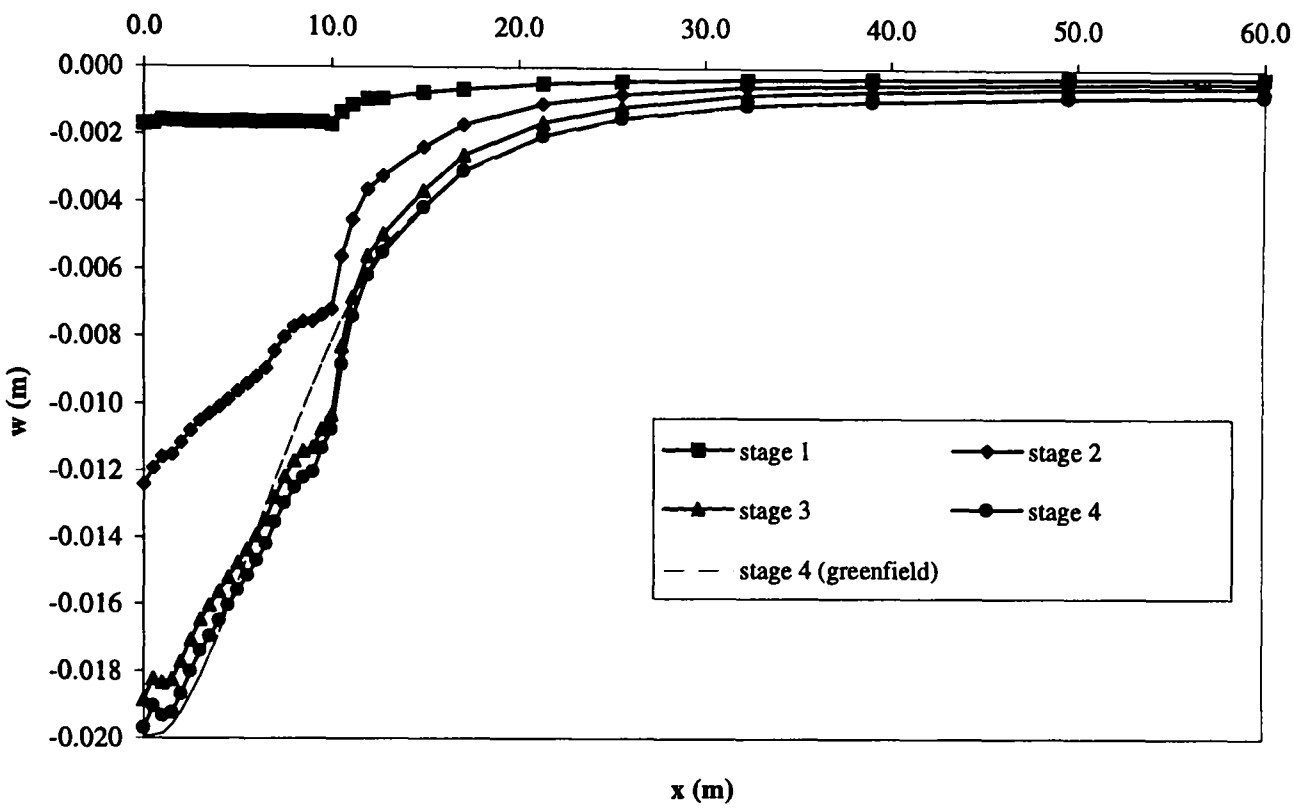
Figure 6.20: Settlement on the Ground Surface at the Final Stage, the Symmetric Combined Analysis with No Tension Light Building (SLN)

Light Elastic Building, Run SLE

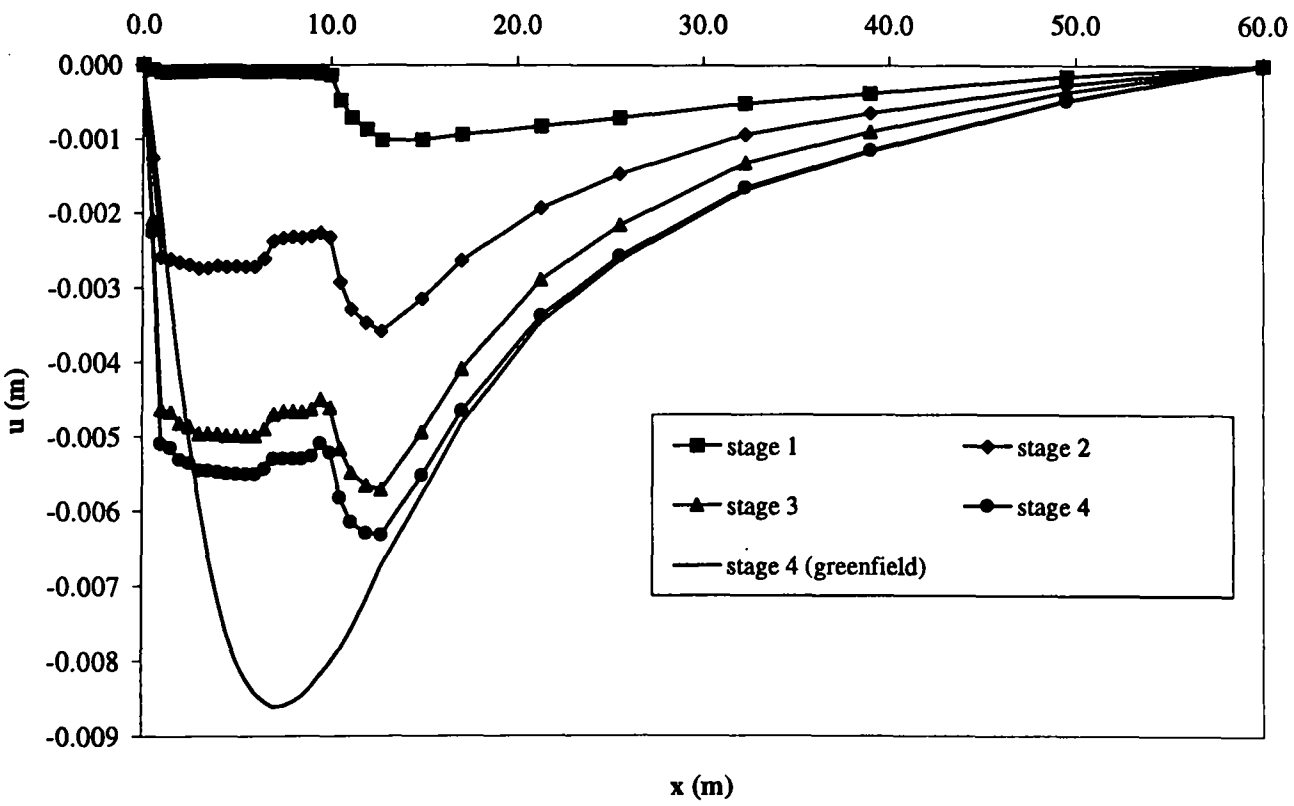
In contrast to the masonry building, the elastic building still has very strong resistance against the settlement because of its shear and tensile stiffness. In Figure 6.23 the elastic building averages the settlement beneath itself, as seen previously in 2-D analyses, and resists the horizontal movements induced by tunnelling.

6.4 Models used in Unsymmetric Runs

The same facade box as used in the symmetric runs but with skew orientation to the tunnel was analysed with the same tunnel as before to investigate the 3-D features of the interaction. But in these analyses the size of the problem to be analysed cannot be halved by exploiting symmetry. It was intended to use the same mesh for the facade and the same size of the block of the ground with similar mesh size as in the symmetric runs. However, such a model would be well beyond the maximum size of the core memory of the computers and would generate larger amounts of data swapping to disk, leading to significantly slower calculation. Thus coarser meshes and a smaller block of the ground had to be employed. The size of the facade box remains 20m $\times$ 10m $\times$ 8m while the

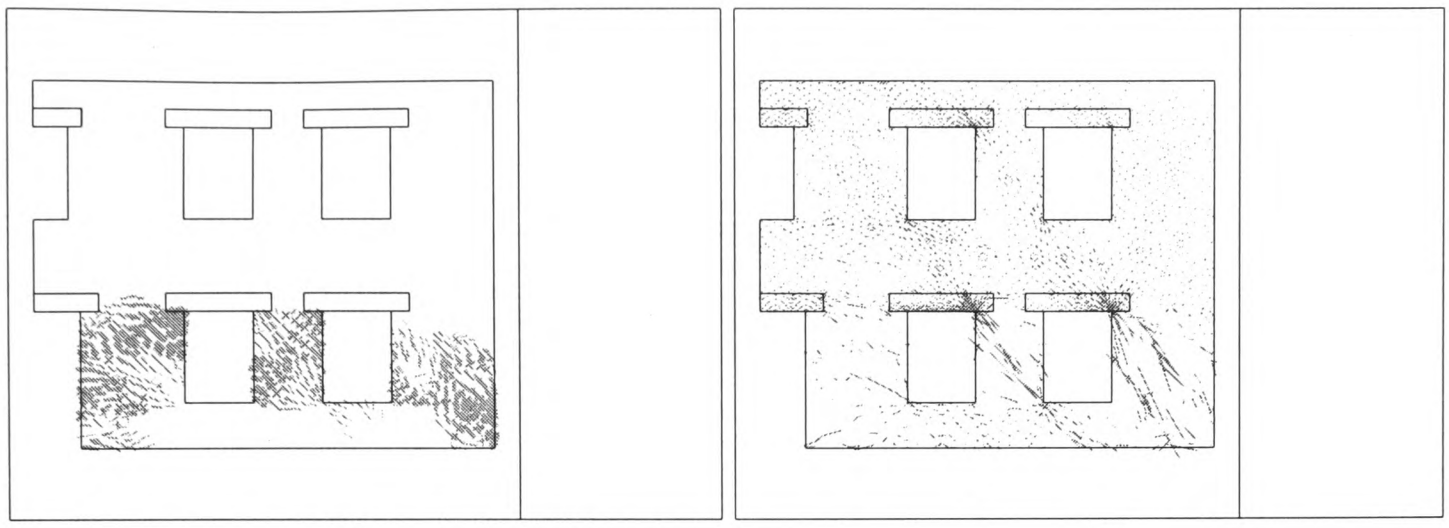


(1) Settlements



(2) Horizontal Movements

Figure 6.21: Ground Movements at y = 25 m, Symmetric Combined Run with No Tension Light Building(SLN)



(1) (2)

Figure 6.22: (1) Cracking Pattern and (2) Stress Trajectory in Front Facade, Symmetric Run Combined with Standard Facade, No Tension Model(SLN)

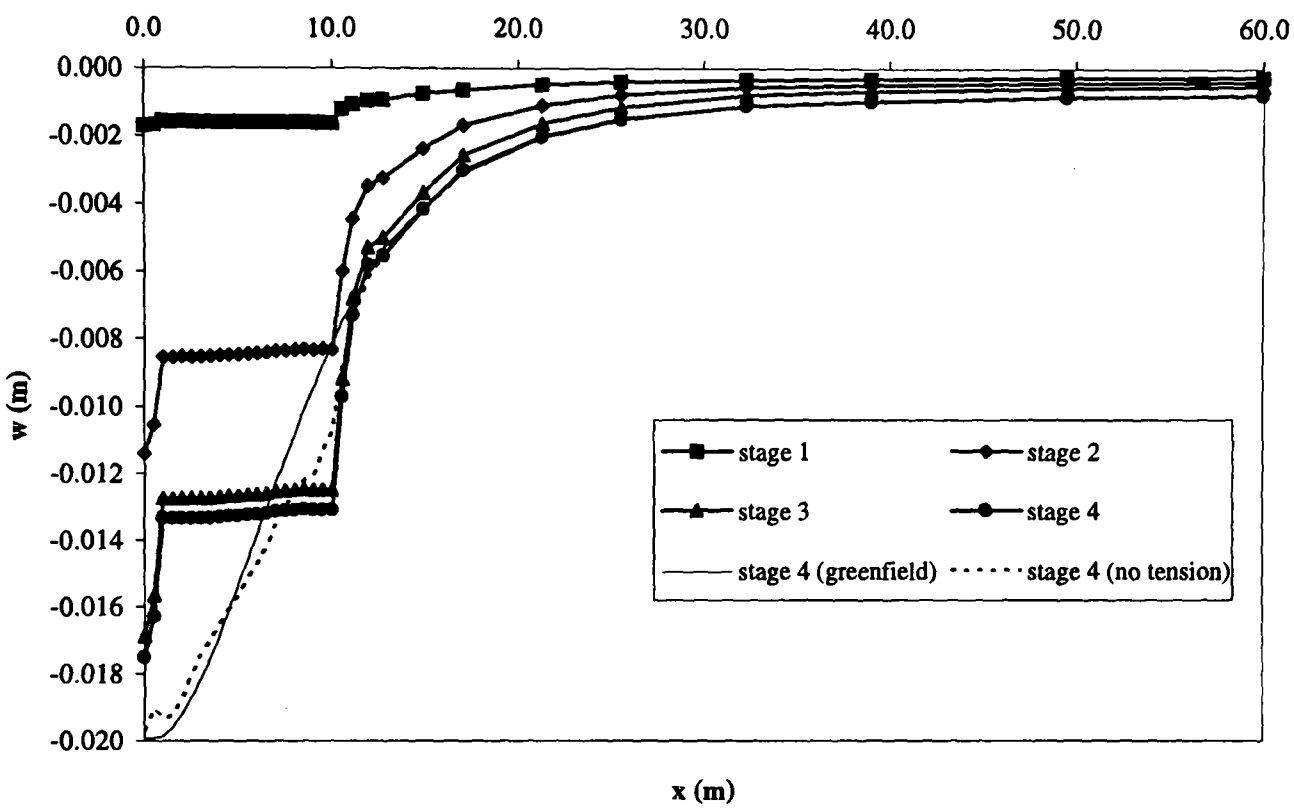
block of the ground changes to 100m × 60m × 50m (Figure 6.24). The facade box is located unsymmetrically at the ground surface with an angle of 45^o to the centreline of the tunnel.

6.4.1 Building

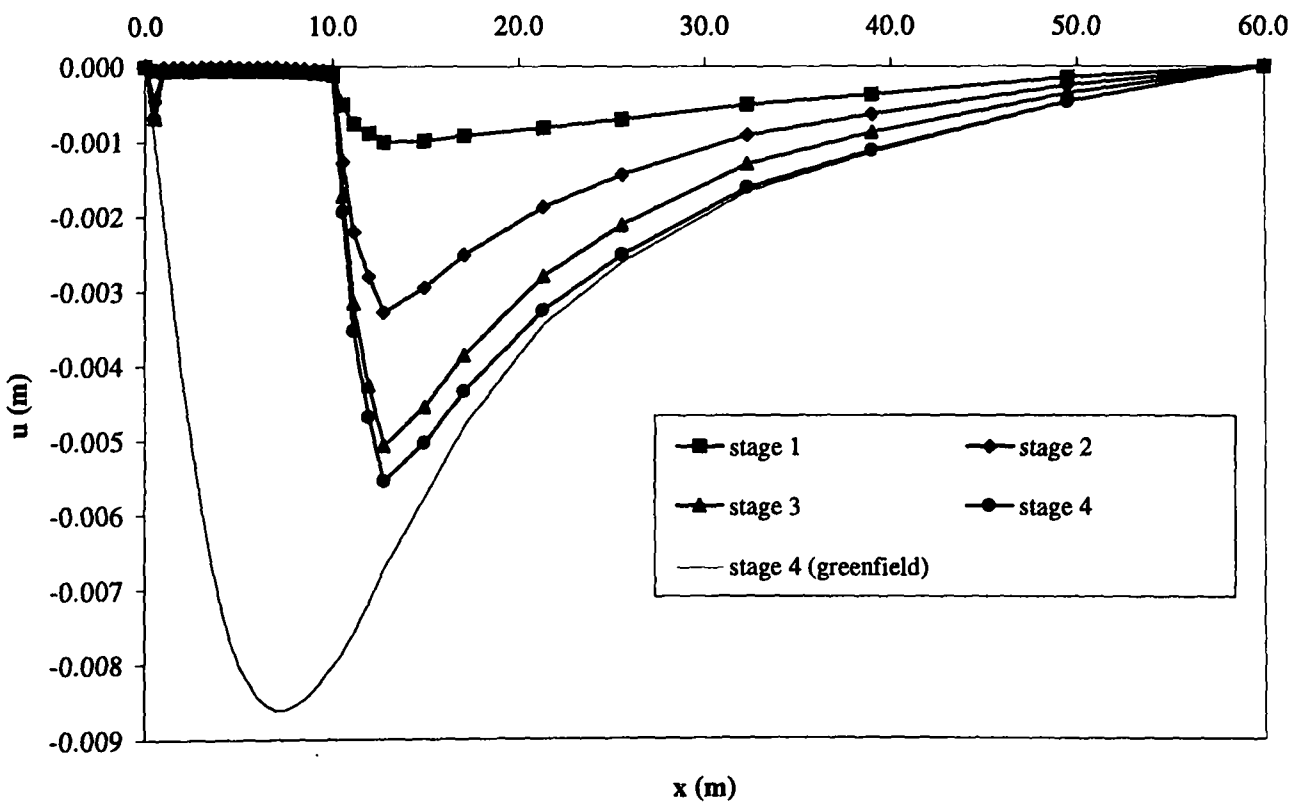
The facade box consists of two standard facades and two plain end walls. The meshes for both facades and both end walls can be found in Figure 6.25.

The local co-ordinate systems of the facades have origins at the centre point of the base of each facade, with local $x-$axes horizontally parallel to the facades, so that the facades extend from -10m to 10m along their local $x-$axes. For the end walls, the origins of the local systems are at the bottom-left corners and $x-$axes are parallel to the end wall plane. The extent of the end walls is $x = 0$ to 10m locally.

In a similar way to the symmetric meshes, tie elements connecting 2-D nodes are used between the facades and end walls. The nodes at the base of the building are connected to the corresponding nodes in the ground mesh by the ties for 2-D and 3-D nodes. No extra boundary conditions are required for the building.



(1) Settlements



(2) Horizontal Movements

Figure 6.23: Ground Movements at y = 25 m, Symmetric Combined Run with Elastic Light Building(SLE)

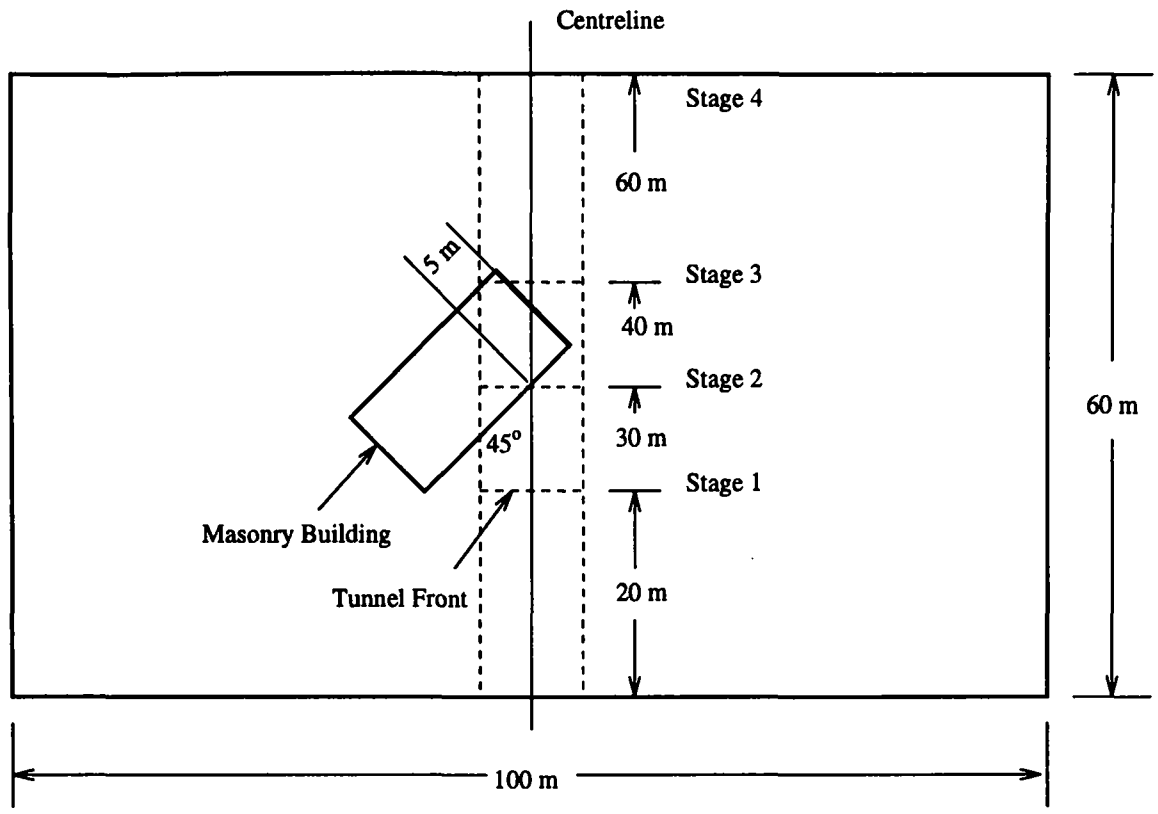


Figure 6.24: Plan View of the Unsymmetric Configuration

6.4.2 Ground

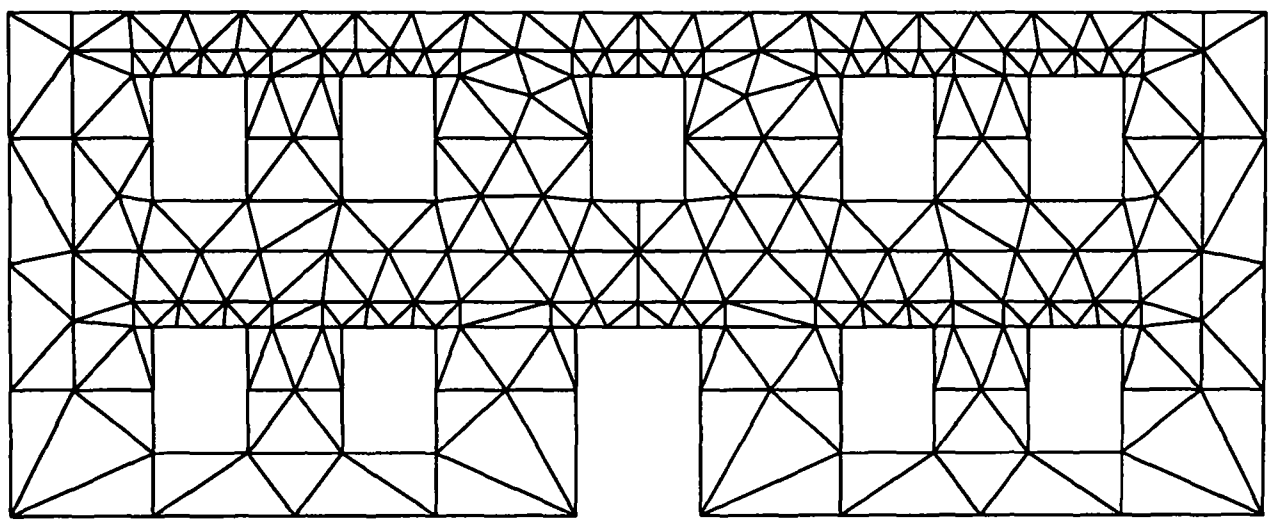
The external view of the finite element mesh of the ground block is shown in Figure 6.26. It consists of 2243 ten-noded tetrahedral solid elements. The tunnel runs at the depth of 10m and its excavation is simulated by four stages (Figure 6.24). The boundary conditions for the ground are the same as in the symmetric runs.

6.5 Unsymmetric Runs

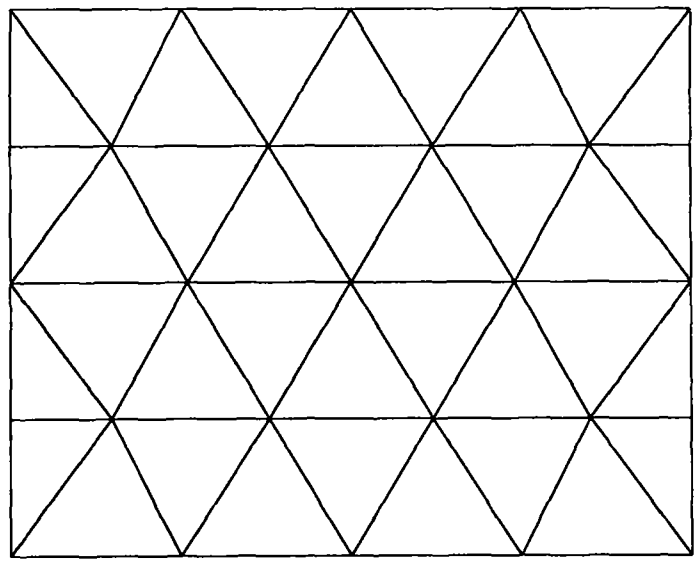
6.5.1 Greenfield, Run UG

The greenfield case was run first for comparison with the combined analysis. Figure 6.27 shows the settlement on the ground surface at the ends of stages 2 and 4. It is seen that the unsymmetric ground mesh gives a very similar prediction of the settlement trough, but with slightly smaller maximum settlement, compared with symmetric runs. The difference is due to the use of different meshes.

The settlement was then applied to the facade box. The settlement profile under the front facade shows a sagging area which moves across the facade (Figure 6.28), and indicates that the most serious cracking area is also moving from the left part to the



(1)
(1) Facade



(2)
(2) End Walls

Figure 6.25: Meshes for Facades and End walls in Unsymmetric Runs

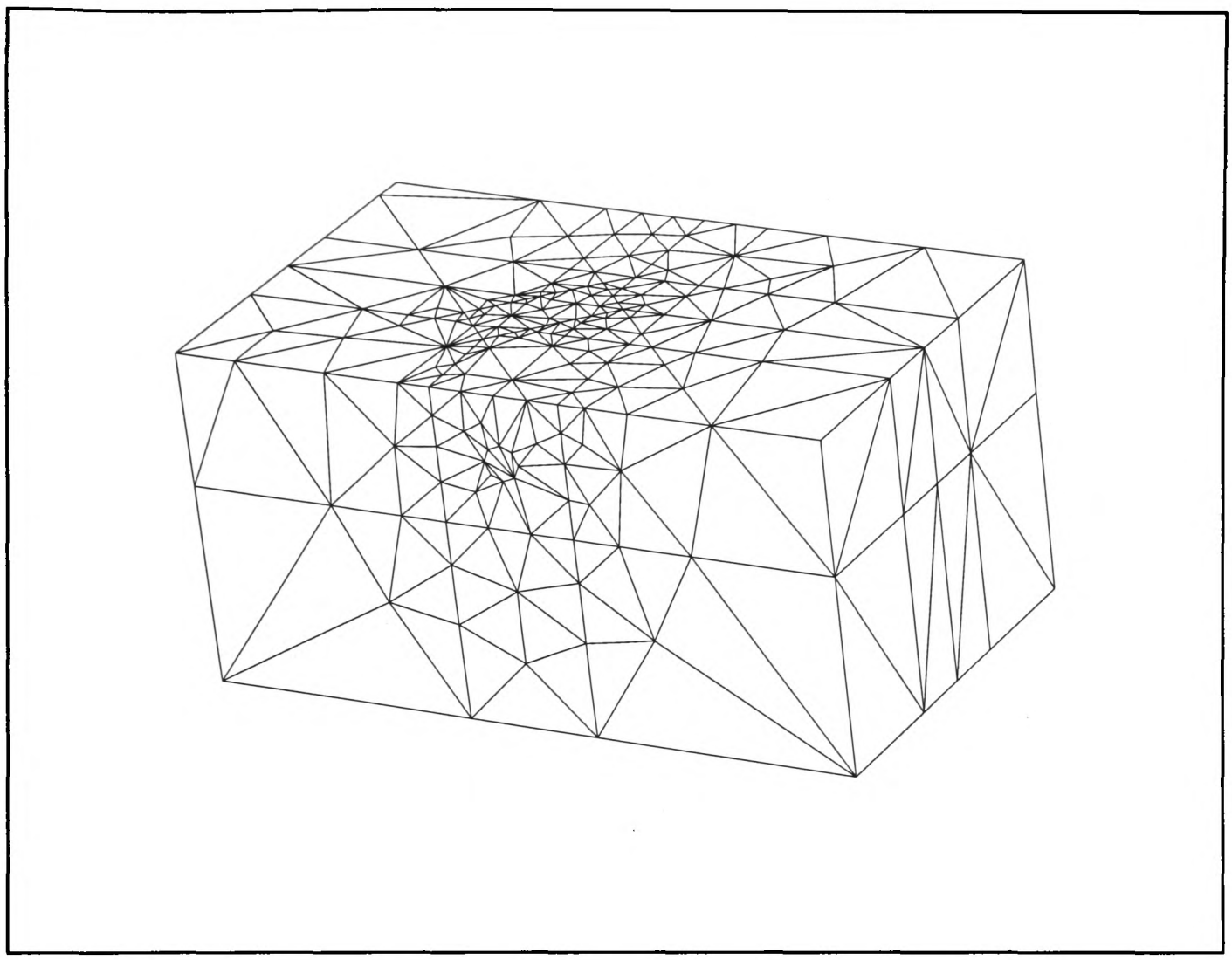


Figure 6.26: 3-D Finite Element Mesh for Ground in Unsymmetric Runs

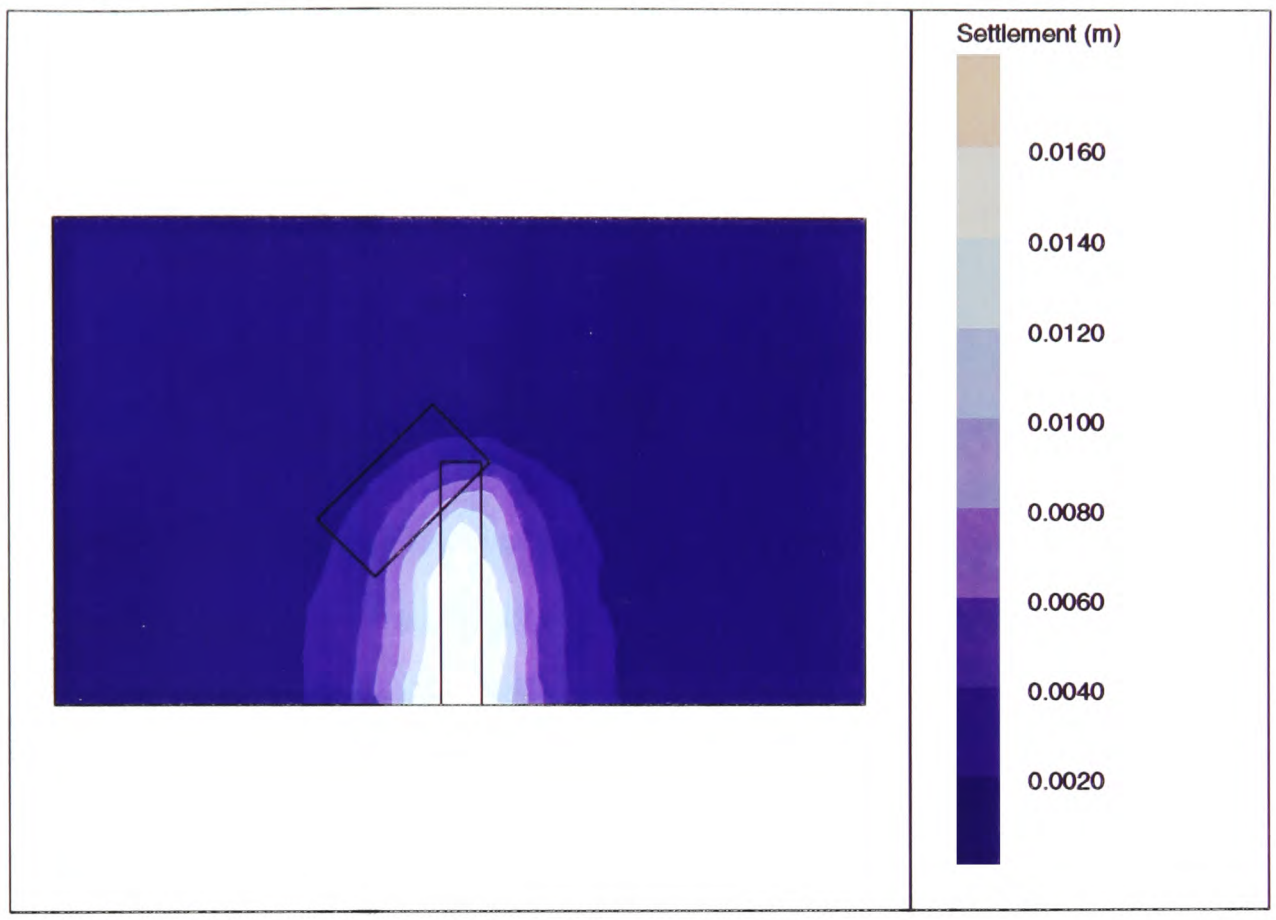
right half (Figure 6.29). The stress arches are observed at all stages.

Because of the settlement trough, a tilt of approximately 1 : 2000 for the whole front facade occurs. This value is less than the general permissible limit of 1 : 1000 tilt for a masonry building (Attewell *et al.*, 1986).

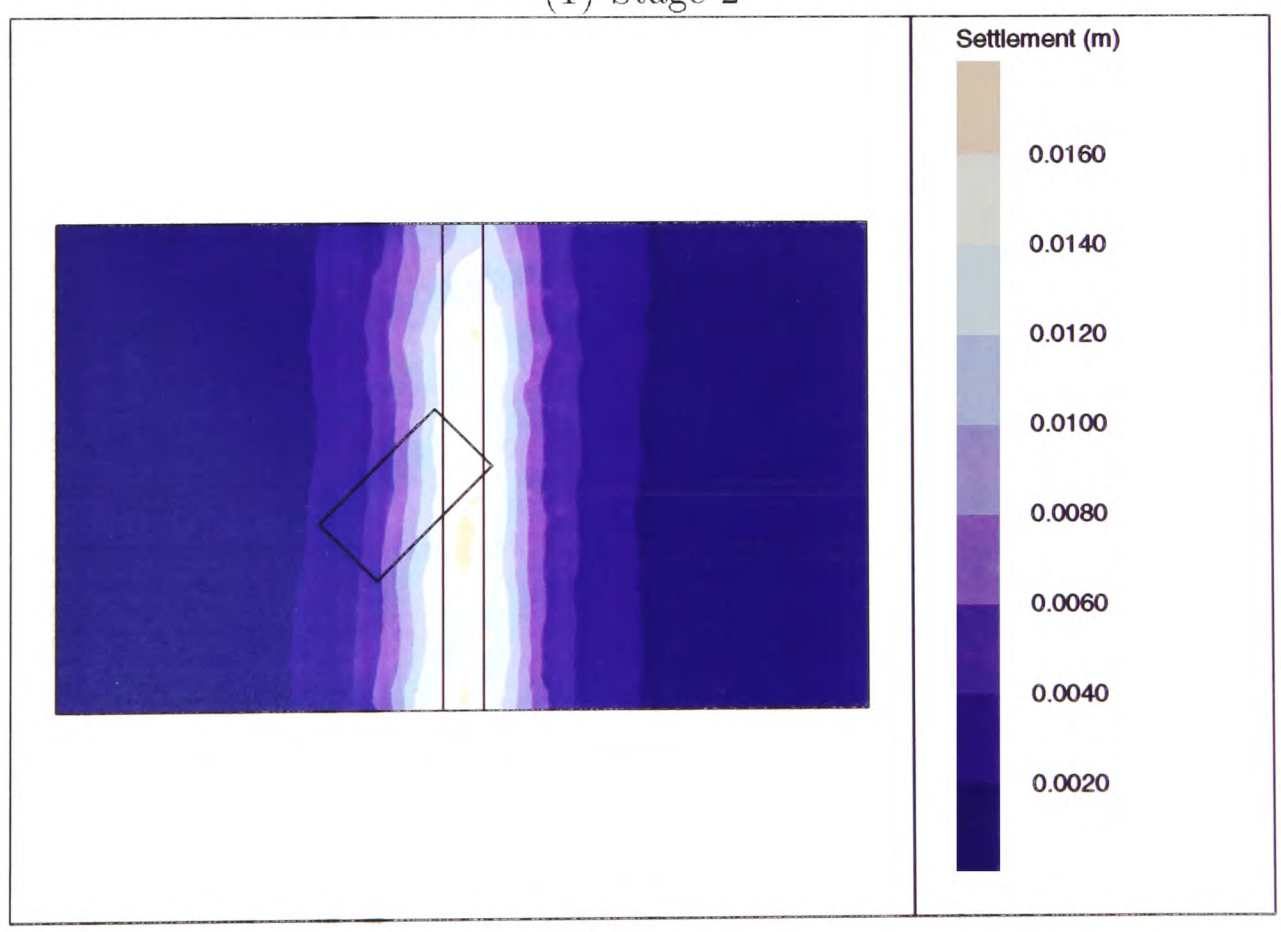
Beneath the back facade, the settlement trough varies from sagging to hogging and finally reaches a hogging mode with a similar tilt value (Figure 6.30). Since the sagging settlement is quite small, it does not cause visible cracking. But the hogging at the final stages causes some vertical cracks with moderate severity (Figure 6.31).

The hogging-sagging process underneath the right end wall shown in Figure 6.32 is reflected by the cracking in the right end wall changing from the vertical cracks at the top to the cracks at the bottom which form a small arch at the end of the excavation (Figure 6.33).

In contrast, the left end wall is always in the hogging mode due to its location far



(1) Stage 2



(2) Stage 4

Figure 6.27: Settlement Wave in Stages 2 and 4, the Unsymmetric Greenfield

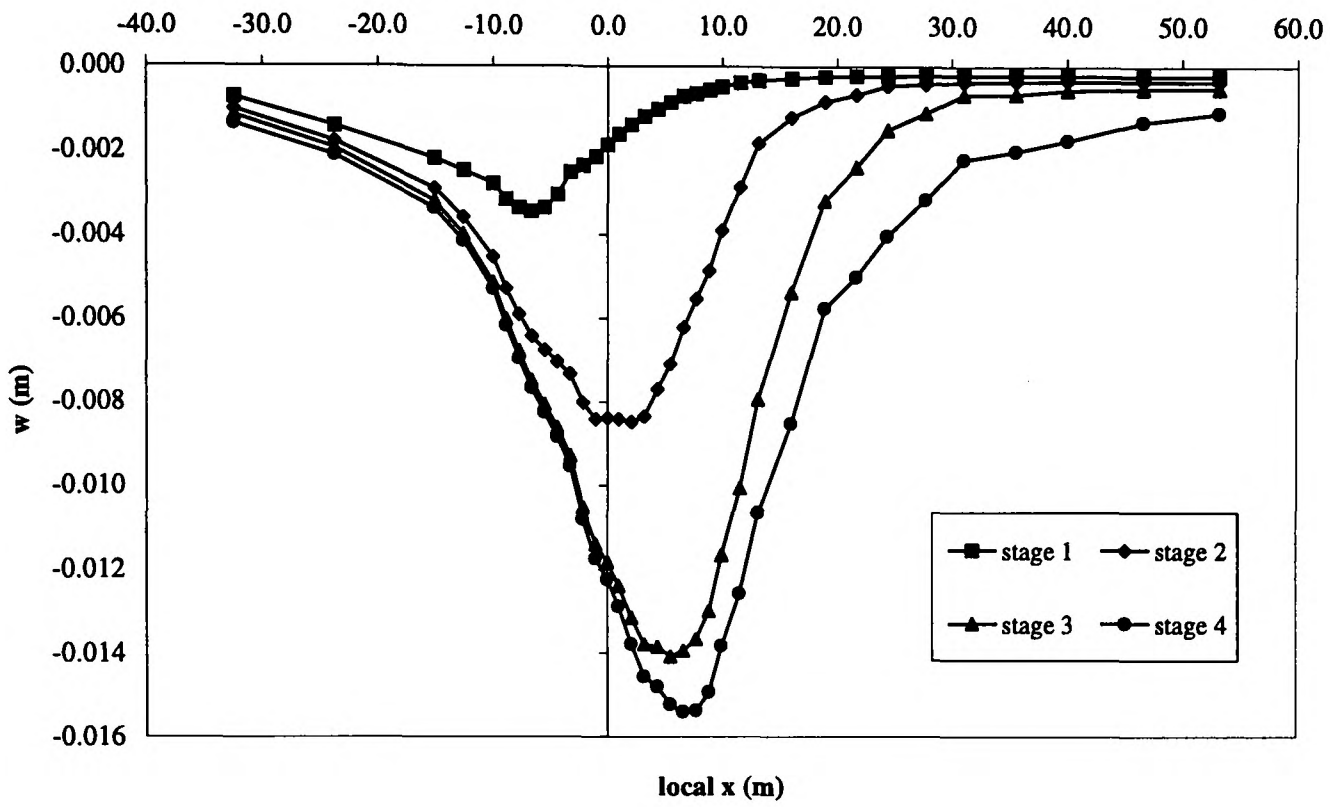
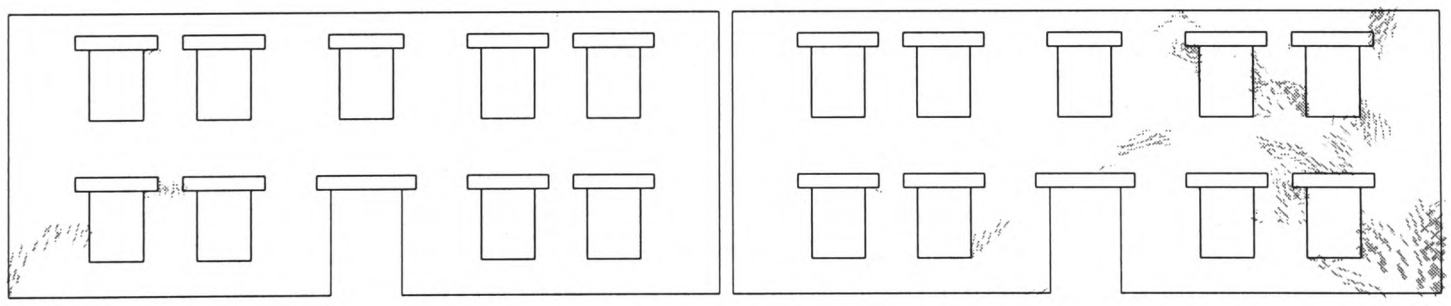


Figure 6.28: Settlement Trough along the Front Facade, Unsymmetric Greenfield Run



(1) (2)

Figure 6.29: Cracking Patterns at (1) Stage 1 and (2) Stage 4 in Front Facade, Unsymmetric Greenfield Run

from the centreline of the tunnel (Figure 6.34). Vertical cracks emerge at the top of the left end wall due to the hogging mode and remain throughout the whole process (Figure 6.35).

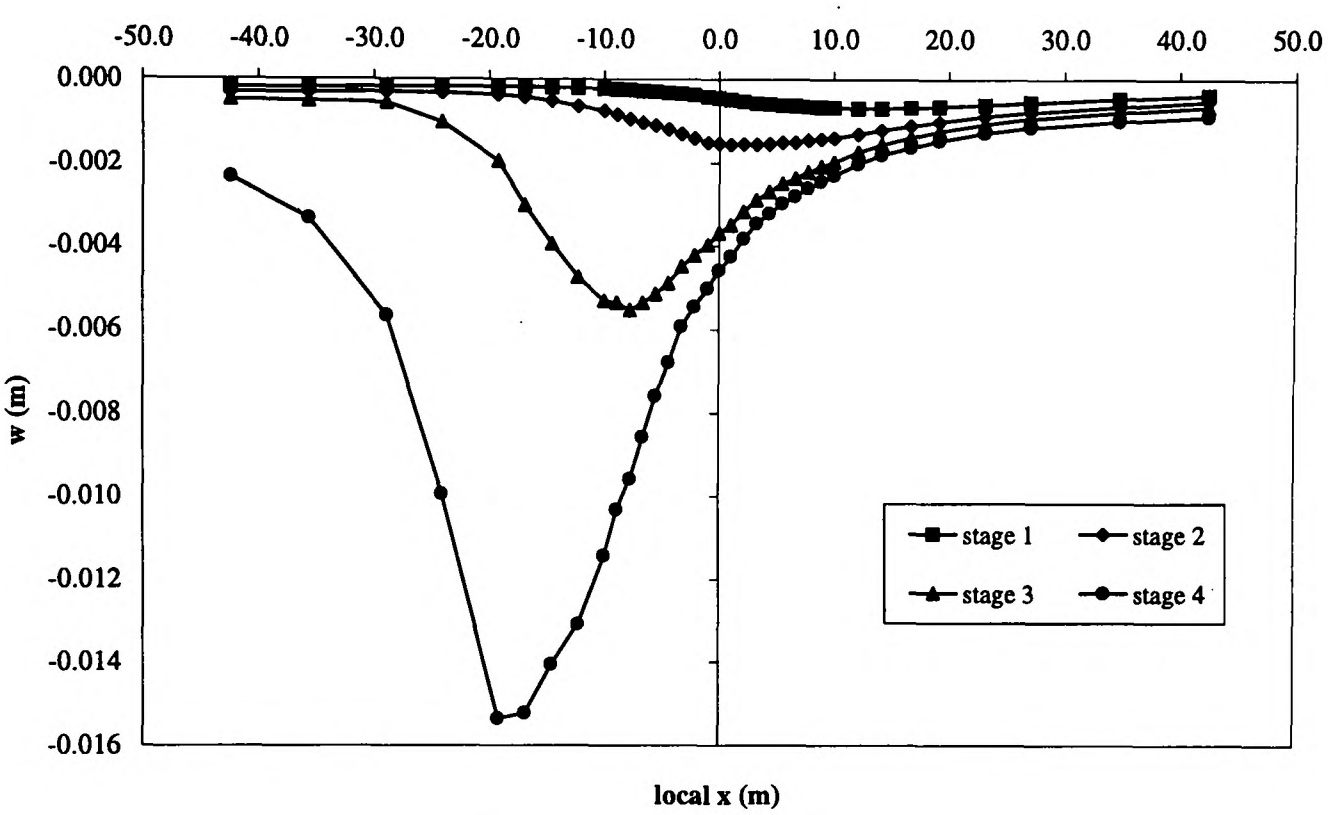


Figure 6.30: Settlement Trough along the Back Facade, Unsymmetric Greenfield(UG)

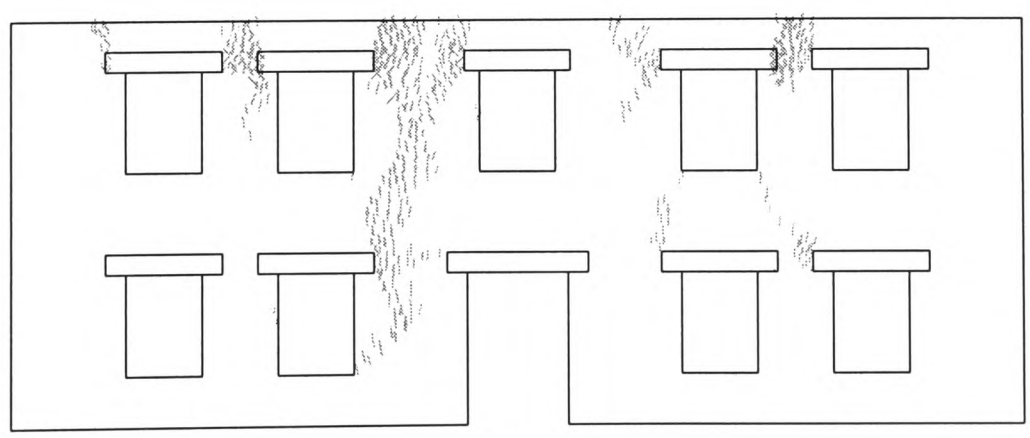


Figure 6.31: Cracking Damage in Back Facade at Stage 4, Unsymmetric Greenfield(UG)

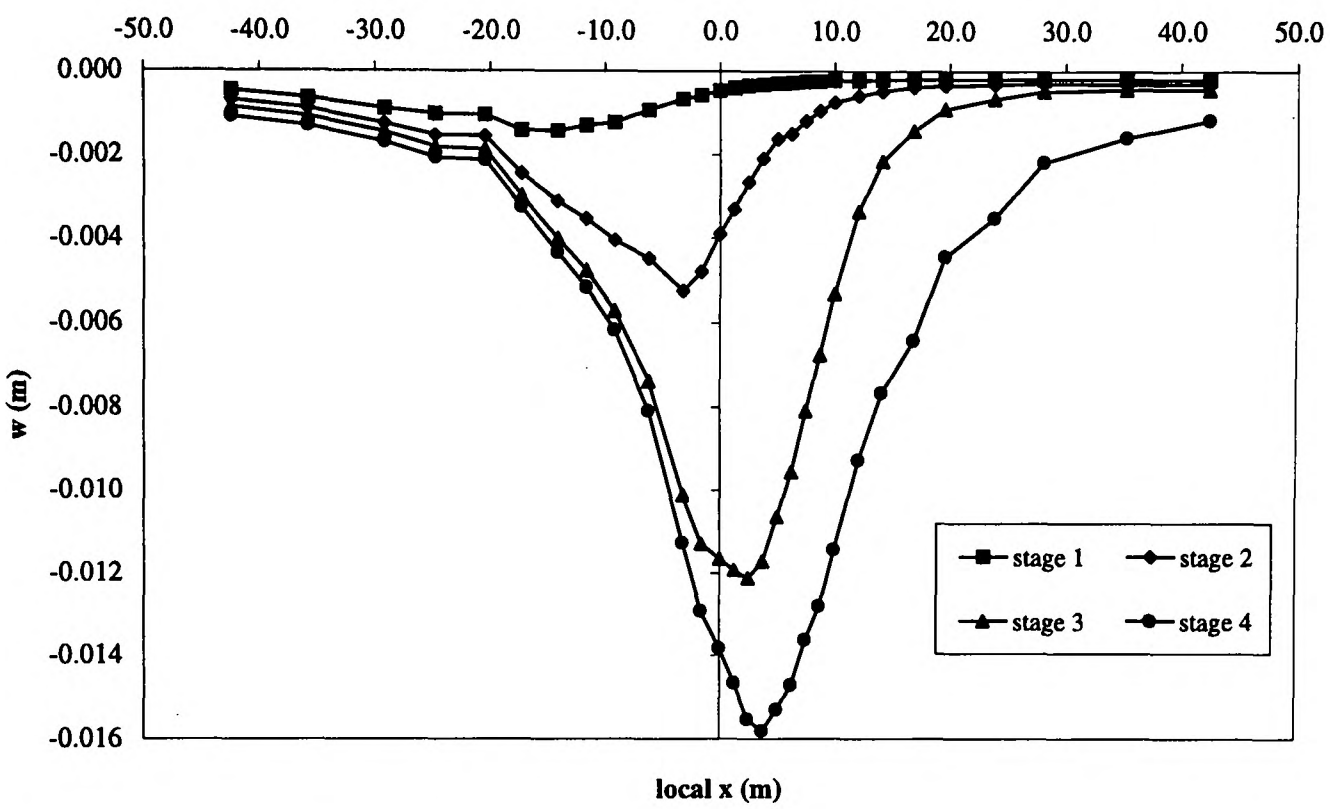


Figure 6.32: Settlement Trough along the Right End Wall, Unsymmetric Greenfield(UG)

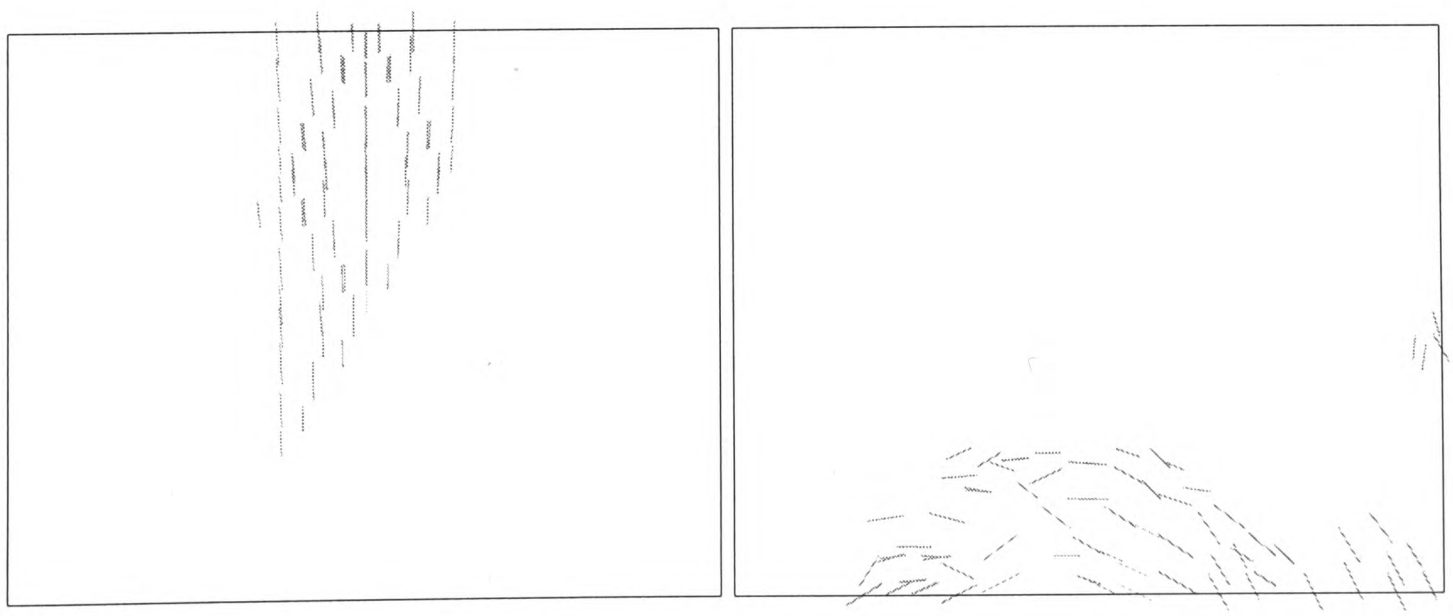


Figure 6.33: Cracking Patterns at (1) Stage 1 and (2) Stage 4 in Right End wall, Unsymmetric Greenfield Run(UG)

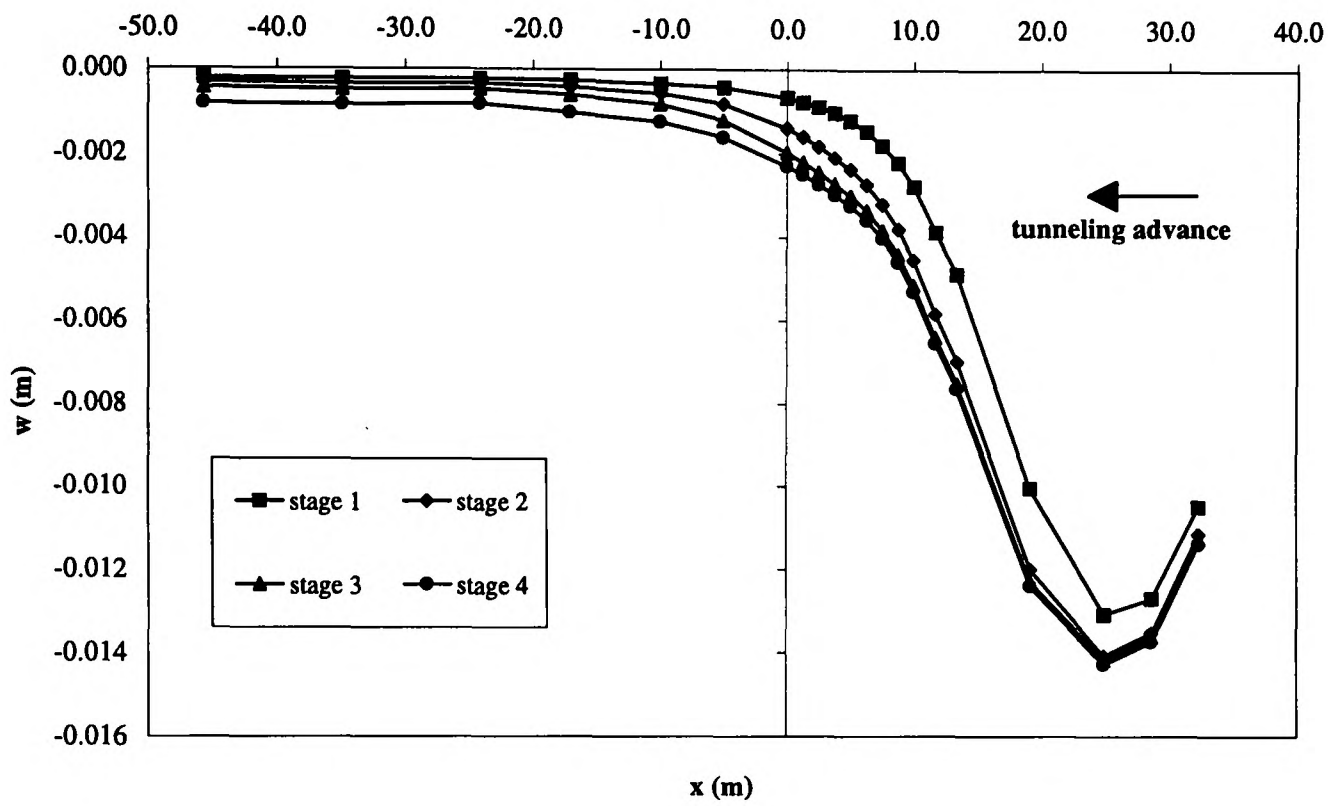


Figure 6.34: Settlement Trough along the Left End Wall, Unsymmetric Greenfield(UG)

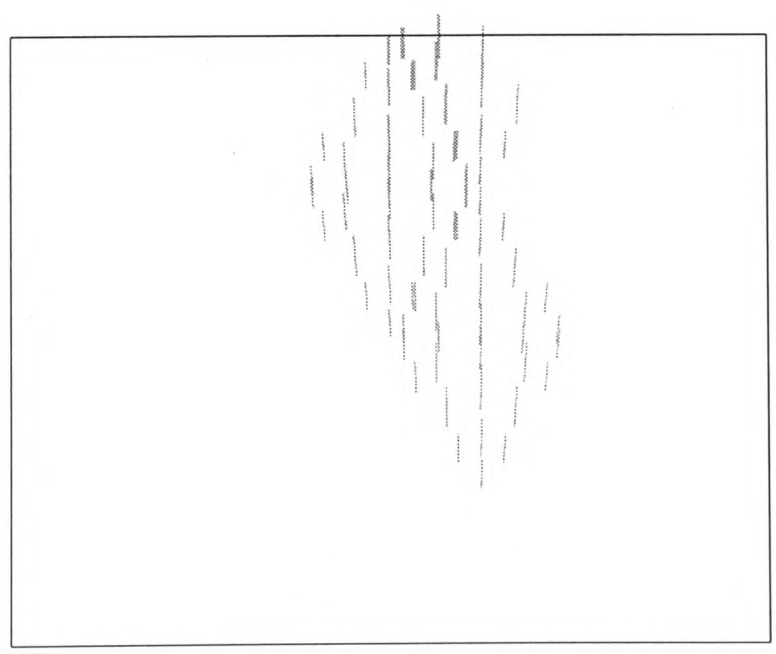


Figure 6.35: Cracking Damage in Left End wall at Stage 4, Unsymmetric Greenfield(UG)

6.5.2 Combined Analysis with Standard Building, Run UHN

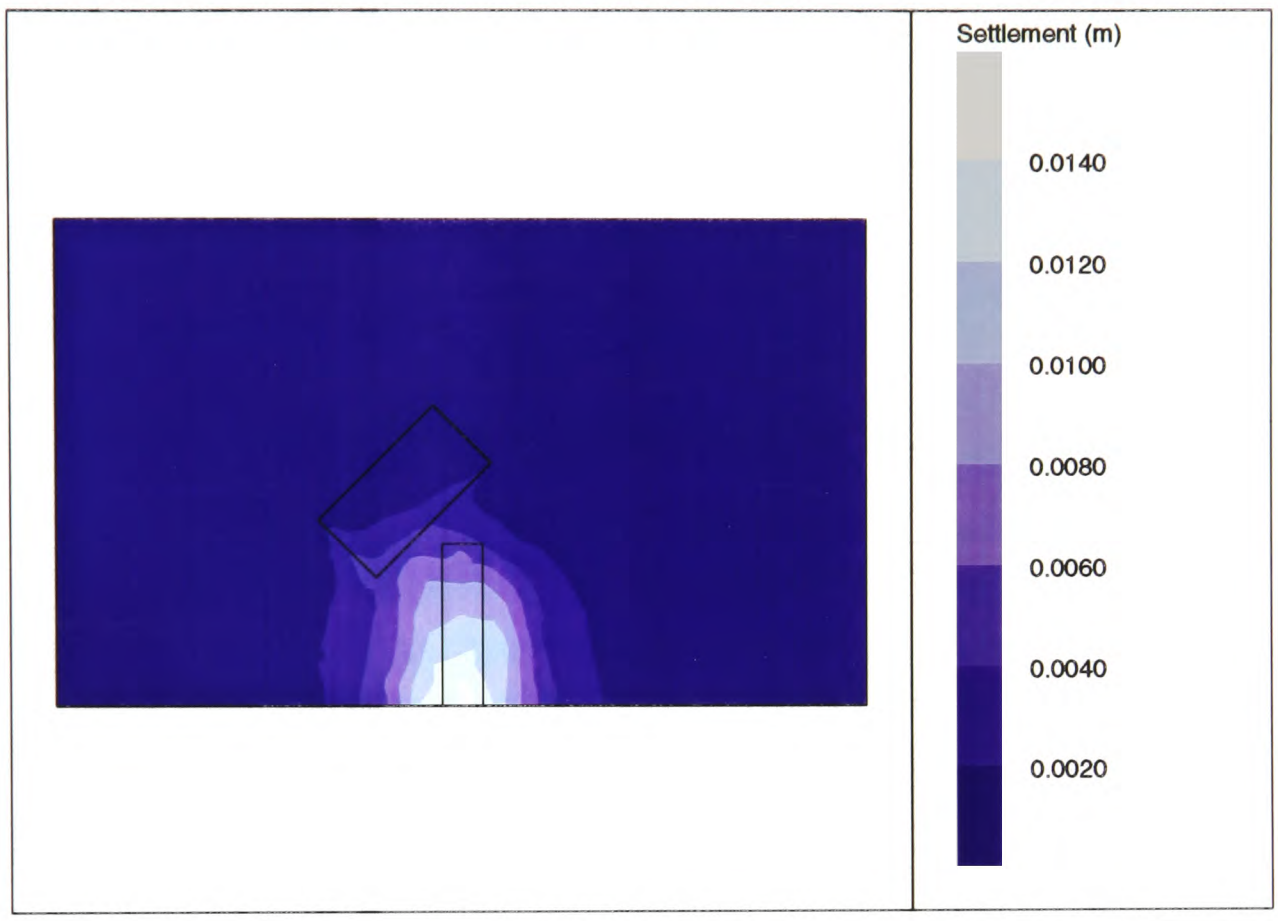
The combined analysis of the tunnelling process with a skewed building shows a different story to the greenfield case due to the interaction between the building and the ground. Figures 6.36 and 6.37 show the settlement at the ground surface at the end of each stage and show that the combined analysis predicts larger settlement than the greenfield, particularly at the corner close to the tunnel. This will be discussed in detail further.

Front Facade

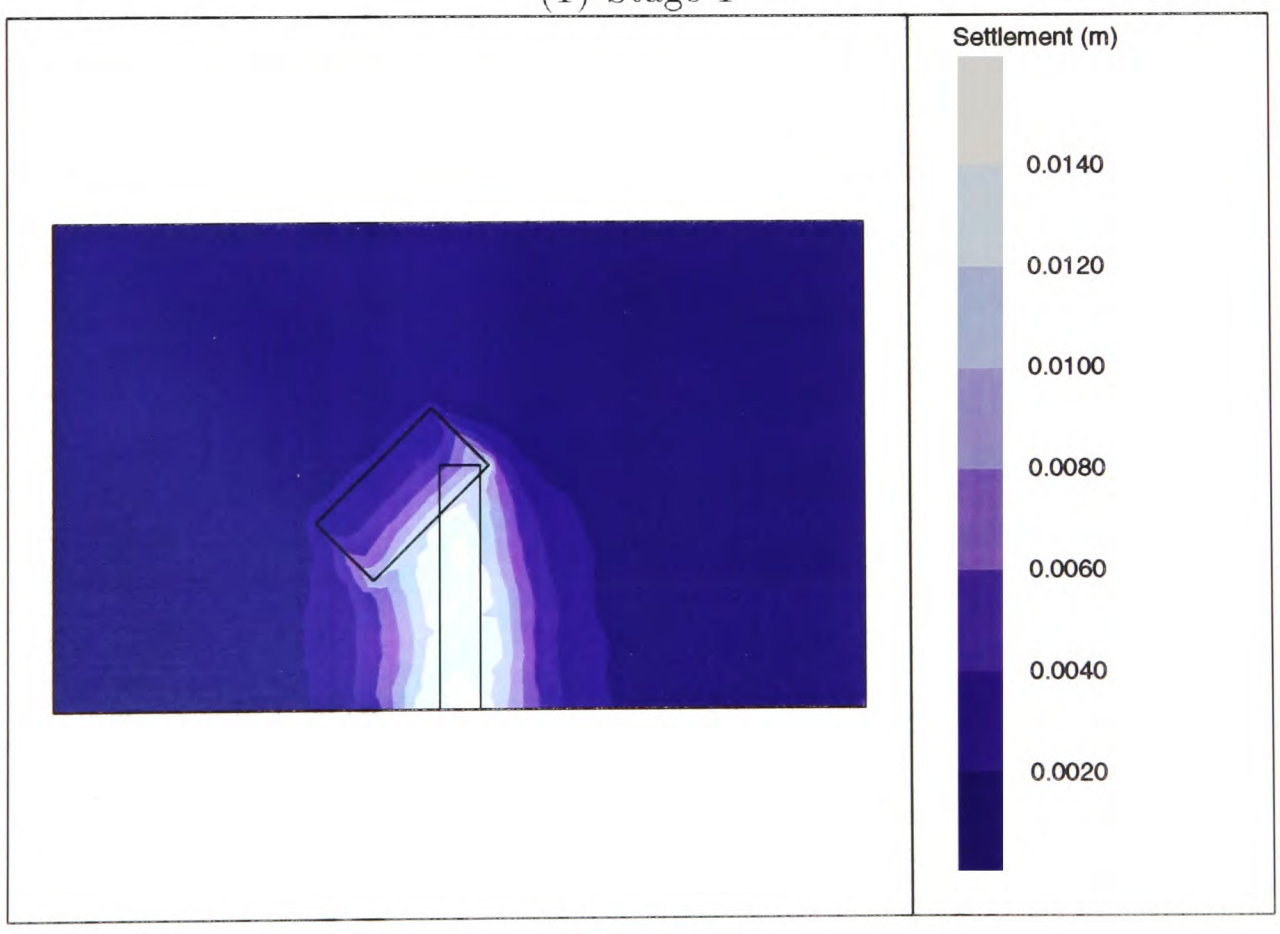
It is seen in Figure 6.38 that at the early stages, when the greenfield trough is in sagging mode and does not show large tilt, the combined analysis gives a flatter and deeper settlement trough beneath the facade (Figure 6.38-(1)), as in the symmetric runs. The facade resists the differential settlement, although the average settlement under the facade is bigger than greenfield, due to the previous loading history. However at the later stages, when an appreciable tilt of approximate 1 : 1000 is observed, the combined analysis shows that the presence of the building magnifies the tilt. The corner close to the tunnel drops most. A slight hogging even appears at the last stage, at the same place as sagging in the greenfield trough. Figure 6.38-(2) shows relatively small horizontal movement beneath the front facade since it is mainly in the area where the excavation induces compressive strain in the ground.

The stress trajectories in the front facade are consistent with these features of the settlement troughs (Figure 6.39). At the early stages, for example at stage 2, stress arches are formed and make the trough flatter. Correspondingly, the major cracking is very slight, but cracks along the major arches still can be seen. At stages 3 and 4, these stress arches disappear and leave the facade without resistance to the hogging and tilt. The visible vertical cracks at the top are a proof.

Another visible cracking area is at the edge near the left end wall, and this can be explained by the uplifting effect from the left end wall being transferred by the tie elements.

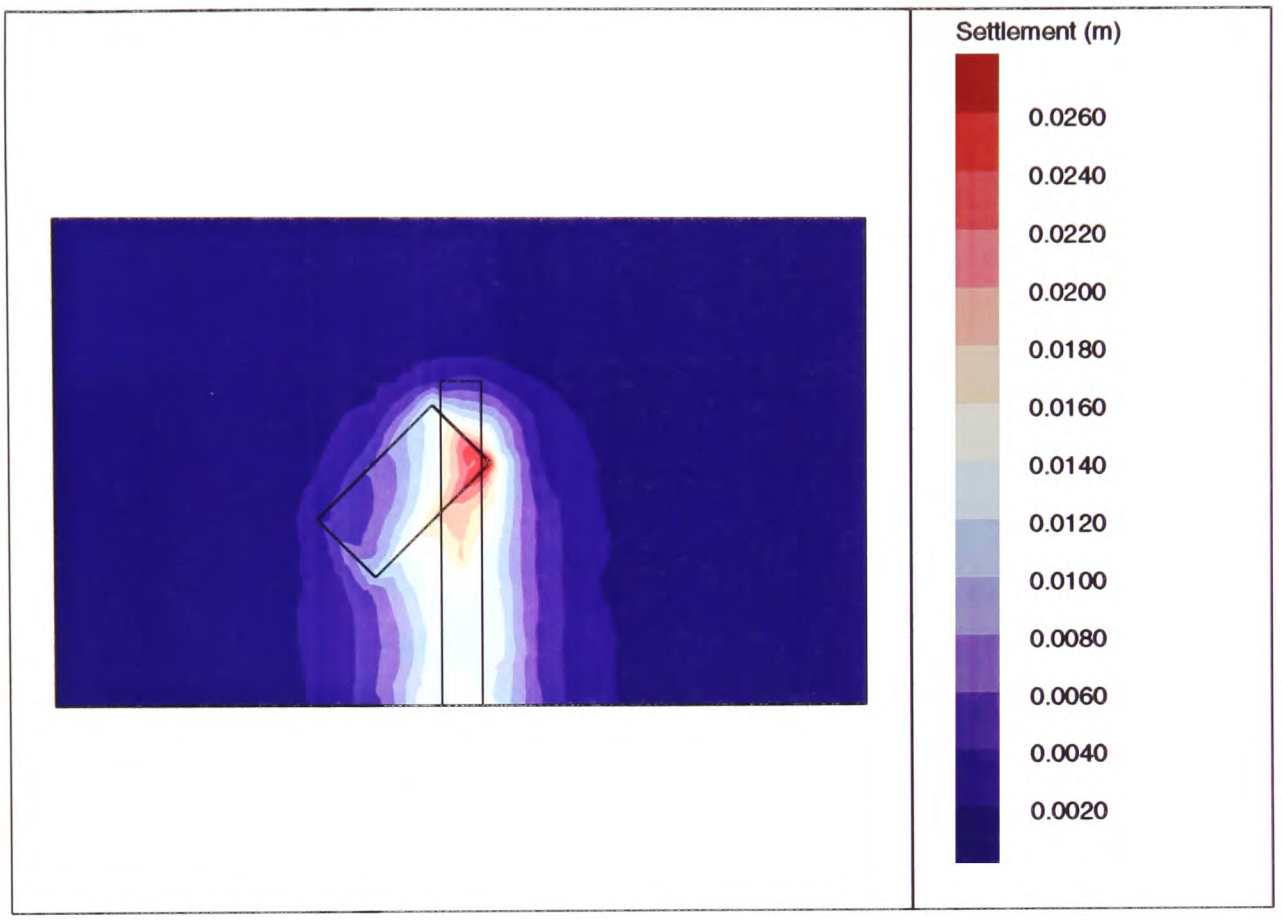


(1) Stage 1

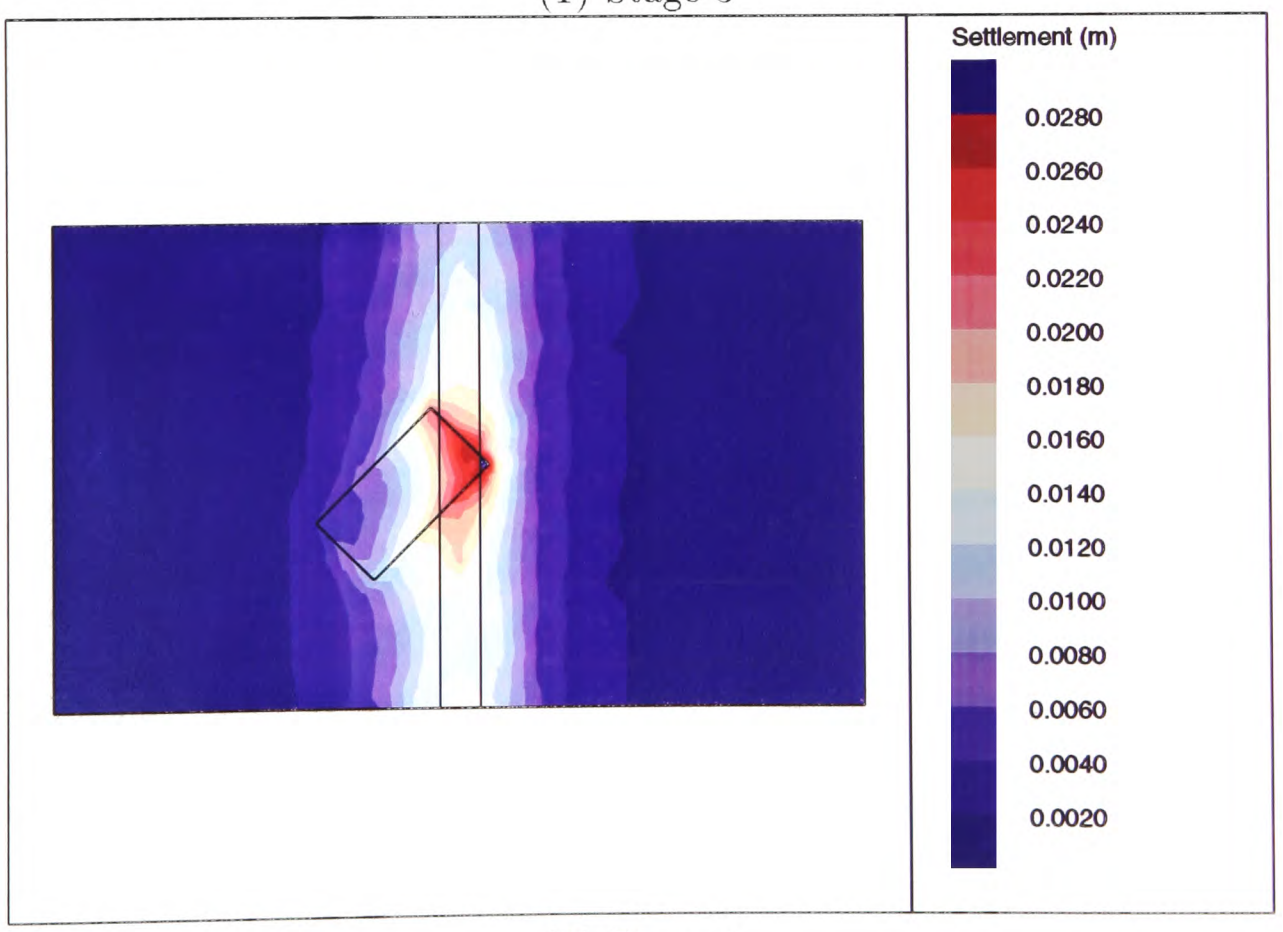


(2) Stage 2

Figure 6.36: Settlement Wave in Stages 1 and 2, the Unsymmetric Combined Analysis (UHN)

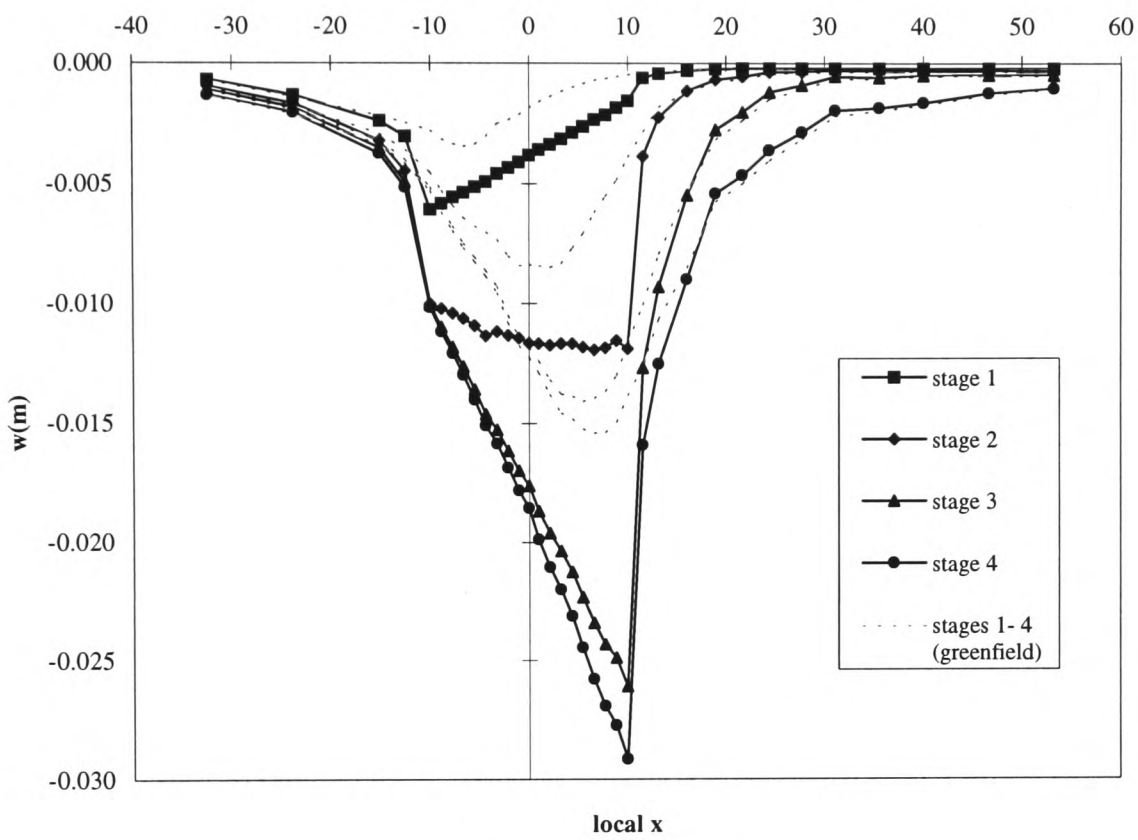


(1) Stage 3

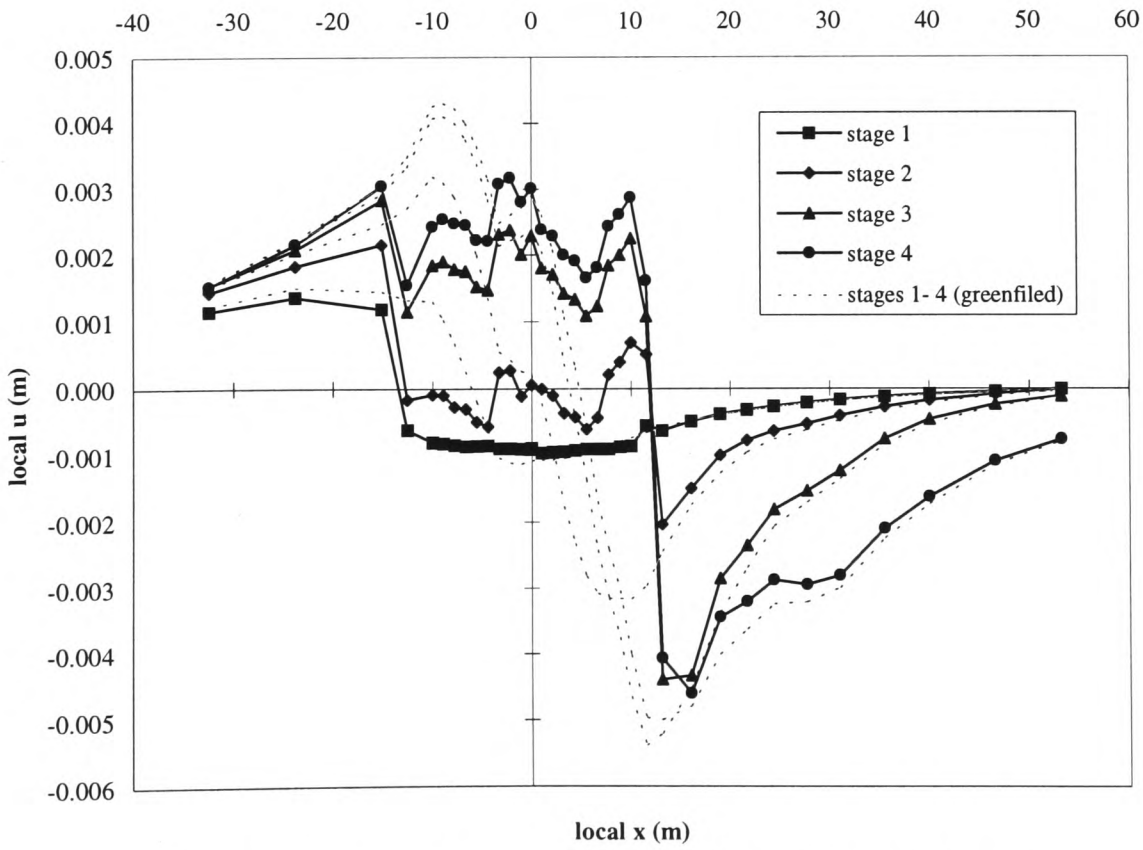


(2) Stage 4

Figure 6.37: Settlement Wave in Stages 3 and 4, the Unsymmetric Combined Analysis (UHN)



(1) Settlement



(2) Horizontal Movement within Plane of Facade

Figure 6.38: Ground Movements beneath the Front Facade, the Unsymmetric Combined Analysis (UHN)

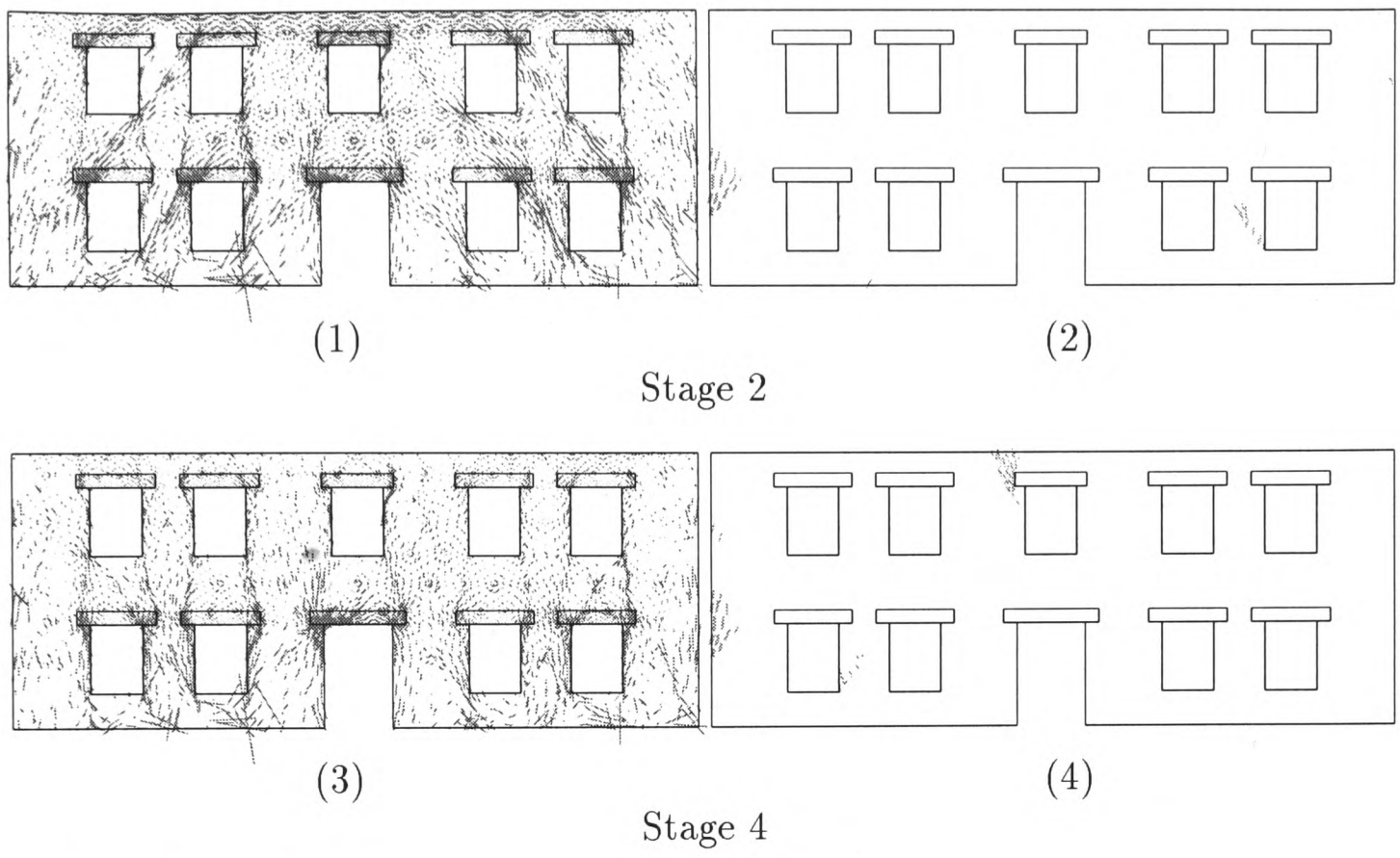
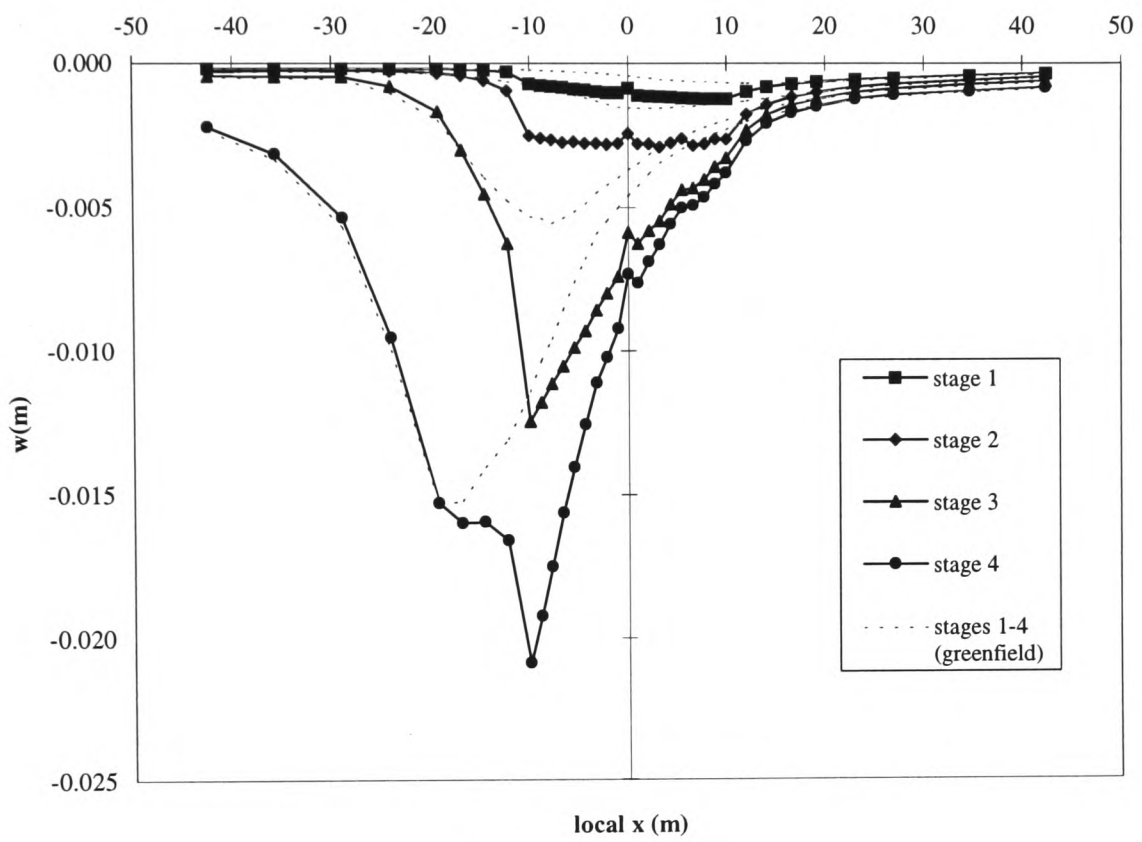


Figure 6.39: Stress Trajectories and Cracking Patterns in Front Facade at (1,2) Stage 2 and (3,4) Stage 4, Unsymmetric Combined Analysis(UHN)

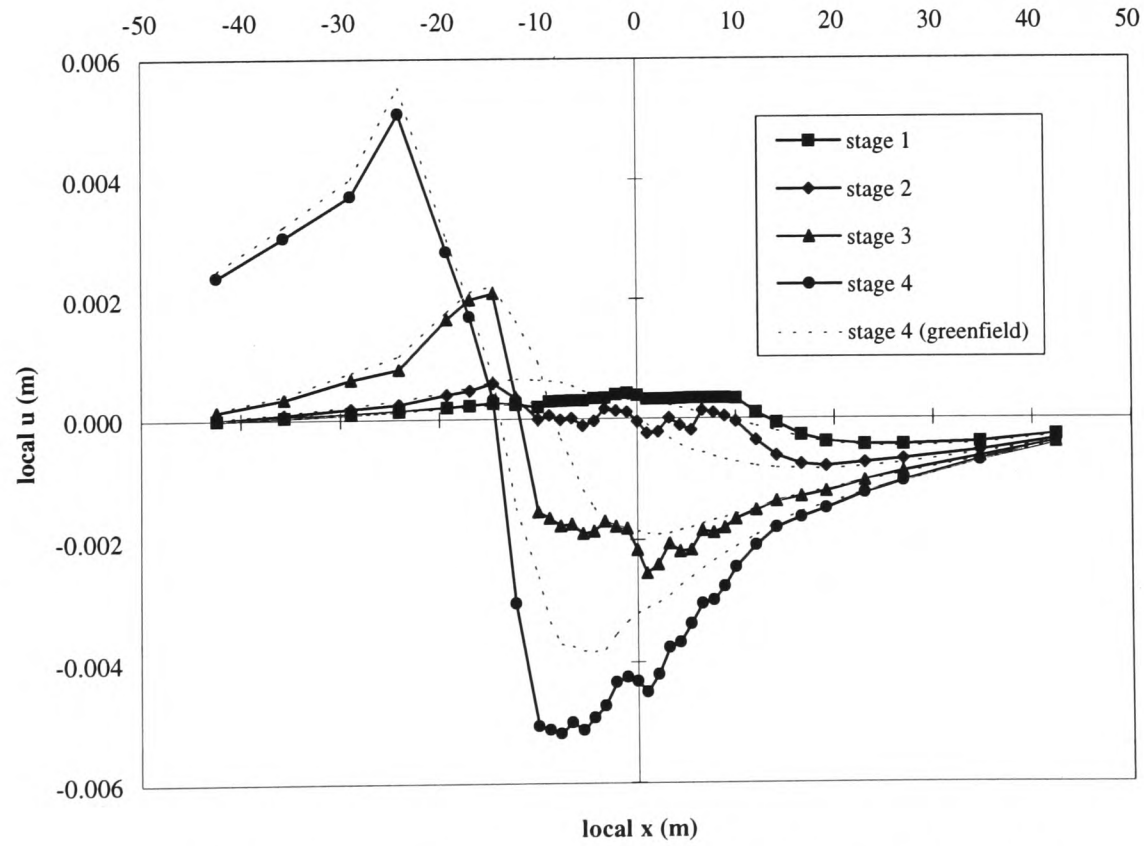
Back Facade

The changes of the settlement troughs under the back facade (Figure 6.40-(1)) are very similar to those under the front facade. In addition to the tilt of the whole facade, the strong hogging mode at the last stage could not be suppressed by the building. Figure 6.40-(2) gives the horizontal movements beneath the back facade. At the early stage, the ground experiences compressive strain and the facade resists the ground movement. However, the excavation induces tensile strain within the extent of the facade. The facade almost follows the ground horizontal movement since it does not have any stiffness against tension.

There are no visible cracks at the stages 1 and 2, but serious vertical cracks emerge from the top of the facade at late stages, when stress arches can not be formed in the hogging mode (Figure 6.41). This is the only case analysed where the combined analysis predicts more serious damage than the greenfield approach.



(1) Settlement



(2) Horizontal Movement within Plane of Facade

Figure 6.40: Ground Movements beneath the Back Facade, the Unsymmetric Combined Analysis (UHN)

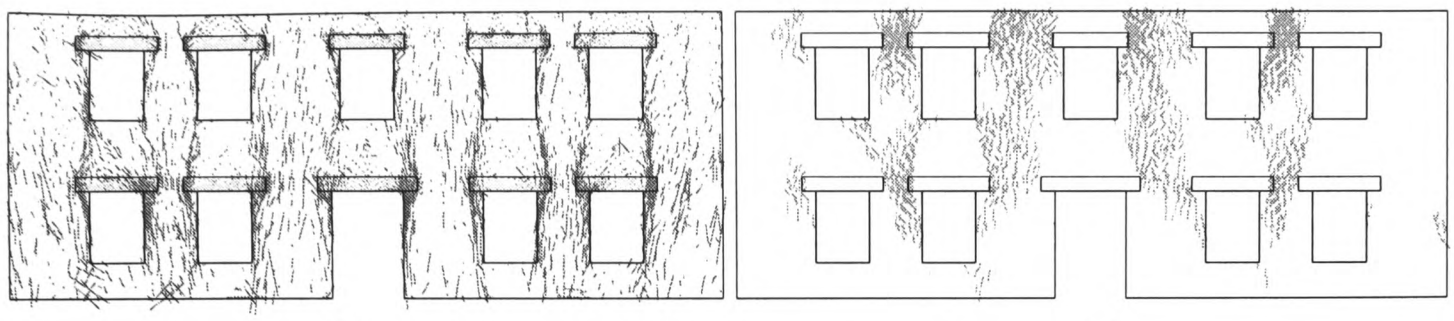


Figure 6.41: Stress Trajectory and Cracking Pattern at the Stage 4 in the Back Facade, Unsymmetric Combined Analysis(UHN)

Right End wall

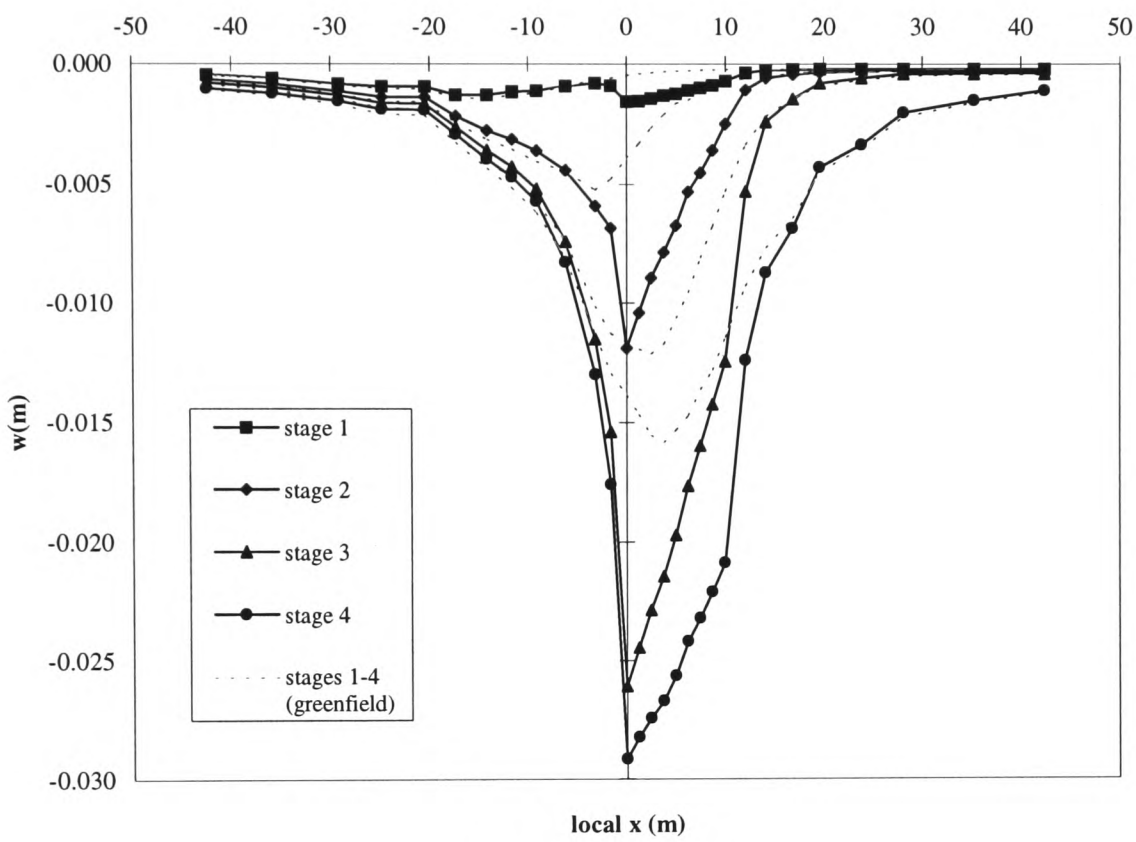
Figure 6.42 shows the settlement troughs and horizontal movement at all stages beneath the right end wall. Hogging mode is observed at the early stages and causes vertical cracks at the top of the end wall. The other cracking area at stage 2 is due to the tensile strain developing in the ground (Figure 6.43), which is enhanced by the corner effect shown in Figure 6.44.

At the late stages the end wall is able to resist sagging, giving a flat settlement trough, and shows no visible sagging cracks. However, tilt occurs through all stages and is magnified by the presence of the building.

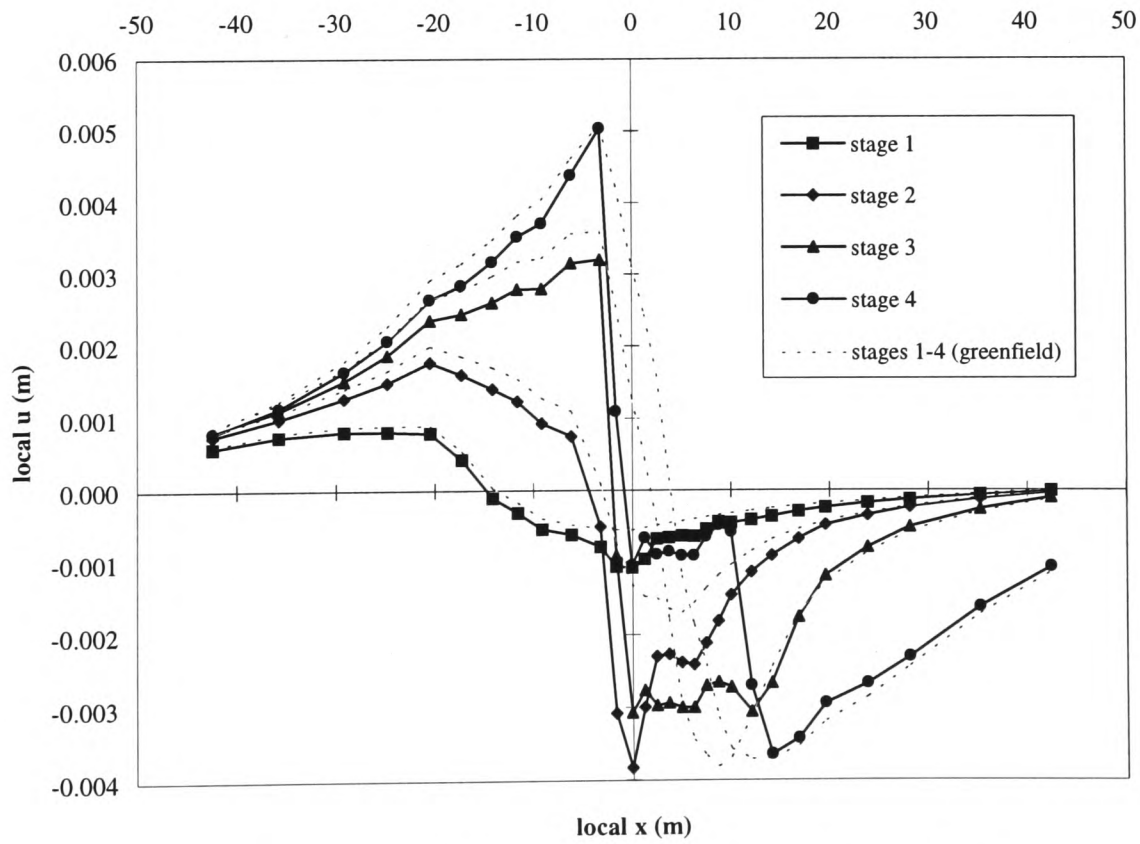
Left End wall

Figure 6.45-(1) shows that the settlement troughs from the combined analysis follow rather closely the hogging and tilt of the ground. In addition, the self-weight of the building causes the end wall to sink in the ground. The interaction between the building and the ground even results in a slight sagging under the left end wall at the end of excavation. The horizontal movements beneath the left end wall also follow the greenfield movements since the wall is located within the region of tensile horizontal strains (Figure 6.45-(2)).

A visible cracked area exists near the right edge through the excavation (Figure 6.46), which is caused by the corner effect. This is consistent with the corresponding cracking in the front facade, and is very different from the greenfield case in Figure 6.35.

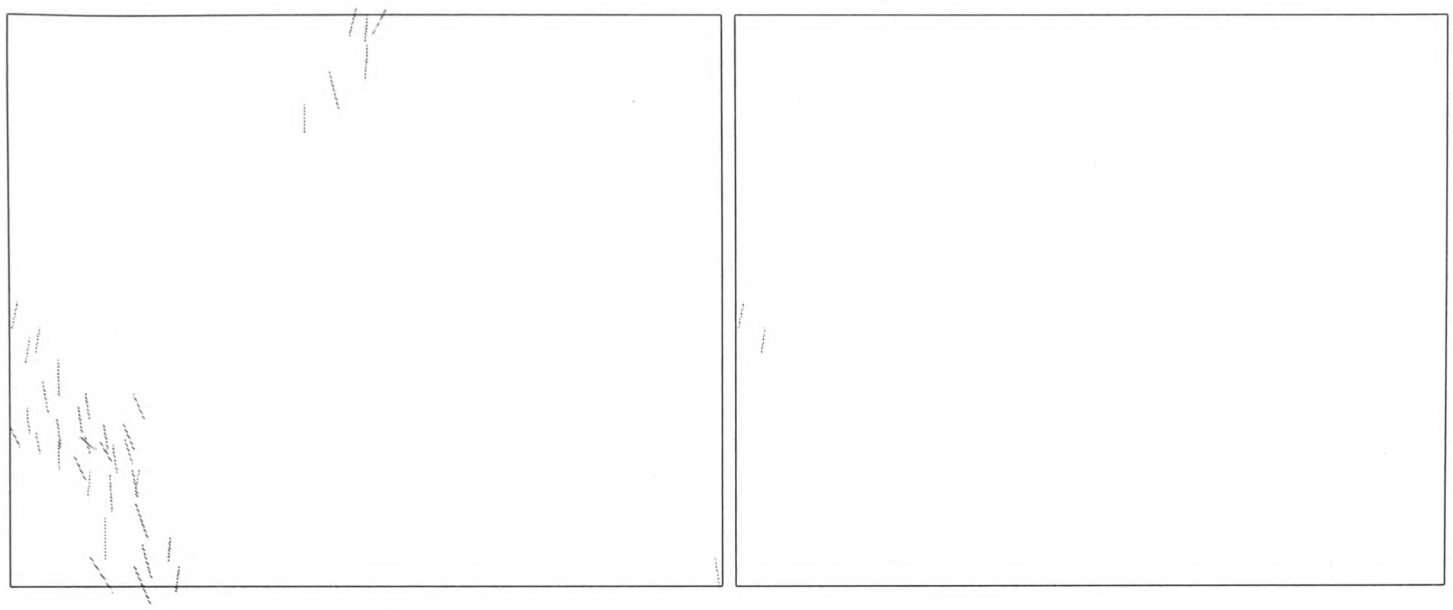


(1) Settlement



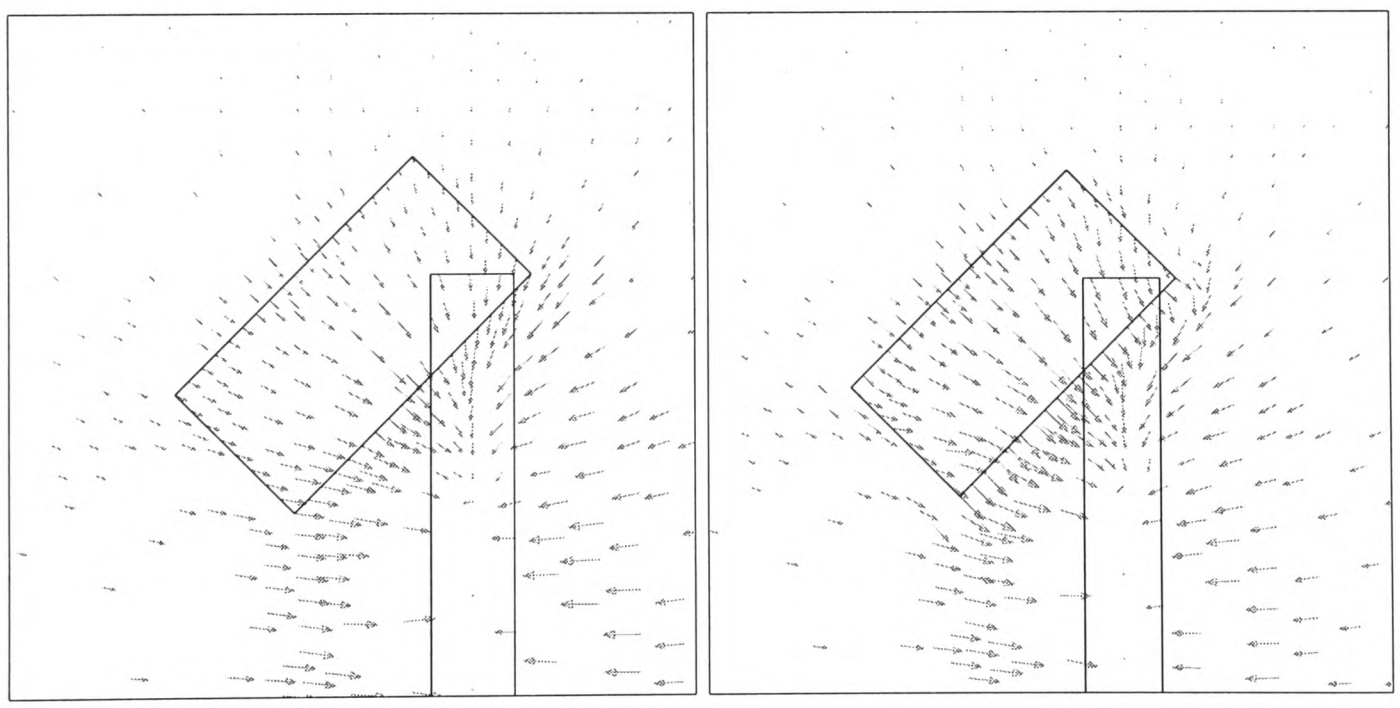
(2) Horizontal Movement within Plane of Wall

Figure 6.42: Ground Movements beneath the Right End Wall, the Unsymmetric Combined Analysis (UHN)



(1) (2)

Figure 6.43: Cracking Patterns at Stages 2 and 4 in the Right End wall, Unsymmetric Combined Analysis

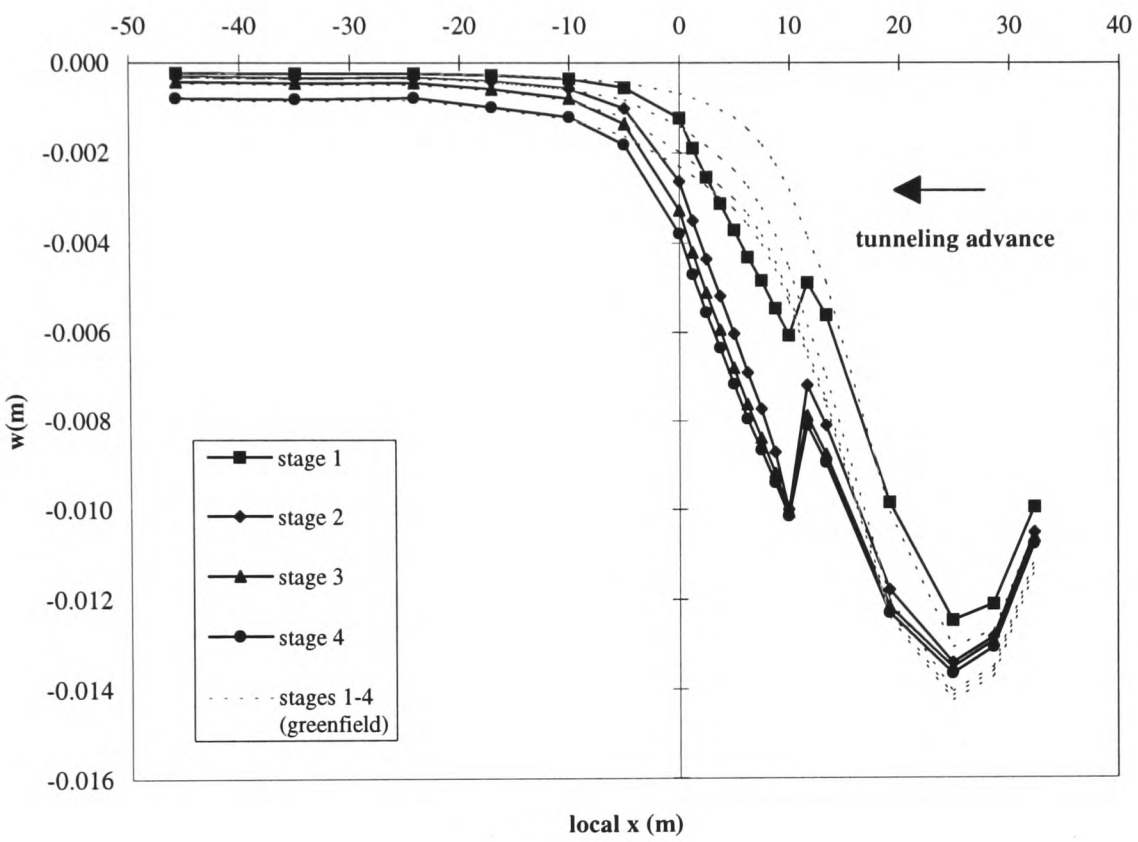


(1) (2)

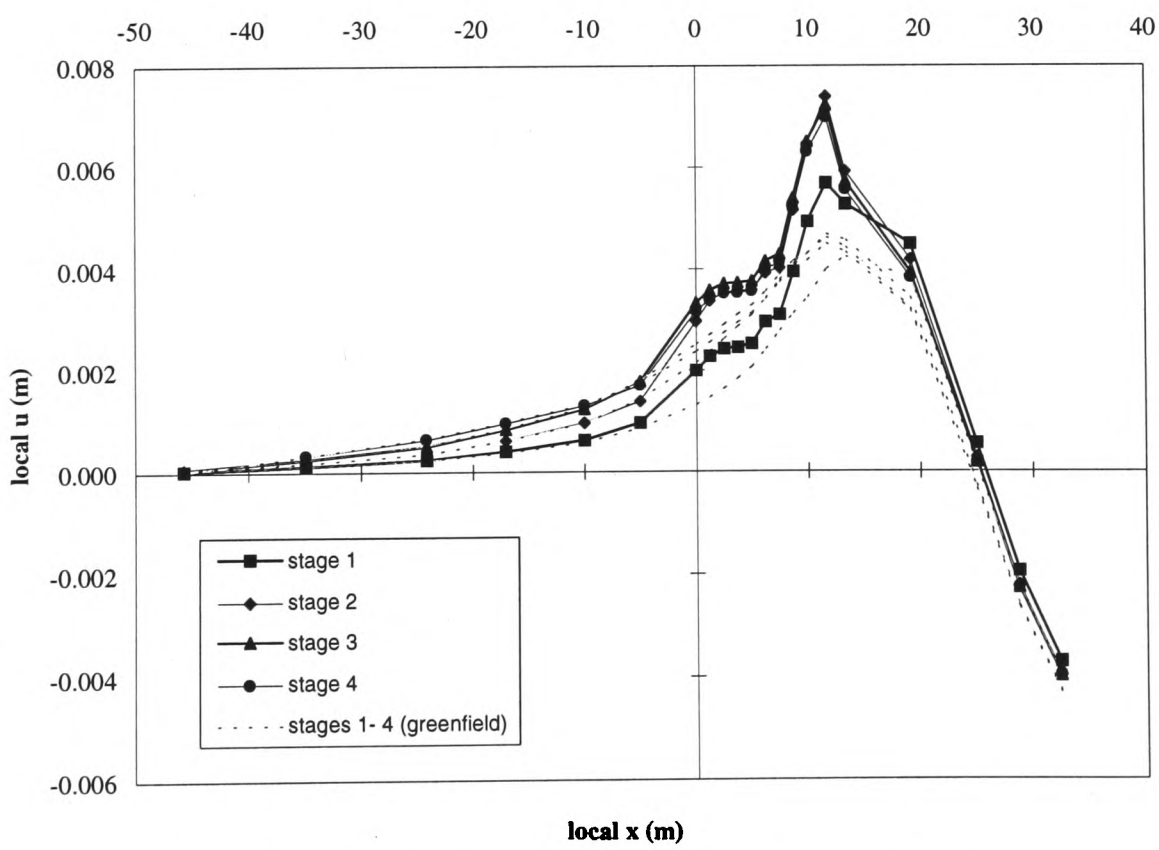
Figure 6.44: Soil Movement Vector Plots around Building, at Stage 2, (1) Greenfield (UG), (2) Combined Analysis (UHN).

6.5.3 A Comment on the Accuracy of the Solution

From Figure 6.44, it can be seen that during each stage the soil moves towards the middle of the excavated distance of the tunnel rather than the face of the tunnel. This problem can be solved by using a larger number of excavation stages. This, however,



(1) Settlement



(2) Horizontal Movement within Plane of Wall

Figure 6.45: Ground Movements beneath the Left End Wall, the Unsymmetric Combined Analysis(UHN)

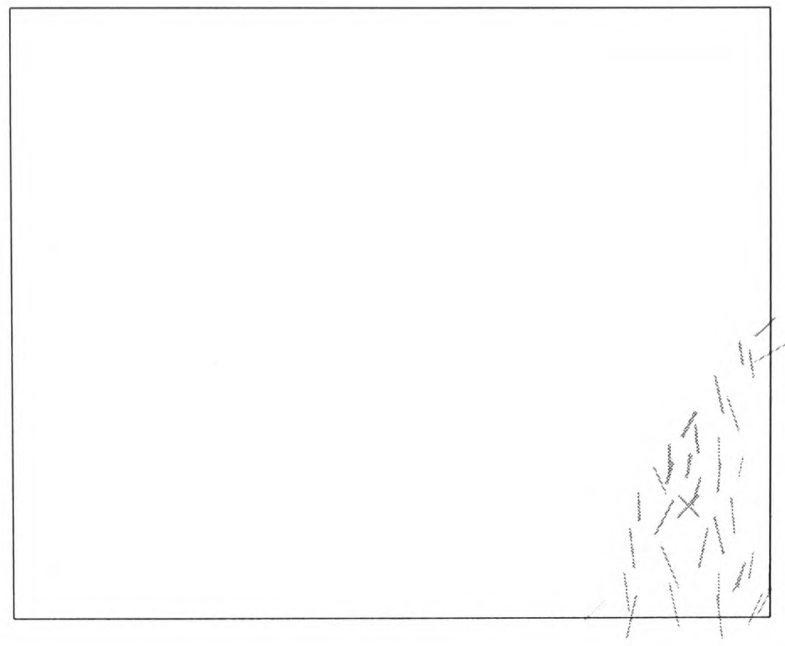


Figure 6.46: Cracking Pattern in Left End Wall, Unsymmetric Combined Analysis(UHN)

will lead to an increase of the computational effort.

For a given calculation amount, there are two options: a small number of stages each with a large number of steps, or a large number of stages each with a small number of steps. Although both numbers of stages and steps will effect the accuracy of the results, the number of stages controls the accuracy of the MODEL, while the number of steps dominates the accuracy of the SOLUTION of the model. Thus a larger number of excavation stages would be preferable.

6.6 Summary and Conclusion

In this chapter seven 3-D analyses were carried out to predict the behaviour of the building subject to ground movements induced by tunnelling. Both symmetric and unsymmetric cases were considered.

Firstly, these analyses have proved that the complete 3-D model for the building-ground system developed in this study and by Augarde (1997) can be used to study the interaction between masonry buildings and a shallow tunnel in soft ground.

Secondly, these test problems also offered a preliminary study of the 3-D behaviour of the settlement damage to masonry buildings due to tunnelling in soft ground.

For the building symmetrically located above the tunnel, because the ground finally

reaches a quasi-plane strain condition, the 3-D analysis shows predictions of settlement and cracking damage very similar to 2-D results. The stress arches are still formed in the masonry building and adjust the pressure between the facade and the ground so as to reduce the differential settlements.

The 3-D analysis also shows the importance of the weight of the building in the interaction, although the stress in the ground is less than in 2-D analysis for the same building. For the standard weight of building the stress in the ground can be reduced to less than half that in the 2-D analysis, thus resulting in smaller settlements, compared with the 2-D case. The 3-D analysis should model the stress in the ground under the building more realistically.

The elastic and masonry buildings with the same weight and elastic modulus have the same settlement at the inflexion point of the greenfield curve. However, the shapes of the settlement troughs are different. For the standard building or heavy building such a difference is small, but the light masonry building can be very flexible and follow the greenfield curve, rather than resembling the elastic building with the same weight.

In the unsymmetric condition, in particular a skew tunnel passing under the corner of the building, hogging and tilt areas are predicted by the greenfield approach. Since the stress arches cannot be formed in the facades or end walls within these areas, the combined analysis indicates more cracking and larger tilt. The presence of the building exaggerates this situation, thus the 3-D analysis is necessary.

In both the symmetric and unsymmetric analyses, local vertical cracking at the bottom corners of the masonry wall has been observed. This can be attributed to the horizontal movement of surface soil around the corners of the building. It is an example of a phenomenon which can only be predicted by 3-D analysis.

All the runs carried out in this chapter show that the influence area of the building on the ground around the building is relatively small.

In conclusion, the 3-D analysis is necessary to predict the behaviour of a building and its damage during tunnelling. Firstly, the practical problems, for example of the skew tunnelling in this chapter, cannot be solved by the simplified 2-D analysis. Second, some ground movements can only be predicted by the 3-D analysis, the typical example is the

corner effect. Lastly, even the 2-D analysis itself requires the 3-D analysis to provide an appropriate estimate of the thickness of the ground block.

7

Concluding Remarks

7.1 Summary and Main Findings of This Study

As a basis for this study, the existing finite element analysis program OXFEM was revised and updated. The modification to the procedures for stress updating was carried out by the author. In addition, a variety of utility programs were written for use in this study.

After a literature review on current masonry models, a macroscopic elastic no tension model was developed in Chapter 2 for the assessment of the cracking damage to masonry buildings due to tunnelling. In this model, the material behaves elastically in compression. If the major principal stress becomes tensile, the masonry cracks in the direction normal to the principal stress, and loses its stiffness correspondingly. A cracking strain is identified to represent the severity of the cracking damage, and to monitor the development or reclosure of the cracks. Some numerical techniques were developed to improve the stability of the calculation.

A complete 3-D model for assessment of the building damage requires connection between different parts of a building and between the building and the ground. This is accomplished by the tying scheme discussed in Chapter 3. The tying scheme accommodates nodes defined in different local co-ordinate systems and with different degrees of

freedom. The connection conditions between different nodes are fulfilled by installing specific tie elements which impose constraints to the relevant degrees of freedom. Several types of tie elements connecting 2-D nodes, a 2-D node with a 3-D node and 3-D nodes were formulated, implemented and validated in this chapter and can be used for connection of the building and the ground, and different parts of the building to each other.

As a preliminary study, the no tension model and elastic model were compared in Chapter 4 for both a plain wall, and a facade with openings, subject to a Gaussian curve settlement trough in 2-D. The results show that the no tension model behaves fundamentally differently from the elastic analysis, with different cracking patterns and damage severity predictions. It was concluded that the elastic model without cracking analysis cannot be used to simulate the behaviour of masonry buildings due to the ground movements induced by tunnelling.

Despite their limitations, the 2-D combined analyses carried out in Chapter 5 are able to provide useful insights into the interaction between the ground and a building. Both a plain wall, and a facade with openings, modelled with plane stress elements are combined with plain strain ground. Tunnel excavation is simulated by removing elements within the tunnel area. The analyses show that the the weight of the building, or more precisely the stresses in the ground before excavation, has a very important role in determining the ground movements during tunnelling. The soil under the building is previously partly yielded due to the self weight of the building, and has lower stiffness than in the greenfield. When the tunnel is constructed, these previously yielded areas enter a more highly non-linear state and relatively large settlement occurs under the building. The settlement under the building increases with the weight of the building. A potential sliding surface of failure can be identified if the building is sufficiently heavy.

Whilst the weight of the building controls the average settlement under a masonry building, its stiffness can only influence the shape of the trough. When the stiffness increases, the settlement trough becomes flatter and causes less damage.

The position of the facade is another critical factor affecting the ground movements. When it is located partially over the tunnel, a highly yielded surface develops from the

tunnel to one edge of the facade, leading to larger settlements and tilts. When the facade is located in the hogging area, the weight of building may even cause a local sagging area beneath it.

As the ground tries to settle, stress arches develop in the masonry facade located in the sagging and horizontally compressive area and cause redistribution of the pressure between the building and the ground. Such a redistribution of pressure leads to a flatter settlement trough underneath the masonry building. Therefore the stress arches are a key aspect in understanding the behaviour of masonry buildings during tunnelling.

The cracks which develop in the facade can be divided into two categories. One category of cracks are caused by the settlement trough and located along the stress arches. The combined analysis predicts less severe cracking of this kind than when the greenfield trough is applied. However, the large arching forces may cause the ground to move outwards horizontally, resulting in the emergence of the second category of cracks, which are approximately vertical. When the building becomes relatively heavy, the ground approaches bearing capacity failure, with large horizontal movements and more serious damage. The vertical cracking due to the horizontal ground movement is also observed when the facade is positioned in the overall hogging area. Since the ground beneath is in horizontal tensile strain, this prevents the formation of stress arches within the building but instead causes vertical cracks to develop from the base of the facade.

In Chapter 6, several 3-D analyses were carried out for a masonry facade box both located symmetrically and at a skewed orientation above a tunnel. In the symmetric case, since the ground finally reaches a quasi-plain strain condition, the results are similar to the equivalent 2-D analysis but with much smaller settlements. This is because the 3-D analyses give a lower, but more realistic, estimate of the stress in the ground than the simplified 2-D analyses. In consequence, the 3-D analysis predicts less damage. In the skew case, which cannot be analysed by 2-D analysis, the ground movements under the building are more complicated. Most parts of the building experience less damage in the combined analyses than when greenfield troughs are applied. But when part of the building is in the hogging region, it cannot resist the settlement and has more serious damage. In the 3-D analyses a corner effect which causes localised vertical

tensile cracking at the corners of the building was observed. This is a good example of the necessity of the 3-D analysis.

In conclusion, the presence of the building changes the ground movements beneath it. In most cases, it reduces the differential settlement and the cracking damage. Thus the conventional approach which applies the greenfield curve to the building overestimates the damage, leading potentially to unnecessary and costly protective measures. On the other hand, the weight of the building also causes highly non-linear conditions in the ground resulting in large average settlements beneath the building. Since the area of influence of the building is relatively small, the difference between the settlement underneath the building and in the surrounding ground may be large enough to cause damage to services. In some extreme situations, the weight of building might bring the soil underneath close to failure and cause serious damage to the building.

7.2 Recommendation for the Future Research

The currently used relationship between the cracking strain and the damage grades was borrowed from the previous work on elastic analyses. An appropriate relationship for a masonry building should be established in the future, based on the back analysis of case histories. In addition to the normal cracking strain, the shear deformation across cracks should also be included in this relationship.

Since the stress history in the ground before the excavation plays an important role in the ground movements during tunnelling, correct analysis of the stress in the ground due to the self-weight of the building is critical for the damage assessment. Currently, the deformation process of the soil under the weight of the building is assumed to be undrained. In fact consolidation in the ground would alter the stress and strength of the soil. Consideration of consolidation would be necessary for building a more precise model in future.

In the current model, the 2-D walls are connected to the non-linear ground directly. For the ground, the self-weight of the building appears as a line load on the ground and causes high stress in the soil underneath. In reality, this load is spread within the

thickness of the wall and is therefore of less intensity. Correctly simulating the base of the wall or the interface with the ground is another future task. This would require consideration of realistic foundation details for buildings.

Due to the lack of time, only a limited parametric study was carried out in this thesis using 2-D analysis. There are other factors affecting the ground movements and damage to the building, for example, the size, depth and construction method of the tunnel and the position, orientation, size and opening layout of the building. These factors could be the topics for future work.

The facade box used in this study is a simplified model for a real building. The other parts of the building and the foundation may also influence the ground movements during tunnelling and need to be included in the model to simulate the real behaviour of a building during the construction of a nearby tunnel.

In spite of the shortcomings implied by the need for this further work, the current research has led to an improved understanding of the interaction between buildings and the ground.

References

Addenbrooke, T. (1996). Holes in one. *Ground Engineering*, 29(3):31–34.

Ali, S. and Page, A. (1988). Finite element model for masonry subjected to concentrated loads. *Journal of Structural Engineering, ASCE*, 114(8):1761–1784.

Attewell, P., Yeates, J., and Selby, A. (1986). *Soil Movements Induced by Tunnelling and Their Effects on Pipelines and Structures.* London: Blackie.

Augarde, C. (1997). *Numerical modelling of tunnelling processes for assessment of damage to buildings.* DPhil thesis, Oxford University.

Boone, S. (1996). Ground-movement-related building damage. *Journal of Geotechnical Engineering, ASCE*, 122(11):886–896.

Boscardin, M. and Cording, E. (1989). Building response to excavation-induced settlement. *Journal of Geotechnical Engineering , ASCE*, 115(1):1–21.

Breth, H. (1974). Settlement behaviour of buildings above subway tunnels in Frankfurt Clay. In *Proceedings of Conf. on Settlement of Structures*, pages 329–336, Cambridge. London:Pentech Press.

Burd, H. (1986). *A large displacement finite element analysis of a reinforced unpaved road.* DPhil thesis, Oxford University.

Burd, H., Houlsby, G., Chow, L., Augarde, C., and LIU, G. (1994). Analysis of settlement damage to masonry structures. In *Numerical Methods in Geotechnical Engineering, Proceedings of ECONMIG 94*, pages 203–208, Manchester. Rotterdam:Balkema.

Burland, J., Broms, B., and De Mello, V. (1977). Behaviour of foundations and structures. In *Proceedings of 9th Int. Conf. Soil Mechanics and Foundation Engineering*, pages 2:495–546, Tokyo.

Burland, J. and Wroth, C. (1974). Settlement of buildings and associated damage.

In *Proceedings of Conf. on Settlement of Structures*, pages 611–654, Cambridge. London:Pentech Press.

Chow, L. (1994). Prediction of surface settlement due to tunnelling in soft ground. MSc thesis, Oxford Univeristy.

Cook, R. (1981). *The Concepts and Applications of Finite Element Method.* Wiley and Sons.

Davis, E., Gunn, M., Mair, R., and Senevivate, H. (1980). The stability of shallow tunnels and ground opening in cohesive material. *Géotechnique*, 30:397–416.

de Borst, R. (1991). Simulation of strain localisation: A reappraisal of the cosserat coninuum. *Engineering Computations*, 8:317–332.

Di Pasquale, S. (1992). New trends in the analysis of masonry structures. *Meccanica*, 28:173–184.

Frischmann, W., Hellings, J., and Snowden, C. (1994). Protection of the Mansion House against damage caused by ground movements due to the Docklands Light Railway extension. *Proceedings of the Institution of Civil Engineers, Geotechnical Engineering*, 107(2):65–76.

Geddes, J. (1991). Discussion on Boscardin and Cording(1989). *Journal of Geotechnical Engineering, ASCE*, 117:1276–1278.

Gunn, M. (1992). The prediction of surface settlement profiles due to tunnelling. In *Predictive Soil Mechanics, Proceeding of Wroth Memorial Symposium*, pages 304–316, Oxford.

Hibbitt and Karlsson and Sorensen, Inc. (1989). *ABAQUS theory manual*, 4.8 edition.

Houlsby, G. (1997). A model for the variable stiffness of undrained clay. (Personal communication).

Ignatakis, C., Stavrakakis, E., and Penellis, G. (1990). Analytical model for masonry using the finite element method. *Software for Engineering Workstations*, 6(April):90–96.

Institution of Structural Engineers (1989). *Soil-structure Interaction.* IStructE, London.

Katzenbach, R. and Breth, H. (1981). Non-linear 3-D analysis for NATM in Frankfurt Clay. In *Proceedings of the 10-th Int. Conf. on Soil Mechanics and Foundation*

Engineering, Vol 1, pages 315–318. Roterdam:Balkema.

Kerisel, J. (1975). Old structures in relation to soil conditions, 25th Rankine Lecture. *Géotechnique*, 25(3):433–482.

Kim, S. (1996). *Model testing and analysis of interactions between tunnels in clay.* DPhil thesis, Oxford University.

Lee, K. and Rowe, R. (1990a). Finite element modelling of three-dimensional ground deformation due to tunnelling in soft cohesive soils: Part 1 - method of analysis. *Computers and Geotechnics*, 10:87–109.

Lee, K. and Rowe, R. (1990b). Finite element modelling of three-dimensional ground deformation due to tunnelling in soft cohesive soils: Part 2 - results. *Computers and Geotechnics*, 10:111–138.

Loo, Y. and Yang, Y. (1991). Cracking and failure analysis of masonry arch bridges. *Journal of Structural Engineering, ASCE*, 117(6):1641–1659.

Lotfi, H. and Shing, P. (1994). Interface model applied to fracture of masonry structures. *Journal of Structural Engineering, ASCE*, 120(1):63–80.

Mair, R. (1979). *Centrifugal modelling of tunnel construction in soft clay.* PhD thesis, Cambridge University.

Mair, R., Taylor, R., and Bracegirdle, A. (1993). Subsurface settlement profiles above tunnels in clays. *Géotechnique*, 43(2):315–320.

Mair, R., Taylor, R., and Burland, J. (1996). Prediction of ground movements and assessment of risk of building damage due to bored tunnelling. In *Proceedings of Int. Symposium on Geotechnical Aspects of Underground Construction in Soft Ground*, pages 623–628, London.

Mensah-Dwumah, F. (1984). *Finite element modeling of brick masonry building behavior in response to deformations induced by shallow soft-ground tunneling.* PhD thesis, Stanford University.

Middleton, J., Pande, G., Liang, J., and Kraji, B. (1991). Some recent advances in computer methods in structural masonry. In *Computer Methods in Structural Masonry*, pages 1–21. Books and Journals International.

New, B. and Bowers, K. (1994). Ground movement model validation at the Heathrow

Express trial tunnel. In *Tunnelling '94*, pages 301–329, London. Chapman and Hall.

New, B. and O'Reilly, M. (1991). Tunnelling induced ground movements: predicting their magnitude and effect. In *Proceedings of 4th Int. Conf. on Ground Movement and Structure*, pages 671–697, Cardiff.

O'Reilly, M. and New, B. (1982). Settlement above tunnels in the United Kingdom, - their magnitude and prediction. In *Tunnelling '82*, pages 173–181, London. IMM.

Page, A. (1978). Finite element model for masonry. *Journal of Structural Division, ASCE*, 104(ST8):1267–1285.

Page, A., Kleeman, P., and Dhanasekar, M. (1985). An in-plane finite element model for brick masonry. In *Structural Masonry Analysis*, pages 1–18. American Society of Civil Engineers.

Pande, G., Liang, J., and Middleton, J. (1989). Equivalent elastic moduli for brick masonry. *Computers and Geotechnics*, 8(3):243–265.

Parry-Jones, M. and Cline, R. (1993). A study using finite element analysis into cracking in buildings caused by ground movements due to tunnelling, fourth year project. Technical report, Oxford University.

Peck, R. (1966). Deep excavations and tunnelling in soft ground. In *Proceedings of 7th Int. Conf. Soil Mechanics and Foundation Engineering, State of the Art Volume*, pages 225–290, Mexico City.

Potts, D. and Addenbrooke, T. (1997). A structure's influence on tunnelling-induced ground movements. *Proceedings of the Institution of Civil Engineers, Geotechnical Engineering*, 125(2):109–125.

Reisman, P. and Pawlik, P. (1980). *Elasticity Theory and Application.* Willey and Sons.

Simpson, B. (1968). Retaining structures: displacement and design, 32nd Rankine Lecture. *Géotechnique*, 18(1):56–66.

Simpson, B. (1994). A model of interaction between tunnelling and a masonry structure. In *Numerical Methods in Geotechnical Engineering, Proceedings of ECONMIG 94*, pages 221–228, Manchester. Rotterdam:Balkema.

Sluys, L. (1992). *Wave propagation, localisation and dispersion in softening solids.* PhD thesis, Delft University of Technology.

St John, H., Potts, D., Jardine, R., and Higgius, K. (1992). Prediction and performance of ground response due to construction of a deep basement at 60 Victoria Embankment. In *Predictive Soil Mechanics, Proceedings of the Wroth Memorial Symposium*, Oxford.

Wright, R., Littlejohn, S., and Sola, P. (1996). Ground treatment at Westminster, London. *AUA News, Journal of the American Underground Construction Association*, 11(1).

Zienkiewicz, O. and Chung, Y. (1967). *The Finite Element Method in Structural and Continuum Mechanics.* London:McGraw-Hill.

Zienkiewicz, O., Valliappan, S., and King, I. (1968). Stress analysis of rock as a 'no tension' material. *Géotechnique*, 18(1):56–66.

Zienkiewicz, O., Valliappan, S., and King, I. (1969). Elasto-plastic solutions of engineering problems 'initial stress', finite element approach. *International Journal for Numerical Methods in Engineering*, 1:75–100.